Bone remodeling and mechanomics : bridging organ, tissue, and cell scales to understand bone structure and function

Madge Martin

Université Paris-Est Créteil

Ecole Doctorale SIE : Sciences Ingénierie et Environnement

Queensland University of Technology

Science and Engineering Faculty

Thèse pour l'obtention du grade de

Docteur / Doctor of Philosophy

Spécialité : Mécanique

Madge MARTIN

Remodelage osseux et mécanome :

connecter les échelles de l'organe, du tissu et de la cellule afin de comprendre la structure et les fonctions de l'os

---

Thèse dirigée par Vittorio Sansalone / Peter Pivonka

Soutenue le 13 décembre 2019

Composition du jury :

M. Salah RAMTANI	Professeur CSPBAT, Université Paris 13 Nord	Président
Mme. Rachele ALLENA	Maître de conférences, HDR Ecole Nationale d'Arts et Métiers Paris	Rapporteur
M. Jean-Francois GANGHOFFER	Professeur LEM3, Université de Lorraine	Rapporteur
Mme. Sara CHECA	Professeur JWI, Charité Universitätsmedizin Berlin	Examinatrice
M. Ridha HAMBLI	Professeur PRISME, Polytech' Orléans	Examinateur
Mme. Marie-Christine HO BA THO	Professeur BMBI, Université Technologique de Compiègne	Examinatrice
M. Vittorio SANSALONE	Professeur MSME, Université Paris-Est Créteil	Directeur de thèse
M. Peter PIVONKA	Professeur Queensland University of Technology	Co-directeur de thèse
M. Thibault LEMAIRE	Professeur MSME, Université Paris-Est Créteil	Membre invité Co-encadrant
M. Guillaume HAIAT	Directeur de recherche CNRS MSME, Université Paris-Est Créteil	Membre invité Co-encadrant

Bone remodeling and mechanomics

Bridging organ, tissue, and cell scales to understand bone structure and function

by

Madge Martin
M.Sc Materials Science, Dipl. Ing. Mechanical Engineering

Faculté des Sciences et Technologie
Université Paris-Est Créteil Val-de-Marne

Sciences and Engineering Faculty
Queensland University of Technology

A dissertation submitted in partial fulfilment
of the requirements for the degree of
Doctor of Philosophy

13th December 2019

Keywords: bone remodeling, mechanobiology, biomechanics, thermodynamics, osteoporosis, drug interventions, vertebral bone adaptation.

In accordance with the requirements of the degree of Doctor of Philosophy in the Faculté des Sciences et Technologie at Université Paris-Est Créteil Val-de-Marne and Sciences and Engineering Faculty at Queensland University of Technology, I present the following thesis entitled:

Bone remodeling and mechanomics

Bridging organ, tissue, and cell scales to understand bone structure and function

This work was performed under the supervision of Professor Vittorio Sansalone, Professor Peter Pivonka, Professor Thibault Lemaire, Research Director Guillaume Haïat and Doctor J Paige Little. I declare that the work submitted in this thesis is my own, except as acknowledged in the text and footnotes, and has not been previously submitted for a degree at Université Paris-Est Créteil Val-de-Marne, Queensland University of Technology or any other institution.

Madge Martin

To my lifelong companion E.
– why make things simple when they can be way tougher?

Acknowledgements

I would first like to thank my large – and efficient – team of advisors. I will start with my married couple of Doktorvatern – although not with each other. Thank you Vittorio for taking me in and for this great partnership throughout the thesis. Thank you Peter for agreeing to this long-distance PhD and for welcoming me to Brisbane – three times, two of them ghost-free. Thank you Guillaume for being there for me, to give me advice or support. Thank you Thibault for your words of wisdom and wit that I will always welcome. Thank you Paige for your constant support and energy since the start of our collaboration.

I would like to thank my jury for making this videoconference work despite the huge strike. In particular, I want to stress how happy I was to see you, Sara, at my defence. It is indeed true that I got into biomechanics because I loved the work you did with Bettina at Charité. I look very much forward to seeing you again.

I thank as well my colleagues at the MSME laboratory. First, I would like to thank Salah Naili who helped me obtain my PhD scholarship and participated in setting up the joint agreement between QUT and UPE. I would like to thank former MSME PhD graduates who supported me in the start of my journey – Erica, Ilaria, Romain and in particular Antoisse who welcomed me in the tranquility of the ground floor PhD lair. Thank you Hai for your constant kindness; we missed you and wish you and your family the best. Thanks also go to my office-mates Ali, Bao, Fakhraddin and Ivan who invaded the lair peacefully and welcomed me back warmly after I deserted to Aussies. Thank you Manon for your steady enthusiasm, especially when it comes to accompanying me to concerts and learning about harpsichord feathers. Thanks also to Yoann for discovering with me a local social initiative, sticking with me and actually

filling up for me many times... My thanks also go to Didier Geiger who trusted me with handling tutorial classes by myself for the first time and gave me the once-in-a-lifetime opportunity to visit the National Criminal Research Institute (IRCGN). I am not forgetting Matthieu Caruel, fellow mechanical enginerering 'camarade' of the Ecole Nationale des Ponts et Chaussées who supported every initiative to bring the biomechanics team together and now bravely handles the upgraded version of MSMondays. Thanks to Sophie for organizing all the team events; I wish you great success. I would like to thank also the other collaborators I have not mentioned – permanents, post-docs, interns – that I met along the way, among which several participated in team-gathering initiatives of mine.

Moreover, I want to thank the Brisbane team. Endless thanks to Maree, who supported me personally and always had a solution to everything. You are a great human being and I am very happy I had the opportunity to meet you. My thanks also go to Dr Labrom and Dr Askin without whom our study would not have started. Thank you Rob for this Paris metro souvenir, which I believe is only one example of your kindness. Pawel, Max and Lionel, you are the Brisbane dream team for a good time. We should meet again for a cheat-banana bread some time in Europe. Thanks to Laure Stickel, I was definitely serious when I wrote that I hope to see you one day on the FWIS stage, I think you did a really great job and hope you will enjoy your future commitments. Many thanks to the rest of the Brisbane team, thank you for making me feel welcome when I came back although I did not know most of you. I am really sorry I did not get to know you better and wish you all the best.

Special thanks to my family who believed in me from day one. I am always grateful for my grandparents who help me understand where I come from and how to be proud of my origins and build something from that. With West Indies pride comes great responsibility and hard work, that is what my family taught me and what drove me until here. I would like to thank my parents who were there for me, literally pushing me at the airport – or, at least, pushing the trolley – so I could get on my plane. Thanks also to my brother Axel, always down to earth and asking questions that push me organize and focus my thoughts.

I would like to thank my friends, who stuck with my very absent self along these

years. Many thanks to the girls – Solange, Marie, Julie – who always had kind words to make me feel better. I would especially like to acknowledge Alexandre who *bon gré, mal gré* was always there for me ever since our eventful Valencia adventure – and even before, always giving me welcome or unwanted advice, but always thoughtful advice. Thank you for being my friend.

Finally, I will thank my partner Sylvain. I cannot thank you enough for keeping up with sleepless nights, appointments and stress crises. Well, who said E-girls could not have a baby?

Résumé (Français)

Notre squelette, structure essentielle du corps humain, a de multiples fonctions, parmi lesquelles on compte la régulation du métabolisme et la protection des organes. Nous étudions ici le remodelage osseux, processus par lequel la structure et la composition chimique de l'os évoluent au cours du temps. Les modifications biochimiques et structurelles du tissu osseux sont orchestrées par les cellules osseuses, capables de synthétiser de la matrice osseuse (ostéoblastes), résorber de l'os minéralisé (ostéoclastes), et aussi de réguler les voies de signalisation biochimiques en fonction de leur environnement mécanique (ostéocytes). Dans ce contexte, nous nous intéressons en particulier au mécanome, c'est-à-dire à la description de l'action de la mécanique sur les tissus biologiques. Nous étudions tout d'abord le mécanome du remodelage osseux à l'échelle cellulaire, où les voies de signalisation sont primordiales. Nous introduisons donc une représentation mathématique fine du remodelage osseux par un système d'équations différentielles décrivant les interactions entre les cellules osseuses des lignées ostéoclastiques et ostéoblastiques ainsi que la régulation de l'environnement biochimique par les ostéocytes. Ce modèle reproduit la perte de masse osseuse dans le cadre du défaut de gravité pendant un vol spatial et de l'ostéoporose post-ménopausique (OPM). La mise au point d'un modèle pharmacocinétique-pharmacodynamique couplé aux dynamiques biochimiques permet de relier la posologie d'un traitement anabolique de l'OPM (romosozumab) et le gain de masse osseuse, ce qui serait bénéfique pour la conception d'un traitement spécifique au patient. Nous proposons également une description macroscopique du remodelage osseux fondée sur un modèle de milieu continu généralisé. Tout d'abord, cette représentation est introduite dans le contexte du remodelage par rotation de la

microstructure osseuse. En effet, l'os est un matériau doté d'une micro-architecture et constitué d'une matrice de collagène minéralisé et d'une phase fluide accueillant les cellules osseuses actives. Dans un premier temps, nous proposons une identification analytique des états d'équilibre stables du remodelage par rotation. Cette théorie est ensuite utilisée dans une étude 2D par éléments finis appliquée à la tête fémorale humaine. Enfin, nous approfondissons ce cadre théorique reliant la mécanique macroscopique à la mécanobiologie : la cinématique du remodelage osseux est décrite à travers l'évolution de la déformation macroscopique, de la rotation de la microstructure, de la fraction de minéral, de la fraction poreuse et des concentrations de cellules. Cette description englobant chimie, biologie et mécanique fournit une structure pour l'étude des interactions entre ces trois domaines dans le contexte du remodelage. Les résultats prometteurs de nos simulations préliminaires permettent une interprétation du remodelage à la petite échelle qui pourra être mise en regard de données cliniques. Enfin, nous présentons une première application clinique de notre théorie multi-échelle dans l'étude du remodelage osseux chez les patients atteints de scoliose idiopathique de l'adolescent (SIA), pathologie d'origine inconnue se manifestant par une déviation tridimensionnelle de la colonne vertébrale. L'analyse des premiers échantillons de corps vertébraux de patients atteints de SIA prélevés en peropératoire suggère une dépendance des propriétés du matériau aux conditions de chargement anormales dues à la pathologie. Ces observations motivent la perspective d'une comparaison de ces résultats à des simulations fondées sur notre théorie mécanistique. En résumé, nous présentons dans cette thèse plusieurs approches de modélisation du remodelage osseux pour aboutir à une théorie unificatrice, et ce dans le but de mieux comprendre et aborder les mécanismes des pathologies osseuses, ce qui a pour objectif à terme le développement de solutions thérapeutiques spécifiques aux patients.

Abstract (English)

Our skeleton, an essential structure for the human body, has multiple functions, among which are the regulation of metabolism and the protection of organs. We focus here on bone remodeling, a process by which the structure and chemical composition of bone evolve over time. The biochemical and structural changes of bone tissue are orchestrated by bone cells, able to synthesize bone matrix (osteoblasts), resorb mineralized bone (osteoclasts), and to regulate biochemical signaling pathways according to their mechanical environment (osteocytes). In this context, we are particularly interested in mechanomics, which is the description of the action of mechanics on biological tissues.

We first study the mechanics of bone remodeling at the cellular level, where signaling pathways are essential. We therefore introduce a fine mathematical representation of bone remodeling by a system of differential equations describing the interactions between bone cells of osteoclastic and osteoblastic lineages, as well as the regulation of the biochemical environment by osteocytes. This model reproduces the bone loss in the contexts of micro-gravity during space flight and postmenopausal osteoporosis (PMO). The development of a pharmacokinetic-pharmacodynamic model coupled with biochemical dynamics makes it possible to link the dosage of an anabolic treatment of PMO (romosozumab) and the gain of bone mass, which would be beneficial for the design of a treatment specific to the patient.

We also propose a macroscopic description of bone remodeling based on a generalized continuum mechanics model. First, this representation is introduced in the context of rotary remodeling of the bone microstructure. Indeed, bone is a material with a micro-architecture, composed of a mineralized collagen matrix and a fluid

phase which hosts active bone cells. First, we propose an analytical identification of stable equilibrium states of rotary remodeling. This theory is then used in a 2D finite element study applied to the human femoral head. Finally, we enrich this theoretical framework by linking macroscopic mechanics to mechanobiology: the kinematics of bone remodeling is described through the evolution of macroscopic deformation, microstructural rotation, mineral fraction, porous fraction and cells concentrations. This description encompassing chemistry, biology and mechanics provides a structure for the study of interactions between these three fields in the context of remodeling. The promising results of our preliminary simulations enable an interpretation of remodeling on a small scale that can be compared with clinical data.

Finally, we present in this thesis a first clinical application of our multi-scale theory with the study of bone remodeling in patients with idiopathic scoliosis of the adolescent (AIS), pathology of unknown origin characterized by a three-dimensional deviation of the spine. The analysis of the first vertebral body samples from AIS patients taken intraoperatively suggests a dependence of the properties of the material on the abnormal loading conditions due to the pathology. These observations motivate the prospect of a comparison of these results with simulations based on our mechanistic theory. In summary, we present in this thesis several bone remodeling modeling approaches, resulting in the development of a novel unifying theory whose purpose is to better understand and address the mechanisms of bone pathologies, which ultimately aim at the development of patient-specific therapeutic solutions.

Résumé détaillé

Le squelette fournit une structure essentielle au corps humain, permettant le mouvement et la protection des organes. L'os est un tissu vivant poreux dont la phase solide est hétérogène, composée de matière organique et minérale organisée selon un arrangement hiérarchique complexe. Le tissu osseux comprend également une phase fluide permettant le transport des nutriments et des cellules souches dont la différenciation engendre une multitude de types de cellules osseuses. Parmi la variété de cellules osseuses, les ostéoclastes ont la capacité de résorber la matrice osseuse minéralisée et les ostéoblastes synthétisent une matrice organique qui se minéralise au cours du temps. Les cellules osseuses sont sensibles à leur environnement biochimique qui régule leur activité. Ainsi, la prolifération, la différenciation, l'apoptose des cellules et leur production de protéines sont des mécanismes qui dépendent de la présence de molécules spécifiques dans leur environnement. De plus, la contribution du chargement mécanique à la régulation des voies de signalisations biochimiques est considérable car celui-ci affecte particulièrement les cellules différenciées incluses dans la matrice osseuse, appelées ostéocytes. Ce mécanisme de régulation du métabolisme osseux faisant intervenir les actions cellulaires mais aussi les *stimuli* biochimiques et mécaniques est appelé remodelage osseux. L'élaboration d'un cadre théorique cohérent pour la description de ce processus multi-physique constitue le sujet principal de ce travail de thèse.

Notre objectif principal est le développement d'un cadre théorique de modélisation du remodelage osseux dans un contexte multi-échelle. En particulier, cette approche du remodelage est conduite du point de vue du mécanome, c'est-à-dire de la description de l'action de la mécanique sur les tissus biologiques. Ainsi, cette dissertation

est centrée sur le rôle de la mécanique dans la régulation du remodelage osseux dans des conditions saines ainsi que dans le contexte de pathologies osseuses.

Dans un premier temps, nous introduisons un modèle de remodelage osseux à l'échelle tissulaire prenant en compte les interactions entre cellules osseuses. Par conséquent, nous introduisons une théorie mathématique mécanobiologique fine du remodelage osseux qui prend en compte les interactions entre les cellules osseuses des lignées ostéoclastiques et ostéoblastiques et leur environnement biochimique. Dans ce modèle, la sensibilité des cellules osseuses aux *stimuli* mécaniques est intégrée en tenant compte de la modulation de la signalisation biochimique par les ostéocytes qui affecte donc l'activité de remodelage des autres cellules osseuses. Ainsi, une altération du remodelage d'origine mécanique induit une altération des propriétés du tissu osseux, modifiant donc la valeur des *stimuli* mécaniques, ce qui crée une boucle de rétroaction régulée par la mécanique. Ce mécanisme de régulation peut être perturbé en cas de modification des conditions biochimiques ou mécaniques. Ces situations ont pu être reproduites par notre modèle lors de simulations de la perte osseuse due à l'ostéoporose post-ménopausique (OPM) et de la micro-gravité pendant un vol spatial. En outre, cette représentation à la micro-échelle a permis la mise au point d'un modèle pharmacocinétique-pharmacodynamique capable de décrire l'évolution de la masse osseuse chez les sujets OPM après le début d'un traitement favorisant la formation osseusse (anabolique) avec le romosozumab, et ce pour des sites anatomiques différents. Nos résultats montrent que le modèle proposé permet de relier la posologie et le gain de masse osseuse, ce qui serait bénéfique pour la conception d'un traitement par romosozumab spécifique au patient. Dans ce modèle, la loi d'évolution du remodelage est introduite *ad hoc* . De plus, seule la variation de porosité est modélisée, sans considérer l'évolution de la micro-architecture osseuse.

La deuxième partie de cette thèse propose une description du remodelage osseux à l'échelle du tissu, dans l'objectif d'obtenir une loi d'évolution du remodelage découlant des principes de la thermodynamique prenant en compte les variations de micro-architecture. Ce point de vue est traduit dans un modèle de milieu continu généralisé. Tout d'abord, cette représentation est introduite dans le contexte du remodelage par rotation de la microstructure osseuse, en fournissant une analyse de la

variation de l'énergie libre en fonction de l'orientation microstructurale du tissu osseux. Nous trouvons en premier lieu un résultat attendu : les variations de l'énergie de déformation sont étroitement liées à la réalisation d'un équilibre de remodelage stable. De plus, nous trouvons une identification analytique des états d'équilibre stables. Ce modèle de remodelage rotatif osseux est ensuite utilisé dans une étude 2D par éléments finis appliquée au fémur proximal. Enfin, nous approfondissons ce cadre théorique en reliant la mécanique de la macro-échelle à la mécanobiologie : la cinématique du remodelage osseux est décrite à travers les évolutions de la déformation macroscopique, de la rotation de la microstructure, de la fraction de minéral, de la fraction poreuse et des concentrations de cellules. Cette description englobant la chimie, la biologie et la mécanique fournit une structure pour l'étude des interactions entre ces trois domaines dans le contexte du remodelage. Les résultats prometteurs de nos simulations préliminaires (carence en calcium, réduction du chargement mécanique) permettent une interprétation du remodelage à la petite échelle qui pourra être mise en regard de données histomorphométriques dans le cadre d'applications cliniques.

Enfin, nous présentons dans cette thèse les premières étapes d'une application de notre modèle multi-échelle à l'étude du remodelage osseux chez les patients atteints de scoliose idiopathique de l'adolescent (SIA), pathologie d'origine inconnue se manifestant par une déviation tridimensionnelle de la colonne vertébrale. Cette déformation se manifeste en particulier chez les jeunes filles durant leur poussée de croissance pubertaire. Notre application clinique est fondée sur l'hypothèse que la modification du chargement mécanique sur les corps vertébraux génère une adaptation de la microarchitecture osseuse. Dans le cadre du protocole accepté par le comité d'éthique de Children's Health Queensland (Human Research Ethics Committee), plusieurs corps vertébraux de patients atteints de SIA ont été prélevés en peropératoire. Le tissu osseux des échantillons de vertèbres a été caractérisé à l'aide de plusieurs techniques (spectroscopie Raman, microscopie électronique qBEI, micro-tomographie). Dans de futurs travaux, les observations expérimentales seront mises en regard de notre modèle de remodelage, appliqué à ce problème 3D à des conditions aux limites et géométrie complexes.

En résumé, cette thèse développe plusieurs approches de modélisation du remodelage osseux ainsi que des outils mathématiques afin de mieux comprendre et aborder les mécanismes des pathologies osseuses, ce qui a pour objectif à terme le développement de solutions thérapeutiques spécifiques aux patients.

Contents

Chapter 1

Introduction

Our skeleton has a variety of purposes, in particular protecting major organs, allowing a determinate range of motion and providing a reservoir of calcium and a main site for hematopoiesis. Bone remodeling refers to the permanent underlying biochemical mechanisms that modify bone structure and composition throughout life. This process is complex and multi-physical as it involves chemistry, biology and mechanics from the cellular to the organ scale.

Theoretical and numerical models of bone remodeling have been developed over the past decades, relying on the widely accepted statement that bone responds to mechanical loading and that this adaptation proceeds towards an optimized structure. This assumption, formulated in the late 19th century by Julius Wolff [206], is nowadays referred to as Wolff's law.

While numerous models are available in the literature, two main challenges remain. Firstly, the multiscale nature of bone remodeling is key. Most models only describe events at the cellular scale, evaluating the influence of a mechanical stimulus or a modified biochemical environment on signalling pathways [101, 117, 110, 156], or at the macroscopic scale, quantifying the biological regulation with a phenomenological law [12, 83]. The evolution of bone tissue properties involves biological events at the micro-scale that are not easily translated to the tissue scale. Conversely, mechanical loads at the macro-scale also need to be interpreted at the cellular scale. A recent attempt to tackle this last point was made by Scheiner et al., who constructed a

micro-mechanical framework to link macroscopic stresses to the stimuli sensed by bone cells [172]. Secondly, most theories only propose *ad hoc* remodeling laws that aim at concomitantly representing diverse phenomena.

The models developed in the present thesis aim at encompassing the variety of mechanisms present in bone remodeling in a physically sound way in order to better address pathological situations. In particular, this thesis will focus on the effects of mechanical disuse and hormonal changes on bone remodeling, and more specifically drug treatment of osteoporosis. Finally, this thesis includes the protocol of a clinical application using a combination of experimental and theoretical methods to assess bone microstructural changes due to altered loads distribution in the context of adolescent idiopathic scoliosis.

1.1 Aims and objectives

This thesis focuses on the following research question: what theoretical framework could describe bone remodeling at the microscale to predict the macroscopic evolution of bone tissue?

This global problem will be addressed through the following objectives:

1. extension of an existing mechanobiological model of bone remodeling to account for mechanosensitivity of specific bone cells (osteocytes) and the influence of drug treatment;

2. development of a comprehensive theory of bone remodeling at the macroscale based continuum on thermodynamics;

3. development of a numerical algorithm translating the novel thermodynamics-based bone remodeling theory into macroscopic bone geometries;

4. initiation of a clinical application via the development of an experimental protocal.

The first objective involves a review and selection of the main signalling pathways regulating bone remodeling and cells turnover. The major aim of bone cell popu-

lation models (BCPM) is to serve as a decision-making tool for bone clinicians and biologists in order to identify molecular targets for drug treatments. The present work focuses on the effect of romosozumab, a recently synthesized monoclonal antibody which stimulates bone formation, in particular in post-menopausal osteoporotic patients. The drug based on this antibody (Evenity®) was recently authorized in Japan, South Korea, USA, Canada and EU. This study includes the development of a pharmacokinetic-pharmacodynamic (PK-PD) model capturing the dynamics of the binding of the drug to its target in the body, its clearance and its effect on bone metabolism. Utilizing this model, one is able to identify the most efficient drug dose and administration interval in terms of bone gain for this treatment of osteoporosis.

The theoretical work entailed by the second objective relies on earlier theories of generalized continuum mechanics [71, 72] and of remodeling [43]. In particular, this work stems from a theory developed by DiCarlo et al. [42] who focused on bone orthotropic remodeling. DiCarlo and coworkers investigated the rotation of material axes as a function of the mechanical environment. In the current thesis, this theory is extended: firstly, by accounting for remodeling in terms of porosity, mineralisation and cellular activity; secondly, by integrating the role of biochemistry and mechanobiology.

The third objective was to integrate the presented tissue scale approach to a macroscopic – *i.e.* organ-scale – description of bone mechanical loading. Numerical modeling enables the connection of tissue scale theoretical developments with clinical applications. In order to do this, a numerical algorithm was developed, coupling a finite-element software (Comsol Multiphysics® 5.3a [1]) and a numerical computing environment (Matlab® [3]). The bone remodeling law derived from theoretical calculations was implemented into Matlab® to calculate the evolution of remodeling state variables in function of the mechanical environment. The mechanical environment was defined using finite-element analysis to compute strains and stresses, that are also affected by the remodeling state. This routine was then tested on several benchmark 2D geometries, including a human femur.

Stemming from numerical and theoretical work described in the first three objectives, this dissertation entails a fourth objective, a clinical application. A study

of bone quality in adolescent idiopathic scoliosis patients started in December 2018, following ethics approval from Children's Health Queensland. Adolescent idiopathic scoliosis (AIS) is a three-dimensional deformity of the spine, characterized by lateral curvature exceeding 10°, rotation of spinal column and loss of the normal sagittal spine profile. This pathology implies an abnormal distribution of loads in the spines of the patients, among which the deformations are highly variable. In order to investigate the relationship between deformity progression in AIS and bone quality, cylindrical samples of vertebral bodies obtained intra-operatively are assessed using various imaging techniques. This clinical study aims at shedding light on the effect of perturbed mechanical loading associated with vertebral bone development and metabolism that may characterize AIS.

1.2 Scope of the work

As mentioned earlier in this introduction, bone remodeling is a highly complex process involving multiple scales and physics. Hence, theoretical modeling is a challenge, especially when one aims at tackling the biological, chemical and mechanical phenomena regulating bone remodeling. The purpose of the present thesis is to address this problem through the development of novel theoretical frameworks.

Here, two main frameworks are developed. The first one stems from mechanobiology and micro-mechanics. While this model stems from previous publications [156, 172], the works presented in this thesis focus on the chemical signaling by bone cells, its impact on bone remodeling, and how drug treatment can affect bone remodeling. This model describes quantitatively the effect of signaling pathways on bone cells activity. The latter directly regulates bone tissue porosity, which affects the mechanical stimulus sensed by bone cells embedded in the bone matrix (osteocytes). The biochemical regulation of bone remodeling is controlled by signaling molecules, including molecules produced by the mechanically-sensitive osteocytes. This mechanistic framework enables the description of bone loss following a decrease in mechanical loading or a hormonal change (post-menopausal osteoporosis), as well as the restoration of bone mass following an increase in mechanical loading, or a treatment

stimulating bone formation (anabolic treatment).

The second framework is a novel theory based on generalized continuum mechanics embracing the multi-physical aspect of bone remodeling. The simultaneous events of biological, chemical and mechanical origin taking place during bone remodeling are accounted for via their energetic contribution. To this end, each material point not only carries information on the current macroscopic displacement, but also on the local microscopic state of the material. Hence, the definition of the continuum involves textural indications: the local micro-architecture, its porosity, its mineral content and concentrations of cells. The evolution of the state variables relies on the expression of the principles of continuum thermodynamics.

This work also entails a protocol for a clinical application aims at demonstrating the links between mechanics and vertebral bone microstructure in adolescents with AIS. This final experimental and modeling application requires fine data, giving information on the microscopic state of bone in a given macroscopic mechanical environment. To this end, a collaborative clinical study with surgeons of the Queensland Children's Hospital in Brisbane started in December 2018 to assess bone structure and composition in adolescent idiopathic scoliosis (AIS) patients. Bone cores collected during scoliosis surgery will provide novel information on the metabolism of the pathology and the influence of mechanics. This thesis will present the protocol of this study.

1.3 Outline of this dissertation

The dissertation by published articles is composed of nine chapters detailing the different aspects of the present work, three of them introducing submitted articles.

First, in Chapter 2 the properties of bone are presented, bone being at the same time a heterogenous micro-architectured material and a living tissue. This chapter depicts bone structure and biology, and how this knowledge impacted the understanding of bone remodeling and its connection with mechanics, from the 18th century until now.

Chapters 3 and 4 depict a mechanobiological framework for bone remodeling. In

particular, Chapter 3 describes the influence of main signalling pathways on bone turnover using a multiscale model (published article [122]). Chapter 4 applies the theory developed to the treatment of post-menopausal osteoporosis through the subcutaneous administration of a drug, romosozumab (tentatively accepted article).

In Chapter 5, the reader will find developments on an existing theoretical framework of bone remodeling [42] focusing on the rotation of bone microstructure (accepted article). This study focuses on the stability of rotary remodeling equilibrium configurations. The application of this model to 2D benchmarks using the previously-introduced thermodynamics-based bone remodeling algorithm is developed in Chapter 6. A macro-scale example is provided, based on the geometry of human femur.

With the aim of integrating the first objective – a mechanobiological description – into a thermodynamics-based framework of bone remodeling (as suggested in the second objective), a novel bio-chemo-mechanical framework for bone remodeling based on thermodynamics is developed in Chapter 7. This model describes the interactions between bone structural changes, mechanics and the biochemical environment. This last theoretical chapter unifies the work presented in previous chapters by providing links between cell population models – based on mechanobiology – and phenomenological models – which provide more global insights. Indeed, this novel theory provides a macroscopic approach to mechanobiology and biochemistry in the context of bone remodeling.

Finally, Chapter 8 is dedicated to the protocol of a clinical application of the previous chapters, investigating bone remodeling in adolescent idiopathic scoliosis patients.

The last chapter - 9 - is dedicated to the conclusions and proposes future perspectives of this work.

Chapter 2

Bone remodeling and mechanomics

From understanding to modeling a complex multiscale biological process

2.1 Bone remodeling, a multiscale biological process

2.1.1 Bone structure: micro-architecture and composition

Bone is a heterogeneous material that can be examined from various perspectives. First of all, from a day-to-day point of view, bone is an organ providing the necessary scaffolding and support for the preservation of major organs and the execution of daily activities. Our bony structure is animated by muscles, tendons and ligaments. Muscles, operated by the nervous system, are attached to the skeleton and induce motion. This motion is limited by ligaments, which are resilient and stiff units of fibrous connective tissue joining bones. Finally, the combination of the aforementioned elements, called the musculoskeletal system, allows vertebrates a determinate range of motion. Aging, hormonal changes and diseases are some of the parameters that can impact the musculoskeletal system. In fact, over the course of life, muscle fibres, connective tissue and bone tissue change properties and therefore modify the stability, resilience, range of motion and protective properties of the skeleton. The analysis and understanding of the change in tissue properties require to examine them

at all different scales. In the present thesis, the focus will be set on bone tissue and the evolution of its micro-architecture and composition over time.

At the tissue level, bone is a composite organic tissue exchanging with the biological environment. Bone is composed of collagen fibers, non-collagenous organic matter, inorganic salts, water and mineral [87]. While bone is built and resorbed by cells (see Section 2.1.2), the bone matrix itself contributes to the cellular metabolism, being a source of ligands and mineral that can be released into the fluid space [15, 32, 138, 148, 87]. There are two main types of bone tissue: cortical and trabecular tissue. Cortical bone, or compact bone, is a dense and stiff structure that accounts for approximately 80% of human bone mass [87]. Compact bone forms the outer layer of bones and is critical for the load-bearing abilities of the skeleton. As shown in Figure 2.1, cortical bone can be found in the diaphysis of long bones, surrounding the marrow cavity. The cortical outer shell of bones is called cortex. Conversely, trabecular bone, also known as spongy bone or cancellous bone, is a porous structure constituted by a network of rods and plates called trabeculae. Typically, bone tissue is cancellous at the epiphysis of long bones, in several flat bones (skull, ribs, shoulder) and on the inside of vertebrae.

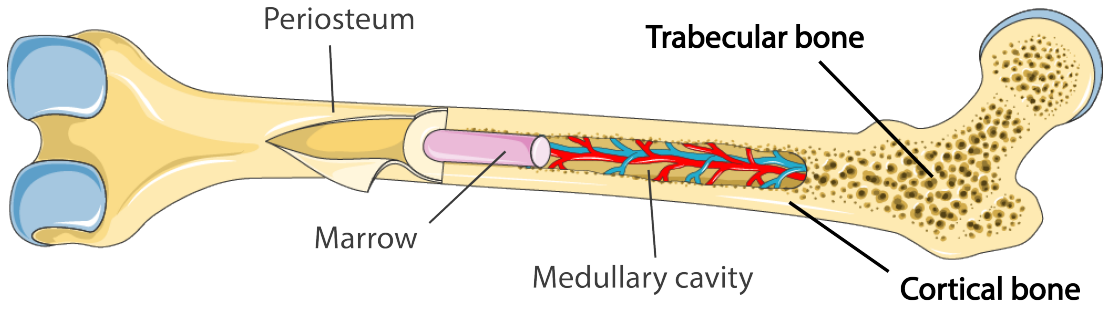

Figure 2.1: Bone tissue types in long bones: example of the femur. Adapted from 'Bone structure" by Servier, licensed under CC BY 3.0.

Mature cortical bone is a dense and stiff tissue often composed of cylindrical collageneous units called osteons. Osteons are made of concentric rings of unit layers (lamellae) surrounding vascular channels, the Haversian canals. The latter contain blood vessels, lymph vessels, and nerves, therefore allowing cell signalling as well as the transport of nutrients and undifferentiated cells from the marrow to the tis-

sue (see Figure 2.2). The haversian porosity is connected to perpendicular canals (Volksmann's canals) and microscopic canals called canaliculi.

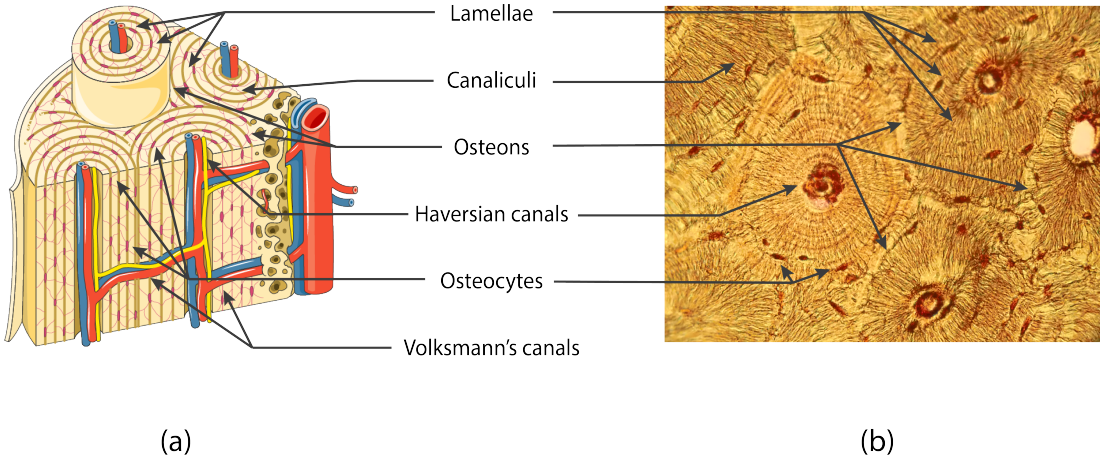

Figure 2.2: Cortical bone structure: (a) simplified illustration, (b) cortical tissue section. Adapted from 'Osteon" by Servier, licensed under CC BY 3.0, and from 'Compact bone with osteons" by Lord of Konrad, licensed under CC0 1.0.

Lamellae are pseudo-cylindrical layers of parallel mineralized collagen fibers. Each adjacent lamella has a specific orientation, which can differ as much as 90° from the next lamella. Figure 2.3 shows the diversity of orientation patterns of the lamellae highlighted by the use of polarized light microscopy (data from Bromage and coworkers [22]). Bone being a living material, new osteons are built by bone cells throughout life in mature cortical tissue. The remaining angular fragments are called interstitial lamellae. Note that some cortical bone patterns do not have an osteonal structure, such as circumferential lamellae at the outer surfaces the cortical shell.

Cancellous (trabecular) bone is a porous and lighter tissue organized in a network of trabeculae. The trabecular network lies in a large vascular space enclosing marrow and blood vessels. Trabeculae are composed of concentric lamellae roughly parallel to the trabecular surface. These structures are sometimes referred to as hemiosteons because the process leading to the formation of trabeculae is similar to the fabrication of osteons by bone cells. In trabecular bone, instead of surrounding a vascular canal, the bone surface (trabecular surface) borders the marrow cavity. Additionally, the arrangement of lamellae in cancellous bone does not replicate the circular appearance of whole secondary osteons.

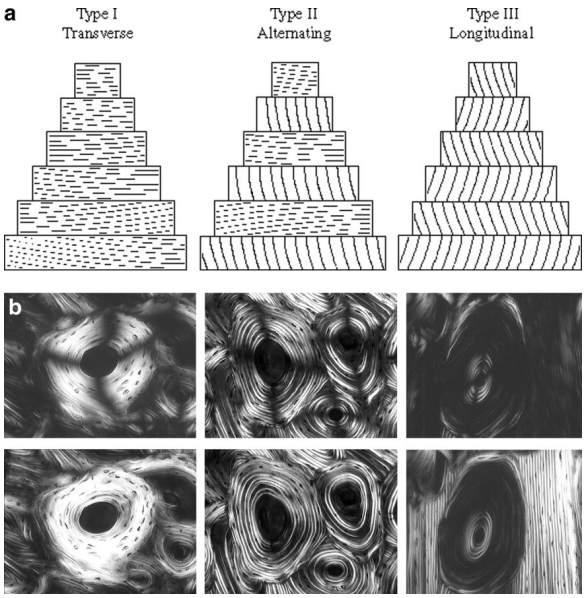

Figure 2.3: Osteonal structure. (a) Schematic illustrating the diversity of orientation patterns in successive lamellae through 3 extreme examples. (b) Sections of osteonal networks under polarized light (first row: linear; second row: circular). Left and middle sections were obtained from a sample of modern human femoral midshaft, and the longitudinal osteon images derive from the femoral midshaft of a brown-headed spider monkey (*Ateles fusciceps*). From Bromage et al. [22], with permission.

2.1.2 Biological actors of bone remodeling

Bone remodeling is a continuous process of formation and resorption driven by bone cells over the course of life. Two bone cell lineages have been identified over the past decades that fall respectively within the lineage of bone-forming or bone-resorbing cells. This section describes how these cells regulate bone remodeling in cortical and cancellous bone.

Some historical landmarks

The osteoblastic lineage was the first to be identified and named. At the beginning of the 19th century, many works already referred to so-called '*osteoplasts*', which only gained their current name 'osteocytes' in the late 1800s. At the time, *osteoplasts* were already described as star-shaped cells embedded in the bone matrix [21, 162][1].

[1] While the definition of *osteoplasts* appeared in dictionaries in the early 19th century, the nature, life and analysis of *osteoplasts* remained a controversy for a long time. The interested reader can refer to the heated discussions at

Figure 2.4 displays selections from Broca's drawings [21] from 1870 (a) and an excerpt from the *Nouveau Dictionnaire lexico graphique et descriptif des sciences médicales et vétérinaires* [158] (b), where osteocytes ('*osteoplasts*' on the drawing) are clearly displayed. The first occurence of the word 'osteocyte' I could find dates to 1893, when Perrier mentions osteocytes as a synonym to bone cells or *cellules osseuses* – reflecting its exact etymological translation, which he defines as the cells which sit in the cavities of the bone matrix (today known as lacunae) that he calls *osteoplasts* [149][2].

The word 'osteoblast' first appeared in 1864 with the works of the German biologist Gegenbauer [67]. The word combines the prefix associated with bone ('osteo') and 'blast', which refers to an undifferentiated cell. As Gegenhauer identified osteoblasts as the bone-forming cells, the lineage relationship between the two cell types was already clear: osteoblasts were defined as undifferentiated cells as they were believed to differentiate into osteocytes (or, back then, *osteoplasts*). Later research led to the verification of this statement that is well accepted nowadays. Alfred Richet states in 1877 [162] (originally in French and translated by myself):

> The cells of the medullary spaces (Gegenbaur [*sic*] osteoblast) become bone cells [osteocytes][3] and surround themselves with calcareous salts, so it becomes easy to understand the use of this limescale, prior to ossification. In endosmosis the calcareous salts, dissolved with the help of the beginning blood circulation, penetrate into the medullary spaces, and provide the solid elements which will surround the osteoblasts so that they become osteoplasts with bone wall. [...] These osteoblasts that Gegenbaur [*sic*] has the first well described are variable in shape: they have 20 to 30 μ [*sic*] in diameter; they are generally fusiform, their membrane is thin at first, and their protoplasm granular; little by little they become encrusted with calcareous salts, and become starry only at this time; then

the French *Académie des Sciences* [136] and to later works confusing *osteoplasts* alternately with lining cells and even osteoblasts.

[2] Note that previous authors mention bone cells as well. To the extent of my research, these researchers were all referring to osteocytes.

[3] The terminology 'bone cells', as presented earlier, usually referred to osteocytes, or *osteoplasts*. However, one can note the remaining confusion between the terms with Tome's reaction to Gegenbauer's works: 'on les appelait autrefois cellules osseuses, les allemands les appellent osteoblastes' ('we used to name them bone cells, Germans now call them osteoblasts') [188].

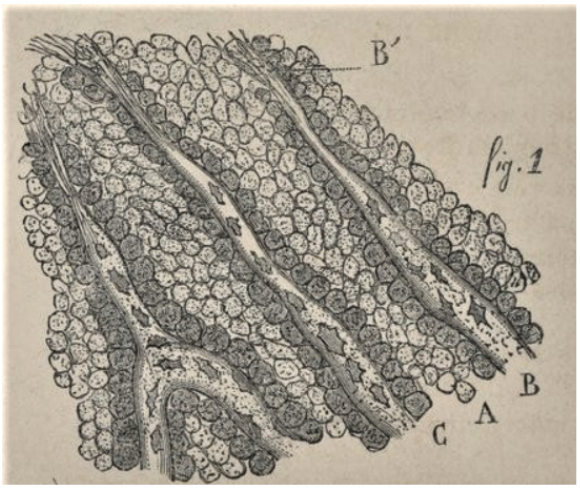

Fig. 1. — Fragment de portion périphérique du frontal d'un embryon de mouton, long de 7 centimètres (400 diamètres).
B, B. — Travées en voie d'ossification avec ostéoplastes.
A. — Cellules embryonnaires.
B'. — Fibrille terminale des travées.
C. — Ostéoblastes.

(a)

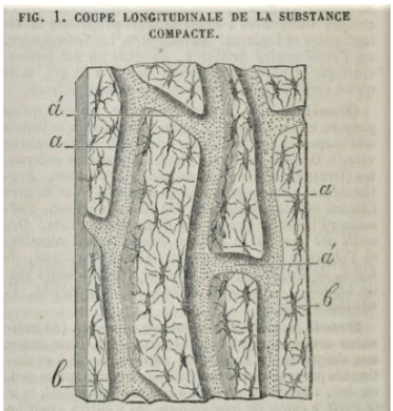

a. Canalicules vasculaires longitudinaux. — a'. Canalic. transversaux. — b. Cavités osseuses ou corpuscules osseux.

FIG. 2. COUPE HORIZONTALE.

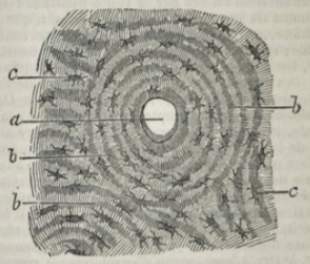

a. Ouverture d'un canalicule osseux. — b. Subst. osseuse disposée en couches concentriques autour du Canalicule vasculaire. — c. Cavités osseuses.

(b)

Figure 2.4: Historical work. (a) Drawing and caption from a microscopic slide of a sheep embryo bone section mentionning osteoplasts (B) and osteoblasts (C) [21]. (b) Illustrations describing sections of a cortical bone from a glossary-graphical dictionnary from 1851 (*Nouveau Dictionnaire lexico graphique et descriptif des sciences médicales et vétérinaires*) mentioning canaliculi (1a, 1a', 2a) defined as vascular channels, bone 'substance' (matrix in 2b) and bone cells/cavities (1b, 2c) [158]

> the canaliculi form, and the osteoblasts become real osteoplast. They are surrounded by a fundamental substance, and arranged circularly around a central cavity, which gradually narrows to the point where it reaches the diameter which it must preserve, that of a Havers canaliculus.

The interested reader will find the original text below, in French:

> Les cellules des espaces médullaires (ostéoblaste de Gegenbaur [*sic*] deviennent des cellules osseuses [ostéocytes] et s'entourent de sels calcaires. Il devient donc facile de comprendre l'usage de ce dépôt calcaire, antérieur à l'ossification, dans la substance fondamentale. Par endosmose les sels calcaires, dissous à l'aide de la circulation sanguine commençante

> pénètrent dans les espaces médullaires, et fournissent les éléments solides qui vont entourer les ostéoblastes pour que ceux-ci deviennent ostéoplastes à paroi osseuse. [...] Ces ostéoblastes que Gegenbaur [*sic*] a le premier bien décrites sont variables de forme : elles ont 20 à 30 μ [*sic*] de diamètre ; elles sont en général fusiformes, leur membrane est d'abord mince, et leur protoplasma granuleux ; peu à peu elles s'incrustent de sels calcaires, et ne deviennent étoilées qu'à cette époque ; alors les canalicules se forment, et les ostéoblastes deviennent de véritables ostéoplastes entourés de substance fondamentale, et disposés circulairement autour d'une cavité centrale qui se rétrécit peu à peu jusque au [*sic*] moment où elle a atteint le diamètre qu'elle doit conserver, celui d'un canalicule de Havers.

Eventually, at the end of the 19th century, the word 'osteocyte' arises, defined as differentiated cells lying in osteoplasts (therefore, changing from the original definition of osteoplasts) [149]. These cells (bone cells, etymologically) are therefore from then identified as the corpuscules lying in the ovoid cavities called *osteoplasts* back then, and *lacunae* today.

Based on personal historical research, the word 'osteoclast' was first defined around 1850 by Mr. Maisonneuve as an instrument designed by M. Robin to break bones [185], in accordance with its etymology – 'osteo-' being the prefix for bone and 'clast' originating from the Greek word *clastos* for 'broken'. This surgical instrument is illustrated in Perrusset's thesis, as displayed in Figure 2.5 [150]. This instrument was invented by Mr. Maisonneuve as a tool for his novel method for amputation, based on the compression of the bone with a tightly-screwed iron crescent and the use of a rod to lift the bone to be amputed. He was convinced that the use of a breaking instrument was less likely to cause phlebitis than the cutting instruments of his time and found that his snatching method avoided purulent infections and bleeding [185].

In the meantime, and until the end of the 19th century, several works identify multinucleated cells at the surface of bone tissue, sometimes called myeloplaxes [119, 141, 164], and sometimes as giant cells [146, 177]. A couple of decades later, Kölliker, assuming that these multinucleated cells are able to resorb bone matrix, attributes them the name 'osteoclasts' (see Klein's words in [95]).

The word 'myeloplaxes' defines today abnormal multinucleated cells. One may

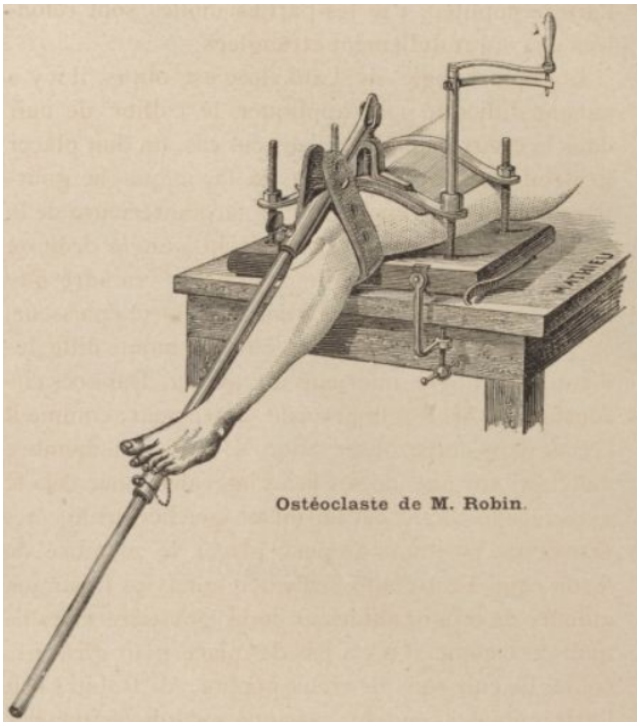

Figure 2.5: Osteoclast, the surgical instrument designed to break bones. Drawing from Perrusset's thesis *Traitement de l'ankylose angulaire du genou par l'ostéoclasie sus-condylienne* [150].

find that the association of this word with bone-resorbing osteoclasts in the 19th century results from the observation that multinucleated cells (tumor cells and osteoclasts) were found in bone tumors [163, 164].

Klein writes the following words in 1889, describing precisely the role and shape of osteoclasts as we know them today [95]:

> Wherever absorption [*sic*] of calcified cartilage or of osseous substance is going on, we meet with the multinucleated huge protoplasmic cells, called the myeloplaxes of Robin. Kölliker showed them to be important for the absorption of bone matrix, and called them therefore *Osteoclasts* [*sic*] [...] we find these myeloplaxes situated in smaller or larger pits, which seems to have been produced by them [...].

To conclude, at the end of the 19th century, thanks to enhanced microscopy and histology techniques, the main biological actors of bone remodeling were already identified: osteoblasts, osteocytes and osteoclasts. Additionally, the structure of bone has been identified (see Quekett's thorough description in [157]), as described earlier

(Section 2.1.1).

Bone cells and remodeling

As previously presented in this section, two bone cells lineages were identified over the 19th century. The interactions between these cells and the bone matrix as well as the influence of their biochemical environment have been widely studied until today. In the present subsection, bone cells and their activity are connected with the continuous structural and physico-chemical evolution of bone, called bone remodeling.

The early works of Milch in 1957 on the deposition of tetracycline in bone formation sites following its injection paved the way for the first studies of the dynamics of bone remodeling [59, 133]. Although changes in bone features are not obvious at the macroscopic scale in healthy subjects, bone tissue actually undergoes a continuous evolution and reorganization at the micro-scale, allowing the renewal of matter, adaptation and self-repair through bone resorption and apposition. This process is called bone remodeling.

Bone remodeling is achieved by so-called *bone multicellular units* (BMUs). A BMU is a group of bone cells that removes and replaces one bone structural unit, being an osteon in cortical bone or a hemi-osteon in cancellous bone (see previous Section 2.1.1 for a quick reminder on bone structure). The remodeling process undertaken by BMUs in cortical bone is illustrated in Figure 2.6: osteoclasts (orange) resorb bone in tunnels by forming so-called 'cutting cones' that are progressively refilled by osteoblasts (green). The remaining channel is the vascular porosity irrigating bone tissue. This process results in the formation of osteons. In cancellous bone, BMUs act in discrete packets on the trabecular surface and create a hemi-osteon after completion of the remodeling event.

On the one hand, the osteoblastic cells lineage comprehends differentiated cells that produce bone matrix (osteoblasts) and that send biochemical signals in response to mechanical and biochemical stimuli (osteocytes). The osteoblastic lineage originates from mesenchymal stem cells in the bone marrow. These multipotent cells can differentiate into cells of various tissue types (fibroblasts, osteoblasts, osteo-

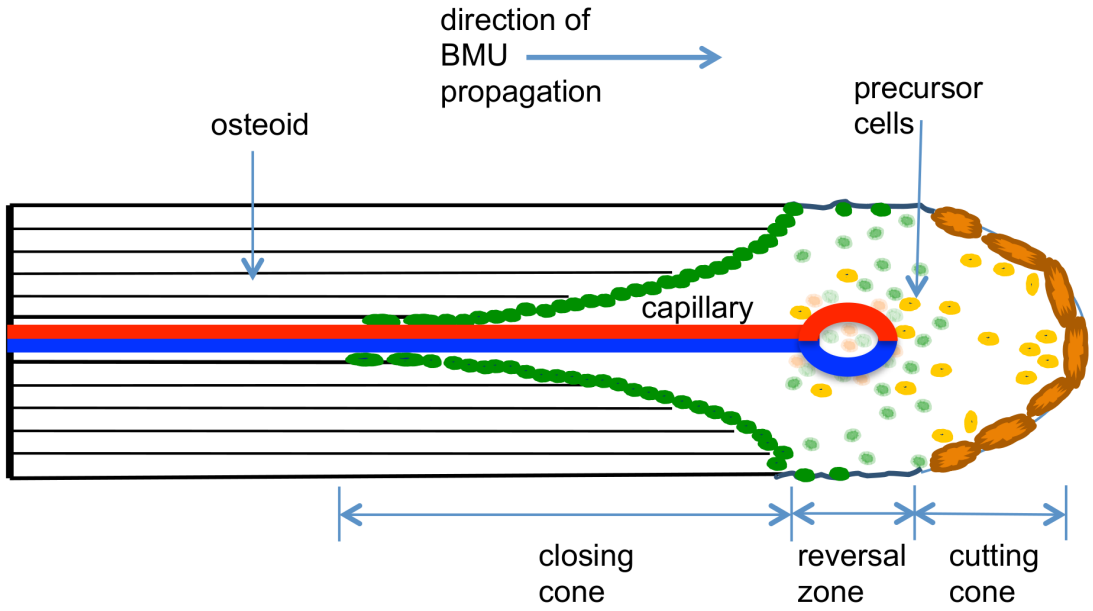

Figure 2.6: Cortical bone remodeling: osteoclasts (orange) resorbing ahead of the remodeling cone and osteoblasts (green) filling the osteon with a collageneous matrix (grey), forming the Haversian structure. From ' Idealized structure of cortical BMU in longitudinal section, showing cutting cone, reversal zone and closing cone.' by Smith et al., licensed under CC.

cytes, adipocytes, chondrocytes in connective tissue, myocytes in muscular tissue). In bone, mesenchymal stem cells differentiate into uncommitted osteochondroprogenitor cells, which, in turn, differentiate into committed pre-osteoblasts. Eventually, pre-osteoblasts differentiate into mature osteoblasts which are bone-forming cells. Ultimately, these osteoblasts can either become apoptotic (cell death), or differentiate into lining cells or osteocytes [118]. Bone lining cells cover quiescent surfaces of bone, which means that no remodeling happens on these surfaces. These cells may regulate the passage of ions and biochemical signals, therefore regulating bone remodeling [200]. Moreover, evidence suggests lining cells can differentiate into committed osteoblasts precursors [134, 200].

The osteoblastic lineage is highly relevant to the regulation of remodeling, in particular through the role of embedded bone cells called osteocytes. Mature osteoblasts can differentiate into osteocytes, whose morphology changes progressively as they develop dendritic processes [10, 18]. While early theories mentioned osteocytogenesis as a passive process resulting from the burying of osteoblasts [57, 140], Holmbeck and

colleagues showed that the formation of osteocytes processes was associated with the cleavage of collagen in the matrix [82]. This result suggests that the differentiation of mature osteoblasts into embedded bone cells is an active process involving the formation of a cellular network. Additionally, in the osteoid (newly-formed bone), early osteocytes regulate mineralization [10]. Eventually, mineralized bone hosts osteocytes in microcoscopic cavities called lacunae connected by canaliculi (lacuno-canalicular network), allowing the transport of biochemical signals and nutrients. This last point is particularly important as it has been well accepted for a couple of decades that osteocytes are responsive to mechanical loading [18, 96, 147] and regulate bone remodeling via the production of various signalling molecules [120].

Osteoclasts derive from the monocytes/granulocytes/macrophages lineage. Osteoclastic cells differentiate from hematopoietic stem cells (HSCs), which are also common progenitors to lymphocytes, red blood cells, platelets and mononuclear phagocytes. While the exact lineage leading to mature osteoclasts is unclear, it is well accepted that HSCs form granulocytes and macrophages, that can differentiate into mononuclear pre-osteoclasts [9, 167, 168]. The latter undergo fusion to become a multinucleated osteoclast precursor cell. Osteoclasts progenitor cells then differentiate into mature active resorbing osteoclasts. Mature osteoclasts are large multinucleated cells – up to 100 μm large – that have the particularity to be capable of resorbing calcified bone matrix [118, 167]. Osteoclasts attach to bone surface with a specialized area of the plasma membrane (clear zone) sealing the soon-to-be-excavated bone area. This structure surrounds a characteristic ruffled border made of finger-shaped projections of the membrane. These cytoplasmic projections mediate the mineral dissolution and organic matrix degradation via the acidification of the created enclosed space. This operation results in the creation of a pit called the Howship's lacuna. The resorption products are removed from the lacuna by endocytosis and then transcytosed and released into the circulation. Eventually, osteoclasts detach from the bone and either move towards a new resorption site or undergo apoptosis.

To conclude, the main roles of bone cells in the microscopic phenomena at stake in bone remodeling were described here. In this thesis, bone remodeling is envisaged as a biological process that is regulated by mechanics, as it has been widely accepted

since Wolff's first observations of bone adaptation [206]. The next section provides a review of the interactions between mechanics and bone remodeling.

2.2 Mechanics and bone remodeling

2.2.1 Evidences of bone remodeling and its link with mechanics

In this section, bone remodeling is envisaged from a macroscopic perspective. At this scale, one can not only retrieve averaged structural properties of bone (tissue orientation, porosity...), but also analyze the surrounding mechanical environment. The connection between these parameters has been widely studied over the past years, stemming from the early works of Frost [60].

The close link between mechanics and stresses has been noted since the 19th century and the early observations of Culmann, Von Meyer, Wolff and Roux [40, 169, 195, 206]. Georg Hermann Von Meyer was a German professor of anatomy with a strong interest in the human skeleton. Benefitting from his interactions with the German civil engineering professor Culmann, he noticed the arched trabecular patterns in bone sections. Culmann noted that the struts appeared to be aligned along principal stress directions. The result of this collaboration deeply influenced the work of Julius Wolff, a German surgeon convinced that Culmann and von Meyer's findings could not be a coincidence [40, 195]. In 1870, Wolff introduced a theory on bone remodeling, nowadays referred to as 'Wolff's law', stating that the mechanical function of bone drives the evolution of its architecture [208]. In the same vein, Whilelm Roux introduces in 1881 a broader mechanistic theory on 'developmental mechanics', suggesting that cellular activity is tailored to adapt the inner structure of various organs – and bone in particular – to their specific function, and that this process is regulated by mechanical stresses [169].

Meanwhile, Wertheim, Rauber and Messerer made the first investigations on bone physical properties [166]. In 1847, Wertheim published the first study of mechanical tensile properties of human tissues, including soft and hard tissues [4, 203].

Wertheim's work on elastic properties of bone inspired Rauber, who designed his own equipment to avoid difficulties with specimen holders [161, 166]. Rauber studied the properties of compact and cancellous bone in tension, compression, shear and torsion. To the best of my knowledge, Rauber was the first scientist to bring to light several features that biomechanical experimenters know well nowadays, such as the influence of humidity and temperature on strength and elasticity and the sensitivity of bone behavior to the loading direction (anisotropy). Later on, Messerer performed the first mechanical tests on fresh human whole bones (500 bones) that he obtained from 90 cadavers [132], providing the largest series of data available during a whole century [126]. One can also note the importance of the works of Koch from the beginning of the 20th century, who performed extensive mechanical testing on the femoral head. Based on contemporary works and his experimental observations, he formulated in 1917 a mathematical theory based on the idea that the anatomy of bones is designed for a maximal mechanical efficiency [99].

While a few experimental works on bone physical properties arose after the beginning of the 20th century (see [13] (1941), [41] (1952) and [126] (1967)), the analysis of the link between mechanics and bone mechanical properties stayed a quiescent field until a regain of interest roughly between 1950 and 1970 (see [41] (1952), [52] (1969) and [166] (1987, review)). Figure 2.7 illustrates Mather's 1967 3-point bending experiment on over 200 femoral shafts developed in the Departments of Surgery and Civil Engineering at the University of Queensland in the late 1960s.

This renewed interest towards bone mechanics research may be explained by increased needs in regards to modern techniques allowing earthbound, airbound and spacebound traffic and to advancing techniques in competitive sports [53, 166]. The intensive study of bone physical properties came along with the rising development of imaging techniques[4]. For instance, at the end of the 20th century, Whitehouse pub-

[4] Standard *in vivo* and *ex vivo* measurements of bone 'quality' as an averaged measurement of disease or healing progression tend to involve computed tomography (CT) techniques. The CT scanner was invented in 1972 by Godfrey N. Hounsfield, allowing already the quantification of density data (Hounsfield units). Moreover, note that scanning electron microscopes were first commercialised in 1965. Another device widely used in bone mechanics, for *in vivo* and *ex vivo* experiments is the strain gauge, allowing to measure the strain experienced by the tissue. This device was invented in 1938 by Arthur Ruge.

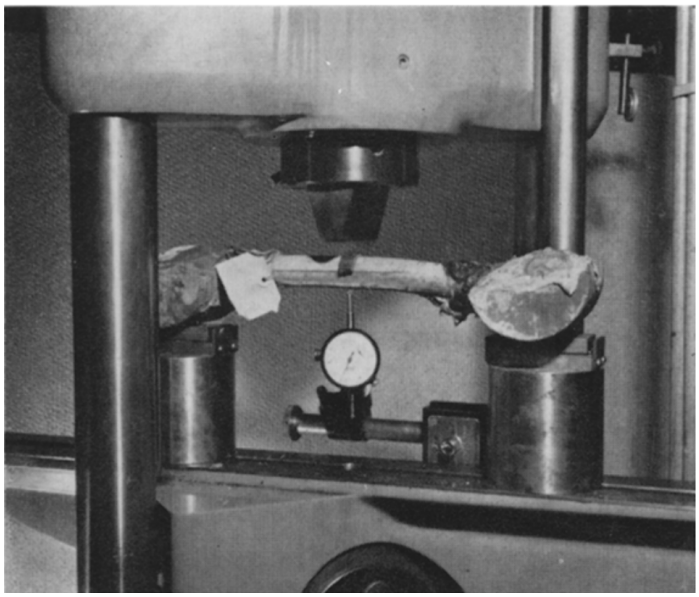

Figure 2.7: Mather's bending test setup with a specimen in place. From Mather et al. [126], with permission.

lished novel works analyzing the anisotropy of bone tissue using low magnification scanning electron microscopy [204]. It is in this time period that the first experimental *in vivo* works on the impact of mechanical environment on bone remodeling were carried on. Experiments on animals [74, 210] and human [104] showed a bone gain in response to increased exercise, as well as the stronger influence of dynamic loading as opposed to static loading [142]. Meanwhile, researchers also showed that the decrease in mechanical stimulation resulted in loss of bone mineral [47, 103, 187].

The revival of interest towards experimental bone mechanics in the mid-20th century also led the path for the first theories of bone adaptation introduced by Cowin. In 1976, Cowin introduced the first theories including bone porosity [38] and, later on, bone anisotropic micro-architecture [34] and their evolution according to mechanical principles. In order to describe the connection between bone remodeling and mechanics, Frost introduced a novel formulation called 'mechanostat theory' [60, 61]. His theory relies on the definition of a mechanics-based setpoint criterion that regulates the cellular activity, in line with the precursor ideas of Roux [169]. This theory was recently extended by Jee et al. to include hormonal and pathological effects on setpoint strain regulation [88].

These pioneer works paved the way for decades of research on the characterization of bone remodeling and its link with mechanics. Since then, there has been extensive experimental research on the mechanosensation of bone cells, and osteocytes in particular. The links between mechanics and bone biology are outlined in the next subsection.

2.2.2 Bone remodeling and mechanomics

The term 'mechanomics' originates from the gathering of the word 'mechanics' and the suffix '-omics'. Numerous words ending in '-ome' and '-omics' have been coined over the past decades, using the terms genome and genomics as a model. Such fields of study, also referred to as omics, embody the description of pools of biological molecules and their function in an organism. A couple of decades ago, Lang described mechanomics as the scientific area focusing on the description of the 'general role of force, mechanics, and machinery in biology'[5][106, 196].

As mentioned previously in Subsection 2.2.1, the physico-chemical environment, and, in particular, mechanics regulates bone cells behavior [19, 175]. Osteocytes, the most numerous cells in bone tissue (more than 90% of bone cells [17]), are thought to be responsible for the sensation of mechanical loads and transduce the mechanical signals into biochemical signals orchestrating recruitment and activity of osteoblasts and osteoclasts. Theories attempting to explain the mechanosensation of macroscopic loads by osteocytes rely on experiments and calculations involving physico-chemical mechanisms at the cellular scale. Main assumptions emphasize the role of interstitial fluid flow, direct cell strain, streaming potentials or hydrostatic pressure as the most likely mechanisms for mechanosensation [96, 109, 159, 170, 173].

Osteocytes regulate bone formation and mineral metabolism through the expression of specific molecules. In particular, osteocytes express DMP1 (Dentin Matrix Protein 1), FGF23 (Fibrobast Growth Factor 23) and Pex (Phosphate Regulating

[5] The first mention to the mechanome is attributed to Professor Kamm, during a presentation at the World Congress of Biomechanics in Munich in 2006 [90]. Lang quotes Kamm's definition in his 2007 presentation at the Frontiers of Engineering Symposium as the 'study of how forces are transmitted and the influence they have on biological function' [106].

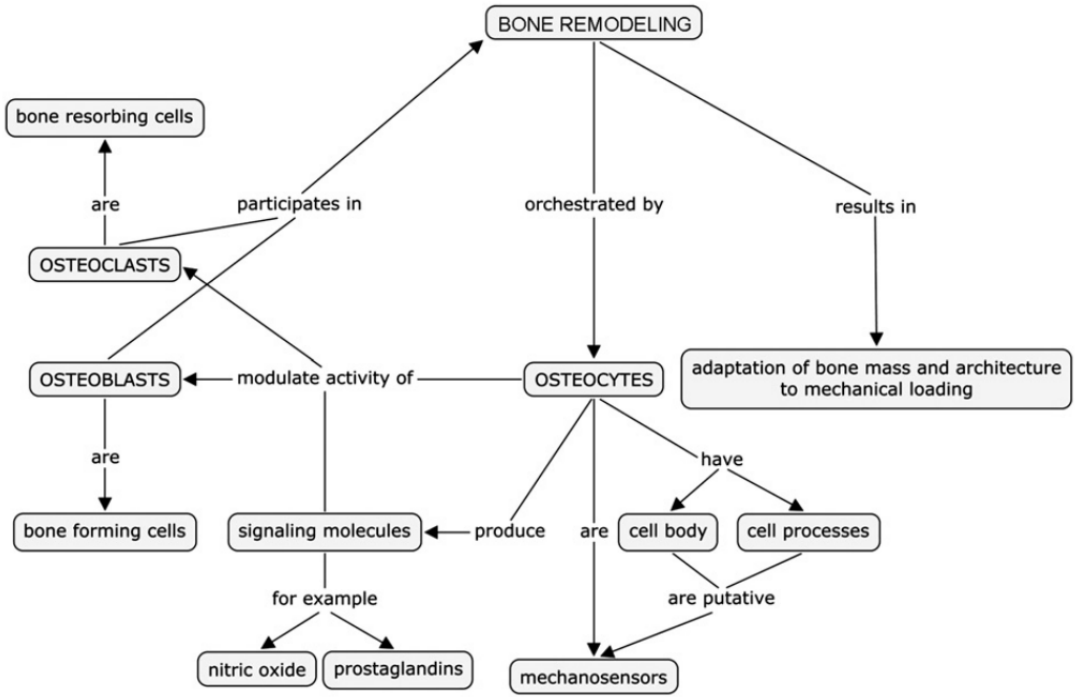

Figure 2.8: Schematic overview of the role of osteocytes in the process of bone remodeling. From Klein-Nulend et al. [96], with permission.

Neutral Endopeptidase on Chromosome X) that regulate phosphate homeostasis [17, 50]. Additionally, osteocytes produce a range of biomolecules including nitric oxide, prostaglandins and sclerostin that regulate bone formation and resorption through their action on osteoblasts and osteoclasts (see Figure 2.8) [96]. Note that osteocytes are capable, to a lesser extent, of resorbing bone and increasing their lacunar space as a response to hormonal changes or calcium restriction through a process called osteolysis [212].

In summary, this section highlighted that bone tissue is able to modify its material properties through the remodeling action of bone-resorbing osteoclasts and bone-forming osteoblasts. Remodeling cells activity is regulated by osteocytes, which are also able to regulate mineral homeostasis.

A main goal of this thesis is to describe the evolution of bone structure and composition in healthy and diseased states. The following sections will provide the reader with an overview of existing macroscopic frameworks for the description of bone remodeling.

2.3 Theoretical models of bone remodeling

There exists a wide variety of theoretical models of bone remodeling. Such frameworks use the understanding of bone biology acquired over the past century to better explain or predict the effect of certain diseases, treatments, environments on bone properties.

While the theories of Wolff [206] and Roux [169], and, later on, Frost [60] built the roots of most recent biomechanical models of bone remodeling, these frameworks are not quantitative. Therefore, the models developed over the past decades, still based on these ideas, aim at providing quantitative estimates. Hence, with the exponential developments in computational power, numerical works on bone remodeling increased.

Mechanistic theories on bone remodeling rely on Wolff's idea of a functional adaptation of bone. As pointed out earlier in this thesis (Subsection 2.2.1), Frost proposed in 1987 the idea of a feedback loop with the concept of mechanostat [60], a regulation process that results in the adaptation of bone mass in function of what he calls the 'mechanical usage'. A positive or negative deviation from the system 'setpoint' would trigger a corresponding net remodeling activity.

From this time point onwards, numerous models have been created based on Frost's mechanostat by implementing a quantitative remodeling law. The mechanostat 'setpoint' is identified with the equilibrium value of a mechanical quantity that drives bone remodeling [84, 137, 201]. Some models also include a 'lazy zone', where bone remodeling is either null [46, 202] or strongly diminished [12]. Note that Schulte et al. recently proposed a Frost-type exponential remodeling law in mice thanks to vertebral bone *in vivo* micro-computed tomography and high-resolution finite element analysis [174]. An example of a lazy zone model is given in Figure 2.9, where the bone apposition/resorption rate is given as a function of the tissue stress stimulus. The evaluation of the mechanical stimulus varies among the works. Most studies assume bone remodeling to be driven by strain energy density [6, 83] or a strain-energy-related stimulus (effective stress $\sigma_{energy} = \sqrt{2EU}$, with E the apparent elastic modulus and U the strain energy density) [12, 46]. Note that, in their pioneer publication in 1987, Carter and coworkers already identified three different relevant quantities for bone density evolution: effective stress, fatigue damage accumulation density and

strain energy density [28]. Several models also use a spatial integration of the signal while assuming a decay in influence with increasing distance to the evaluation point [83, 116, 193]. Hart classifies the models presented so far as phenomenological [78] – one of the three existing model types, the others being optimization-based and mechanistic. Phenomenological models are engineering based, quantifying stimulus and response towards the goal of predicting bone adaptation. They bear a particular importance in the context of remodeling around implants, which is determinant to their stability through osseointegration [127, 194].

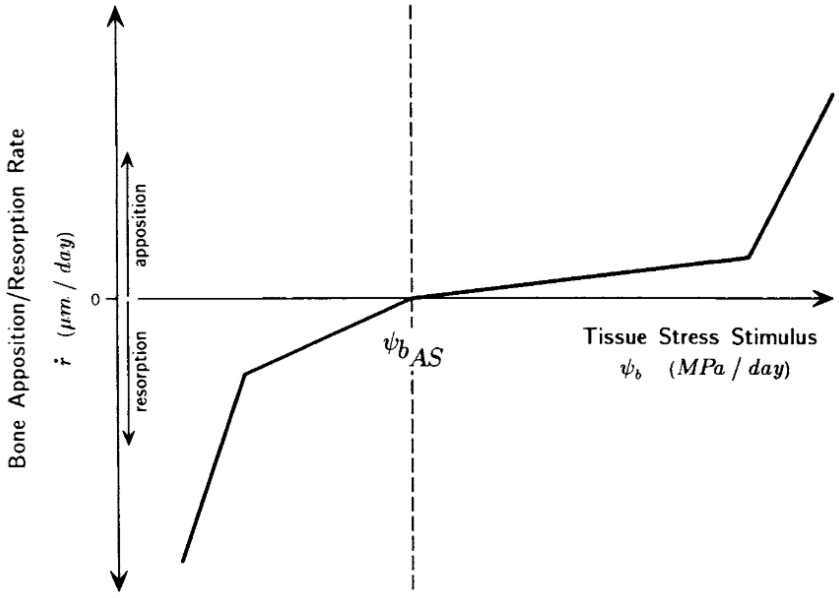

Figure 2.9: Idealized, piecewise linear rate relation describing bone apposition/resorption rate as a function of tissue stress stimulus. From Beaupre et al. [12], with permission.

Other models translate the idea of functional adaptation into the concept of structural optimization. These algorithms do not rely on an actual time scale and instead provide insights on how the tissue structure may evolve towards a potential steady-state. Carter and coworkers introduced an algorithm driving the evolution of bone apparent density [28, 25]. This property was used to calculate the stiffness and stresses, given certain loads and boundary conditions. Apparent density, also defined as a function of the daily load, was then recalculated at each step, as shown in Figure 2.10 for the example of the proximal femur. In particular, several theories used an

optimization approach in the context of anisotropic remodeling, using strain energy as an objective function [36, 63]. In the same vein, Fernandes and coworkers proposed in 1999 a global optimization model based on a cost function accounting for both the structural stiffness and metabolism of the bone tissue, capturing optimal densities and microstructure orientation [55].

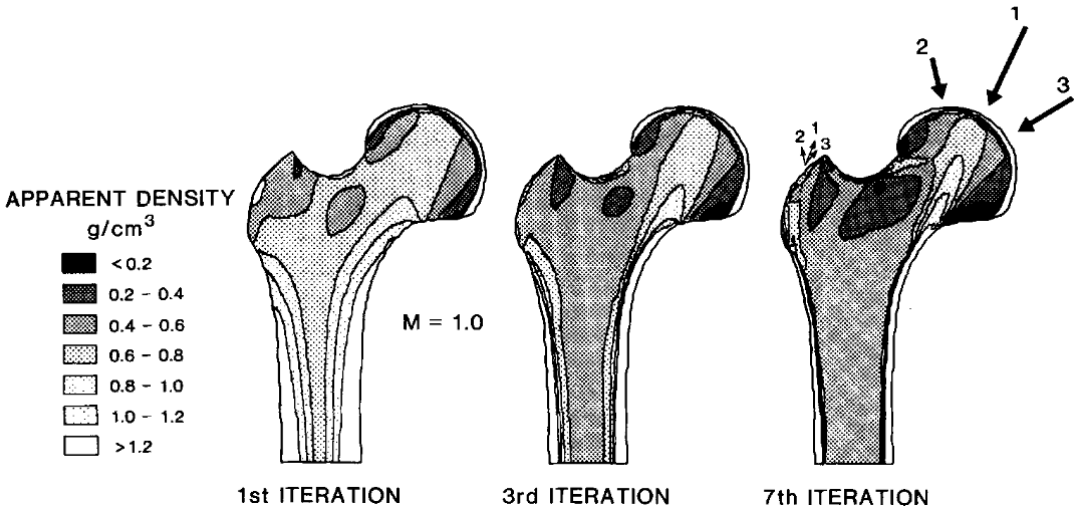

Figure 2.10: Remodeling solutions for the multiple-load-direction stress. From Carter et al. [25], with permission.

A third model type arose at the beginning of the 21st century with the increase of knowledge in bone biology. Mechanistic models link biological activity in bone to the mechanical environment. The corresponding field of study, mechanobiology, was born at the end of last century and aims at understanding the behavior of load-bearing tissues [191]. In particular, research in mechanobiology provides insights as to the signalling pathways involved in bone remodeling and the influence of mechanics [19, 49]. With the advances in experimental biology and computer science, several mechanistic models for bone remodeling have been proposed. For instance, computational biology allows a quantification of the effects of a disease or hormonal imbalance or nutrients availability on bone remodeling and cells turnover [29, 56, 68, 100, 110, 117, 156, 145]. This microscopic point of view allows a finer representation of the mechanisms at stake. Moreover, the quantification of the roles of the pathways also allows to better understand the dynamics of drug treatment [76, 154]. The translation of mechanobi-

ological concepts to the organ structural evolution is complex. A couple of works have addressed this question, connecting a macro-scale stimulus to biological activity [117, 172]. In summary, computational mechanobiology provides a much higher insight in the actual intrinsic mechanisms of bone remodeling and therefore enable the use of more physical and measurable parameters and including the influence of drugs or biochemical/biophysical cues in a much more representative and reliable way.

We know today much more about the biology of bone remodeling than in the eighties and nineties of the last century when most phenomenological models were introduced. However, the latter are still useful for a rapid understanding of a general problem or for a better design of prostheses, since they allow a fast view of the long term macroscopic influence of changes in the external stress field into the overall trend of bone material properties, despite the actual causes are hugely averaged and therefore simplified. One may also note that, while many of the remodeling evolution laws are written down in an *ad hoc* manner, several works do derive these laws from general theoretical frameworks [42, 124, 160].

The next chapter introduces a comprehensive numerical mechanobiological approach describing the cross-talk between bone cells turnover and tissue-scale mechanics via a quantification of osteocytes feedback.

Chapter 3

Mechanobiological osteocyte feedback drives mechanostat regulation of bone in a multiscale computational model

This chapter presents an article published in Biomechanics and Modeling in Mechanobiology [122].

The present chapter introduces a mechanobiological model of bone remodeling. As explained earlier (Chapter 2, Section 2.3), bone mechanobiology focuses on the mechanical regulation of signalling pathways affecting bone cells activity. In particular, osteocytes are essential to bone remodeling, as they sense mechanical loading and respond with a modulation of their biochemical signalling [19]. In order to account for the key role of osteocytes, a computational model was developed and is presented in the following published article corresponding to this chapter.

This model stems from previous works of Pivonka, Scheiner and coworkers [154, 172] that proposed a multiscale framework for bone remodeling while integrating the action of main regulating pathways (see Figure 3.1 for an illustration of the pathways in the model presented in this chapter, where the actions of sclerostin and nitric oxide were added):

- RANK-RANKL-OPG catabolic pathway (pathway (a) in Figure 3.1): regulates

the differentiation of osteoclasts;

- action of TGF-β (pathway (b) in Figure 3.1), which is released through the resorption of bone matrix implemented according to earlier studies [110, 156]: up-regulation of the differentiation of uncommitted osteoblasts (Ob_u) differentiation into osteoblast precursor cells (Ob_p), inhibition of the differentiation of osteoblast precursor cells (Ob_p) and promotion of the apoptosis of active osteoclasts (Oc_a);
- action of PTH: increased levels of PTH raise RANKL concentration, while simultaneously reducing the OPG production.

In the mentioned previous models, bone remodeling is depicted with deterministic ordinary differential equations which govern the evolution of cell numbers and bone matrix volume fraction in a given representative volume element. Cell differentiation, proliferation, apoptosis and ligand production are regulated by a number of binding reactions. The action of the latter on cells behavior is modeled via the introduction of multiplicative regulatory Hill functions based on receptor occupancy.

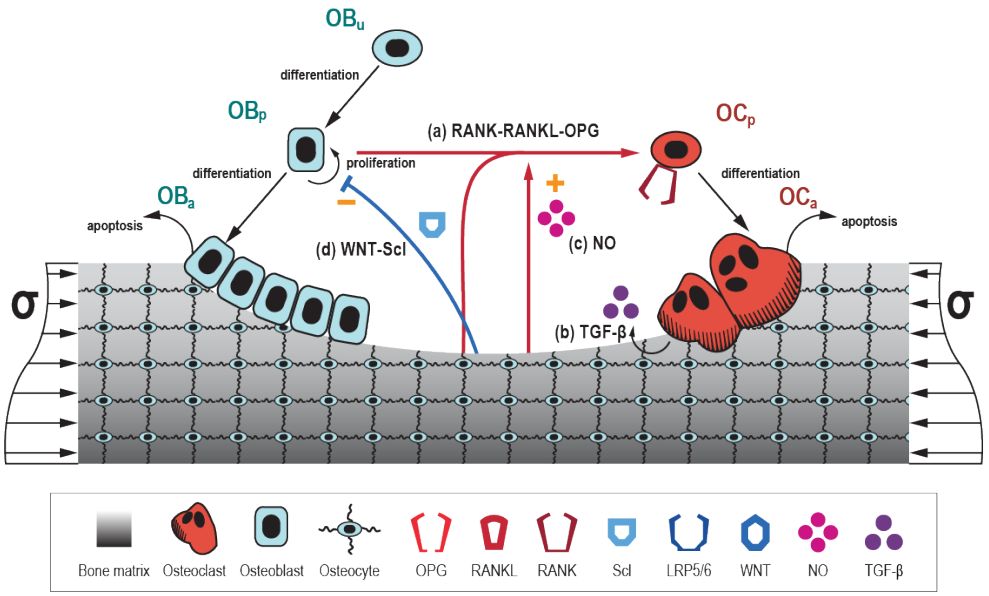

Figure 3.1: Illustration of the pathways of the mechanostat model.

In the mechanical multiscale approach developed by Scheiner et al. [172], the principle of mechanostat introduced by Frost [60] (see Chapter 2, Subsection 2.2.1) is

applied via the evaluation of a mechanical stimulus Ψ_{bm} that is defined as the strain energy density in the bone matrix. In their paper, Scheiner et al. define a macroscopic load that generates a stimulus Ψ_{bm} which regulates osteoblast precursors proliferation and their RANKL production. Figure 3.2 depicts the variation of the functions representing the mechanical regulation of bone cells activity: for values of the stimulus under the defined setpoint, the production of RANKL is increased (Figure 3.2(b)), which stimulates osteoclastogenesis and therefore bone resorption. Conversely, above the setpoint, the proliferation of osteoblasts precursors increases (Figure 3.2(a)), eventually promoting bone formation. The regulation of bone formation and resorption by mechanics introduces a mechanostat: for a given macroscopic stress, a low bone mass will result in a high strain energy and therefore bone formation, and *vice versa*.

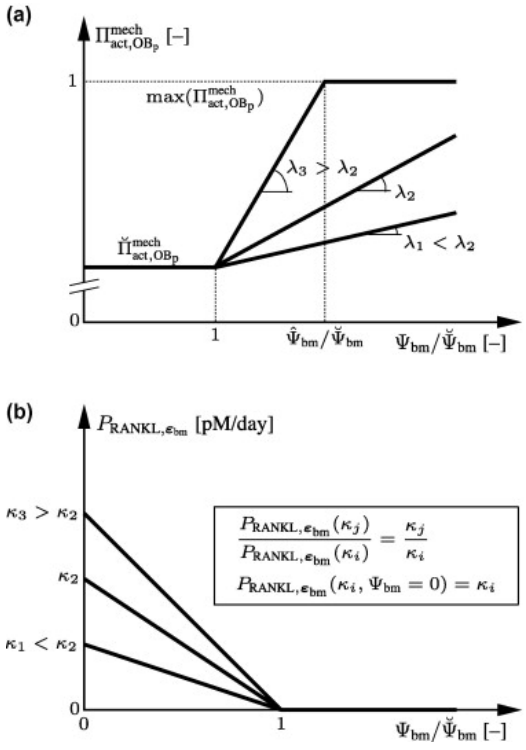

Figure 3.2: Scheiner et al.'s mathematical functions for mechanical regulation of osteoblasts proliferation (a) and production of RANKL (b). From [172], with permission.

The paper presented here has three main novel features. First, as explained earlier, the model integrates osteocyte mechanical feedback. Osteocytes signalling is acknowledged via the role of two molecules they express, which regulate bone remod-

eling: nitric oxide (NO, pathway (c) in Figure 3.1), driving the catabolic regulation [54, 31, 213] and sclerostin (Scl, pathway (d) in Figure 3.1), driving the anabolic regulation [93].

Another novel feature of this model is the co-regulation of RANKL production by NO and PTH. In order to model this combined action, a coregulation function was implemented, integrating the activating action of PTH and the repressive action of NO.

The third and last novel feature is the implementation of the competitive binding of Wnt proteins and sclerostin (Scl) to LRP5/6 receptors on Ob_p: high levels of sclerostin due to a diminished mechanical stimulus decrease Wnt signalling and therefore osteoblastogenesis and bone formation (pathway (d) in Figure 3.1).

In the article presented hereafter, the model is calibrated in terms of the catabolic and anabolic pathways, respectively referring to the metabolic cascades leading to bone resorption and formation. A disuse is simulated by lowering the macroscopic stress, resulting in bone loss mediated by osteocytes nitric oxide expression (catabolic pathway). Reuse (by a reinstatement of the initial loading conditions) triggers bone volume increase towards its initial value. The anabolism was tested in simulations of post-menopausal osteoporosis for several bone sites of varying average bone volume fraction (femoral neck, lumbar spine, distal radius). Hormone-induced bone loss was simulated via an increase in RANKL and reduced sclerostin degradation, leading to a stimulation of the anabolic Wnt pathway and an increase in bone formation. It is worth noting that, while mitigating bone loss to reach a steady bone mass, the anabolism orchestrated by osteocytes does not compensate for the total bone loss. These encouraging first results of this mechanobiological bone remodeling model were also the first steps towards the clinical application to anabolic anti-sclerostin therapy developed in Chapter 4.

Biomechanics and Modeling in Mechanobiology
https://doi.org/10.1007/s10237-019-01158-w

ORIGINAL PAPER

Mechanobiological osteocyte feedback drives mechanostat regulation of bone in a multiscale computational model

Madge Martin[1,2] · Vittorio Sansalone[1] · David M. L. Cooper[3] · Mark R. Forwood[4] · Peter Pivonka[2]

Received: 29 November 2018 / Accepted: 23 April 2019

Abstract
Significant progress has been made to identify the cells and signaling molecules involved in the mechanobiological regulation of bone remodeling. It is now well accepted that osteocytes act as mechanosensory cells in bone expressing several signaling molecules such as nitric oxide (NO) and sclerostin (Scl) which are able to control bone remodeling responses. In this paper, we present a comprehensive multiscale computational model of bone remodeling which incorporates biochemical osteocyte feedback. The mechanostat theory is quantitatively incorporated into the model using mechanical feedback to control expression levels of NO and Scl. The catabolic signaling pathway RANK–RANKL–OPG is co-regulated via (continuous) PTH and NO, while the anabolic Wnt signaling pathway is described via competitive binding reactions between Wnt, Scl and the Wnt receptors LRP5/6. Using this novel model of bone remodeling, we investigate the effects of changes in the mechanical loading and hormonal environment on bone balance. Our numerical simulations show that we can calibrate the mechanostat anabolic and catabolic regulatory mechanisms so that they are mutually exclusive. This is consistent with previous models that use a Wolff-type law to regulate bone resorption and formation separately. Furthermore, mechanical feedback provides an effective mechanism to obtain physiological bone loss responses due to mechanical disuse and/or osteoporosis.

Keywords Mechanostat · Bone remodeling · Osteocytes · RANK–RANKL–OPG pathway · Nitric oxide · Wnt pathway · Sclerostin · Co-regulation · Bone cell population model

1 Introduction

Bone modifies its composition and structure as a response to mechanical demands. While this ability has been observed and studied since the 1800s, Frost formulated in 1986 a so-called mechanostat theory (Frost 1987, 1996) describing this mechanism. This theory proposes that bone responds to changes in the minimum effective strain (MES) by triggering modeling and/or remodeling responses depending on the applied mechanical loads, hormonal and/or genetic regulations. Frost's proposal relies on the action of basic multicellular units (BMUs) constituted of bone forming (osteoblasts) and resorbing (osteoclasts) cells, which typically have a net negative impact on bone mass (Frost 1987). Frost argued that increased mechanical usage tends to conserve or increase bone mass, as overuse would lead to a decrease in the number of BMUs and make the balance between resorption and subsequent formation of each BMU less negative. Conversely, disuse prevents the global net resorption from decreasing, leading to an increased remodeling activity and therefore to thinning of the trabeculae, loss of trabeculae and increased cortical porosity (Frost 1987; Langdahl et al. 2016). Frost suggested an analogy of the mechanostat theory with a thermostat (regulating temperature). The mechanostat theory is useful for interpreting a variety of experimental data in orthopedic applications, basic bone biology and clinical research. Furthermore, this theory has been extended to include hormonal and pathological effects on setpoint strain

✉ Madge Martin
madge.martin@u-pec.fr

[1] Université Paris-Est, Laboratoire Modélisation et Simulation Multi Echelle, MSME UMR 8208 CNRS, 61 avenue du Général de Gaulle, 94010 Créteil Cedex, France

[2] School of Chemistry, Physics and Mechanical Engineering, Queensland University of Technology, 2 George St, Brisbane, QLD 4000, Australia

[3] Department of Anatomy, Physiology and Pharmacology, University of Saskatchewan, 107 Wiggins Road, Saskatoon, SK, Canada

[4] School of Medical Science, Griffith University, Gold Coast, QLD 4222, Australia

Published online: 13 May 2019

regulation (Jee and Tian 2005). While this conceptual theory is useful for a qualitative understanding of bone tissue level responses to mechanical loading, no quantitative estimates of changes in bone cell numbers and bone volume [or bone mineral density (BMD)] can be made. Also, no details of the underlying cellular mechanisms can be incorporated into such a theory.

In this paper, we aim to translate Frost's mechanostat theory into a mathematical quantitative theory of bone remodeling based on current knowledge of biochemical and biomechanical regulatory mechanisms. To do so, we start with a brief overview of the most important regulatory factors that have been identified in the bone biology literature in the recent years and which need to be included in such a model. We then apply this multiscale computational model of bone remodeling to investigate a variety of mechanisms deregulating bone remodeling, including mechanical unloading and re-loading experiments and age-related osteoporosis.

Over the last decade, significant progress has been made to identify the cells and signaling molecules involved in the mechanical adaptation of bone [see Bonewald and Johnson (2008) for a comprehensive review]. It is now well accepted that osteocytes act as mechanosensory cells in bone (Bonewald 2011). Osteocytes embedded in the bone matrix form a highly connected network (i.e., lacunae–canaliculi system) which maintains gap junctions between neighboring osteocytes and bone lining cells (Bonewald and Johnson 2008; Bonewald 2011). In particular, the latter connection (osteocytes-lining cells) seems to provide an efficient mechanism for osteocytes to directly influence bone remodeling. On the other hand, signaling molecules produced by osteocytes due to mechanical loading can be transported out of the lacunae–canaliculi system and so indirectly act on bone cells to modify bone remodeling. Application of mechanical loading to bone leads to bone matrix deformation. This deformation of the bone matrix (surrounding osteocytes) induces hydrostatic pressure in the osteocytes lacunae and shear stress in the canaliculi (Scheiner et al. 2016). These stimuli act on osteocytes and contribute to mechanosensation and mechanotransduction (Bonewald and Johnson 2008; Duncan and Turner 1995). Depending on the time scale of osteocyte cellular response, the following molecular mechanisms can be distinguished: rapid signaling response including changes in intracellular Ca^{2+}, nitric oxide release, release of prostaglandin E2 (PGE2), increase in cAMP levels and decrease in sclerostin expression affecting Wnt signaling (Bonewald 2011). Below, we briefly summarize some of the most commonly reported actions of mechanical loading on bone cellular response.

Osteocytes produce high levels of nitric oxide (NO) in response to mechanical loading both in vitro and in vivo (Zaman et al. 1999). Rahnert and coworkers point out that both mechanical loading and NO have positive effects on bone mass (Rahnert et al. 2008). NO production is induced rapidly by mechanical loading via up-regulation of eNOS mRNA and protein, eNOS being the predominant nitric oxide synthase (NOS) in adult bone. Because of the short half-life of NO, its effects are primarily mediated locally. At the same time, loading causes decreased expression of receptor activator nuclear factor kappa beta ligand (RANKL), a critical factor to osteoclastogenesis. Depending on the animal model, NO may also cause an increase in osteoprotegerin (OPG), a decoy receptor for RANKL inhibiting osteoclast formation (Fan et al. 2004). More generally, NO decreases the RANKL/OPG ratio, which is a major driver for osteoclast formation independent of species. Furthermore, involvement of NO in bone's adaptive response to mechanical loading has been demonstrated by two in vivo studies showing that nonselective inhibitors of NOS activity L-NMMA and L-NAME abrogated the osteogenic response to a short period of loading in rat tail vertebrae (Chow et al. 1998) and rat tibiae (Zaman et al. 1999), respectively.

Based on the discovery of sclerostin as a major potent mechanosensory signal, recent studies have focused on effects of mechanical loading/unloading on Sost/sclerostin expression (Gaudio et al. 2010; Moustafa et al. 2012; Nguyen et al. 2013; Robling et al. 2008; Spatz et al. 2015). Several studies investigated regulation of Sost/sclerostin by the mechanical environment using different models of mechanotransduction: dynamic axial stimulation [rodent ulnar (Robling et al. 2008) or tibial (Moustafa et al. 2012; Nguyen et al. 2013; Zaman et al. 2010) loading] and reduced loading [mouse hindlimb unloading (Robling et al. 2008), simulated micro-gravity on osteocyte cell lines (Spatz et al. 2015) or human bed rest (Gaudio et al. 2010)]. Immunohistochemistry and PCR (polymerase chain reaction) gene expression quantification coupled to strain gauge measurements (Robling et al. 2008) or computed tomography imaging and finite element analysis (FEA) (Moustafa et al. 2012) enabled the correlation between sclerostin expression levels and the local strain. While initial studies looking at mechanical unloading could only demonstrate increased SOST expression without increased sclerostin concentration (Robling et al. 2008), later studies both in vitro and in vivo demonstrated that mechanical unloading leads to increased sclerostin concentration (Galea et al. 2017). Furthermore, Spatz and coworkers found that sclerostin is up-regulated by mechanical unloading in osteocytes in vitro (Spatz et al. 2015) and Gaudio et al. showed an increase in sclerostin serum concentration in bedridden patients (Gaudio et al. 2010). Conversely, mechanical loading is associated with bone anabolism and a decrease in sclerostin expression in rodent models (Moustafa et al. 2012; Nguyen et al. 2013; Robling et al. 2008; Zaman et al. 2010). Hence, skeletal unloading induces osteocyte and osteoblast apoptosis, reduces osteoblast proliferation and inhibits osteoblast differentiation. Moreover, at least two

of these effects are induced by sclerostin's action on Wnt signaling (inhibition of osteoblastogenesis) (Bodine and Komm 2007). Consequently, activated Wnt signaling is a mechanism for increased bone formation during enhanced mechanical stimulation.

Despite the importance of Ca^{2+} in the signaling cascade following mechanical loading, its response is a prerequisite for all other biochemical responses to take place. Here, we are not concerned with the Ca^{2+} responses due to mechanical loading, but assume that these take place. Consequently, we will model only effects downstream from the Ca^{2+} response.[1]

Parallel to the extensive experimental research investigating bone's ability to adapt to changes in the mechanical environment, there have been many efforts to develop mathematical models describing bone adaptation. The majority of these models are based on mechanical rather than biological concepts and usually employ structural engineering approaches combining FEA with structural optimization (Beaupré et al. 1990; Doblaré and García 2001; Huiskes et al. 2000). On the other hand, several researchers have proposed biological models of bone remodeling to investigate biochemical feedback (Lemaire et al. 2004; Pivonka et al. 2008; Pivonka and Komarova 2010). A next step in the development of models for bone remodeling was to include mechanobiological feedback. This is based on directly linking a mechanical quantity (e.g., strain energy density) to cell proliferation or regulation of ligand concentration. While some of these models are useful in studying particular aspects of bone adaptation and bone remodeling, no insight into the underlying biochemical changes caused by mechanical loading can be made.

There have been only a few attempts to include biochemical signals identified with mechanical loading into a bone cell population model (Maldonado et al. 2006). Maldonado et al. included the action of mechanical loading on osteocytes to produce prostaglandin E2 (PGE2) and NO. Indeed, studies have shown that PGE2 release is regulated by mechanical loading (Bonewald and Johnson 2008; Rawlinson et al. 1991). In turn, PGE2 promotes the β-catenin signaling pathway triggered by the Wnt binding to the LRP and Frizzled receptors (see Sect. 2.1). The mechanical anabolism through PGE2 is therefore coupled to Wnt signaling. In their study, Maldonado and coworkers developed a local remodeling law where NO regulated OPG and RANKL levels and the anabolic feedback was orchestrated through PGE2. While the dynamics of the crosstalk between the β-catenin pathway and PGE2 remains unclear, the Wnt pathway has been widely studied over recent years and shown to be strongly anabolic (Bodine and Komm 2007; Bonewald and Johnson 2008). Therefore, in our study, we chose to focus on Wnt signaling and its interactions with sclerostin.

The most comprehensive approach to date has been developed by Pivonka and coworkers (Scheiner et al. 2013) who constructed a multiscale bone remodeling framework coupling the macroscopic mechanical loading and the effects on cell populations. They described the evolution of the tissue mechanical properties with respect to the bone matrix fraction resulting from remodeling at the microscale utilizing a micro-mechanical framework. Note that, in the aforementioned model and in the present study, bone tissue is assumed to be a two-phase medium made of a solid bone matrix and a macroscopic porosity (irrespectively of the bone site). The volume fraction of the former is referred to as bone matrix fraction f_{bm} throughout the rest of this paper and keeps the same definition in both cortical and trabecular bones.

Based on the current knowledge of mechanobiological regulation and computational models of bone remodeling, we propose the following new model features to account for mechanobiological feedback:

1. osteocytes taken into account as an individual cell population regulating mechanical feedback;
2. anabolic feedback via sclerostin which modulates Wnt signaling in osteoblast precursor cells and so regulates osteoblasts proliferation;
3. catabolic feedback via NO, which associates underuse with an increase in RANKL expression and in turn leads to bone resorption.

In addition, the model includes the following features:

- competitive binding reactions between sclerostin, Wnt and LRP5/6;
- functional co-regulation of RANKL by PTH and NO;
- RANKL production both by osteocytes and by osteoblast precursor cells;
- consistent formulation of the RANK/RANKL/OPG binding reactions, leading to a system of differential algebraic equations (DAEs).

This paper is organized as follows: in Sect. 2, we extend a recently developed coupled bone cell population micromechanical model of bone remodeling. This model explicitly takes into account osteocytes acting as mechanosensory cells which regulate both anabolic and catabolic feedback responses. Unlike the previous phenomenological representation of mechanical stimuli on bone cells (Scheiner et al. 2013), we assign specific biochemical regulatory molecules as detailed in the bone biology literature. Anabolic feedback is regulated by Wnt signaling via adjustment of sclerostin

[1] For applications where it is necessary to simulate a perturbation of the Ca^{2+} response, a model which considers shorter time scales of Ca^{2+} exchange is required. This is beyond the scope to this paper.

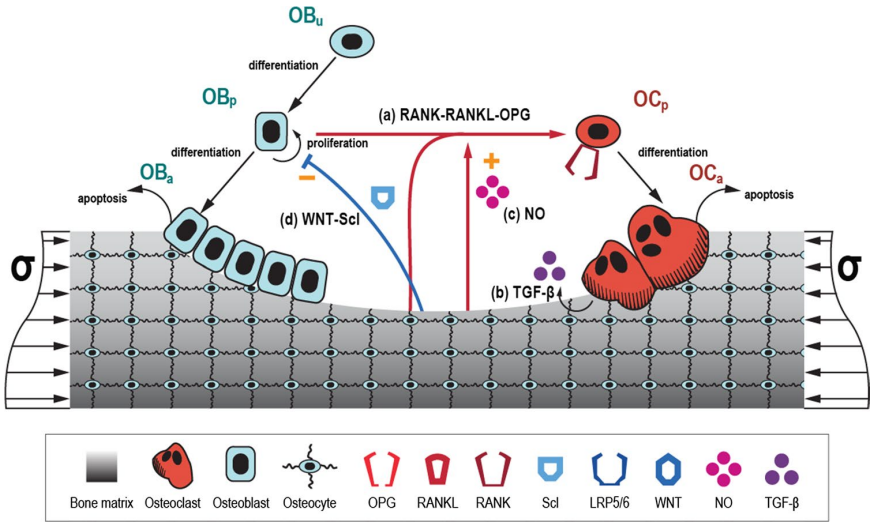

Fig. 1 Overview of the biochemical mechanostat feedback

concentrations. The catabolic feedback loop is regulated via NO expression which regulates the RANKL/OPG ratio. The mechanostat theory is quantitatively incorporated into our model using a setpoint strain energy density criterion (together with the principle of cellular accommodation), but is actuated through known bone biology. To the authors' knowledge, this is the first model which incorporates the mechanostat theory based on osteocyte mechanobiological feedback mechanisms.

2 Mathematical model of bone remodeling including biochemical mechanostat feedback

2.1 Model structure

In the following, a description of our extended mechanobiological computational model of bone cell interactions in bone remodeling is provided with emphasis on the newly introduced model features. This model takes into account catabolic and anabolic signaling pathways including the RANK–RANKL–OPG pathway and the Wnt–Scl–LRP5/6 signaling pathway together with the action of PTH, NO and TGF-β on bone cells [for details on original models (see Pivonka et al. 2008; Buenzli et al. 2013; Pastrama et al. 2018; Pivonka et al. 2013; Scheiner et al. 2013)]. This new model has been developed in such a way that the original model structure has been preserved and only additional model features relevant to the formulation of the mechanostat have been taken into account. The above described mechanisms of bone cell interactions in bone remodeling are schematically illustrated in Fig. 1.

The bone cell types (i.e., state variables) considered in this model are: (1) osteoblast precursor cells (Ob_p), (2) active osteoblasts (Ob_a), (3) osteocytes (Ot) and (4) active osteoclasts (Oc_a). Figure 1 displays an overview of the cell populations included in the model. The cell pools of uncommitted osteoblasts (Ob_u) and osteoclast precursors (Oc_p) are assumed to be much larger than the other cell pools and thus are not included explicitly into the model (Fig. 1). After identification of cell types involved in bone remodeling, we now identify essential signaling pathways and regulatory factors linking these various cell types (Fig. 2).

We introduce the Wnt–Scl–LRP5/6 anabolic signaling pathway as a first new model feature (see Fig. 2d). As depicted in Fig. 3, Wnt signaling, activated through β-catenin, is an anabolic pathway promoting osteoblasts proliferation and bone formation (Fig. 3a). Extracellular Wnt ligands (produced by bone marrow stromal cells) bind to Frizzled receptor proteins and lipoprotein receptor-related proteins (LRP5/6), triggering intracellular activation of β-catenin. As shown in Fig. 3, sclerostin modulates the signaling pathway by interacting with LRP5/6 receptors (Fig. 3b), therefore preventing the formation of a Wnt–Frizzled–LRP5/6 complex.

It is beyond the scope of this paper to model the Wnt/β-catenin signaling pathway in full detail. As described in introduction, there exist many Wnt ligands and receptors and we choose here not to differentiate Wnt protein types nor LRP5/6 receptors between them. Hence, as an approximation, we introduce the action of sclerostin via its competitive binding to LRP5/6. In this model, we assume that Wnt is produced by uncommitted osteoblasts (Ob_u), while LRP5/6, i.e., a Wnt receptor, is expressed on osteoblast precursor cells (Ob_p). Scl is produced by osteocytes responding to changes in mechanical loading and competes with Wnt to bind to LRP5/6. In other words, the action of Scl

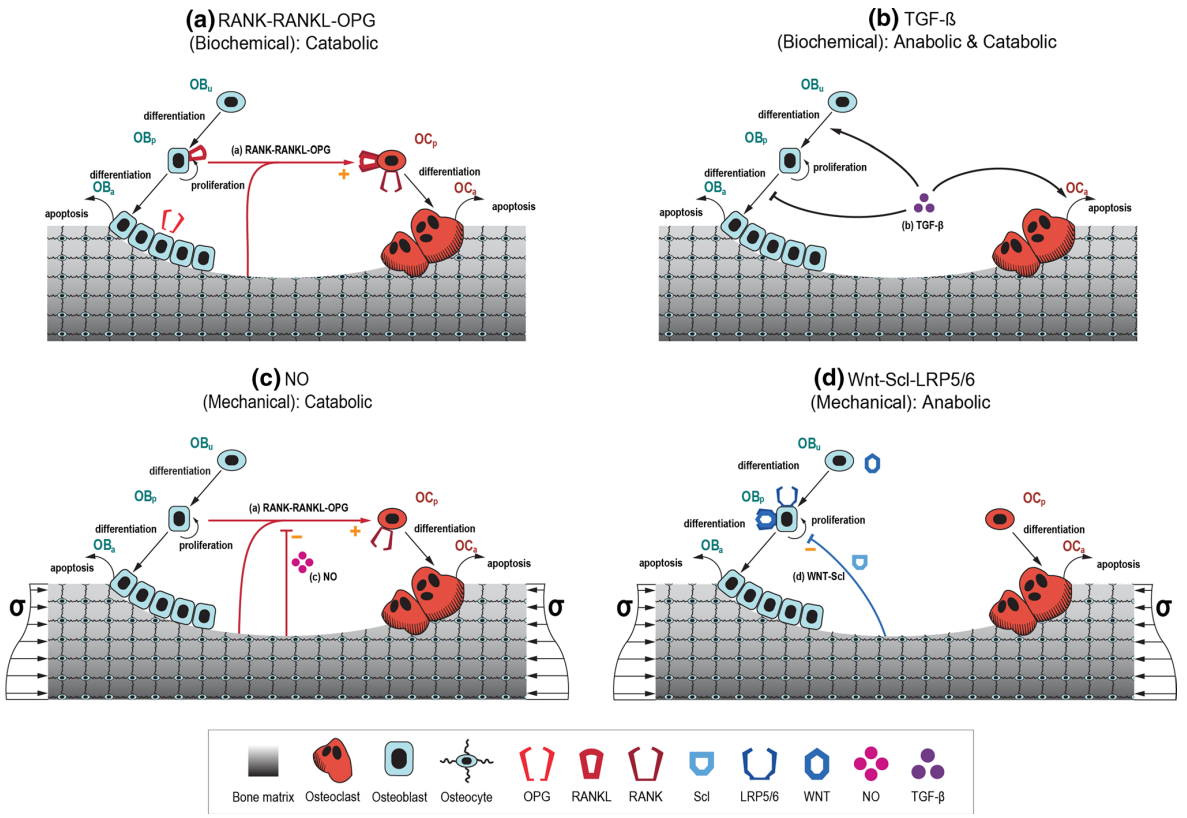

Fig. 2 Mechanobiological regulatory pathways involved in bone remodeling: **a** biochemical RANK–RANKL–OPG regulation (catabolic), **b** biochemical TGF-β regulation (coupling), **c** mechanical NO regulation (catabolic), **d** mechanical Scl–Wnt regulation (anabolic)

is incorporated via regulation of proliferation of osteoblast precursor cells.

We incorporate the RANK–RANKL–OPG catabolic signaling pathway as previously described (Pivonka et al. 2012) (see Fig. 2a). The receptor RANK is expressed on osteoclast precursor cells. RANKL, a membrane bound ligand, is expressed by osteoblast precursor cells, while OPG is produced by active osteoblasts. Catabolic action of continuous PTH administration is incorporated in the model by increasing the RANKL concentration, while simultaneously reducing the OPG production.

The second new model feature is the co-regulation of RANKL (expressed on osteoblast precursor cells) by NO as part of the biochemical mechanostat feedback which is depicted in Fig. 2c. NO is produced by osteocytes responding to changes in mechanical loading.

Action of TGF-β on bone cells is taken into account as previously described (Lemaire et al. 2004; Pivonka et al. 2008) (see Fig. 2b): TGF-β increases osteoblast precursor cells concentration ($\mathrm{Ob_p}$) by up-regulating differentiation of uncommitted osteoblasts and down-regulating the differentiation of osteoblast precursor cells. The action of TGF-β exerted on osteoclasts is to up-regulate apoptosis of active osteoclasts.

Using the above described regulatory mechanisms, the mechanobiological model of bone remodeling can be formulated as cell balance equations describing in- and outflow of cells of the respective cell pools (see Table 1 for numerical values and initial concentrations):

$$\frac{\mathrm{dOb_p}}{\mathrm{d}t} = D_{\mathrm{Ob_u}}\mathrm{Ob_u}\pi^{\mathrm{TGF}\text{-}\beta}_{\mathrm{act,Ob_u}} + P_{\mathrm{Ob_p}}\mathrm{Ob_p}\pi^{\mathrm{Wnt}}_{\mathrm{act,Ob_p}} - D_{\mathrm{Ob_p}}\mathrm{Ob_p}\pi^{\mathrm{TGF}\text{-}\beta}_{\mathrm{rep,Ob_p}} \tag{1}$$

$$\frac{\mathrm{dOb_a}}{\mathrm{d}t} = D_{\mathrm{Ob_p}}\mathrm{Ob_p}\pi^{\mathrm{TGF}\text{-}\beta}_{\mathrm{rep,Ob_p}} - \Delta_{\mathrm{Ob_a}}\mathrm{Ob_a} \tag{2}$$

$$\frac{\mathrm{dOc_a}}{\mathrm{d}t} = D_{\mathrm{Oc_p}}\mathrm{Oc_p}\pi^{\mathrm{RANK}}_{\mathrm{act,Oc_p}} - A_{\mathrm{Oc_a}}\mathrm{Oc_a}\pi^{\mathrm{TGF}\text{-}\beta}_{\mathrm{act,Oc_a}} \tag{3}$$

$$\frac{\mathrm{dOt}}{\mathrm{d}t} = \eta\frac{\mathrm{d}f_{\mathrm{bm}}}{\mathrm{d}t} \tag{4}$$

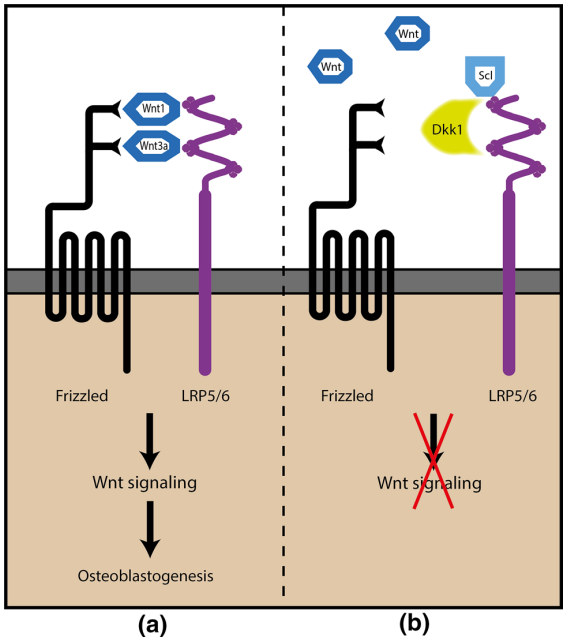

Fig. 3 **a** Wnt ligands bind to Frizzled and LRP5/6 receptors, triggering Wnt signaling; **b** Dkk1 and Scl bind to LRP5/6 receptors, therefore inhibiting Wnt signaling

Table 1 Values of parameters for differentiation (D_X), proliferation (P_X) and apoptosis (A_X) rates of bone cells

Symbol	Value	Unit
Ob_a^0	$8.939\,10^{-4}$	pM
Ob_p^0	$1.129\,10^{-3}$	pM
Ob_u^0	$1.000\,10^{-2}$	pM
Oc_a^0	$1.788\,10^{-5}$	pM
Oc_p^0	$5.592\,10^{-3}$	pM
$D_{\mathsf{Ob_u}}$	$8.300\,10^{-2}$	day^{-1}
$P_{\mathsf{Ob_p}}$	2.203	day^{-1}
$D_{\mathsf{Ob_p}}$	$1.850\,10^{-1}$	day^{-1}
$\Delta_{\mathsf{Ob_a}}$	$2.120\,10^{-1}$	day^{-1}
$D_{\mathsf{Oc_p}}$	$1.958\,10^{-2}$	day^{-1}
$A_{\mathsf{Oc_a}}$	10.00	day^{-1}
α	1.000	–
k_{res}	2500	$\text{pM}^{-1}\,\text{day}^{-1}$
k_{form}	50.00	$\text{pM}^{-1}\,\text{day}^{-1}$
$K_{D,\text{act}}^{\text{TGF-}\beta}$	$5.633\,10^{-4}$	pM
$K_{D,\text{rep}}^{\text{TGF-}\beta}$	$1.754\,10^{-4}$	pM
$K_{D,\text{act}}^{\text{RANK}}$	16.70	pM
η	$4.143\,10^{-8}$ ($4.143\,10^{-2}$)	pmol mm^{-1} (pM)

$K_{D,-}^X$ are the dissociation constants for the activator/repressor functions $\pi_{\text{act/rep},X}^Y$ appearing in Eqs. (1)–(4). η is the concentration of osteocytes in the bone matrix

where $D_{\mathsf{Ob_u}}$, $D_{\mathsf{Ob_p}}$, $D_{\mathsf{Oc_p}}$ are differentiation rates of uncommitted osteoblast progenitor cells and osteoblast/osteoclast precursor cells, respectively. $P_{\mathsf{Ob_p}}$ denotes the proliferation rate of osteoblast precursor cells, $\Delta_{\mathsf{Ob_a}}$ is the rate of clearance of active osteoblasts through apoptosis or differentiation and $A_{\mathsf{Oc_a}}$ is the apoptosis rate of active osteoclasts. Equation (4) indicates that we assume that the change in osteocyte population is proportional to the change in bone matrix fraction $\frac{\mathrm{d}f_{\mathsf{bm}}}{\mathrm{d}t}$. The factor η indicates the average concentration of osteocytes embedded in the bone matrix and was evaluated through the data of Metz et al. (2003), applied to the 1-mm-large representative volume element (RVE). In the previous set of Eqs. (1)–(4), the populations are accounted as concentrations (numerical values in pM, as shown in Table 1) in the RVE.

In the following, all concentrations of regulatory factors and cell numbers are evaluated with respect to the RVE. Note that the present formulation of the evolution of the osteocytes is the combination of the differentiation of osteoblasts into osteocytes (increase in Ot), and the clearance by osteoclasts (decrease in Ot), as exposed in Appendix 1.

Similar to previous model formulations, we assume that the change in bone matrix fraction (f_{bm}) depends on the number of active osteoclasts and osteoblasts [Eq. (5)] and their respective bone resorption and formation rates (Pivonka et al. 2012, 2008; Scheiner et al. 2013):

$$\frac{\mathrm{d}f_{\mathsf{bm}}}{\mathrm{d}t} = -k_{\mathsf{res}}\mathsf{Oc}_\mathsf{a} + k_{\mathsf{form}}\mathsf{Ob}_\mathsf{a}, \tag{5}$$

where k_{res} and k_{form} are, respectively, the rates of bone resorption and formation (see Table 1).

Furthermore, differentiation, proliferation and apoptosis are regulated by several 'activator' ($\pi_{\text{act},X}^Y$) and 'repressor' functions ($\pi_{\text{rep},X}^Y$), i.e., functions which promote or inhibit differentiation, proliferation or apoptosis of cells, as well as ligand production. These regulating functions are described in the following section.

2.2 Mathematical formulation of activator and repressor regulations

In this section, we derive the mathematical formulation of the influence of the listed binding reactions on the cell population evolution and how it deviates from the original formulation of Lemaire et al. (2004). In order to account for the influence of receptor–ligand binding on the system, we make a steady-state assumption: we postulate that the kinetics of the binding reactions are very fast compared to the processes they influence (namely the cell population's evolution and ligand production). Therefore, in line with Pivonka et al. (2008), we find that the production rate P_L of a ligand

L must be balanced with its degradation D_L, which itself can be assumed to be proportional to the concentration of L:

$$P_L + D_L = P_L - \left(\tilde{D}_L[L] + \sum_S \tilde{D}_{L-S}[L-S] \right) = 0, \tag{6}$$

where $\tilde{D}_Y$ is the degradation rate of the species Y and $[L-S]$ represents the concentration of ligand L bound to S, a species in solution that can bind to L.

The production rate can be decomposed into a term accounting for body production $P_{L,b}$ and an additional term corresponding to the external dosage $P_{L,d}$ [see Eq. (8)]. The expression of the endogenous term stems from the assumption that the production of the ligand L is regulated by its own concentration $[L]$, which cannot exceed a limit $[L]_{\max}$ [see Eq. (7)]:

$$P_{L,b} = \sum_{X,Y} \beta_{L,X} \pi^Y_{\text{act/rep},X} X \left(1 - \frac{[L]}{[L]_{\max}} \right), \tag{7}$$

$$P_{L,b} + P_{L,d} = \tilde{D}_L[L] + \sum_S \tilde{D}_{L-S}[L-S], \tag{8}$$

where X is the concentration of the cell type X producing L, with a production rate $\beta_{L,X}$ regulated by the species Y by means of the regulating activator or repressor function $\pi^Y_{\text{act/rep},X}$.

Note that, in order to account for the degradation of the ligand in all its forms, the degradation D_L also comprises the degradation of the bound complexes $L-S$.

TGF-β levels were calculated as derived in Pivonka et al. (2008). Using the observation that TGF-β is stored in the bone matrix and released during resorption by osteoclasts, Pivonka and coworkers postulated that TGF-β levels were proportional to osteoclasts concentration: $[\text{TGF-}\beta] = \alpha\, \text{Oc}_a$, where α is a parameter listed in Table 1.

As described in Pivonka et al. (2012), the activation of the proliferation, differentiation or ligand production of a cell population X caused by the formation of the complex $L-R$ is defined by the ratio between the occupied receptors R by ligands L and the total number of receptors. Its mathematical formulation reads:

$$\pi^L_{\text{act},X} = \frac{[L-R]}{[R]_{\text{tot}}} = \frac{[L-R]}{[R] + \sum_{L'}[L'-R]}, \tag{9}$$

where $[L-R]$ is the concentration of ligands bound to the receptor R and L' is any ligand that can bind to the receptor R (therefore including L).

In the same way, the repressor action of the receptor–ligand binding reads:

$$\pi^L_{\text{rep},X} = \frac{[R]_{\text{tot}} - [L-R]}{[R]_{\text{tot}}} = \frac{[R] + \sum_{L' \neq L}[L'-R]}{[R] + \sum_{L'}[L'-R]} \tag{10}$$

In the case of a single ligand (absence of competitive binding), under the previously defined steady-state assumption, we find the first-order Hill activator and repressor functions:

$$\pi^L_{\text{act},X} = \frac{[L-R]}{[R] + [L-R]} = \frac{[L]}{K^{L-R}_{D,\text{act}} + [L]} \tag{11}$$

$$\pi^L_{\text{rep},X} = \frac{[R]}{[R] + [L-R]} = \frac{1}{1 + \frac{[L]}{K^{L-R}_{D,\text{rep}}}}, \tag{12}$$

where the coefficient $K^{L-R}_{D,\text{act/rep}}$ is the dissociation constant of the ligand–receptor binding reaction.

These functions are exactly the π factors accounting for receptor occupancy used by Lemaire et al. (2004) to account for the influence of the biochemical environment on cell differentiation. In the present model, the first-order Hill activator and repressor functions are used to describe the action of simple ligand–receptor binding:

- TGF-β binding to its receptors: $\pi^{\text{TGF-}\beta}_{\text{rep,Ob}_u}$, $\pi^{\text{TGF-}\beta}_{\text{act,Ob}_p}$, $\pi^{\text{TGF-}\beta}_{\text{act,Oc}_a}$;
- Antagonistic influences of PTH and NO on RANKL production and action of PTH on OPG production: $\pi^{\text{PTH}}_{\text{act,RANKL}}$, $\pi^{\text{NO}}_{\text{rep,RANKL}}$, $\pi^{\text{PTH}}_{\text{rep,OPG}}$.

Some binding schemes are more complex as they involve competition with other ligands or receptors, namely:

- Wnt binding to Frizzled[2]: $\pi^{\text{Wnt}}_{\text{act,Ob}_p}$;
- RANKL binding to RANK: $\pi^{\text{RANKL}}_{\text{act,Oc}_p}$.

Additional functions regulate the production of Scl and NO by osteocytes to account for the influence of mechanical loading on osteocytes ligand production. In turn, these functions regulate the RANKL and Wnt signaling pathways. Instead of using a piecewise linear function to describe the response of the system to mechanical stimuli (either overuse or disuse), we here extended the existing formulation (Scheiner et al. 2013) by creating smooth functions embracing the whole range of stimuli:

- Up-regulation of osteocytes' nitric oxide production by the mechanical stimulus Ψ_{bm}: $\pi^{\Psi_{\text{bm}}}_{\text{act,NO}}$;
- Down-regulation of osteocytes' sclerostin production by the mechanical stimulus Ψ_{bm}: $\pi^{\Psi_{\text{bm}}}_{\text{rep,Scl}}$.

[2] See Sect. 2.1 for details on this ligand–receptor binding.

The above listed activator/repressor functions are detailed in Sect. 2.5 [see Eq. (26, 27) and Table 4]. Here, the mechanical stimulus Ψ_{bm} is the strain energy density in the bone matrix. While strain energy is widely used in the literature as a stimulus to bone remodeling and adaptation (Huiskes et al. 1987; Van Rietbergen et al. 1993), Scheiner et al. (2013) proposed to evaluate this quantity in the bone matrix, implying a dependency on bone's microstructure and macroscopic porosity.

The strain energy in the bone matrix is calculated thanks to a micro-mechanical model developed by Scheiner et al. (2013) representing bone as a porous material saturated by water. The homogenization is performed with the Mori-Tanaka method based on Eshelby's classical matrix-inclusion problem. The properties of the matrix and fluid are listed in Appendix 3 [Eqs. (32, 33)].

Using the above functions, the mechanobiological feedback loop is complete: osteocytes sense the mechanical stimulus, leading to a change in ligand production, namely Scl and NO. The latter factors act on different cells in the BMU, therefore changing the BMU remodeling response which then modifies bone matrix fraction. The change in material properties directly influences the mechanical stimulus Ψ_{bm} via the micro-mechanical representation.

2.3 Competitive Wnt–Scl–LRP5/6 binding

As described in Sect. 2.1, the ligand–receptor competitive binding on the LRP5/6 osteoblastic receptors is complex. A comprehensive description of the competitive binding reactions between all ligands and receptors is beyond the scope of the current paper. As depicted in Fig. 3, Wnt signaling is an anabolic pathway promoting osteoblasts proliferation and bone formation (Fig. 3a). Extracellular Wnt ligands (produced by bone marrow stromal cells) bind to Frizzled and lipoprotein receptor-related proteins (LRP5/6), triggering intracellular activation of β-catenin. As shown in Fig. 3, sclerostin modulates the signaling pathway by interacting with LRP5/6 receptors (Fig. 3b), therefore preventing the formation of a Wnt–Frizzled–LRP5/6 complex.

In the present study, we simplify the dynamics and assume that Scl and Wnt bind directly to LRP5/6 (Fig. 2d). Utilizing this receptor–ligand binding model, Wnt signaling can be quantified (similarly to previous bone cell population models) by the receptor occupancy $\pi^{\mathrm{Wnt}}_{\mathrm{act,Ob_p}}$, defined as the ratio between $\mathsf{Wnt–LRP5/6}$ complexes and the total concentration of LRP5/6 receptors $[\mathsf{LRP5/6}]_{\mathrm{tot}}$, including the ones binding to sclerostin:

$$\pi^{\mathrm{Wnt}}_{\mathrm{act,Ob_p}} = \frac{[\mathsf{Wnt–LRP5/6}]}{[\mathsf{LRP5/6}]_{\mathrm{tot}}}, \tag{13}$$

where

$$[\mathsf{LRP5/6}]_{\mathrm{tot}} = [\mathsf{LRP5/6}] + [\mathsf{Wnt–LRP5/6}] + [\mathsf{Scl–LRP5/6}]. \tag{14}$$

$[\mathsf{LRP5/6}]$ is the concentration of free LRP5/6 receptors, whereas $[\mathsf{Wnt–LRP5/6}]$ and $[\mathsf{Scl–LRP5/6}]$ are, respectively, the concentration of $\mathsf{Wnt–LRP5/6}$ and $\mathsf{Scl–LRP5/6}$ complexes expressed on osteoblast precursors.

Using the steady-state assumption, the total number of receptors $[\mathsf{LRP5/6}]_{\mathrm{tot}}$ can also be expressed as the sum of free and bound receptors as follows:

$$[\mathsf{LRP5/6}]_{\mathrm{tot}} = [\mathsf{LRP5/6}] \left(1 + \frac{[\mathsf{Wnt}]}{K_D^{\mathsf{Wnt–LRP5/6}}} + \frac{[\mathsf{Scl}]}{K_D^{\mathsf{Scl–LRP5/6}}}\right), \tag{15}$$

where $K_D^{\mathsf{Wnt–LRP5/6}}$ and $K_D^{\mathsf{Scl–LRP5/6}}$ are the dissociation constants of the Wnt–LRP5/6 and Scl–LRP5/6 complexes, respectively.

Additionally, given that we assume that the binding reactions are much faster than the processes they regulate (steady-state assumption), there is a balance between the production and degradation of LRP5/6, leading to:

$$[\mathsf{LRP5/6}] = \frac{P_{\mathsf{LRP5/6}}}{\tilde{D}_{\mathsf{LRP5/6}} + \frac{\tilde{D}_{\mathsf{Wnt–LRP5/6}}}{K_D^{\mathsf{Wnt–LRP5/6}}}[\mathsf{Wnt}] + \frac{\tilde{D}_{\mathsf{Scl–LRP5/6}}}{K_D^{\mathsf{Scl–LRP5/6}}}[\mathsf{Scl}]}. \tag{16}$$

We assume that the concentration $[\mathsf{Wnt}]$ of available Wnt proteins stays constant, given as a basal concentration of free Wnt proteins in the medium. This assumption is based on the assumption that the degradation of the complex Wnt–LRP5/6 is negligible and on the fact that bone marrow mesenchymal stem cells (uncommitted osteoblasts $\mathsf{Ob_u}$) are producing Wnt, while the latter population is assumed constant in our model. Note that Wnt antagonists such as Dkk1 and Scl can also bind to LRP5/6 receptors and Kremen co-receptors, which leads to the internalization of LRP5/6 receptors and therefore a diminution of the number of LRP5/6 receptors per cell. Nonetheless, in the present study, we assume that the total number of LRP5/6 receptors per osteoblast precursor cell $N^{\mathsf{LRP5/6}}_{\mathsf{Ob_p}}$ is constant[3]: $[\mathsf{LRP5/6}]_{\mathrm{tot}} = N^{\mathsf{LRP5/6}}_{\mathsf{Ob_p}}\mathsf{Ob_p}$.

[3] The effect of the co-receptor binding to Kremen could be taken into account by acknowledging the dependency of the number of LRP5/6 receptors on osteoblast precursor cells $N^{\mathsf{LRP5/6}}_{\mathsf{Ob_p}}$ via a decreasing function f_{Kr} such that $N^{\mathsf{LRP5/6}}_{\mathsf{Ob_p}} = f_{\mathsf{Kr}}([\mathsf{Kr}])$.

Table 2 Parameters of the competitive binding in the anabolic Wnt pathway

Symbol	Value	Unit
$N_{\mathrm{Ob_p}}^{\mathrm{LRP5/6}}$	50	–
$K_D^{\mathrm{Wnt-LRP5/6}}$	$1.000\,10^3$	pM
$K_D^{\mathrm{Scl-LRP5/6}}$	10.00	pM
$\tilde{D}_{\mathrm{Scl-LRP5/6}}$	50.00	day^{-1}
$\tilde{D}_{\mathrm{Scl}}$, $\tilde{D}^0_{\mathrm{Scl}}$	1.000	day^{-1}
$[\mathrm{Scl}]_{\mathrm{max}}$	70.00	pM Scl
$\beta_{\mathrm{Scl,Ot}}$	$3.000\,10^8$	pM Scl/pmol cell/day
$[Wnt]$	170.0	pM

The sclerostin balance is a function of the local sclerostin production by osteocytes which is regulated via the mechanical repressor function $\pi^{\Psi_{\mathrm{bm}}}_{\mathrm{rep,Scl}}$, as follows:

$$P_{\mathrm{Scl},b} + P_{\mathrm{Scl},d} = \tilde{D}_{\mathrm{Scl}}[\mathrm{Scl}] + \tilde{D}_{\mathrm{Scl-LRP5/6}}[\mathrm{Scl-LRP5/6}] \tag{17}$$

$$P_{\mathrm{Scl},b} = \beta_{\mathrm{Scl,Ot}}\pi^{\Psi_{\mathrm{bm}}}_{\mathrm{rep,Scl}}[\mathrm{Ot}]\left(1 - \frac{[\mathrm{Scl}]}{[\mathrm{Scl}]_{\mathrm{max}}}\right) \tag{18}$$

where $P_{\mathrm{Scl},d}$ is an external sclerostin dosage term, which is set to zero throughout the rest of this paper, and the other terms are as previously defined (see Sect. 2.2). The concentration of Scl obtained from the previous equations (17,18) regulates the Wnt binding to LRP5/6 [Eqs. (14,16)], therefore driving the osteoblast precursors proliferation.

Moreover, the balance of LRP5/6 receptors [Eq. (16)] shows that setting the degradation of the bound Scl–LRP5/6 complex $\tilde{D}_{\mathrm{Scl-LRP5/6}}$ to 0 (no degradation by endocytosis) would lead to a constant number of *free* LRP5 receptors, which means that the total number of receptors would vary as a function of the number of bound sclerostin proteins. In other words, in order to ensure the consistency of the model, one needs to account for the Scl–LRP5/6's degradation rate. With this consideration, the expression of the concentration of free sclerostin [Scl] can be written as a second-order polynomial equation deriving directly from Eq. (8) (see Appendix 4 for more details):

$$A[\mathrm{Scl}]^2 + B[\mathrm{Scl}] + C = 0 \tag{19}$$

Finally, we show in Appendix 4 that Eq. (19) has one and only one physiologically meaningful solution, i.e., the positive root of this equation, allowing us to find the values of the concentration of free sclerostin, and therefore the LRP5/6 receptor occupancy.

The competitive binding described in Eqs. (13,14) is characterized by the reaction parameters as well as the production and degradation rates summarized in Table 2. Several studies investigated the kinetics of receptor binding reactions involved in the Wnt pathway. Holdsworth and collaborators measured the dissociation constant of sclerostin binding to LRP6-E1E2-Fc (Holdsworth et al. 2012). In the present study, we do not differentiate the receptor types within the LRP5/6 family. Additionally, in line with Li et al. (2005), we postulate that Dkk1 and Scl have a similar affinity to the LRP5/6 receptors, and therefore only account for the binding affinity of sclerostin. Moreover, Li and collaborators showed that the presence of Wnt3a did not affect the binding of sclerostin-AP to LRP5R12, which is consistent with Bourhis et al.'s findings that the dissociation constant of Wnt protein is significantly higher than that of Dkk1 (Bourhis et al. 2010). Hence, we set the binding constant $K_D^{\mathrm{Wnt-LRP5/6}}$ 100-fold higher than that of sclerostin, as displayed in Table 2.

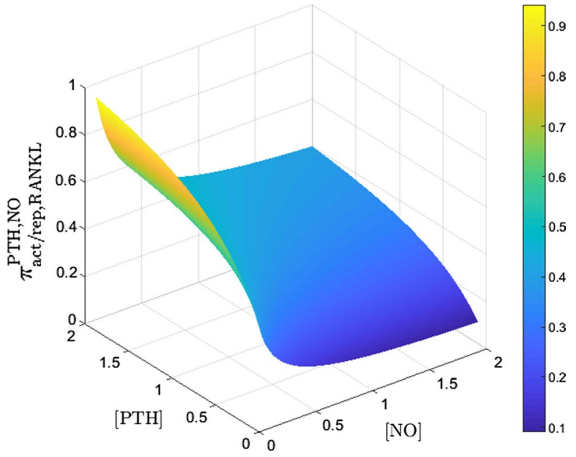

Fig. 4 Co-regulatory function $\pi^{\mathrm{PTH,NO}}_{\mathrm{act/rep,RANKL}}$ accounting for antagonistic influences of the parathyroid hormone (PTH) and nitric oxide (NO) on RANKL production

2.4 Co-regulation of RANKL via parathyroid hormone and nitric oxide concentration

In most previous models of mechanobiological regulation of bone remodeling, the ligand and receptor concentration is regulated via a single factor (Lemaire et al. 2004; Pivonka et al. 2008). One exception is the model of multiple myeloma (Wang et al. 2011), where multiple myeloma cell proliferation was regulated via two factors. This phenomenon is referred to as co-regulation. Increasing model complexity is likely to result in occurrence of co-regulation phenomena given that many intracellular signaling pathways interact with each other (Fig. 4).

In our model, we account for both the up-regulation of RANKL transcription by the parathyroid hormone (PTH) and its inhibition by nitric oxide (NO). These antagonistic influences were merged into a co-regulatory function $\pi^{\mathrm{PTH,NO}}_{\mathrm{act/rep,RANKL}}$ capturing both effects. The competition between the two actions is accounted for by the definition of the co-regulatory function as a weighted sum of the total of the activator and repressor actions and a term accounting for the combined influence:

$$\pi^{\mathrm{PTH,NO}}_{\mathrm{act/rep,RANKL}} = \lambda_s\left(\pi^{\mathrm{PTH}}_{\mathrm{act,RANKL}} + \pi^{\mathrm{NO}}_{\mathrm{rep,RANKL}}\right) + \lambda_c\, \pi^{\mathrm{PTH}}_{\mathrm{act,RANKL}}\pi^{\mathrm{NO}}_{\mathrm{rep,RANKL}}, \tag{20}$$

where λ_s and λ_c are constants, respectively, describing single and combined influences of respective activator/repressor functions. Note that, unlike the classical Hill functions, this competitive regulatory function $\pi^{\mathrm{PTH,NO}}_{\mathrm{act/rep,RANKL}}$ can take values higher than 1 ($\pi^{\mathrm{PTH,NO}}_{\mathrm{act/rep,RANKL}} \in [0, 1.3514]$).

The balance between NO production and degradation reads as follows:

$$P_{\mathrm{NO},b} + P_{\mathrm{NO},d} = \tilde{D}_{\mathrm{NO}}[\mathrm{NO}], \tag{21}$$

$$P_{\mathrm{NO},b} = \beta_{\mathrm{NO,Ot}}\pi^{\Psi_{\mathrm{bm}}}_{\mathrm{act,NO}}\mathrm{Ot}\left(1 - \frac{[\mathrm{NO}]}{[\mathrm{NO}]_{\mathrm{max}}}\right), \tag{22}$$

with the previously defined notations and the external dosage term set to $P_{\mathrm{NO},d} = 0$. The concentration of NO obtained from the previous equation drives the repressive action on RANKL through the Hill repressor function $\pi^{\mathrm{NO}}_{\mathrm{rep,RANKL}}$.

Meanwhile, the RANK–RANKL–OPG pathway involves a competitive binding between OPG and RANK on RANKL. Hence, as derived by Pivonka et al. (2012) and Pastrama et al. (2018), the RANKL concentration reads as follows:

$$[\mathrm{RANKL}] = \frac{P_{\mathrm{RANKL}}}{\tilde{D}_{\mathrm{RANKL}} + \frac{\tilde{D}_{\mathrm{RANK-RANKL}}[\mathrm{RANK}]}{K_D^{\mathrm{RANK-RANKL}}} + \frac{\tilde{D}_{\mathrm{OPG-RANKL}}[\mathrm{OPG}]}{K_D^{\mathrm{OPG-RANKL}}}}, \tag{23}$$

where P_{RANKL} is the sum of the body production rate of RANKL (total from osteoblast precursors $\mathrm{Ob_p}$ and osteocytes Ot production $P_{\mathrm{RANKL},b}$) and an external dosage $P_{\mathrm{RANKL},d}$ (set to zero here, unless otherwise stated). This formulation accounts for the role of osteocytes in bone homeostasis through RANKL production. Appendix 2 gives the mathematical definition of P_{RANKL}, as well as an illustration of the osteopetrotic phenotype observed in osteocyte-specific Tnfsf11-deficient mice (disrupting RANKL expression) (Nakashima et al. 2011).

The RANK and OPG concentrations are functions of the RANKL concentration:

Table 3 Parameters of the competitive binding in the catabolic RANKL pathway

Symbol	Value	Unit
$k^{\mathrm{PTH}}_{D,\mathrm{act}}$	0.6500	pM
$k^{\mathrm{PTH}}_{D,\mathrm{rep,OPG}}$	0.2226	pM
$k^{\mathrm{NO}}_{D,\mathrm{rep}}$	$5.344\,10^3$	pM
$\tilde{D}_{\mathrm{PTH}}$	86.00	day^{-1}
$\tilde{D}_{\mathrm{NO}}$	$2.100\,10^{-3}$	day^{-1}
$\mathrm{NO_{max}}$	$2.000\,10^8$	pM NO
β_{PTH}	$2.500\,10^2$	pM PTH/day
$\beta_{\mathrm{NO,Ot}}$	$2.852\,10^7$	pM NO/pmol cell/day
λ_s	0.4505	–
λ_c	0.9009	–
$N^{\mathrm{RANK}}_{\mathrm{Oc_p}}$	$1.000\,10^3$	–
$K_D^{\mathrm{OPG-RANKL}}$	$1.511\,10^{-2}$	pM
$K_D^{\mathrm{RANK-RANKL}}$	10.00	pM
$\tilde{D}_{\mathrm{OPG}}$	$5.326\,10^5$	day^{-1}
$\tilde{D}_{\mathrm{RANKL}}$	10.13	day^{-1}
$\tilde{D}_{\mathrm{OPG-RANKL}}$	10.13	day^{-1}
$\tilde{D}_{\mathrm{RANK-RANKL}}$	10.13	day^{-1}
$[\mathrm{RANKL}]_{\mathrm{max}}$	$3.051\,10^3$	pM RANKL
$\beta_{\mathrm{RANKL,Ob_p}}$	$2.360\,10^4$	pM RANKL/pM cell/day
$\beta_{\mathrm{RANKL,Ot}}$	$5.660\,10^6$	pM RANKL/pM cell/day
$\beta_{\mathrm{OPG,Ob_a}}$	$1.625\,10^8$	pM OPG/pM cell/day

$$[\mathrm{RANK}] = \frac{N^{\mathrm{RANK}}_{\mathrm{Oc_p}}\mathrm{Oc_p}}{1 + \frac{[\mathrm{RANKL}]}{K_D^{\mathrm{RANK-RANKL}}}} \tag{24}$$

$$[\mathrm{OPG}] = \frac{P_{\mathrm{OPG}}}{\tilde{D}_{\mathrm{OPG}} + \frac{\tilde{D}_{\mathrm{OPG-RANKL}}[\mathrm{RANKL}]}{K_D^{\mathrm{OPG-RANKL}}}}, \tag{25}$$

where $N^{\mathrm{RANK}}_{\mathrm{Oc_p}}$ is the number of RANK receptors per osteoclast precursor and P_{OPG} is the OPG production rate by active osteoblasts $\mathrm{Ob_a}$. The last equations (24,25) can be incorporated into Eq. (23), leading to one algebraic equation giving the numerical value of the RANKL concentration. The parameters involved in the catabolic RANKL pathway are shown in Table 3.

2.5 Mechanobiological feedback driven by osteocyte signaling

In the present section, we describe how the mechanical stimulus drives nitric oxide and sclerostin concentration, which themselves regulate the remodeling processes. We present here the mechanostat feedback from the osteocytes, based on a set-point strain energy criterion. The feedback activator function

$\pi^{\Psi_{bm}}_{act,NO}$ takes the mechanical stimulus (strain energy in the bone matrix Ψ_{bm}) as an input and drives the osteocytes NO production. In the same manner, $\pi^{\Psi_{bm}}_{rep,Scl}$ represents the influence of the value of the strain energy density on osteocyte sclerostin production. Both actions are represented via sigmoidal Hill functions as suggested by Peterson and Riggs (2010):

$$\pi^{\Psi_{bm}}_{act,NO} = \rho_{act} + \frac{(\alpha_{act} - \rho_{act})\Psi_{bm}{}^{\gamma_{act}}}{\delta^{\gamma_{act}}_{act} + \Psi_{bm}{}^{\gamma_{act}}} \tag{26}$$

$$\pi^{\Psi_{bm}}_{rep,Scl} = \alpha_{rep} - \frac{(\alpha_{rep} - \rho_{rep})\Psi_{bm}{}^{\gamma_{rep}}}{\delta^{\gamma_{rep}}_{rep} + \Psi_{bm}{}^{\gamma_{rep}}}, \tag{27}$$

where $\rho_{\sim}$, $\alpha_{\sim}$, $\gamma_{\sim}$, $\delta_{\sim}$ are, respectively, the minimum anticipated response, the maximum anticipated response, the sigmoidicity term influencing the steepness of response and the value of the stimulus that produces the half-maximal response (Peterson and Riggs 2010) and were calibrated (see Sect. 2.7). Here, in order for the modulation of osteocytes' production to be comprised between 0 and 1 similar as the Hill functions $\pi^{Y}_{act/rep,X}$ described previously, we set the same parameters for the mechanical activator and repressor functions so that $\rho_{act} = \rho_{rep} = 0$ and $\alpha_{act} = \alpha_{rep} = 1$. Moreover, the value of both mechanical feedback functions for a homeostatic stimulus is set to 95% of their maximal value, in the aim of ensuring that both actions do not overlap (see Discussion and Fig. 11): $\pi^{\Psi_{bm}}_{rep,Scl}(\Psi_{bm}(\sigma_{ss})) = \pi^{\Psi_{bm}}_{act,NO}(\Psi_{bm}(\sigma_{ss})) = 0.95$, where σ_{ss} is stress value leading to the homeostatic strain energy in the bone matrix $\breve{\Psi}_{bm} = \Psi_{bm}(\sigma_{ss})$. Here, we only calibrated the strength of the response, given by the parameters γ_{act} and γ_{rep}. The values of the parameters defining the activator and repressor mechanical functions are shown in Table 4.

The stimulus corresponding to a steady-state osteocytes' response $\Psi_{bm}(\sigma_{ss}) = \breve{\Psi}_{bm}$ was defined as listed in Table 4. This stimulus corresponds to the strain energy density in the bone matrix when the a piece of bone is subjected to a uniaxial load $\Sigma(t) = \sigma_{ss}\, e_3 \otimes e_3$. The compressive load σ_{ss} was calibrated for a forearm bone tissue ($f_{bm} = 20\%$) to obtain a strain in the bone matrix such that $\epsilon_{33} = 800\mu\epsilon$, which is within the *in vivo* typical range reported in the literature (Rosa et al. 2015). The homeostatic stimulus $\breve{\Psi}_{bm}$ hereby defined (corresponding to the steady-state osteocytes feedback $\pi^{\Psi_{bm}}_{rep,Scl}(\Psi_{bm}(\sigma_{ss})) = \pi^{\Psi_{bm}}_{act,NO}(\Psi_{bm}(\sigma_{ss})) = 0.95$) is assumed to be the same for any bone matrix fraction as our assumption is that osteocytes sense the load in the bone matrix and respond accordingly via biochemical signaling.

Table 4 Parameters of the mechanical regulation

Symbol	Value	Unit
ρ_{act}	0.000	–
ρ_{rep}	0.000	–
α_{act}	1.000	–
α_{rep}	1.000	–
γ_{act}	7	–
γ_{rep}	9	–
δ_{act}	$4.368\,10^{-6}$	–
δ_{rep}	$9.226\,10^{-6}$	–
σ_{ss}	− 3.350	MPa
σ_{dis}	− 2.479	MPa
$\breve{\Psi}_{bm}$	$6.652\,10^{-6}$	MPa

2.6 Numerical implementation

As detailed in Sect. 2.1, we described the bone response due to changes in the biochemical and/or mechanical environment through the regulation of bone cells in the RVE. Therefore, the bone density evolution is obtained by solving a system of five differential equations [Eq. (1)–(5)] accounting for the changes in bone cells (Oc_a, Ob_p, Ob_a, Ot and f_{bm}) , as well as one algebraic equation for the concentration of RANKL [Eq. (23)]. These equations were solved with MATLAB R2017b Stiff Differential Algebraic Equations solver subject to suitable initial conditions (see Table 1). In Sect. 2.7, we apply the above described model to investigate changes in the mechanical environment. Based on the formulated setpoint strain energy density criterion, we can investigate the dynamics of bone adaption, i.e., how the bone remodeling process adjusts to changes in mechanical loading.

2.7 Model calibration

While most model parameters are based on previous model formulations, the introduction of the biochemical osteocyte feedback required additional model calibration. Based on the fact that osteocytes regulate both anabolic and catabolic pathways, applications are chosen accordingly. To calibrate the catabolic pathway, we chose a mechanical disuse scenario, while for the anabolic pathway we chose a post-menopausal osteoporosis (PMO) simulation (see Fig. 6). Note that, while post-menopausal osteoporosis is a catabolic disease, the mechanical feedback regulates bone remodeling toward anabolism, therefore counteracting the hormonal bone loss.

We simulated the mechanical unloading inherent to spaceflight by decreasing the applied load from a habitual (i.e., homeostatic) loading state σ_{ss} to $\sigma_{dis} = 80\%\,\sigma_{ss}$ (see Table 4). These values were estimated based on the study of Genc et al. (2009). Figure 5 shows a parametric study of the

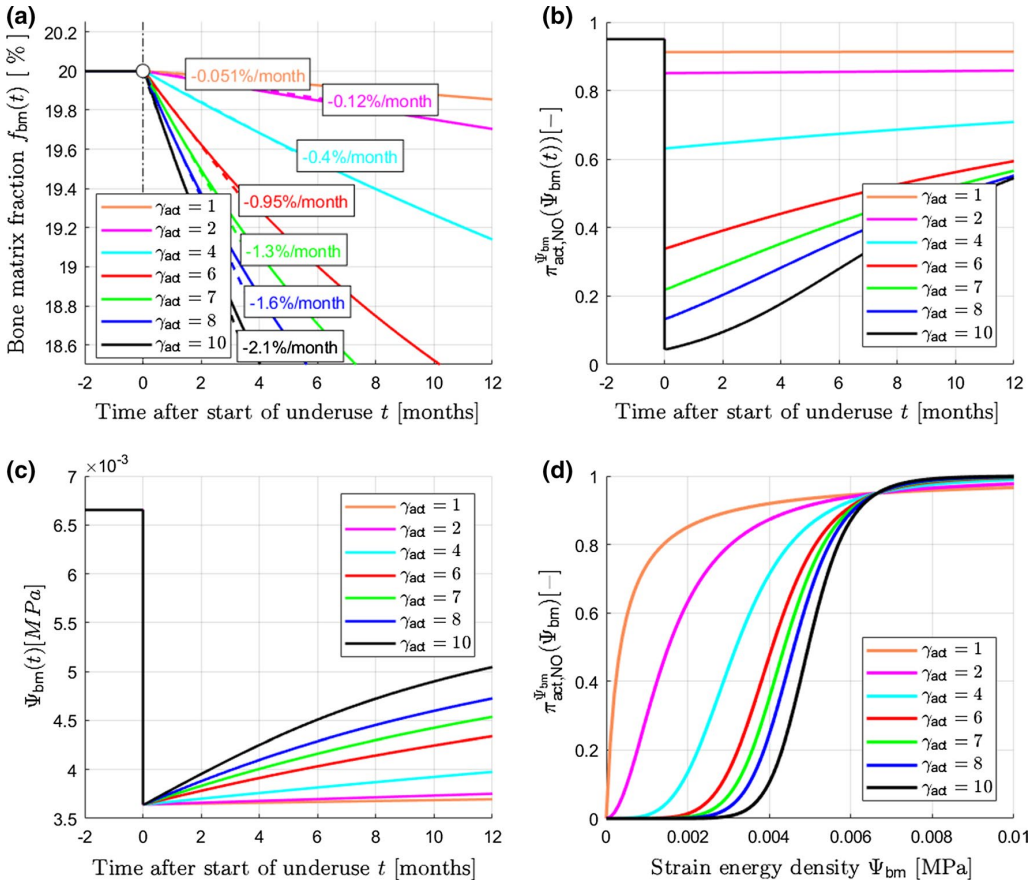

Fig. 5 Effect of steepness of NO activator function on changes in bone matrix fraction f_{bm}: **a** f_{bm} vs time t for different values of γ_{act} (dashed lines indicate constant rate of bone loss, and solid lines indicate model results); **b** $\pi^{\Psi_{bm}}_{act,NO}$ activator function vs time for different steepnesses of γ_{act} values; **c** bone matrix strain energy density (Ψ_{bm}) vs time; and **d** $\pi^{\Psi_{bm}}_{act,NO}$ activator function vs bone matrix strain energy density (Ψ_{bm})

steepness of NO activator function $\pi^{\Psi_{bm}}_{act,NO}$ which depends on the Hill coefficient γ_{act}. Looking at the changes of trabecular bone matrix fraction (f_{bm}) over time under micro-gravity conditions, one can appreciate that the value of γ_{act} regulates the catabolic pathway, i.e., the amount of bone lost[4]. The mechanical activator NO regulation function $\pi^{\Psi_{bm}}_{act,NO}$ [Eq. (26)] and its effect on RANKL concentration were calibrated such as to obtain a 1-1.5% bone loss per month (see blue curve in Fig. 5a), to adequately represent experimental data (LeBlanc et al. 2007).

We calibrated the anabolic mechanobiological feedback pathway according to a longitudinal experimental study by Nordin et al. (1990) on evolution of the BMD in the forearm of post-menopausal women. Here, we do not account for variations in mineral content and assume the bone matrix fraction to evolve in the same way as the BMD. Using this piece of data, we investigated the effect of γ_{rep} on changes in f_{bm}. In the following numerical simulations, we used the example of the forearm (and the subsequent bone matrix fraction and corresponding stress), unless otherwise stated. In previous studies, increased RANKL/OPG ratios have been reported in post-menopausal osteoporotic patients (Jabbar et al. 2011; Lerner 2006; McClung 2007), which might be resulting from the decreasing levels of estrogen which stimulates both osteoclast proliferation and activity (Lerner 2006). Hence, we simulate here post-menopausal osteoporosis by means of an external injection of RANKL ($P_{RANKL,d}$). As shown in Fig. 6b, the initial slope of the decrease in bone density is determined by the value of the injection, which

[4] Note that although we represented the influence of mechanical loading via a Hill function, the function ($\pi^{\Psi_{bm}}_{act,NO}$) does not merely represent a chemical binding reaction but rather summarizes the highly complex phenomenon of osteocytes mechanosensation.

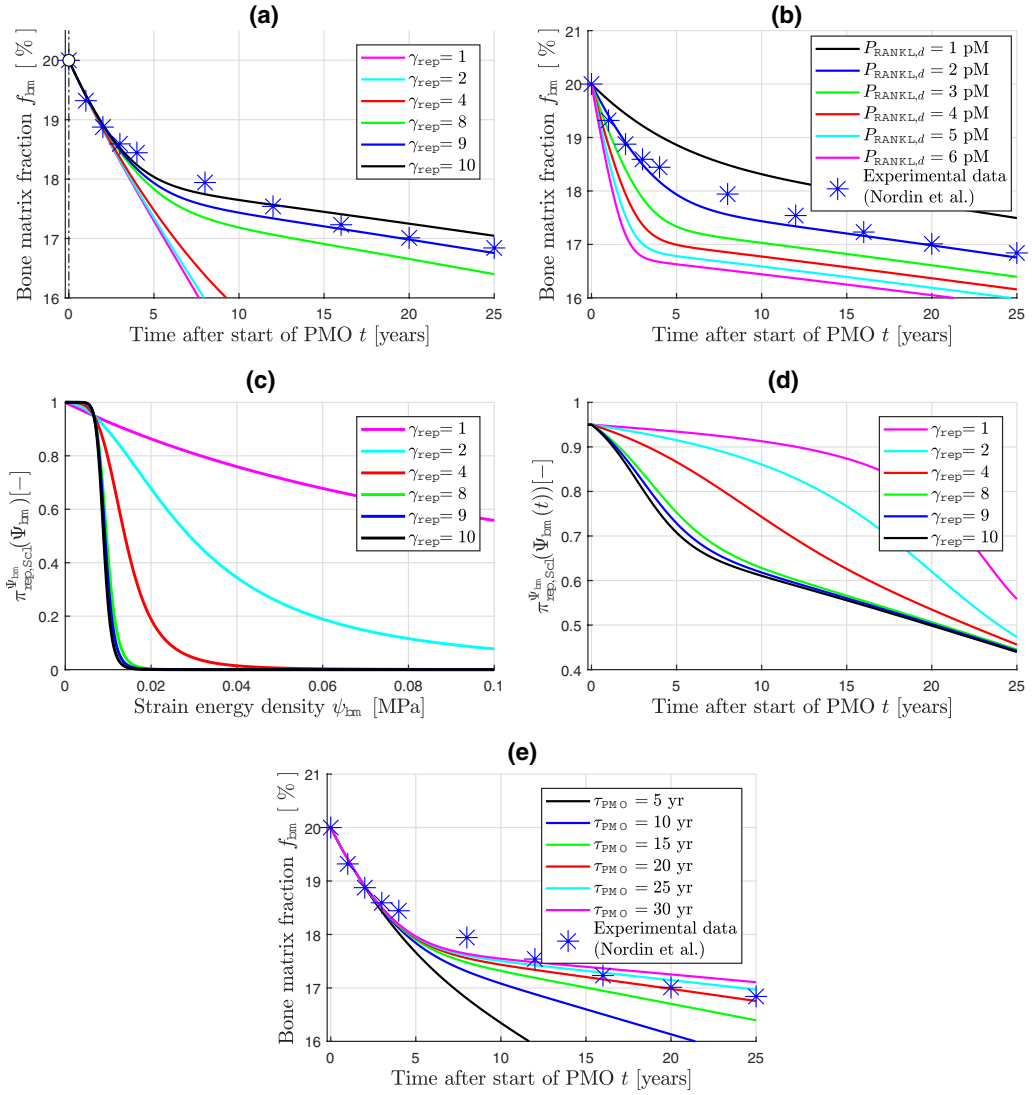

Fig. 6 Effect of various parameters of PMO and mechanobiological feedback on the evolution of bone matrix fraction f_{bm}: **a** f_{bm} vs time for different values of γ_{rep}; **b** f_{bm} vs time for different injection rates of $P_{RANKL,d}$ simulating PMO, indicating that 2 pM/day matches the Nordin et al. data best (Nordin et al. 1990); **c** repressor function $\pi^{\Psi_{bm}}_{rep,Scl}$ vs strain energy density Ψ_{bm}; **d** $\pi^{\Psi_{bm}}_{rep,Scl}$ repressor function vs time and **e** f_{bm} vs time for different characteristic times τ_{PMO} of sclerostin degradation

was here calibrated to $P_{RANKL,d} = 2.000\,\mathrm{pM\,day^{-1}}$ to simulate osteoporosis.

Furthermore, studies have shown an increase in serum sclerostin in post-menopausal subjects (Ardawi et al. 2011; Jastrzebski et al. 2013), while sclerostin expression (local mRNA levels) was found to decrease in animal models of menopause (Jastrzebski et al. 2013). We chose to acknowledge this discrepancy between the serum levels and the local expression of sclerostin by assuming an exponential decay of the degradation rate of sclerostin: $\tilde{D}_{Scl}(t = t_{menop} + \tau) = \tilde{D}_{Scl,PMO}(\tau)$, where $\tilde{D}_{Scl,PMO}$ is the function defined in Eq. (28) and illustrated in Fig. 7a:

$$\tilde{D}_{Scl,PMO}(\tau) = \tilde{D}^0_{Scl}\,\exp\left(-\frac{\tau}{\tau_{PMO}}\right), \tag{28}$$

where $\tau_{PMO} = 20\,\mathrm{yrs}$ is the characteristic time of the decay. We calibrated τ_{PMO} according to experimental data from Nordin et al. (1990) (Fig. 6e). One can observe that this

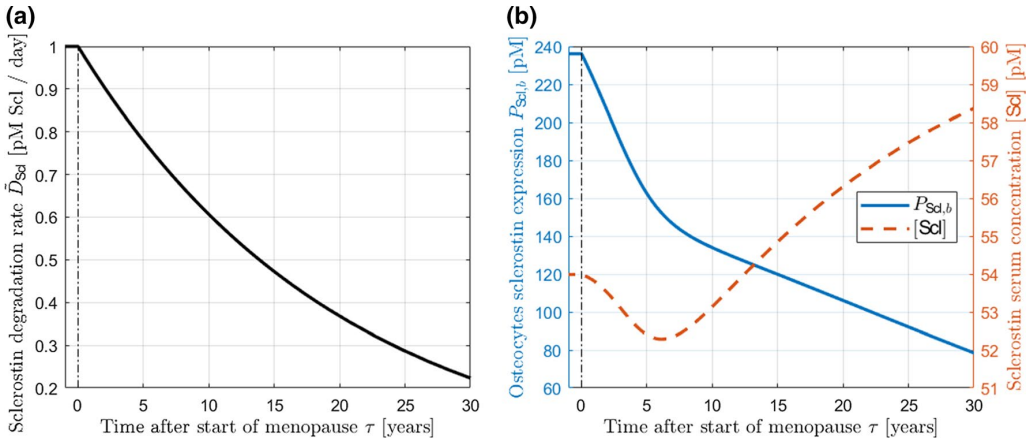

Fig. 7 Evolution of **a** sclerostin degradation rate $\tilde{D}_{\text{Scl,PMO}}(\tau)$ and **b** sclerostin expression (measured with the quantity $P_{\text{Scl},b}$) and serum levels with respect to time after the menopause ($t = t_{menop} + \tau$)

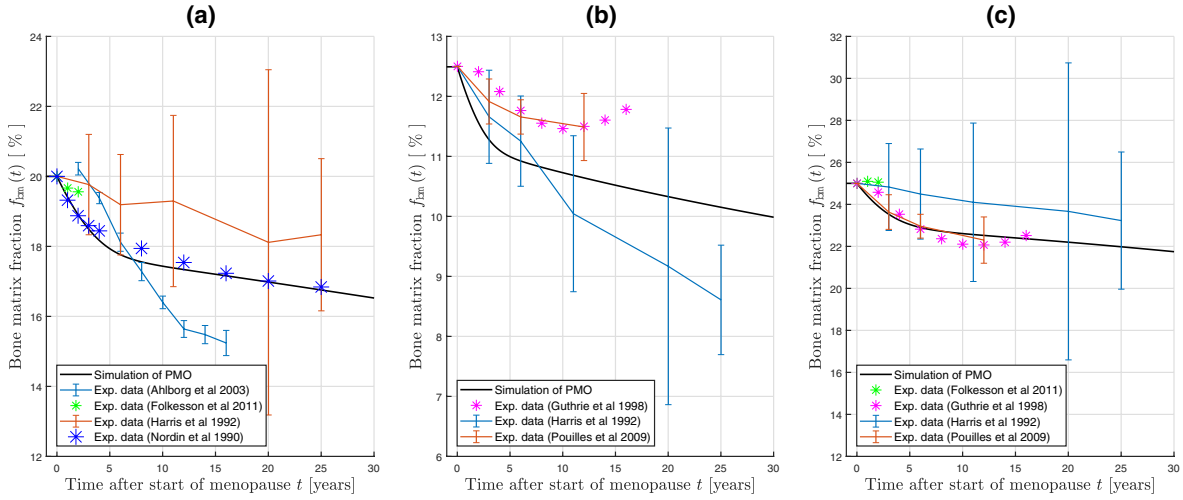

Fig. 8 Evolution of the bone matrix fraction (f_{bm}) with time: comparison of the simulations in **a** distal radius, **b** lumbar spine and **c** femoral neck with experimental results on the evolution of BMD in post-menopausal osteoporosis

characteristic time τ_{PMO} determines the rate of bone loss in the later years after the start of menopause ($\tau > 5$ yrs). The dynamics of the regulation of the sclerostin levels in our model are illustrated in Fig. 7, which displays the evolution of the degradation rate of sclerostin after the start of the menopause (a) and the expression and serum levels of sclerostin (b). Additionally, the steepness of the osteocyte anabolic response to loading is influenced by the parameter γ_{rep} (see Fig. 6a), which directly impacts the osteocyte sclerostin production rate.

We tested the sensitivity of our model with respect to various parameters against experimental data from Nordin et al. (1990). This study is illustrated in Fig. 6, where we investigated the influence of γ_{rep} (a,c,d), $P_{\text{RANKL},d}$ (b) and τ_{PMO} (e). In particular, in Fig. 6(c,d), we observed the anabolic mechanobiological feedback in function of the strain energy density in the bone matrix Ψ_{bm} (c) and over time (d).

3 Results

3.1 Validation of the post-menopausal osteoporosis model

We compared our model of post-menopausal osteoporosis to several existing longitudinal studies in human at different bone sites (Ahlborg et al. 2003; Folkesson et al. 2011; Guthrie et al. 1998; Harris and Dawson-Hughes 1992;

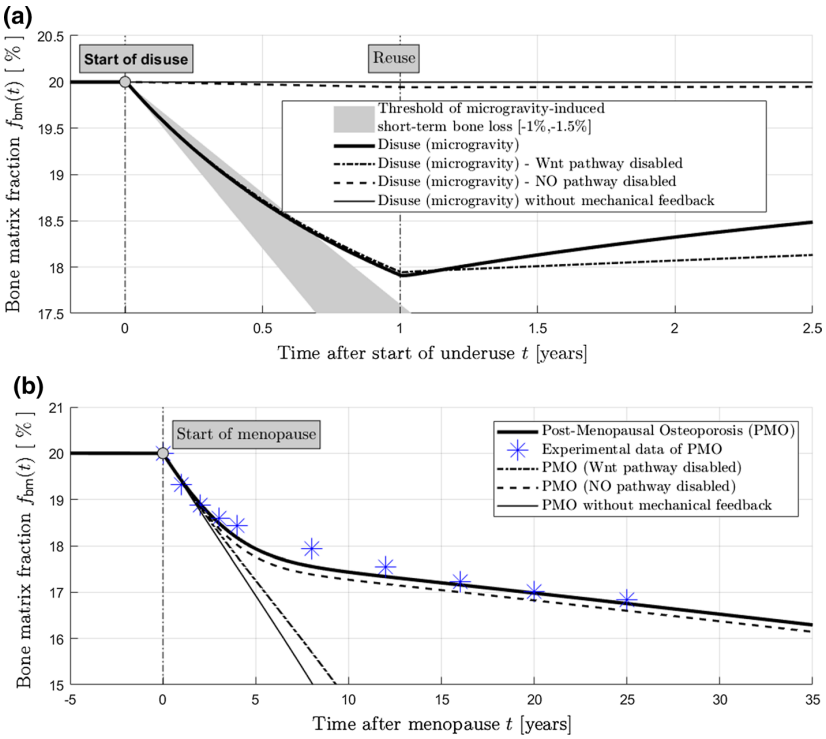

Fig. 9 Influence of active/inactive signaling pathways regulating mechanobiological feedback in remodeling response: **a** simulation of mechanical disuse for 12 months, followed by reuse and **b** simulation of post-menopausal osteoporosis (PMO)

Nordin et al. 1990; Pouilles et al. 2009). Note that each bone site is characterized by a different value of the bone matrix fraction f_{bm} and therefore a specific value of the habitual stress σ_{ss}. While acknowledging that the experimental measurements of BMD do not reflect the exact evolution of the bone matrix fraction, we assume here that they are close enough for us to compare their trend to our simulations. The values of the stresses in Table 4 relate to the mechanical environment in the forearm ($f_{bm} = 20\%$). Now, based on data from the literature, we assumed, respectively, for the femoral neck and the lumbar spine that their steady-state bone matrix fractions were $f_{bm} = 25\%$ (Nazarian et al. 2007) and $f_{bm} = 12.5\%$ (Legrand et al. 2000), which corresponds to habitual stresses $\sigma^{FN} = -4.405$ MPa and $\sigma^{LS} = -2.041$ MPa. Figure 8 displays the literature experimental results for the evolution of BMD with time in post-menopausal osteoporosis at different bone sites [(a) distal radius, (b) lumbar spine and (c) femoral neck], along with our simulation results (solid lines). While the experimental data exhibit large standard deviations, the model is able to predict the mean trends providing confidence in our model formulation.

3.2 Respective contributions of the pathways

We investigated the contribution of different signaling pathways involved in mechanobiological feedback on changes of the trabecular bone matrix fraction (f_{bm}) (Fig. 9). For this purpose, we activated/inactivated the NO production term and/or the Wnt activator function. For instance, in order to disable the NO pathway, we artificially kept the osteocyte NO production rate constant (no regulation: $\forall t$, $\pi^{\Psi_{bm}}_{act,NO}(\Psi_{bm}(t)) = \pi^{\Psi_{bm}}_{act,NO}(\check{\Psi}_{bm})$), corresponding to the initial homeostatic state. This allowed to visualize what part the catabolic NO regulation played in the remodeling. In the same way, we were able to disable the Scl pathway by maintaining the regulatory function $\pi^{\Psi_{bm}}_{rep,Scl}$ constant, in order to analyze the role of Wnt signaling in the mechanobiological feedback. This strategy was applied to two simulations, i.e., mechanical disuse for 12 months followed by reuse (Fig. 9a) and post-menopausal osteoporosis (Fig. 9b).

In Fig. 9, the thin solid line represents the absence of mechanical feedback, i.e., no model response to changes in mechanical loading. The thick solid line represents both the anabolic and catabolic pathways active in the bone remodeling model, which corresponds to the complete model. The dashed–dotted and dashed lines represent, respectively, the cases where the Wnt pathway feedback and the NO pathway feedback are disabled. In the disuse–reuse simulation, one can note that when the homeostatic mechanical loading is reinstated, the bone matrix fraction increases toward its original value. This bone gain is significantly slower than the bone loss induced by load

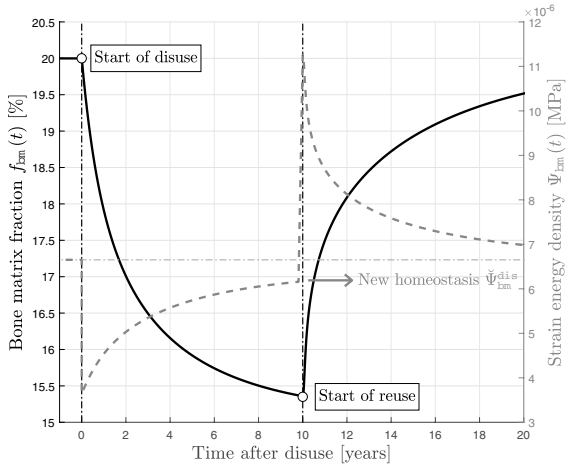

Fig. 10 Simulation of mechanical disuse for 120 months, followed by reuse: evolution of bone matrix fraction (left axis, solid) and strain energy density (right axis, dashed).The horizontal line gives the value of the original setpoint $\check{\Psi}_{bm}$

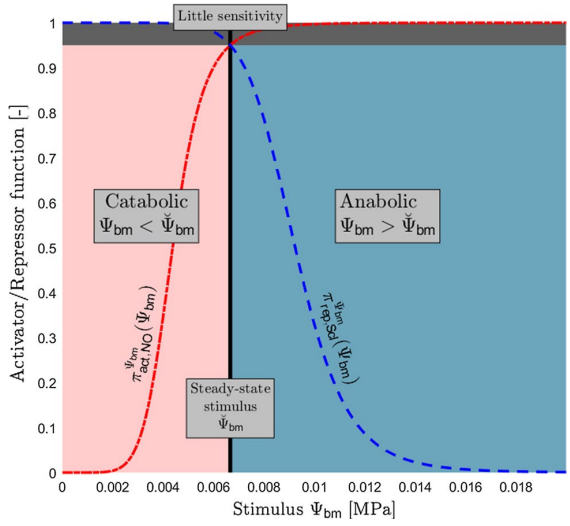

Fig. 11 Separation of the mechanical feedback pathways: mechanical activator and repressor functions as functions of the strain energy density (Ψ_{bm}). Blue dashed curve is the anabolic sclerostin repressor function $\pi^{\Psi_{bm}}_{rep,Scl}$ while red dashed–dotted curve represents the catabolic NO activator function $\pi^{\Psi_{bm}}_{act,NO}$

reduction. When artificially setting the osteocyte production of NO constant to its initial value (dashed curve), the system only weakly responds to the lack of mechanical stimulus. In this case, the catabolic response is driven via $\pi^{\Psi_{bm}}_{rep,Scl}$ only which indicates that the NO contribution is key to the catabolic mechanical feedback to simulate excessive bone loss in mechanical disuse scenarios. Conversely, when $\pi^{\Psi_{bm}}_{rep,Scl}$ is set constant (dashed–dotted curve), the catabolic model response still represents the excessive bone loss under mechanical disuse. However, the anabolic bone response is strongly impaired indicating that the anabolic feedback is mostly due to the $\pi^{\Psi_{bm}}_{rep,Scl}$ function. In the simulation of post-menopausal osteoporosis, the impact of NO production on the overall bone response due to osteoporosis is small, which indicates that the catabolic feedback is secondary in the mechanostat feedback in an osteoporotic state. On the other hand, when setting the sclerostin expression to a constant value, bone loss increases significantly (see Fig. 9b), meaning that the mechanical feedback is weaker. This suggests that osteocyte sclerostin production drives the anabolic feedback response.

4 Discussion

Disuse–Reuse simulation Several years after the start of disuse, the system approaches a new homeostasis, driving the system toward a new strain energy (see Fig. 10). As suggested by Frost (1987), a change in bone's environment shifts the mechanostat setpoint. Here, the disuse creates a loading environment that decreases the homeostatic strain energy ($\check{\Psi}^{dis}_{bm} < \check{\Psi}_{bm}$). Hence, when reinstating the initial loading conditions, neither the bone matrix fraction nor the stimulus is in accordance with the setpoint. This discrepancy induces an anabolic remodeling, decreasing the strain energy toward the initial setpoint. Note that, at the start of the disuse and at the start of the reuse, there is a discrepancy between the homeostatic strain energy and the current stimulus. The difference is negative the first time, causing bone resorption to overtake bone apposition, and positive the second time, resulting in bone gain. Although the discrepancy is the same, the rate of bone gain is much slower than that of bone loss, which is consistent with experimental findings.

Post-Menopausal Osteoporosis When introducing an external RANKL injection term to model osteoporosis, the osteoclasts' action is stimulated. As bone loss occurs, the mechanical loading is higher than the habitual homeostatic loading. As a result, osteocytes create an anabolic feedback leading to new bone formation until a new remodeling equilibrium is reached. Our simulations replicated trends of bone loss in post-menopausal osteoporosis experimentally reported for numerous bone sites (distal radius, femoral neck, lumbar spine). This result (Fig. 8) gives confidence that our model can represent in vivo pathological conditions, which is the first step to the simulation of different possibilities of treatments.

Separation of anabolic and catabolic mechanobiological feedback pathways As explained in Sect. 2.5, where the Scl and NO regulatory functions have been introduced, the mechanobiological feedback proposed in this paper is an

extension of the original formulation of Scheiner et al. (2013). In the original model, the anabolic and catabolic regulatory pathways (i.e., $\pi^{\Psi_{bm}}_{act/rep}$ and $P_{RANKL,d}$) were separated by setting the regulatory function values constant in the respective catabolic and anabolic regions. However, in the present study, mechanobiological regulations via biochemical feedback are C^1 continuous functions depending on Ψ_{bm}. Consequently, $\pi^{\Psi_{bm}}_{rep,Scl}$ not only has a anabolic region, but also a catabolic region (Fig. 11). The same is true for $\pi^{\Psi_{bm}}_{act,NO}$, which has a catabolic region for disuse state ($\Psi_{bm} < \check{\Psi}_{bm}$) and an anabolic region for overloading states ($\Psi_{bm} > \check{\Psi}_{bm}$). One interesting question to address was whether the respective anabolic and catabolic regulatory functions are also effective for opposite loading states, i.e., whether $\pi^{\Psi_{bm}}_{rep,Scl}$ is also effective in simulating catabolic loading states and whether $\pi^{\Psi_{bm}}_{act,NO}$ is also effective in simulating anabolic loading states. As shown in the simulation of spaceflight (Fig. 9a), $\pi^{\Psi_{bm}}_{rep,Scl}$ does not significantly contribute to the catabolic response which is largely due to $\pi^{\Psi_{bm}}_{act,NO}$. On the other hand, the PMO simulations (Fig. 9b) demonstrated that the anabolic response is largely due to $\pi^{\Psi_{bm}}_{rep,Scl}$, while NO only has a minor contribution. These results illustrated in Fig. 11, together with the findings in Fig. 9, indicate that these two pathways are mostly separated, with Scl ($\pi^{\Psi_{bm}}_{rep,Scl}$) regulating the anabolic responses and NO ($\pi^{\Psi_{bm}}_{act,NO}$) regulating the catabolic responses.

The above considerations only account for the osteocyte response to loading, which is dominated by one pathway or the other. The outcome of the osteocytic feedback in terms of species in solution and cell population is seen as a global concentration as we do not describe here the behavior of single BMUs. Moreover, the separation of the pathway in this model is governed by the value $\pi^{\Psi_{bm}}_{rep,Scl}(\check{\Psi}_{bm}) = \pi^{\Psi_{bm}}_{act,NO}(\check{\Psi}_{bm}) = 0.95$. One could account for a coupling of the two pathways by setting this value lower and therefore allowing a competition between the NO and Wnt pathways with respect to anabolic and catabolic regulations.

RANKL competitive binding formulation One of the main features of the present study is the proposal of a consistent formulation of the RANK–RANKL–OPG pathway. Instead of considering the RANKL concentration to be proportional to the number of osteoblasts (Komarova et al. 2003) or assuming a constant concentration of receptors RANK (Lemaire et al. 2004; Pivonka et al. 2008), we wrote the binding reactions and linked the concentration of receptors to the concentration of cells that bear RANK receptors. This allows to account quantitatively for the role of OPG and RANKL in bone catabolism, and in particular when simulating post-menopausal osteoporosis (Fig. 6), or an anti-catabolic treatment acting on the RANK–RANKL–OPG pathway (Scheiner et al. 2014).

Note that, in the present study, we only model a subset of RANKL's actions and not all osteoclast lineage cell types it acts on. For instance, we do not account for the role of RANKL in the fusion of uncommitted osteoclasts into multinucleated cells.

Other models of mechanical feedback Note that previous models included sclerostin (Van Oers et al. 2011) and nitric oxide (Maldonado et al. 2006) to drive bone adaptation based on mechanical loads, including osteocytes as mechanotransducers. While Van Oers and coworkers did not include the description of the biochemical regulation (Van Oers et al. 2011), Maldonado et al. (2006) did include the regulation of the RANKL pathway by NO and the promotion of bone formation by PGE_2. However, although there is experimental evidence that PGE_2 enables Wnt signaling (Bonewald and Johnson 2008), the interaction between the latter remains unclear. Additionally, in their study, Maldonado and coworkers implemented a local law and therefore did not account for the multiscale nature of bone. Finally, the present model, by acknowledging the role of sclerostin in a constistent way, gives the opportunity to study the potential of anabolic monoclonal antibody treatments targeting the Wnt pathway.

5 Summary and conclusions

To investigate skeletal adaptation, we extended an earlier model of bone cell populations that describes bone remodeling. This new model incorporates additional cell types such as osteoclast precursor cells and osteocytes. In particular, osteocytes are crucial for the formulation of mechanical adaptation via the production of sclerostin and nitric oxide that, respectively, inhibit osteoblastogenesis and the catabolic RANK–RANKL–OPG pathway. Based on our numerical simulations, the following conclusions can be made:

- The bone cell population model describes the dynamics of bone remodeling in the case of a change in mechanical loading, as well as hormonal changes (post-menopausal osteoporosis).
- Separation of anabolic and catabolic bone remodeling responses was achieved in the model based on two separate signaling pathways.
- Catabolic model responses were linked to the nitric oxide (NO) pathway. This model feature was capable of driving resorptive osteoclastic activity. Hence, NO production by osteocytes was connected to bone loss as well as achievement of a new steady state.
- Conversely, anabolic model responses were linked to the Wnt signaling pathway. The latter model feature is

a key factor for the observed bone formation response. Furthermore, it helps stabilizing the bone matrix fraction in PMO as it counters the enhanced resorptive action of the RANKL pathway.

While our results indicate that the proposed model is able to capture essential features of bone remodeling, further testing of the model on various experimental data is required. One important model extension could be toward assessing the effect of sclerostin antibody treatment on PMO. Recent clinical trials on the latter treatment have shown it to be highly effective in restoring bone mass in osteoporosis (Keaveny et al. 2017; Langdahl et al. 2017; Padhi et al. 2014).

Acknowledgements Miss Madge Martin received a 12-month QUT School of Chemistry, Physics and Mechanical Engineering (CPME) Scholarship.

Compliance with ethical standards

Conflict of interest The authors declare that they have no conflict of interest.

Appendix 1: Formulation of the evolution of the osteocytes population

As written in Eq. (4), we chose here to represent the change in osteocytes concentration Ot as a function of bone matrix fraction f_{bm}. It is well accepted that osteocytes are differentiated osteoblastic cells buried in the bone matrix. As a result, one could argue that the evolution of the osteocytes population could be written as follows:

$$\frac{\mathrm{dOt}}{\mathrm{d}t} = D_{\mathrm{Ob_a}}\mathrm{Ob_a} - R_{\mathrm{Ot}}^{\mathrm{Oc_a}}\mathrm{Oc_a}, \tag{29}$$

where one can note that the sink term is proportional to the concentration of osteoclasts $\mathrm{Oc_a}$. Osteoclasts resorb bone and trigger osteocyte apoptosis by means of a local acidification. This action is quantified through the factor $R_{\mathrm{Ot}}^{\mathrm{Oc_a}}$ in Eq. (29). If we set the osteoblasts differentiation coefficient to $D_{\mathrm{Ob_a}} = \eta k_{\mathrm{form}}$ and the resorption coefficient to $R_{\mathrm{Ot}}^{\mathrm{Oc_a}} = \eta k_{\mathrm{res}}$, we obtain readily the formulation given in Eq. (4) in Sect. 2.1.

Appendix 2: Formulation of the RANKL production

We made the assumption that RANKL is expressed by osteocytes and osteoblasts precursors, following experimental evidence (Nakashima et al. 2011; Xiong et al. 2015). Therefore, the body production term for RANKL reads as follows:

$$\begin{aligned} P_{\mathrm{RANKL},b} = {} & \beta_{\mathrm{RANKL,Ot}}\mathrm{Ot}\left(1 - \frac{[\mathrm{RANKL}]_{\mathrm{tot}}}{[\mathrm{RANKL}]_{\mathrm{max}}}\right) \\ & + \beta_{\mathrm{RANKL,Ob_p}}\pi_{\mathrm{act/rep,RANKL}}^{\mathrm{PTH,NO}}\mathrm{Ob_p}\left(1 - \frac{[\mathrm{RANKL}]_{\mathrm{tot}}}{[\mathrm{RANKL}]_{\mathrm{max}}}\right), \end{aligned} \tag{30}$$

where the total concentration of RANKL (bound and free) $[\mathrm{RANKL}]_{\mathrm{tot}}$ is defined as follows:

$$[\mathrm{RANKL}]_{\mathrm{tot}} = [\mathrm{RANKL}] \left(1 + \frac{[\mathrm{RANK}]}{K_D^{\mathrm{RANK-RANKL}}} + \frac{[\mathrm{OPG}]}{K_D^{\mathrm{OPG-RANKL}}}\right). \tag{31}$$

The parameters used in Eqs. (30), (31) are displayed in Table 3. When knocking out numerically the expression of RANKL by osteocytes ($\beta_{\mathrm{RANKL,Ot}} = 0$), we obtain the osteopetrotic phenotype observed experimentally (Nakashima et al. 2011). This result is illustrated in Fig. 12, where the steady state (dashed line) is compared to the RANKL-deficient state (solid line).

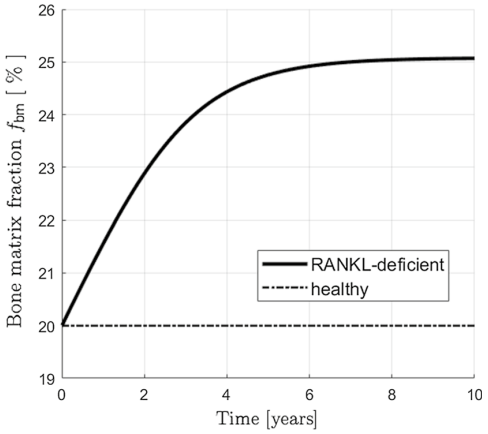

Fig. 12 Influence of osteocytes' RANKL production on bone homeostasis: we compare the steady state (dashed–dotted line) to the RANKL-deficient state (solid line)

Appendix 3: Properties of matrix and fluid in the micro-mechanical model

The stiffness tensor of the bone matrix reads as follows (Kelvin notation):

$$\mathbb{c}_{\text{bm}} = \begin{pmatrix} 18.5 & 10.3 & 10.4 & 0 & 0 & 0 \\ 10.3 & 20.8 & 11.0 & 0 & 0 & 0 \\ 10.4 & 11.0 & 28.4 & 0 & 0 & 0 \\ 0 & 0 & 0 & 12.9 & 0 & 0 \\ 0 & 0 & 0 & 0 & 11.5 & 0 \\ 0 & 0 & 0 & 0 & 0 & 9.3 \end{pmatrix} \text{GPa} \tag{32}$$

The stiffness tensor of the saturating fluid is:

$$\mathbb{c}_{\text{vas}} = k_{\text{H}_2\text{O}}\mathbb{J} + \mu_{\text{H}_2\text{O}}\mathbb{K}, \tag{33}$$

where the bulk modulus and the shear modulus are, respectively, $k_{\text{H}_2\text{O}} = 2.3$ GPa and $\mu_{\text{H}_2\text{O}} = 0$ GPa, and $\mathbb{J}$ is the volumetric part of the fourth-order unit tensor $\mathbb{I}$, and $\mathbb{K}$ is its deviatoric part, $\mathbb{K} = \mathbb{I} - \mathbb{J}$.

Appendix 4: Derivation of free sclerostin concentration

The following equation describes sclerostin balance:

$$\begin{aligned} P_{\text{Scl},b} + P_{\text{Scl},d} &= \tilde{D}_{\text{Scl}}[\text{Scl}] \\ &+ D_{\text{Scl}-\text{LRP5/6}}[\text{Scl} - \text{LRP5/6}] \end{aligned} \tag{34}$$

with

$$\begin{aligned} [\text{Scl} - \text{LRP5/6}] &= \frac{[\text{LRP5/6}][\text{Scl}]}{K_D^{\text{LRP5/6}-\text{Scl}}} \\ &= \frac{[\text{Scl}][\text{LRP5/6}]_{\text{tot}}}{K_D^{\text{LRP5/6}-\text{Scl}}(1 + \frac{[\text{Wnt}]}{K_D^{\text{Wnt,LRP5/6}}} + \frac{[\text{Scl}]}{K_D^{\text{Scl,LRP5/6}}})}. \end{aligned} \tag{35}$$

After inserting Eqs. (18) and (35) into Eq. (34), we uncover a second-order polynomial equation on the concentration of free sclerostin [Scl]:

$$A[\text{Scl}]^2 + B[\text{Scl}] + C = 0, \tag{36}$$

where

$$\begin{aligned} A &= \tilde{D}_{\text{Scl}} + \frac{\beta_{\text{Scl}}[\text{Ot}]\pi_{\text{rep,Scl}}^{\Psi_{\text{bm}}}}{[\text{Scl}]_{\text{max}}} \\ B &= K_D^{\text{Scl}-\text{LRP5/6}}(\tilde{D}_{\text{Scl}} \\ &\quad + (\beta_{\text{Scl}}[\text{Ot}]\pi_{\text{rep,Scl}}^{\Psi_{\text{bm}}})/[\text{Scl}]_{\text{max}}) \\ &\quad (1 + [\text{Wnt}]/K_D^{\text{Wnt}-\text{LRP5/6}}) \\ &\quad + \tilde{D}_{\text{Scl}-\text{LRP5/6}}[\text{LRP5/6}]_{\text{tot}} - P_{\text{Scl},d}\beta_{\text{Scl}}[\text{Ot}]\pi_{\text{rep,Scl}}^{\Psi_{\text{bm}}} \\ C &= -P_{\text{Scl},d}\beta_{\text{Scl}}[\text{Ot}]\pi_{\text{rep,Scl}}^{\Psi_{\text{bm}}}(1 + [\text{Wnt}]/K_D^{\text{Wnt}-\text{LRP5/6}}) \end{aligned}$$

The term A is a sum of positive quantities, one of them being strictly positive, and the term C is the opposite of the product of strictly positive quantities except for the concentration of osteocytes that we can assume to be non-null. From linear algebra, we know the product of the solutions is equal to $\frac{C}{A} < 0$. Thus, provided solutions are in the real space, there are exactly two roots of opposed signs satisfying this equation. Hence, as the solution of the equation is a concentration, the only acceptable root is:

$$[\text{Scl}] = \frac{-B + \sqrt{B^2 - 4AC}}{2A}$$

Appendix 5: Nomenclature

The abbreviations used in the present paper are summarized in Table 5.

Table 5 Nomenclature

Symbol	Description
Cells	
Ob_u	Osteoblast uncommited precursor cells
Ob_p	Osteoblast precursor cells
Ob_a	Active osteoblasts
Oc_p	Osteoclast precursor cells
Oc_a	Active osteoclasts
Ot	Osteocytes
η	Osteocytes concentration in the bone matrix
Ligands, hormones	
LRP5/6	Lipoprotein receptor-related proteins 5/6
NO	Nitric oxide
OPG	Osteoprotegerin
PGE2	Prostaglandin E2
PTH	Parathyroid hormone
RANK	Receptor activator of nuclear factor kappa-B
RANKL	RANK ligand
Scl	Sclerostin
TGF-β	Transforming growth factor beta
Mechanics	
Ψ_{bm}	Strain energy density
$\breve{\Psi}_{\text{bm}}$	'Homeostatic' strain energy density
f_{bm}	Bone matrix fraction
BMD	Bone mineral density

References

Ahlborg HG, Johnell O, Turner CH, Rannevik G, Karlsson MK (2003) Bone loss and bone size after menopause. N Engl J Med 349(4):327–334. https://doi.org/10.1056/NEJMoa022464

Ardawi MSM, Al-Kadi HA, Rouzi AA, Qari MH (2011) Determinants of serum sclerostin in healthy pre- and postmenopausal women. J Bone Miner Res 26(12):2812–2822. https://doi.org/10.1002/jbmr.479

Beaupré GS, Orr TE, Carter DR (1990) An approach for time-dependent bone modeling and remodeling-theoretical development. J Orthop Res 8(5):651–661. https://doi.org/10.1002/jor.1100080506

Bodine PVN, Komm BS (2007) Wnt signaling and osteoblastogenesis. Rev Endocr Metab Disord 7(1–2):33–39. https://doi.org/10.1007/s11154-006-9002-4

Bonewald LF (2011) The amazing osteocyte. J Bone Miner Res 26(2):229–238. https://doi.org/10.1002/jbmr.320

Bonewald LF, Johnson ML (2008) Osteocytes, mechanosensing and Wnt signaling. Bone 42(4):606–615. https://doi.org/10.1016/j.bone.2007.12.224

Bourhis E, Tam C, Franke Y, Bazan JF, Ernst J, Hwang J, Costa M, Cochran AG, Hannoush RN (2010) Reconstitution of a Frizzled8-Wnt3a-LRP6 signaling complex reveals multiple Wnt and Dkk1 binding sites on LRP6. J Biol Chem 285(12):9172–9179. https://doi.org/10.1074/jbc.M109.092130

Buenzli PR, Thomas CDL, Clement JG, Pivonka P (2013) Endocortical bone loss in osteoporosis: the role of bone surface availability. Int J Numer Method Biomed Eng. https://doi.org/10.1002/cnm.2567

Chow JWM, Fox SW, Lean JM, Chambers TJ (1998) Role of nitric oxide and prostaglandins in mechanically induced bone formation. J Bone Miner Res 13(6):1039–1044. https://doi.org/10.1359/jbmr.1998.13.6.1039

Doblaré M, García JM (2001) Application of an anisotropic bone-remodelling model based on a damage-repair theory to the analysis of the proximal femur before and after total hip replacement. J Biomech 34(9):1157–1170. https://doi.org/10.1016/S0021-9290(01)00069-0

Duncan RL, Turner CH (1995) Mechanotransduction and the functional response of bone to mechanical strain. Calcif Tissue Int 57:344–358. https://doi.org/10.1007/BF00302070

Fan X, Roy E, Zhu L, Murphy TC, Ackert-Bicknell C, Hart CM, Rosen C, Nanes MS, Rubin J (2004) Nitric oxide regulates receptor activator of nuclear factor-κB ligand and osteoprotegerin expression in bone marrow stromal cells. Endocrinology 145(2):751–759. https://doi.org/10.1210/en.2003-0726

Folkesson J, Goldenstein J, Carballido-Gamio J, Kazakia G, Burghardt AJ, Rodriguez A, Krug R, de Papp AE, Link TM, Majumdar S (2011) Longitudinal evaluation of the effects of alendronate on MRI bone microarchitecture in postmenopausal osteopenic women. Bone 48(3):611–621. https://doi.org/10.1016/j.bone.2010.10.179

Frost HM (1987) Bone "mass" and the "mechanostat": a proposal. Anat Rec 219(1):1–9. https://doi.org/10.1002/ar.1092190104

Frost HM (1996) Perspectives: a proposed general model of the "Mechanostat" (Suggestions from a new skeletal-biologic paradigm). Anat Rec 244(2):139–147. https://doi.org/10.1002/ar.1092190104

Galea GL, Lanyon LE, Price JS (2017) Sclerostin's role in bone's adaptive response to mechanical loading. Bone 96:38–44. https://doi.org/10.1016/j.bone.2016.10.008

Gaudio A, Pennisi P, Bratengeier C, Torrisi V, Lindner B, Mangiafico RA, Pulvirenti I, Hawa G, Tringali G, Fiore CE (2010) Increased sclerostin serum levels associated with bone formation and resorption markers in patients with immobilization-induced bone loss. J Clin Endocrinol Metab 95(5):2248–2253. https://doi.org/10.1210/jc.2010-0067

Genc K, Gopalakrishnan R, Kuklis MM, Maender CC, Rice AJ, Cavanagh P (2009) Using the enhanced daily load stimulus model to quantify the mechanical load and bone mineral density changes experienced by crew members on the international space station. In: Orthopaedic Research Society 56th annual meeting, New Orleans, LA, USA, p 1

Guthrie JR, Ebeling PR, Hopper JL, Barrett-Connor E, Dennerstein L, Dudley EC, Burger HG, Wark JD (1998) A prospective study of bone loss in menopausal Australian-born women. Osteoporos Int 8(3):282–290. https://doi.org/10.1007/s001980050066

Harris S, Dawson-Hughes B (1992) Rates of change in bone mineral density of the spine, heel, femoral neck and radius in healthy postmenopausal women. Bone Miner 17(1):87–95. https://doi.org/10.1016/0169-6009(92)90713-N

Holdsworth G, Slocombe P, Doyle C, Sweeney B, Veverka V, Le Riche K, Franklin RJ, Compson J, Brookings D, Turner J, Kennedy J, Garlish R, Shi J, Newnham L, McMillan D, Muzylak M, Carr MD, Henry AJ, Ceska T, Robinson MK (2012) Characterization of the interaction of sclerostin with the low density lipoprotein receptor-related protein (LRP) family of wnt co-receptors. J Biol Chem 287(32):26,464–26,477. https://doi.org/10.1074/jbc.M112.350108

Huiskes R, Weinans H, Grootenboer HJ, Dalstra M, Fudala B, Slooff TJ (1987) Adaptive bone-remodeling theory applied to prosthetic-design analysis. J Biomech 20(11–12):1135–1150. https://doi.org/10.1016/0021-9290(87)90030-3

Huiskes R, Ruimerman R, van Lenthe GH, Janssen JD (2000) Effects of mechanical forces on maintenance and adaptation of form in trabecular bone. Nature 405(6787):704–706. https://doi.org/10.1038/35015116

Jabbar S, Drury J, Fordham JN, Datta HK, Francis RM, Tuck SP (2011) Osteoprotegerin, RANKL and bone turnover in postmenopausal osteoporosis. J Clin Pathol 64(4):354–357. https://doi.org/10.1136/jcp.2010.086595

Jastrzebski S, Kalinowski J, Stolina M, Mirza F, Torreggiani E, Kalajzic I, Won HY, Lee SK, Lorenzo J (2013) Changes in bone sclerostin levels in mice after ovariectomy vary independently of changes in serum sclerostin levels. J Bone Miner Res 28(3):618–626. https://doi.org/10.1002/jbmr.1773

Jee WS, Tian XY (2005) The benefit of combining non-mechanical agents with mechanical loading: A perspective based on the Utah paradigm of skeletal physiology. J Musculoskelet Neuronal Interact 5(2):110–118

Keaveny TM, Crittenden DB, Bolognese MA, Genant HK, Engelke K, Oliveri B, Brown JP, Langdahl BL, Yan C, Grauer A, Libanati C (2017) Greater gains in spine and hip strength for romosozumab compared with teriparatide in postmenopausal women with low bone mass. J Bone Miner Res 32(9):1956–1962. https://doi.org/10.1002/jbmr.3176

Komarova SV, Smith RJ, Dixon SJ, Sims SM, Wahl LM (2003) Mathematical model predicts a critical role for osteoclast autocrine regulation in the control of bone remodeling. Bone. https://doi.org/10.1016/S8756-3282(03)00157-1

Langdahl B, Ferrari S, Dempster DW (2016) Bone modeling and remodeling: potential as therapeutic targets for the treatment of osteoporosis. Ther Adv Musculoskelet Dis 8(6):225–235. https://doi.org/10.1177/1759720X16670154

Langdahl BL, Libanati C, Crittenden DB, Bolognese MA, Brown JP, Daizadeh NS, Dokoupilova E, Engelke K, Finkelstein JS, Genant HK, Goemaere S, Hyldstrup L, Jodar-Gimeno E, Keaveny TM, Kendler D, Lakatos P, Maddox J, Malouf J, Massari FE, Molina JF, Ulla MR, Grauer A (2017) Romosozumab (sclerostin monoclonal antibody) versus teriparatide in postmenopausal women with osteoporosis transitioning from oral bisphosphonate therapy: a randomised, open-label, phase 3 trial. Lancet 390(10102):1585–1594. https://doi.org/10.1016/S0140-6736(17)31613-6

LeBlanc AD, Spector ER, Evans HJ, Sibonga JD (2007) Skeletal responses to space flight and the bed rest analog: a review. J Musculoskelet Neuronal Interact 7(1):33–47

Legrand E, Chappard D, Pascaretti C, Duquenne M, Krebs S, Rohmer V, Basle MF, Audran M (2000) Trabecular bone microarchitecture, bone mineral density, and vertebral fractures in male osteoporosis. J Bone Miner Res 15(1):13–19. https://doi.org/10.1359/jbmr.2000.15.1.13

Lemaire V, Tobin FL, Greller LD, Cho CR, Suva LJ (2004) Modeling the interactions between osteoblast and osteoclast activities in bone remodeling. J Theor Biol 229(3):293–309. https://doi.org/10.1016/j.jtbi.2004.03.023

Lerner U (2006) Bone remodeling in post-menopausal osteoporosis. J Dent Res 85(7):584–595. https://doi.org/10.1177/154405910608500703

Li X, Zhang Y, Kang H, Liu W, Liu P, Zhang J, Harris SE, Wu D (2005) Sclerostin binds to LRP5/6 and antagonizes canonical Wnt signaling. J Biol Chem 280(20):19,883–19,887. https://doi.org/10.1074/jbc.M413274200

Maldonado S, Borchers S, Findeisen R, Allgöwer F (2006) Mathematical modeling and analysis of force induced bone growth. In: International conference of the IEEE engineering in medicine and biology society, vol 1, pp 3154–3157. https://doi.org/10.1109/IEMBS.2006.260532

McClung M (2007) Role of RANKL inhibition in osteoporosis. Arthritis Res Ther 9(SUPPL.1):1–6. https://doi.org/10.1186/ar2167

Metz LN, Martin RB, Turner AS (2003) Histomorphometric analysis of the effects of osteocyte density on osteonal morphology and remodeling. Bone 33(5):753–759. https://doi.org/10.1016/S8756-3282(03)00245-X

Moustafa A, Sugiyama T, Prasad J, Zaman G, Gross TS, Lanyon LE, Price JS (2012) Mechanical loading-related changes in osteocyte sclerostin expression in mice are more closely associated with the subsequent osteogenic response than the peak strains engendered. Osteoporos Int 23(4):1225–1234. https://doi.org/10.1007/s00198-011-1656-4

Nakashima T, Hayashi M, Fukunaga T, Kurata K, Oh-Hora M, Feng J, Bonewald L, Kodama T, Wutz A, Wagner E, M Penninger J, Takayanagi H (2011) Evidence for osteocyte regulation of bone homeostasis through rankl expression. Nat Med 17:1231–4. https://doi.org/10.1038/nm.2452

Nazarian A, Muller J, Zurakowski D, Müller R, Snyder BD (2007) Densitometric, morphometric and mechanical distributions in the human proximal femur. J Biomech 40(11):2573–2579. https://doi.org/10.1016/j.jbiomech.2006.11.022

Nguyen J, Tang SY, Nguyen D, Alliston T (2013) Load regulates bone formation and Sclerostin expression through a TGFβ-dependent mechanism. PLoS ONE. https://doi.org/10.1371/journal.pone.0053813

Nordin BEC, Need AG, Chatterton BE, Horowitz M, Morris HA (1990) The relative contributions of age and years since menopause to postmenopausal bone loss. J Clin Endocrinol Metab 70(1):83–88. https://doi.org/10.1210/jcem-70-1-83

Padhi D, Allison M, Kivitz AJ, Gutierrez MJ, Stouch B, Wang C, Jang G (2014) Multiple doses of sclerostin antibody romosozumab in healthy men and postmenopausal women with low bone mass: a randomized, double-blind, placebo-controlled study. J Clin Pharmacol 54(2):168–178. https://doi.org/10.1002/jcph.239

Pastrama MI, Scheiner S, Pivonka P, Hellmich C (2018) A mathematical multiscale model of bone remodeling, accounting for pore space-specific mechanosensation. Bone 107:208–221. https://doi.org/10.1016/j.bone.2017.11.009

Peterson MC, Riggs MM (2010) A physiologically based mathematical model of integrated calcium homeostasis and bone remodeling. Bone 46(1):49–63. https://doi.org/10.1016/j.bone.2009.08.053

Pivonka P, Komarova SV (2010) Mathematical modeling in bone biology: from intracellular signaling to tissue mechanics. Bone. https://doi.org/10.1016/j.bone.2010.04.601

Pivonka P, Zimak J, Smith DW, Gardiner BS, Dunstan CR, Sims NA, John Martin T, Mundy GR (2008) Model structure and control of bone remodeling: a theoretical study. Bone 43(2):249–263. https://doi.org/10.1016/j.bone.2008.03.025

Pivonka P, Buenzli P, Dunst C (2012) A systems approach to understanding bone cell interactions in health and disease. In: Cell interaction. InTech. https://doi.org/10.5772/51149

Pivonka P, Buenzli PR, Scheiner S, Hellmich C, Dunstan CR (2013) The influence of bone surface availability in bone remodelling—a mathematical model including coupled geometrical and biomechanical regulations of bone cells. Eng Struct. https://doi.org/10.1016/j.engstruct.2012.09.006

Pouilles J, Tremollieres F, Ribot C (2009) Effect of menopause on femoral and vertebral bone loss. J Bone Miner Res 10(10):1531–1536. https://doi.org/10.1002/jbmr.5650101014

Rahnert J, Fan X, Case N, Murphy TC, Grassi F, Sen B, Rubin J (2008) The role of nitric oxide in the mechanical repression of RANKL in bone stromal cells. Bone 43(1):48–54. https://doi.org/10.1016/j.bone.2008.03.006

Rawlinson SCF, El-haj AJ, Minter SL, Tavares IA, Bennett A, Lanyon LE (1991) Loading-related increases in prostaglandin production in cores of adult canine cancellous bone in vitro: a role for prostacyclin in adaptive bone remodeling? J Bone Miner Res 6(12):1345–1351. https://doi.org/10.1002/jbmr.5650061212

Robling AG, Niziolek PJ, Baldridge LA, Condon KW, Allen MR, Alam I, Mantila SM, Gluhak-Heinrich J, Bellido TM, Harris SE, Turner CH (2008) Mechanical stimulation of bone in vivo reduces osteocyte expression of Sost/sclerostin. J Biol Chem 283(9):5866–5875. https://doi.org/10.1074/jbc.M705092200

Rosa N, Simoes R, Magalhães FD, Marques AT (2015) From mechanical stimulus to bone formation: a review. Med Eng Phys 37(8):719–728. https://doi.org/10.1016/j.medengphy.2015.05.015

Scheiner S, Pivonka P, Hellmich C (2013) Coupling systems biology with multiscale mechanics, for computer simulations of bone remodeling. Comput Methods Appl Mech Eng 254:181–196. https://doi.org/10.1016/j.cma.2012.10.015

Scheiner S, Pivonka P, Smith DW, Dunstan CR, Hellmich C (2014) Mathematical modeling of postmenopausal osteoporosis and its treatment by the anti-catabolic drug denosumab. Int J Numer Method Biomed Eng 30(1):1–27. https://doi.org/10.1002/cnm.2584

Scheiner S, Pivonka P, Hellmich C (2016) Poromicromechanics reveals that physiological bone strains induce osteocyte-stimulating lacunar pressure. Biomech Model Mechanobiol 15:9–28. https://doi.org/10.1007/s10237-015-0704-y

Spatz JM, Wein MN, Gooi JH, Qu Y, Garr JL, Liu S, Barry KJ, Uda Y, Lai F, Dedic C, Balcells-Camps M, Kronenberg HM, Babij P, Pajevic PD (2015) The Wnt inhibitor sclerostin is up-regulated by mechanical unloading in osteocytes in vitro. J Biol Chem 290(27):16,744–16,758. https://doi.org/10.1074/jbc.M114.628313

Van Oers RFM, Van Rietbergen B, Ito K, Hilbers PAJ, Huiskes R (2011) A sclerostin-based theory for strain-induced bone formation. Biomech Model Mechanobiol 10(5):663–670. https://doi.org/10.1007/s10237-010-0264-0

Van Rietbergen B, Huiskes R, Weinans H, Sumner DR, Turner TM, Galante JO (1993) The mechanism of bone remodeling and resorption around press-fitted THA stems. J Biomech 26(4):369–382. https://doi.org/10.1016/0021-9290(93)90001-U

Wang Y, Pivonka P, Buenzli PR, Smith DW, Dunstan CR (2011) Computational modeling of interactions between multiple myeloma

and the bone microenvironment. PLoS ONE 6(11):14–16. https://doi.org/10.1371/journal.pone.0027494

Xiong J, Piemontese M, Onal M, Campbell J, Goellner JJ, Dusevich V, Bonewald L, Manolagas SC, O'Brien CA (2015) Osteocytes, not osteoblasts or lining cells, are the main source of the RANKL required for osteoclast formation in remodeling bone. PLoS ONE 10(9):1–19. https://doi.org/10.1371/journal.pone.0138189

Zaman G, Pitsillides aa, Rawlinson SCF, Suswillo RFL, Mosley JR, Cheng MZ, Platts LaM, Hukkanen M, Polak JM, Lanyon LE (1999) Mechanical strain stimulates nitric oxide production by rapid activation of endothelial nitric oxide synthase in osteocytes. J Bone Miner Res 14(7):1123–1131. https://doi.org/10.1359/jbmr.1999.14.7.1123

Zaman G, Saxon LK, Sunters A, Hilton H, Underhill P, Williams D, Price JS, Lanyon LE (2010) Loading-related regulation of gene expression in bone in the contexts of estrogen deficiency, lack of estrogen receptor α and disuse. Bone 46(3):628–642. https://doi.org/10.1016/j.bone.2009.10.021

Chapter 4

Insights of a mechanobiological model: dynamics of bone turnover during sclerostin antibody administration in post-menopausal osteoporosis

This chapter presents an article tentatively accepted in BONE.

The following chapter presents an application of the mechanobiological model presented in Chapter 3 in a clinical context. A major clinical question in bone endocrinology is finding an optimal treatment of postmenopausal osteoporosis with a chosen drug. This type of questions is typically addressed using pharmacokinetic-pharmacodynamic (PK-PD) models of the biological system. In this chapter, a PK model is developed for a sclerostin monoclonal antibody, romosozumab, which binds with sclerostin with high affinity. The mathematical model of bone remodeling developed in Chapter 3 is applied here to describe the effects of anti-sclerostin therapy on bone turnover via the quantification of the action of romosozumab on sclerostin levels, and therefore Wnt signalling. The aim of numerical simulations is to help identify a

drug treatment regimen most efficient to halt bone loss in PMO, and ideally increase bone mass.

This introduction first develops the discovery of sclerostin in 1999 and the investigation of its role in bone remodeling in the following years. A second section presents post-menopausal osteoporosis and its inherent challenges. Section 4.3 presents a novel treatment targeting sclerostin based on a humanised antibody, romosozumab. Then, Section 4.4 introduces an application of the model proposed in the following article based on the bone cell population model presented in the previous chapter (Chapter 3). This extension is based on a competitive binding scheme and pharmocokinetics of romosozumab.

4.1 Sclerostin, a recently-discovered key protein in bone mass regulation

Sclerostin and its effects on bone mass and composition were first discovered by Brunkow and coworkers [23]. The latter filed a patent in 1999 where they acknowledged a rare genetic mutation on chromosome 17 in sclerosteosis patients. Sclerosteosis is a medical condition involving severe sclerosing skeletal dysplasia. Affected individuals typically exhibit bone overgrowth and very high bone mass. Brunkow and collaborators identified a 'Human BEER' gene encoding a novel protein of the TGF-β family regulating bone homeostasis. In 2001, Brunkow, Balemans and their respective colleagues named this newly-discovered gene 'SOST' and found that the SOST gene product mediated bone formation [7, 23]. Brunkow and coworkers named this novel protein 'sclerostin'.

The SOST gene is critical to bone remodeling, and its effects have been assessed in numerous studies in the past decades. In particular, sclerosteosis models in human and rodent models helped understanding the role of sclerostin in bone biology. In their human study, Van Lierop and coworkers showed that the absence or decreased synthesis of sclerostin in affected patients lead to an increase in bone formation markers [192]. Additionally, SOST knockout rodent models showed that the absence of scle-

rostin enhanced bone mass and reduced mineralisation [112, 153], which is a similar finding to what has been reported in human patients.

Osteocytes produce sclerostin, and the latter binds to low-density lipoprotein receptor-related protein (LRP), therefore inhibiting Wnt signaling and the anabolic β-catenin pathway [19]. Therefore, sclerostin levels are directly connected to bone turnover and are negatively correlated to bone formation.

In the past decade, several studies assessed the influence of sclerostin monoclonal antibody, inhibiting sclerostin regulation of bone formation. Warmington and collaborators led in 2004 the first research testing the therapeutic potential of sclerostin neutralizing antibodies [198]. They found that a sclerostin monoclonal antibody mediated blockade led to a significant BMD increase in adult mice and rats, including up to 64% in tibial metaphysis trabecular bone. Since then, various studies investigated the administration of a sclerostin monoclonal antibody as a means to counter osteoporosis-induced bone loss [93, 144] or promote bone fracture healing [93, 105]. The next section details the challenges associated with a disabling bone disease, osteoporosis, which is the focus of this chapter.

4.2 Osteoporosis, a major bone disease

Osteoporosis is a bone disease characterized by a low bone mass and micro-architectural deterioration associated with a negative net balance between bone formation and resorption during bone remodeling [107]. This imbalance results in bone fragility and an increased risk of bone fracture, as stated in the definition given at the Consensus Development Conference in 1991 [33].

While a small bone loss probably occurs since the thirties in men and women in a similar extent, women are likely to experience a significant bone loss around and after the menopause (around 1-2% per year) until stabilization [77, 211]. This phenomenon, called postmenopausal osteoporosis (PMO), is of major concern as it affects approximately one-tenth of women in their sixties [91]. In particular, a Swedish study demonstrated that approximately 6% of men and 21% of women aged 50-84 years could be classified as having osteoporosis using a DXA criterion (bone density

measurement) based on female-derived reference ranges at the femoral neck [92].

The cost of osteoporosis to health systems is tremendous as the disease can involve long-term treatment after diagnosis. Moreover, long hospital stays, surgeries and even nursing homes for disabled patients can be indicated in the case of osteoporotic fractures [189]. As an example, costs attributable to osteoporotic fractures in the European Union have been estimated at 37 billion euros in 2010 [81]. With the rising global elderly population, the burden on the budget is expected to increase [81, 91] (Hernlund et al. reported an expected increase of 25 % in 2025), which motivates the development of effective medical therapies.

There are two categories of existing medications to treat osteoporosis. Anti-resorptive treatments (denosumab, bisphosphonnates, hormonal therapies) aim primarily at decreasing bone resorption [189]. Conversely, the only available anabolic therapies are based on the administration of parathyroid hormone (PTH) analogues as they stimulate bone formation via the stimulation of the osteoblastic activity.

4.3 Anabolic anti-sclerostin treatment to counter osteoporosis-induced bone loss

This chapter focuses on a novel anabolic treatment for osteoporosis that has been developed in the recent years which is based on the development of an anti-sclerostin antibody commercialized under the name Evenity® [5]. This drug treatment is approved for marketing in Japan, South Korea, US and Canada, and recently in EU.

As explained earlier, Evenity® treatment relies on a humanized anti-sclerostin antibody, called romosozumab. While the antibody injections have a short-term significantly positive impact on bone mass [128, 143], the influence of the treatment on bone mass and turnover markers [181, 205] as well as its interaction with other pathways [186] are not fully understood.

Target-mediated drug disposition models help understand how drugs interact with the biological systems, in particular in the case of monoclonal antibodies [24, 48]. Therefore, they have the potential to shed light on the dynamics of bone resorption

and formation during a treatment. To the best of my knowledge, only two studies have developed pharmacokinetic models of sclerostin antibody so far [51, 184]. While these two studies do aim at recovering the dynamics of the bone mineral density, the scope of their models is limited as they do not consider the dynamics of the pathways affected by and governing bone remodeling.

4.4 Modeling the effects of anabolic treatment of post-menopausal osteoporosis with romosozumab on bone turnover

Numerical modeling provides a way to quantify the effects of drug treatment, in particular on bone turnover. In this application of the model presented in Chapter 3, the humanized sclerostin antibody romosozumab is introduced as a ligand binding to sclerostin, and, thus, inhibiting sclerostin's down-regulation of bone formation. Mathematically, osteoblasts precursors proliferation is regulated by a Hill activator function based on its LRP5/6 receptor occupancy by Wnt proteins. Using a balance of production and degradation of sclerostin, free and bound sclerostin levels can be calculated. As a result, the receptor occupancy increases with increased levels of romosozumab.

A pharmacokinetic one-compartment model is developed for subcutaneous injections of romosozumab. This framework describes the absorption of the drug into the serum and its clearance dynamics based on Michaelis-Menten kinetics. As described earlier (Section 4.1), the evolution of romosozumab levels directly affects sclerostin levels, and therefore bone remodeling. Pharmacokinetics, which involves the description of the action of the drug on the target site (here, sclerostin) and its consequences on the biological system, are described here with the bone cell population model presented in Chapter 3.

This work describes the role of osteocytes expression of sclerostin in the anabolism subsequent to anti-sclerostin treatment. Site-specific results were obtained which were in good accordance with clinical data, therefore confirming the model's ability

to represent the complex dynamics of bone turnover in romosozumab treatment. Further, the model highlights the non-linear relationship between monthly romosozumab dosage and bone density changes. Results suggest that the use of quantitative pharmacodynamic models such as the one proposed would allow a more efficient calibration of treatments.

Assessment of romosozumab efficacy in the treatment of postmenopausal osteoporosis: results from a mechanistic PK-PD mechanostat model of bone remodeling

Madge Martin[a,b], Vittorio Sansalone[b], David M. L. Cooper[c], Mark R. Forwood[d], Peter Pivonka[a,]

[a] *School of Chemistry, Physics and Mechanical Engineering, Queensland University of Technology, 2 George St, Brisbane, QLD 4000, Australia*
[b] *Laboratoire Modélisation et Simulation Multi-Echelle (MSME), UMR CNRS 8208, Université Paris-Est Créteil, 61 avenue du Général de Gaulle, 94010 Créteil, France*
[c] *Department of Anatomy, Physiology and Pharmacology, University of Saskatchewan, 107 Wiggins Road, Saskatoon, SK, Canada*
[d] *School of Medical Science, Griffith University, Gold Goast, QLD 4222, Australia*

Abstract

Romosozumab is a humanised monoclonal antibody targeting sclerostin which has recently been developed for the treatment of osteoporosis. Approval of this drug, based on promising results from phase III clinical trials, is currently pending in the European Union and was recently granted in Japan, South Korea, Canada and the United States.

In order to study efficacy of romosozumab, we developed a comprehensive mechanistic pharmacokinetic-pharmacodynamic (PK-PD) model of the effect of drug on bone remodeling in postmenopausal osteoporosis (PMO). We utilized a one-compartment PK model to represent subcutaneous injections of romosozumab and subsequent absorption into serum. The PD model is based on a recently-developed bone cell population model describing the bone remodeling process at the tissue scale. The latter accounts for mechanical feedback via incorporating nitric oxide (NO) and sclerostin (Scl) as biochemical feedback molecules. Utilizing a competitive binding model, where Wnt and Scl compete for binding to LRP5/6, allows to regulate anabolic bone remodeling responses.

Email address: peter.pivonka@qut.edu.au (Peter Pivonka)

Here, we extended this model with respect to romosozumab binding to sclerostin.

For the currently approved monthly injections of 210 mg, the model predicted a 6.59%, 10.38% and 15.25% increase in BMD at the lumbar spine after 6 , 12 and 24 months respectively. These results are in good agreement with the data reported by McClung et al. [1] of 8.41 ± 1.24%, 12.10 ± 1.29% and 15.71 ± 1.57%. Our model is also able to distinguish the bone-site specific drug effects. For instance, at the femoral neck, our model predicts a BMD increase of 3.85% after 12 months of 210 mg injections, which is consistent with literature observations from Langdahl et al [2] (3.20 ± 0.60%) and Ishibashi et al [3] (3.76 ± 1.08%). Finally, our simulations indicate rapid bone loss after treatment discontinuation, as observed by McClung et al. [1], indicating that some additional interventions such as use of bisphosphonates is required to maintain bone.

Keywords: romosozumab, bone remodeling, sclerostin, Frost's mechanostat, postmenopausal osteoporosis, mechanistic PK-PD, pharmacokinetics, pharmacodynamics, multiscale modeling

1. Introduction

Bone remodeling is the concerted action of bone resorption and bone formation taking place throughout life. Cells involved in the bone remodeling process are osteoclast (bone resorbing cells), osteoblasts (bone forming cells) and osteocytes (cells embedded in the bone matrix) [4]. In particular, osteocytes have been identified as the conductors of bone remodeling. A key regulatory molecule in anabolic bone remodeling, sclerostin, has been shown to be almost exclusively produced by osteocytes [5, 6]. Imbalanced bone remodeling is linked to bone pathologies with the most serious one being osteoporosis (OP). In OP, bone resorption outweighs bone formation which, consequently, induces a negative bone balance [7]. This leads to a gradual decline in bone mass and ultimately results in bone fractures. Clinical bone research is concerned with developing new drugs or combining different drugs able to halt or even reverse bone loss.

Sclerostin, encoded by the SOST gene, is an inhibitor of the canonical Wnt signaling pathway which has a pivotal role in skeletal development, adult skeletal homeostasis, and bone remodeling. Osteocytes produce sclerostin, and the latter binds to low-density lipoprotein receptor-related protein 5/6 (LRP5/6) expressed on osteoblasts and osteocytes, which inhibits Wnt signaling and the anabolic β-catenin signaling pathway [8]. Sclerostin levels are directly linked to bone turnover and are negatively correlated to bone formation. Consequently, targeting sclerostin has great potential for controlling the anabolic axis of bone remodeling [9].

In the past decade, several studies assessed the therapeutic potential of sclerostin neutralizing antibodies on bone mass. A first study led by Warmington et al. in 2004 identified that utilizing a sclerostin monoclonal antibody gives rise to significant BMD increase in adult mice and rats, including up to 64% in tibial metaphysis trabecular bone [10]. Since then, various studies investigated the administration of a sclerostin monoclonal antibody as a means to counter osteoporosis-induced bone loss [11, 9] or promote bone fracture healing [9, 12].

A humanized monoclonal antibody against sclerostin, called romosozumab is currently under phase 3 clinical trial. This drug has been developed by Amgen and UCB and is known under its commercial name EVENITY$^{\text{TM}}$. Romosozumab has been shown to have a significantly positive impact on bone mass [13, 1], which led to approval of the drug in Japan, Canada, South Korea and the US and is under regulatory review as a post-menopausal osteoporosis treatment for patients at high fracture risk in the European Union. The approved adult dosage of romosozumab is 210 mg administered subcutaneously (SC) once a month for 12 months. Results of the effect of long-term romosozumab treatment on bone mass and turnover markers as well as its interaction with other signaling pathways are still lacking.

The efficacy of the anabolic treatment of PMO through the injection of romosozumab is not yet fully understood. Numerical modelling aims at filling this gap, as well as providing a long-term vision of the treatment. In particular, pharmacokinetics and pharmacodynamics (PK-PD) help understand how drugs

are released into the system (pharmacokinetics) and interact with pharmacological target sites (here, the target is sclerostin) in order to exert an effect on biological systems (pharmacodynamics). PK-PD models have a great potential to better understand the effects of monoclonal antibodies on disease progression [14, 15]. Only a few studies have so-far developed PK-PD models for analyzing sclerostin antibody efficacy on disease progression in osteoporosis [16, 17]. While these two studies accurately reproduce the dynamics of bone turnover markers (BTMs) and bone mineral density (BMD), the scope of their models is limited. In particular they do not consider any mechanical aspects of bone, but treat bone tissue as a separate "compartment" to the BTMs. Different bone sites such as lumbar spine and femoral neck are modeled with different sets of parameters that are fitted to the experimental data. In contrast, work by Pivonka and co-workers have highlighted that it is relevant to link bone cellular activities to respective BMD or bone volume fraction [18, 19, 20, 21]. Furthermore, we have recently shown that it is not necessary to treat different bone sites as different compartments in order to simulate differential drug effects [22] or hormonal changes [21]. One requires only a consistent mechanical formulation of bone tissue.

The present paper aims at development of a comprehensive mechanistic PK-PD model of the effects of romosozumab on bone remodeling in PMO. In particular, we are interested in drug efficacy. The model consists of a recently developed multiscale model of bone remodeling which quantitatively takes into account Frost's mechanostat theory [4]. The latter concept is translated into a biochemical feedback loop in which osteocytes respond to changes in mechanical environment by regulating production on sclerostin (Scl) and nitric oxide (NO). The sclerostin-driven anabolic feedback regulates osteoblast proliferation via Wnt signaling. On the other hand, NO catabolic feedback regulates RANKL expression on osteoblast precursor cells. A simplified competitive binding model including Wnt proteins, sclerostin and LRP5/6 receptors (Scl-Wnt-LRP5/6 pathway) was used in this model to drive osteoblast proliferation [21]. We further develop here a one compartment PK model of romosozumab.

Utilizing binding affinities between Scl and romosozumab, we then extend our Scl-Wnt-LRP5/6 competitive binding model towards another binding partner. The developed pharcodynamic model is first calibrated on monthly injections of 210 mg as per the lumbar spine trial data from Langdahl et al [2] to determine the elimination rate of the bound complex of sclerostin to its antibody. Model validation is then performed on a complementary set of data involving various bone sites and injection dosages [3, 1, 2] (see Subsection 3).

The paper is organized as follows. Firstly, Section 2 introduces the mechanistic PK-PD model of romosozumab effects on PMO. This section consists of a detailed description of a one-compartment model of subcutaneous injections of romosozumab (Subsection 2.1), a bone cell population model (BCPM) able to simulate PMO (Subsection 2.2), a competitive binding model of the Scl-Wnt-LRP5/6 pathway and romosozumab (Subsection 2.3), and an overview of the numerical model implementation (Subsection 2.4). Numerical results are presented in Section 3 together with experimental data. The results are discussed and compared with findings in the literature in Section 4. A summary and conclusions are provided in Section 5.

2. Mechanistic PK-PD model of bone remodeling simulating the effect of romosozumab on PMO

2.1. PK-PD modelling of sclerostin antibody anabolic therapy

Pharmacokinetic-pharmacodynamic models are frameworks capturing the dynamics of the binding of a drug to its target in the body and the clearance of that drug. We define here a PK-PD model for romosozumab as a one-compartment PK model where the subcutaneous injection is accounted for by adding a depot (D), from which the drug is absorbed into the central compartment (i.e., serum). Fig. 1 describes the framework of our pharmocokinetic model. To our knowledge, there is currently no evidence that romosozumab binding to plasma proteins would prevent it from reaching bone tissue, which would motivate the need for an additional compartment.

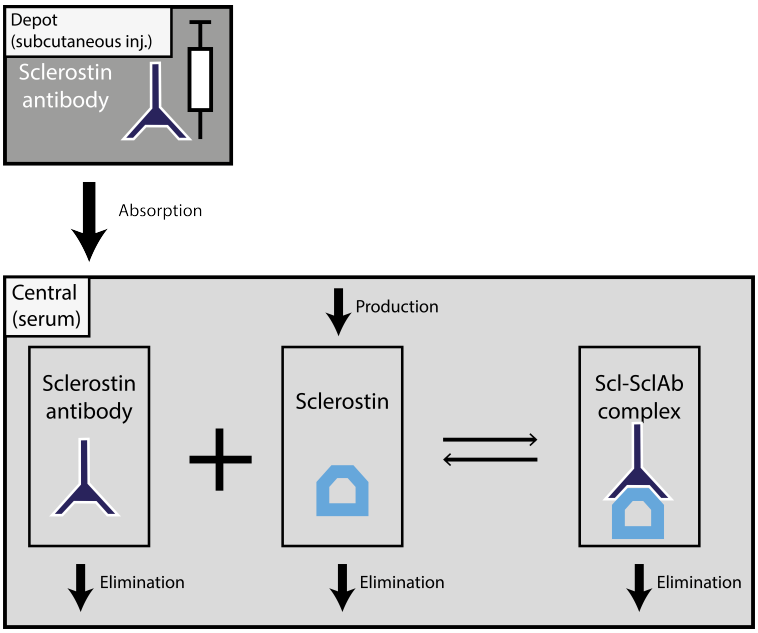

Figure 1: Schematic of the pharmacokinetic (PK) one-compartment model with depot for sclerostin antibody.

The kinetics of the drug concentration in the depot $C^{\mathsf{D}}_{\mathsf{SclAb}}$ are described as follows:

$$\frac{dC^{\mathsf{D}}_{\mathsf{SclAb}}}{dt} = -k_a C^{\mathsf{D}}_{\mathsf{SclAb}}, \tag{1}$$

where k_a is the absorption coefficient of the monoclonal antibody into the serum. Our model is a quasi-equilibrium model derived from Michaelis-Menten kinetics. Hence, we assume that the formation of the complex of sclerostin with its specific antibody has a characteristic time that is negligible compared to absorption and elimination processes. This leads to the assumption that that the antibody binding reaction is at equilibrium. Furthermore, the Michaelis-Menten model implies that the sclerostin concentration is small relative to that of the antibody [15]. The evolution of the sclerostin antibody concentrations in the

depot ($C^{\mathsf{D}}_{\mathsf{SclAb}}$) and in the central compartment ($C^{\mathsf{C}}_{\mathsf{SclAb}}$) are as follows:

$$\frac{dC^{\mathsf{C}}_{\mathsf{SclAb}}}{dt} = k_a C^{\mathsf{D}}_{\mathsf{SclAb}} - \left(\frac{V_{max}/(V_c/F)}{K_M + C^{\mathsf{C}}_{\mathsf{SclAb}}} + \tilde{D}_{\mathsf{SclAb}} \right) C^{\mathsf{C}}_{\mathsf{SclAb}}, \tag{2}$$

$$C^{\mathsf{C}}_{\mathsf{SclAb}}(t = t_0) = C^{\mathsf{C,res}}_{\mathsf{SclAb}}, \tag{3}$$

$$C^{\mathsf{D}}_{\mathsf{SclAb}}(t = t_0) = C^{\mathsf{D,res}}_{\mathsf{SclAb}} + \frac{\mathsf{Dose}}{V_c/F},\ \mathsf{Dose} = \frac{\mathsf{Dose}^{\mathsf{mg}}}{M_{\mathsf{SclAb}}}, \tag{4}$$

where V_{max} is the maximum binding reaction velocity achieved by the system, K_M is the Michaelis constant, $\tilde{D}_{\mathsf{SclAb}}$ is the elimination rate of romosozumab (SclAb) and V_c/F is the volume of the central compartment adjusted for bioavailability. V_c is the central compartment volume and the factor F is the bioavailability approximated from literature [23, 24]. The latter is equal to 1 when the drug is administered intravenously. The administered dose is generally given in unit mass (we will use milligrams here), implemented here with the parameter $\mathsf{Dose}^{\mathsf{mg}}$. We note that all ligand receptor binding reactions and ligand levels presented in the following sections are evaluated with units pmol/L (pM). Hence, Eq. (4) classically uses the molar mass of romosozumab M_{SclAb} given in Evenity FDA Prescribing Information [25] (see Table 1) for the conversion of the dose $\mathsf{Dose}^{\mathsf{mg}}$. The initial concentration of drug in the central compartment and the depot are respectively accounted for via $C^{\mathsf{C,res}}_{\mathsf{SclAb}} \geq 0$ and $C^{\mathsf{D,res}}_{\mathsf{SclAb}} \geq 0$, indicating a potential remainder of drug resulting from previous injections.

The solution of Eq.(2) provides the romosozumab concentration in serum. The latter interacts with the osteocyte derived sclerostin concentration introduced in the next section (Equations (5)-(9)). Due to the fact that Eq.(2) is independent of the bone cell population model (BCPM), the equations governing drug kinetics (Equations (1)-(4)) can be solved independently. The concentration of drug in the depot at a given time point t is calculated by the algorithm explained in Appendix B.

The parameters defined in Table 1 are determined to reproduce the pharmocokinetic behavior of romosozumab, and therefore its effects on bone metabolism. While these parameters are specific to this drug, the model structure would allow to simulate the pharmacodynamics of any other anti-sclerostin monoclonal

Table 1: Typical parameter values for the one compartment PK model of romosozumab according to [25]. Values were either calculated from clinical data (CALC), obtained from an optimization based on clinical data (OPTI) or retrieved from manufacturer data (MANU).

Symbol	Value	Unit	Source
k_a	0.450	day^{-1}	OPTI, from [23]
V_{max}	$1.50\,10^6$	ng.day^{-1}	OPTI, from [23]
V_c	3.92	L	MANU, from [25]
F	0.692	-	CALC, from [23]
K_M	$1.70\,10^3$	ng.mL^{-1}	OPTI, from [23]
$\tilde{D}_{\mathsf{SclAb}}$	$6.00\,10^{-2}$	day^{-1}	OPTI, from [23]
M_{SclAb}	149	kDa	MANU, from [25]

antibody, once PK parameters have been carefully adjusted against clinical data.

2.2. Bone cell population model (BCPM) of bone remodeling

The present work is based on the bone cell population model (BCPM) developed by Martin et al. [21]. The aim of the BCPM is to mechanistically describe the bone remodeling process at the tissue scale. Furthermore, the BCPM allows to simulate the influence of biochemical and mechanical environment on bone remodeling together with imposing bone pathologies such as PMO onto the system. While previous attempts have been made to connect mechanical loading and biochemistry at the cellular scale [26, 27, 28, 29, 18, 20], our model is unique in the sense that it places the osteocytes as conductors of mechanical feedback which is biochemically actuated via nitric oxid (NO) and sclerostin (Scl). Furthermore, this model incorporates competitive binding reactions between Wnt, Sclerostin and LRP5/6 which regulates proliferation of osteoblast precursor cells. This comprehensive model is schematically shown in Fig. 2.

Below, we briefly describe the main features of the model. A detailed description and mathematical formulation of all model features is presented in [21]. As seen in Fig. 2, four main signalling pathways are considered in order

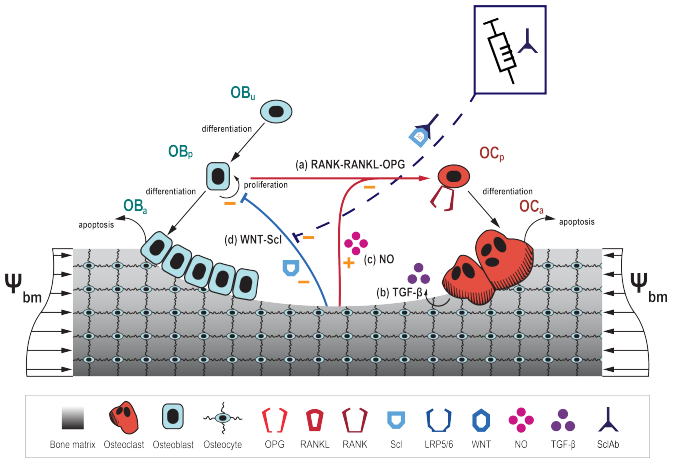

Figure 2: Overview of the bone cell population model (BCPM) containing both biochemical and mechanical feedback. In this model Wnt and Scl compete for binding to LRP5/6 expressed on osteoblast precursor cells which regulates OB_p proliferation. Romosozumab interacts with the latter binding reactions to modify osteoblast precursor proliferation.

to describe the interactions between various bone cells and ligands involved in bone remodelling:

- RANK-RANKL-OPG catabolic pathway: regulates differentiation of osteoclasts;
- action of TGF-β implemented according to earlier studies [30, 18, 21]: up-regulation of the differentiation of uncommitted osteoblasts (Ob_u) differentiation into osteoblast precursor cells (Ob_p), the inhibition of differentiation of osteoblast precursor cells (Ob_p) and promotion of apoptosis of active osteoclasts (Oc_a);
- osteocyte mechanical feedback: described via nitric oxide (NO) catabolic regulation [31, 32, 33] and via sclerostin (Scl) anabolic regulation [9];
- Competitive binding of Wnt proteins and sclerostin (Scl) to LRP5/6 receptors on Ob_p: sclerostin is produced by osteocytes in response to mechanical loading [34, 35]. A comprehensive description of these binding reactions

is given in Section 2.3.

As described in Martin et al. [21], macroscopic physiological loading of bone gives rise to stresses and strains in the bone matrix which are sensed by osteocytes. In our model, we use the strain energy density in the bone matrix (Ψ_{bm}) as a mechanical signal for osteocyte feedback (see Figs. 2,3). Osteocytes translate the mechanical loads into a biochemical feedback, i.e. catabolic feedback via nitric oxide (NO) and anabolic feedback via sclerostin (Scl). NO regulates the RANKL expression on Ob_p and affects the RANKL/OPG ratio. On the other hand, sclerostin interacts with Wnt-LRP5/6 to regulate Ob_p proliferation. For a detailed description of the micromechanical model for computing the strain energy density in the bone matrix (Ψ_{bm}), one can refer to [20]. Osteocytes production of NO and Scl relies on two sigmoidal regulatory functions defined in Appendix A, and the properties of the bone matrix and pores of the tissue (see Appendix C).

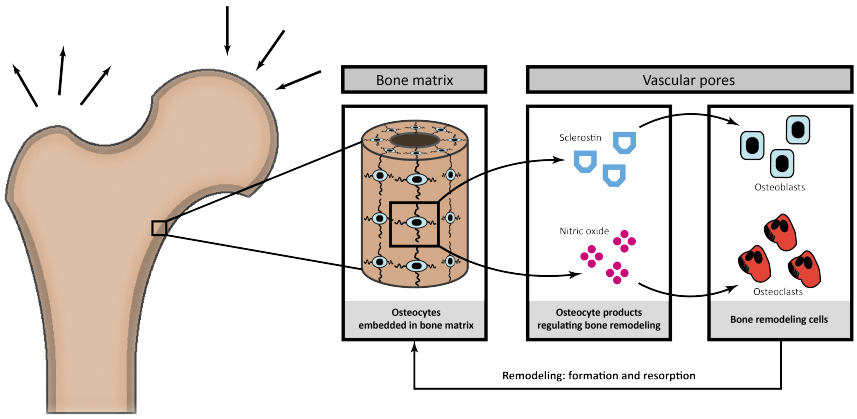

Figure 3: Overview of the regulation of the mechanobiological feedback by osteocytes through Scl and NO signalling. Scl regulates osteoblast precursors proliferation by inhibiting Wnt signalling (see Subsection 2.3). romosozumab inhibits the anti-anabolic action of sclerostin by binding to sclerostin proteins.

The above described features of the BCPM can be presented by the following

evolution laws for bone cells [21]:

$$\frac{d\mathsf{Ob}_p}{dt} = D_{\mathsf{Ob}_u}\mathsf{Ob}_u\pi^{\mathsf{TGF}-\beta}_{\mathsf{act},\mathsf{Ob}_u} + P_{\mathsf{Ob}_p}\mathsf{Ob}_p\pi^{\mathsf{Wnt}}_{\mathsf{act},\mathsf{Ob}_p} - D_{\mathsf{Ob}_p}\mathsf{Ob}_p\pi^{\mathsf{TGF}-\beta}_{\mathsf{rep},\mathsf{Ob}_p} \quad (5)$$

$$\frac{d\mathsf{Ob}_a}{dt} = D_{\mathsf{Ob}_p}\mathsf{Ob}_p\pi^{\mathsf{TGF}-\beta}_{\mathsf{rep},\mathsf{Ob}_p} - \Delta_{\mathsf{Ob}_a}\mathsf{Ob}_a \quad (6)$$

$$\frac{d\mathsf{Oc}_a}{dt} = D_{\mathsf{Oc}_p}\mathsf{Oc}_p\pi^{\mathsf{RANK}}_{\mathsf{act},\mathsf{Oc}_p} - A_{\mathsf{Oc}_a}\mathsf{Oc}_a\pi^{\mathsf{TGF}-\beta}_{\mathsf{act},\mathsf{Oc}_a} \quad (7)$$

$$\frac{df_{\mathsf{bm}}}{dt} = k_{\mathsf{form}}\mathsf{Ob}_a - k_{\mathsf{res}}\mathsf{Oc}_a \quad (8)$$

$$\frac{d\mathsf{Ot}}{dt} = \eta\frac{df_{\mathsf{bm}}}{dt} \quad (9)$$

where D_{Ob_u}, D_{Ob_p}, D_{Oc_p} and D_{Oc_a} are differentiation rates of uncommitted osteoblast progenitor cells, osteoblast/osteoclast precursor cells, and active osteoclasts respectively. P_{Ob_p} denotes the proliferation rate of osteoblast precursor cells. Δ_{Ob_a} is the rate of clearance of active osteoblasts through apoptosis and differentiation. A_{Oc_a} is the apoptosis rate of active osteoclasts. Eq. (9) indicates that we assume that change in osteocyte population is proportional to the change in bone matrix volume fraction $\frac{df_{\mathsf{bm}}}{dt}$. The factor η indicates the average concentration of osteocytes embedded in the bone matrix. The aforementioned parameters are listed in Table 2.

The various regulation mechanisms inherent to bone remodeling controlling the proliferation, differentiation or ligand production of cell populations are implemented classically via Hill functions: $\pi^{Y}_{\mathsf{act/rep},X}$. These functions are described in more detail in Appendix A.

2.3. Competitive binding Scl-Wnt-LRP5/6 interactions with romosozumab

In this section, we develop the implementation of the Scl-Wnt-LRP5/6 signalling pathway and its interactions with romosozumab. The competitive binding of Wnt and sclerostin proteins to the LRP5/6 receptor is complex. As depicted in Fig. 4(a), Wnt signaling is an anabolic pathway triggered by the binding of extracellular Wnt ligands to Frizzled and lipoprotein receptor-related proteins (LRP5/6) co-receptors on osteoblastic cell surfaces. This event triggers the intracellular activation of β-catenin, which promotes proliferation of

Table 2: Values for differentiation (D_X), proliferation (P_X) and apoptosis (A_X) rates of bone cells from Martin et al [21]. $K^X_{D,-}$ are the dissociation constants for the activator/repressor functions $\pi^Y_{\mathsf{act/rep},X}$ appearing in Equations (5)-(9). η is the concentration of osteocytes in the bone matrix.

Symbol	Value	Unit
D_{Ob_u}	$1.660\,10^{-1}$	day^{-1}
P_{Ob_p}	2.203	day^{-1}
D_{Ob_p}	$1.850\,10^{-1}$	day^{-1}
Δ_{Ob_a}	$2.120\,10^{-1}$	day^{-1}
D_{Oc_p}	$1.958\,10^{-2}$	day^{-1}
A_{Oc_a}	10.00	day^{-1}
α	1.000	-
k_{res}	2500	$\text{pM}^{-1}.\text{day}^{-1}$
k_{form}	50.00	$\text{pM}^{-1}.\text{day}^{-1}$
$K^{\mathsf{TGF}-\beta}_{D,\mathsf{act}}$	$5.633\,10^{-4}$	pM
$K^{\mathsf{TGF}-\beta}_{D,\mathsf{rep}}$	$1.754\,10^{-4}$	pM
$K^{\mathsf{RANK}}_{D,\mathsf{act}}$	16.70	pM
η	$4.143\,10^{-8}$ $(4.143\,10^{-2})$	pmol.mm^{-1} (pM)

osteoblast precursor cells (among others). The formation of a Wnt-Frizzled-LRP5/6 complex is inhibited by the presence of sclerostin (Fig. 4(b)). Sclerostin (Scl) binds to LRP5/6 receptors, forming a complex with Kremen proteins and preventing Wnt signaling. Note that literature suggests that sclerostin has a significantly higher affinity to LRP5/6 than Wnt [36, 37]. The latter fact was accounted for in our model via the values of the dissociation constants of the complexes Scl-LRP5/6 and Wnt-LRP5/6 (see Table A.4). This property highlights that, in presence of Scl, LRP5/6 receptors will be likely to bind faster to Scl than Wnt proteins. Note that, in the present study, the binding of Frizzled, Kremen and Dkk1, is not explicitly taken into account. We only consider the dynamics of Scl binding as a first approximation, which has a similar affinity to

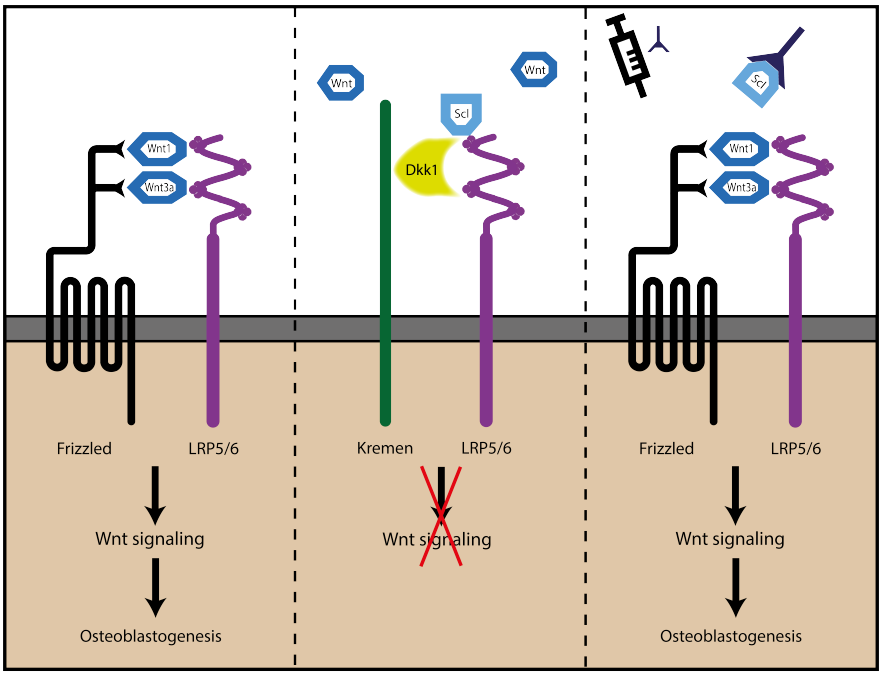

Figure 4: (a) Wnt ligands bind to Frizzled and LRP5/6 receptors, triggering Wnt signaling; (b) Dkk1 and Scl bind to LRP5/6 receptors, therefore inhibiting Wnt signaling; (c) The monoclonal antibody romosozumab (SclAb) binds to Scl, therefore preventing it from competitively binding to LRP5/6 receptors. Adapted from Martin et al [21].

the LRP5/6 receptors as Dkk1, according to experimental data [36]. We simplify the dynamics of the Wnt pathway: we do not account for the diversity of Wnt proteins and assume that Scl and Wnt bind directly to LRP5/6 as depicted in Fig. 2.

As explained earlier, the sclerostin antibody (SclAb) romosozumab has the potential to counteract bone loss by binding to sclerostin (see Fig. 4(c)). Based on the structure of our competitive binding model it is straight forward to include the action of romosozumab on Wnt-signaling. Romosozumab has a significantly higher affinity to sclerostin than sclerostin to LRP5/6 receptors [36, 37, 38], therefore promoting the Scl-SclAb binding over Scl-LRP5/6 binding.

In the present model, Wnt signaling affects osteoblast precursors proliferation via a multiplying factor $\pi^{\mathsf{Wnt}}_{\mathsf{act},\mathsf{Ob}_p}$ (Eq. (5)). This regulating function accounts for the LRP5/6 receptor occupancy, which translates the strength of Wnt/β-catenin signaling. Hence, one can calculate the ratio between $\mathsf{Wnt}-\mathsf{LRP5/6}$ complexes and the total concentration of LRP5/6 receptors $[\mathsf{LRP5/6}]_{\mathsf{tot}}$ – including the ones binding to sclerostin – as follows:

$$\pi^{\mathsf{Wnt}}_{\mathsf{act},\mathsf{Ob}_p} = \frac{[\mathsf{Wnt}-\mathsf{LRP5/6}]}{[\mathsf{LRP5/6}]_{\mathsf{tot}}} = \frac{[\mathsf{Wnt}][\mathsf{LRP5/6}]}{K_D^{\mathsf{Wnt}-\mathsf{LRP5/6}}[\mathsf{LRP5/6}]_{\mathsf{tot}}}, \tag{10}$$

where

$$\begin{aligned}[\mathsf{LRP5/6}]_{\mathsf{tot}} &= [\mathsf{LRP5/6}] + [\mathsf{Wnt}-\mathsf{LRP5/6}] + [\mathsf{Scl}-\mathsf{LRP5/6}] &(11)\\ &= [\mathsf{LRP5/6}]\left(1 + \frac{[\mathsf{Wnt}]}{K_D^{\mathsf{Wnt}-\mathsf{LRP5/6}}} + \frac{[\mathsf{Scl}]}{K_D^{\mathsf{Scl}-\mathsf{LRP5/6}}}\right). &(12)\end{aligned}$$

$[\mathsf{LRP5/6}]$ is the concentration of free LRP5/6 receptors, whereas $[\mathsf{Wnt}-\mathsf{LRP5/6}]$ and $[\mathsf{Scl}-\mathsf{LRP5/6}]$ are respectively the concentration of $\mathsf{Wnt}-\mathsf{LRP5/6}$ and $\mathsf{Scl}-\mathsf{LRP5/6}$ complexes expressed on osteoblast precursors and $K_D^{\mathsf{Wnt}-\mathsf{LRP5/6}}$ and $K_D^{\mathsf{Scl}-\mathsf{LRP5/6}}$ are their respective dissociation constants. Note that we assume here that the binding reactions are much faster than the evolution of the bone cell populations (steady-state assumption), which allows us to use the equilibrium constants in Eq. ((12)). We assume here that the degradation of the complex Wnt-LRP5/6 is negligible and that bone marrow mesenchymal stem cells (uncommitted osteoblasts Ob_u, whose concentration is assumed to be constant in the model) are producing Wnt. Hence, we postulate here a basal concentration $[\mathsf{Wnt}]$ of available Wnt proteins in the medium (see Table A.4). Additionally, the total number of LRP5/6 receptors per osteoblast precursor $N^{\mathsf{LRP5/6}}_{\mathsf{Ob}_p}$ is assumed to be constant (Table A.4), as we do not account for receptor internalization phenomena (e.g., Scl binding to Kremen).

The only variables in Eq. (10) is the concentration of unbound LRP5/6 receptors $[\mathsf{LRP5/6}]$ and the concentration of osteoblasts precursors, embedded in the total concentration $[\mathsf{LRP5/6}]_{\mathsf{tot}} = N^{\mathsf{LRP5/6}}_{\mathsf{Ob}_p}\mathsf{Ob}_p$. The concentration of unbound LRP5/6 receptors $[\mathsf{LRP5/6}]$ can be calculated as a function of the

total concentration $[\mathsf{LRP5/6}]_{\mathsf{tot}}$ and the concentration of free sclerostin proteins $[\mathsf{Scl}]$ (see Eq. (12)). Moreover, the steady-state assumption implies a balance between the production and degradation of sclerostin, leading to:

$$\begin{aligned} P_{\mathsf{Scl}} = \quad & \tilde{D}_{\mathsf{Scl}}[\mathsf{Scl}] + \tilde{D}_{\mathsf{Scl}\ \cdot\mathsf{LRP5/6}}[\mathsf{Scl}\cdot\mathsf{LRP5/6}] + \tilde{D}_{\mathsf{Scl}\ \cdot\mathsf{SclAb}}[\mathsf{Scl}\cdot\mathsf{SclAb}], \quad (13) \\ = \quad & \tilde{D}_{\mathsf{Scl}}[\mathsf{Scl}] + \tilde{D}_{\mathsf{Scl-LRP5/6}}\frac{[\mathsf{Scl}][\mathsf{LRP5/6}]}{K_D^{\mathsf{Scl-LRP5/6}}} + \tilde{D}_{\mathsf{Scl-SclAb}}\frac{[\mathsf{Scl}]C^{\mathsf{C}}_{\mathsf{SclAb}}}{K_D^{\mathsf{Scl-SclAb}}}, \quad (14) \end{aligned}$$

where the production of sclerostin P_{Scl} can be decomposed into a term accounting for body production $P_{\mathsf{Scl},b}$ and an additional term corresponding to the external dosage $P_{\mathsf{Scl},d}$ as follows:

$$\begin{aligned} P_{\mathsf{Scl}} = \quad & P_{\mathsf{Scl},b} + P_{\mathsf{Scl},d} \quad (15) \\ P_{\mathsf{Scl},b} = \quad & \beta_{\mathsf{Scl,Ot}}\pi^{\Psi_{\mathsf{bm}}}_{\mathsf{rep,Scl}}[\mathsf{Ot}]\left(1-\frac{[\mathsf{Scl}]}{[\mathsf{Scl}]_{\mathsf{max}}}\right) \quad (16) \end{aligned}$$

In the above equations, $\tilde{D}_X$ is the degradation rate of X, and $[\mathsf{Scl}]_{\mathsf{max}}$ is a saturation sclerostin concentration. Note that, in the expression of the body production of sclerostin (Eq. 16), the mechanical repressor function $\pi^{\Psi_{\mathsf{bm}}}_{\mathsf{rep,Scl}}$ regulates the local sclerostin production by osteocytes. As explained above, the concentration of unbound LRP5/6 receptors $[\mathsf{LRP5/6}]$ can be expressed as a function of the concentration of free sclerostin $[\mathsf{Scl}]$ (see Eq. (12)). As a result, the balance equation (13) can be written as a quadratic equation of unknown $[\mathsf{Scl}]$ as follows:

$$A[\mathsf{Scl}]^2 + B[\mathsf{Scl}] + C = 0, \quad (17)$$

where:

$$\begin{aligned} A = \tilde{D}_{\mathsf{Scl}} + \tilde{D}_{\mathsf{Scl-SclAb}}\ \frac{C^{\mathsf{C}}_{\mathsf{SclAb}}}{K_D^{\mathsf{Scl-SclAb}}} + \frac{\beta_{\mathsf{Scl}}\ [\mathsf{Ot}]\ \pi^{\Psi_{\mathsf{bm}}}_{\mathsf{rep,Scl}}}{\mathsf{Scl}_{\mathsf{max}}} > 0, \quad (18) \\ B = A\cdot K_D^{\mathsf{Scl-LRP5/6}}\ (1+\frac{[\mathsf{Wnt}]}{K_D^{\mathsf{Wnt-LRP5/6}}}) + \tilde{D}_{\mathsf{Scl-LRP5/65}}[\mathsf{LRP5/6}]_{\mathsf{tot}} \\ -(P_{\mathsf{Scl},d} + \beta_{\mathsf{Scl}}[\mathsf{Ot}]\pi^{\Psi_{\mathsf{bm}}}_{\mathsf{rep,Scl}}) \quad (19) \\ C = -(P_{\mathsf{Scl},d} + \beta_{\mathsf{Scl}}[\mathsf{Ot}]\pi^{\Psi_{\mathsf{bm}}}_{\mathsf{rep,Scl}})\ (1+\frac{[\mathsf{Wnt}]}{K_D^{\mathsf{Wnt-LRP5/6}}}) < 0 \quad (20) \end{aligned}$$

We showed in a previous study that that Eq. (17) has one and only one physiologically sensible solution [21]. Therefore, the only admissible root to

Eq. (17) allows to find the values of the concentration of free sclerostin, and consequently the LRP5/6 receptor occupancy.

Note that, in Equation (13), the complex degradation $\tilde{D}_{\mathsf{Scl-SclAb}}$ cannot be determined directly from a single injection PK study. A parametric study involving bone metabolism dynamics is therefore necessary (see Section 3).

2.4. Numerical implementation of the model of treatment of PMO with romosozumab

Numerical implementation. We used Matlab Stiff Differential Algebraic Equations solver to solve a system of differential equations consisting of the evolution laws of bone cells (Eqs. (5)-(9)) and that of the sclerostin antibody in the serum (Eq. (2), as well as one algebraic equation governing the balance of RANKL (see Eq. A.7 and Appendix A).

Simulation of post-menopausal osteoporosis. We use a RANKL injection term of $P_{\mathsf{RANKL}} = 2\ \mathsf{pM}$ to simulate post-menopausal osteoporosis, and an exponential decay law for sclerostin degradation rate (see Appendix D) as implemented and validated by Martin and coworkers [21]. This strategy is supported by experimental evidence of increased RANKL/OPG ratios in post-menopausal subjects [39, 40, 41]. Additionally, studies showed an increase of serum sclerostin in post-menopausal subjects [42, 43] while its expression (local mRNA levels) decreased in animal models [43]. The increase in RANKL ratio alone is not able to reproduce the biomarker profile of sclerostin, therefore justifying the assumption of a gradual modification of sclerostin degradation.

Bone density gain. Simulations give the evolution of the bone volume fraction f_{bm} as a consequence of the differential equations (2) and (5)-(9). We assume here the changes in bone matrix volume fraction f_{bm} from our model to be equal to the changes in the bone mineral density (BMD). Therefore, in order to compare our model results with literature, we computed the bone density gain at an instant t using the following equation:

$$\mathsf{BDG}_{\%} = \frac{f_{\mathsf{bm}}(t) - f_{\mathsf{bm}}(\tau_{\mathsf{treat}})}{f_{\mathsf{bm}}(\tau_{\mathsf{treat}})}, \tag{21}$$

where τ_{treat} is defined as the instant when the simulated anabolic treatment with romosozumab starts.

Calibration of the PK-PD model. The pharmacokinetic (PK) model was calibrated against clinical data from Padhi et al. [23] for a subcutaneous injection dose of 3 mg/kg (see Figure 5). We assumed an average subject weight of 70 kg as per Evenity prescribing information [25]. The calibration of the PD model consisted in determining the complex elimination constant $\tilde{D}_{\mathsf{Scl{\cdot}SclAb}}$. To this end, we used one set of the lumbar spine trial data from Langdahl et al.[2], corresponding to 210 mg monthly injections for 12 months (Figure 7).

Validation of the model. We compare our numerical bone volume fraction (f_{bm}) results to experimental data from monthly romosozumab injections of 70 mg, 140 mg and 210 mg at the lumbar spine and the femoral neck [1, 3, 2]. As discussed in Martin et al., at homeostasis, each bone site is characterized by a different value of the bone matrix volume fraction and therefore a specific value of the habitual stress σ [21]. This relation between loading and the bone matrix volume fraction f_{bm} determines the bone turnover, i.e. the number of bone cells in the representative volume element (RVE). We assign different values for baseline bone volume fractions, i.e., $f^0_{\mathsf{bm}} = 12.5\%$ for lumbar spine (LS) and $f^0_{\mathsf{bm}} = 25\%$ for the femoral neck (FN), which are within ranges suggested in literature [44, 45]. and compute the respective tissue-scale stress σ and associated cell numbers in steady state (see Table 3).

3. Simulation results

Validation of the PK model. We used the trial data from Padhi et al. [23] to calibrate and validate our PK model. Note that the model was calibrated for a subcutaneous injection dose of 3 mg/kg (approved dose), while the 1, 5 and 10mg/kg injections doses served for validation. Note that the 3 mg/kg injection dose represented the approved recommended dosage for a 70 kg woman, assuming an average subject weight of 70 kg as per Evenity prescribing information

Table 3: Steady state values of bone cell numbers and tissue-scale stress σ for bone site-specific remodeling simulations. Baseline bone matrix volume fractions are $f^0_{\mathsf{bm}} = 12.5\%$ for lumbar spine (LS) and $f^0_{\mathsf{bm}} = 25\%$ for femoral neck (FN).

Symbol	Value	Unit
	Lumbar spine	
Ob^0_a	$9.382\,10^{-4}$	pM
Ob^0_p	$1.190\,10^{-3}$	pM
Ob^0_u	$1.000\,10^{-2}$	pM
Oc^0_a	$1.876\,10^{-5}$	pM
Oc^0_p	$5.592\,10^{-3}$	pM
σ_{LS}	-2.041	MPa
	Femoral neck	
Ob^0_a	$8.831\,10^{-4}$	pM
Ob^0_p	$1.114\,10^{-3}$	pM
Ob^0_u	$1.000\,10^{-2}$	pM
Oc^0_a	$1.766\,10^{-5}$	pM
Oc^0_p	$5.592\,10^{-3}$	pM
σ_{FN}	-4.405	MPa

[25]. In Fig. 5, we used the parameters listed in Table 1 to simulate the injections and observed the evolution of the serum sclerostin antibody concentration $C^{\mathsf{C}}_{\mathsf{SclAb}}$.

The sclerostin antibody concentration increases as the drug is absorbed from the depot, and is then degraded or bound to sclerostin, respectively via the elimination coefficient $\tilde{D}_{\mathsf{SclAb}}$ or via the Michaelis Menten kinetics with the constant K_M (see Figure 6).

Subcutaneous romosozumab injection as a treatment for osteoporosis. In order to simulate the effects of a single sclerostin monoclonal antibody injection, we used our PK model to account for subcutaneous injections. In this study, we

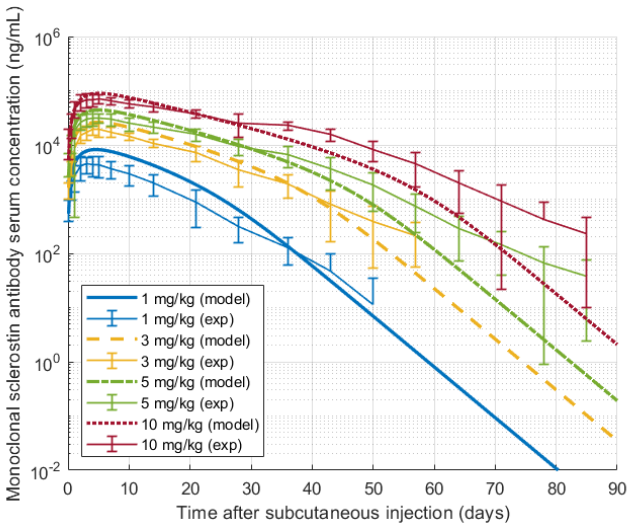

Figure 5: Evolution of sclerostin antibody levels in the central compartment (serum), for subcutaneous injections of 1, 3, 5 and 10 mg/kg: comparison of simulations (model) with experimental results (exp) from [23].

account for an advanced PMO state and the start of the treatment arbitrarily takes place 15 years after the start of PMO, corresponding approximately to the average age of the trial cohorts (around 70) [2, 3, 1].

In Figure 6, we start with an initial bone matrix fraction of 25% to simulate the drug dynamics in the femoral neck, and we model a single 210 mg injection. Figure 6 displays the evolution of sclerostin levels and bone volume fraction after the start of PMO (a), and sclerostin antibody levels in the depot and central compartments after injection (b). One can note that after one injection, the concentration of sclerostin antibody in serum is much higher than that of sclerostin (several orders of magnitudes higher (see Fig. 6 (a)).

Calibration of the bound complex elimination constant. We performed the calibration of the bound complex elimination constant as displayed in Fig. 7. We simulated 12 monthly injections of 210 mg of sclerostin monoclonal antibody as per the trial data from Langdahl et al [2]. We ran this simulation for various

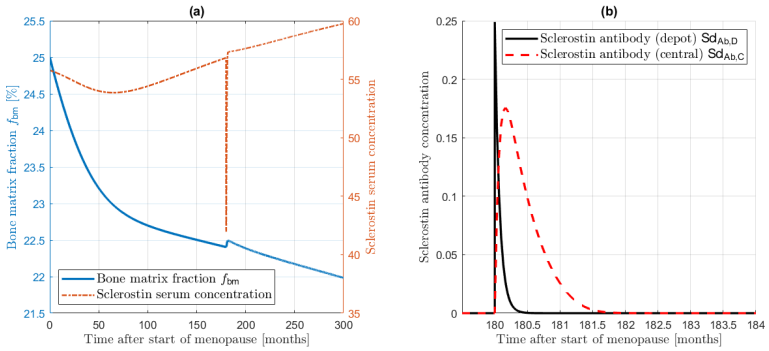

Figure 6: Simulation of PMO and a 210 mg single injection after 180 months (15 years) of PMO. Evolution of (a) sclerostin concentratino and bone volume fraction (f_{bm}) (simulation, experimental data from Nordin et al. [46]) in the femoral neck ($f^0_{\mathsf{bm}} = 25\%$) and (b) sclerostin antibody levels in the depot and central compartments from the start of PMO in the femoral neck.

values of the complex elimination constant $\tilde{D}_{\mathsf{Scl}\cdot\mathsf{SclAb}}$, observing the changes in bone volume fraction at the lumbar spine (LS).

In light of the results of the calibration study depicted in Fig. 7, we set the bound complex elimination constant to $\tilde{D}_{\mathsf{Scl}\cdot\mathsf{SclAb}} = 3.2$ day^{-1}.

Monthly romosozumab injections: model validation. We confronted our model to other clinical trial data in the literature [3, 2, 1], as displayed in Fig. 8. We simulated the evolution of bone volume fraction in the femoral neck (FN) with monthly injections of 70 mg, 140 mg and 210 mg of romosozumab, and 210 mg for lumbar spine (LS).

We note that simulation results for the lumbar spine are in excellent agreement with the data of Langdahl et al. and McClung et al. [1, 2], while the BMD results for the Japanese population lies somewhat higher [3], especially when considering lumbar spine. The model is also able to reproduce the bone loss after discontinuation of romosozumab treatment [1].

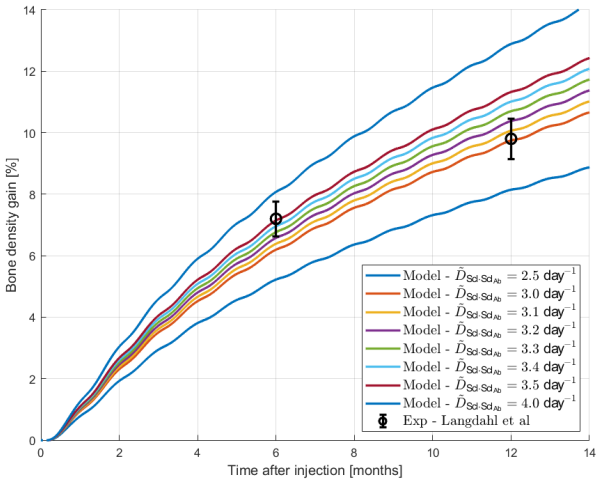

Figure 7: Evolution of bone volume fraction after the first injection in lumbar spine: simulation of monthly injections over a 14-month period, for different values of the bound complex elimination constant $\tilde{D}_{\mathsf{Scl{\cdot}SclAb}}$.

4. Discussion

Description of the pharmacodynamics of romosozumab. The efficacy of romosozumab treatment is well represented by our model, as it can be observed in Fig. 8. One may notice that the results from Ishibashi et al. are different from the other studies we accounted for here. Ishibashi and coworkers focused their study on Japanese post-menopausal women, while Langdahl et al. and McClung et al. considered European and North American sites. [1]

Finkelstein et al. studied in 2002 the ethnic variation in bone mineral density in lumbar spine and femoral neck in premenopausal and early perimenopausal American women (mean age, 46.2 years) [47]. Their study demonstrated significant differences in bone mineral density and apparent density between ethnic groups. In particular, unadjusted lumbar spine BMD was 5% higher in the

[1] McClung et al.'s study also comprised Latin American centres.

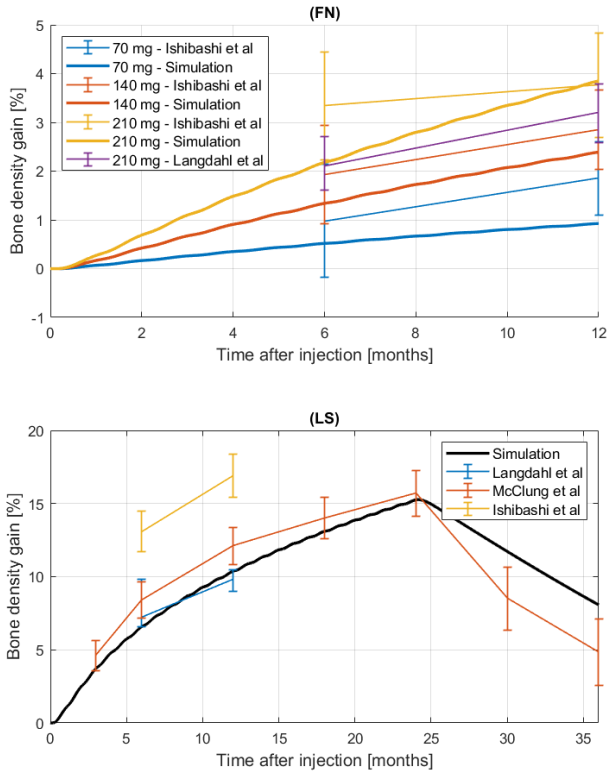

Figure 8: Simulations of PMO treatment with monthly injections of romosozumab: bone volume fraction f_{bm} (%) versus time (months): (top) femoral neck (FN) response (doses: 70 mg, 140 mg and 210 mg), and (bottom) lumbar spine (LS) response (dose: 24 monthly 210 mg injections, followed by placebo). Experimental data from Langdahl et al., McClung et al. and Ishibashi et al. [2, 1, 3].

Caucasian than in the Japanese subjects, and when adjusting for covariates, the lumbar spine BMD was 3% lower in Caucasians than in Japanese. Un-
380 adjusted femoral neck BMD was 9% higher in Caucasians than in Japanese, and the adjusted values were very similar between those groups. These findings could explain the difference in evolution of BMD in the lumbar spine when comparing Ishibashi et al.'s data (Japanese population) with the results from

McClung et al., Langdahl et al as well as our model results.

Moreover, one may also note that the Japanese subjects may have a smaller volume of distribution, leading to different kinematics of the drug. Actually, in their FDA briefing document of the Bone, Reproductive and Urologic Drugs Advisory Committee states that "Romosozumab exposure is higher in subjects with lower body weight", which supports our hypothesis.

On romosozumab pharmacokinetics and pharmacodynamics. Our PK-PD model retrieves the dynamics of the drug absorption and elimination depicted in the literature and retrieves the expected impact on bone mass and sclerostin serum concentration (Fig. 5). On the other hand, our model uses Michaelis Menten kinetics assumption which required the assumption that the concentration of sclerostin antibody is much higher than that of sclerostin at time of injection. Fig. 6 shows that this is indeed the case, as the concentration of sclerostin does not exceed about 10^2 pM, while the sclerostin antibody concentration does not get lower than about 10^4 pM during the treatment, which is two orders of magnitude higher.

On treatment planning. Our model allows to simulate and therefore study the effects of romosozumab treatment on bone porosity. As an application, we investigated the changes in bone volume fraction after a certain time (6 months, 1 year, 2 years or 5 years), as a function of the monthly dose. This study is depicted in Figure 9.

Firstly, one can observe that the bone gain at a given time point does not evolve linearly with the dosage. Hence, one interest of pharmacodynamics modelling is to better predict the long-term effect of the treatment, and aim at a patient-specific therapy. In Figure 9, we take two examples. We assume a physician desires a 2.5% or a 5% bone density gain after 1 year of treatment. The values of the corresponding dosage of the treatment can be easily recovered graphically (145 mg and 267 mg, respectively). With our model, we can see that the dose necessary to achieve a 5% bone density gain is smaller than the double of the dose necessary to achieve a 2.5% bone density gain (267¡145x2).

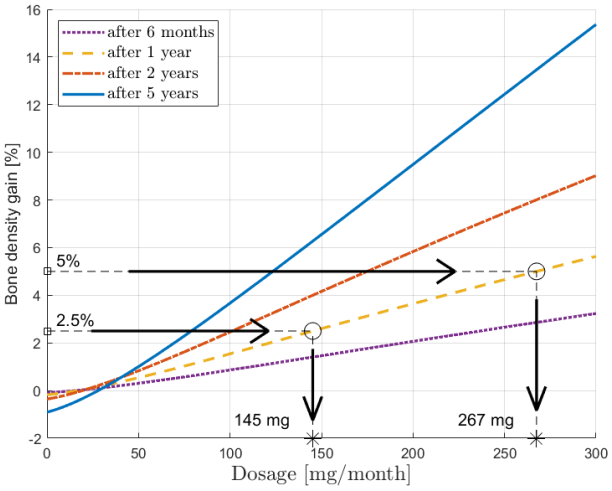

Figure 9: Influence of the dosage on the bone volume after 6 months, 1 year, 2 years and 5 years.

This means that PK modelling allows to minimize doses by being quantitative, and therefore to minimize side effects.

Note that the treatment does not seem to compensate the bone loss due to postmenopausal osteoporosis when the dosage is not sufficiently high. This is highlighted in Figure 9. Under a 50 mg monthly dose, the bone gain after 5 years is below 1%. Additionally, one can see that for very small dosages (¡ 20 mg), the bone gain is negative, meaning that the treatment does not override bone loss.

Antibody injection and bone metabolism. One of the benefits of the present model is that it allows to follow changes in cell numbers. Therefore, we are able to get a more comprehensive understanding of the remodeling process, in particular during the anabolic romosozumab treatment.

More specifically, Figure 10 depicts the changes subsequent to monthly romosozumab 210 mg injections in terms of (a) osteoclasts and osteoblasts cell numbers (directly linked to resorption and formation rates), (b) percentage of

LRP5/6 receptor occupancy by Wnt proteins (evaluated through the Hill function $\pi^{\mathsf{Wnt}}_{\mathsf{act},\mathsf{Ob}_p}$), (c) sclerostin and nitric oxide expression and (d) serum levels.

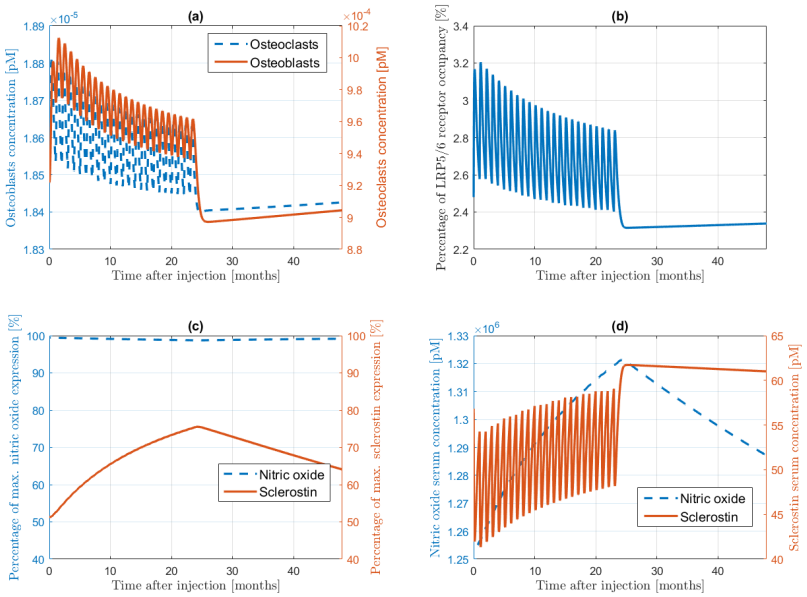

Figure 10: Evolution of osteoblasts and osteoclasts concentration (a), LRP5/6 occupancy by Wnt proteins $\pi^{\mathsf{Wnt}}_{\mathsf{act},\mathsf{Ob}_p}$ (b), percentage of maximum nitric oxide and sclerostin expression by osteocytes (c) and their serum levels (d), after the first injection of a 24 months treatment of 210 mg monthly subcutaneous injections (femoral neck).

As expected, osteoblast numbers increase following the first injection (a), as the receptor occupancy increases (b) while sclerostin serum levels decrease significantly (d). Bone gain arising from the treatment modifies the mechanical environment, resulting in an anti-anabolic osteocyte feedback reflected in an augmentation of sclerostin expression (c). Meanwhile, the variations in nitric oxide in terms of expression by osteocytes and serum levels stay small (¡ 5%) in comparison to that of sclerostin (c,d).

Stolina et al. studied bone histomorphometry in ovariectomized rats receiving sclerostin antibody or vehicle [48]. They noticed a clear increase in bone

formation markers and reduction of bone resorption parameters at 6 weeks. However, at 26 weeks, they noticed that, in comparison to controls, the increase of bone formation rate due to the antibody dropped (130% at 6 weeks, versus 74% at week 26), if adjusted with respect to bone surface (BFR/BS). This value corresponds to the actual cell bone forming activity. In Figure 10(a), we also see clearly a diminished osteoblastic activity after a few months, in parallel with the decrease in LRP5/6 receptor occupancy.

We find here that the decrease in osteoblast numbers also coincides with an increase in osteocytes expression of sclerostin as a result of the feedback regulation. This observation is consistent with Stolina et al's observations and hypotheses. Conversely, the changes in nitric oxide expression are very small (a few percents) compared to sclerostin expression by osteocytes, which increases significantly.

As highlighted in Subsection 2.1, our study reflects the pharmacodynamics of romosozumab based on its specific profile. However, the pharmacokinetics parameters listed in Table 1 could be modified in order to account for another sclerostin monoclonal antibody if necessary.

5. Conclusions

In the present paper, we introduced a target-mediated drug disposition model for sclerostin monoclonal antibody therapy and connecting it to a bone remodelling model relying on osteocytes mechanosensation.

After calibration, the model was able to reproduce with good adequation the bone gain induced by sclerostin antibody treatment reported in the literature.

Additionally, we found that sclerostin expression by osteocytes during the treatment is the main regulator of bone cells turnover. The increase in sclerostin expression during the treatment seems to be responsible for the decrease in bone formation markers after a few months of treatment. This mechanism is a result of the mechanostat, as the anabolic treatment shifts the mechanical stimulus (strain energy density in the bone matrix Ψ_{bm}, dependent on the tissue porosity)

to a lower value, therefore increasing sclerostin production.

Our comprehensive mechanistic pharmacokinetic/pharmacodynamic modelling allowed to depict the relationship between bone gain and dosage. These results – and, more generally, our proposed framework – could help towards more patient-specific treatment approach.

This model offers the possibility to analyze different treatment options and how they could affect the efficacy of the treatment on bone gain. The present model is limited as it only focuses on bone tissue and bone cells pathways. In this regard, potential side effects affecting other sites or pathways not taken into account in this model cannot be accounted for here. Nonetheless, other limitations regarding the observation of mineralisation or the combination with other drugs can definitely be adressed in the future.

Appendix A. Parameters and functions of the bone cell population model

In this section, we describe the parameters and functions used in the model to account for the effects of biochemistry on the remodeling process.

Cell differentiation, proliferation, apoptosis and ligand production are regulated by a number of binding reactions. We account for main regulating pathways via the introduction of multiplicative regulatory Hill functions.

As described in earlier works [49], the promotion X caused by the formation of the complex $L-R$ is defined by the ratio between the occupied receptors R by ligands L and the total number of receptors. Its mathematical formulation reads:

$$\pi^{L}_{\mathsf{act},X} = \frac{[L-R]}{[R]_{\mathsf{tot}}} = \frac{[L-R]}{[R]+\sum_{L'}[L'-R]}, \tag{A.1}$$

where $[L-R]$ is the concentration of ligands bound to the receptor R, and L' is any ligand that can bind to the receptor R.

In the same way, the repressor action of the receptor-ligand binding reads:

$$\pi^{L}_{\mathsf{rep},X} = \frac{[R]_{\mathsf{tot}}-[L-R]}{[R]_{\mathsf{tot}}} = \frac{[R]+\sum_{L'\neq L}[L'-R]}{[R]+\sum_{L'}[L'-R]} \tag{A.2}$$

In the absence of competitive binding, under the previously-defined steady-state assumption, we find the first-order Hill activator and repressor functions:

$$\pi^L_{\mathsf{act},X} = \frac{[L-R]}{[R]+[L-R]} = \frac{[L]}{K^{L-R}_{D,\mathsf{act}}+[L]} \tag{A.3}$$

$$\pi^L_{\mathsf{rep},X} = \frac{[R]}{[R]+[L-R]} = \frac{1}{1+\frac{[L]}{K^{L-R}_{D,\mathsf{rep}}}}, \tag{A.4}$$

where the coefficient $K^{L-R}_{D,\mathsf{act/rep}}$ is the dissociation constant of the ligand-receptor binding reaction.

Additionally, we work here under a steady-state assumption: the kinetics of the binding reactions are assumed to be fast compared to the processes they influence (namely, the cell population's evolution and ligand production). Therefore, in line with Pivonka et al [18], we find that the production rate P_L of a ligand L must be balanced with its degradation D_L, which itself can be assumed to be proportional to the concentration of L:

$$P_L + D_L = P_L - \sum_S \tilde{D}_{L-S}[L-S] = 0, \tag{A.5}$$

where $[L-S]$ represents the concentration of ligand L bound to S, a species in solution that can bind to L.

The production rate can be decomposed into a term accounting for body production $P_{L,b}$ and an additional term corresponding to the external dosage $P_{L,d}$. The expression of the endogenous term stems from the assumption that the production of the ligand L is regulated by its own concentration $[L]$, which cannot exceed a limit $[L]_{\mathsf{max}}$:

$$P_{L,b} = \textstyle\sum_{X,Y} \beta_{L,X} \pi^Y_{\mathsf{act/rep},X} X(1 - \frac{[L]}{[L]_{\mathsf{max}}}) \tag{A.6}$$

$$P_{L,b} + P_{L,d} = \tilde{D}_L[L] + \textstyle\sum_S \tilde{D}_{L-S}[L-S], \tag{A.7}$$

where X is the concentration of the cell type X producing L, with a production rate $\beta_{L,X}$ regulated by the species Y by means of the regulating activator or repressor function $\pi^Y_{\mathsf{act/rep},X}$. These balance equations allow to calculate the concentration of the different ligands.

We also have the equilibrium of binding reactions:

$$[L][R] = K^{L-R}_{D,\mathsf{act}}[L-R], \tag{A.8}$$

where the coefficient $K^{L-R}_{D,\mathsf{act/rep}}$ is the dissociation constant of the ligand (L) - receptor (R) binding reaction.

The following binding reactions are considered, corresponding to the parameters listed in Table A.4.

- Wnt and Scl binding competitively to LRP5/6 receptors, acting on pre-osteoblasts via $\pi^{\mathsf{Wnt}}_{\mathsf{act},\mathsf{Ob}_p}$;
- OPG binding to RANKL, as well as RANKL binding to RANK receptors, entering in RANKL balance to calculate the inhibiting influence through $\pi^{\mathsf{RANK}}_{\mathsf{act},\mathsf{Oc}_p}$;
- TGF-β binding to its receptors on osteoblasts and osteoclasts, whose concentration is proportional to the concentration of osteoclasts by a factor $\alpha_{\mathsf{TGF}-\beta} = 1.0\%$;
- NO and PTH acting on RANKL production by pre-osteoblasts via the function

$$\pi^{\mathsf{PTH,NO}}_{\mathsf{act/rep,RANKL}} = \lambda_s \left(\pi^{\mathsf{PTH}}_{\mathsf{act,RANKL}} + \pi^{\mathsf{NO}}_{\mathsf{rep,RANKL}}\right) + \lambda_c \, \pi^{\mathsf{PTH}}_{\mathsf{act,RANKL}} \pi^{\mathsf{NO}}_{\mathsf{rep,RANKL}},$$

  where NO is produced by osteocytes and PTH is an assumed to be produced externally and has a constant concentration, and the respective contributions of the single and combined influence of the NO and PTH actions are $\lambda_s = 0.45$ and $\lambda_c = 0.90$;
- NO and Scl expression by osteocytes regulated by the mechanical stimulus Ψ_{bm} via functions $\pi^{\Psi_{\mathsf{bm}}}_{\mathsf{act,NO}}$ and $\pi^{\Psi_{\mathsf{bm}}}_{\mathsf{rep,Scl}}$ described below (Equations (A.9)-(A.10));

The mechanical feedback is driven by sigmoidal Hill functions as suggested by Peterson and Riggs [50]:

$$\pi^{\Psi_{\mathsf{bm}}}_{\mathsf{act,NO}} = \frac{{\Psi_{\mathsf{bm}}}^{\gamma_{\mathsf{act}}}}{\delta^{\gamma_{\mathsf{act}}}_{\mathsf{act}} + {\Psi_{\mathsf{bm}}}^{\gamma_{\mathsf{act}}}} \tag{A.9}$$

$$\pi^{\Psi_{\mathsf{bm}}}_{\mathsf{rep,Scl}} = \frac{{\Psi_{\mathsf{bm}}}^{\gamma_{\mathsf{rep}}}}{\delta^{\gamma_{\mathsf{rep}}}_{\mathsf{rep}} + {\Psi_{\mathsf{bm}}}^{\gamma_{\mathsf{rep}}}}, \tag{A.10}$$

where $\gamma_\sim$,$\delta_\sim$, are respectively the sigmoidicity term influencing the steepness of response and the value of the stimulus that produces the half-maximal response [50]. These parameters are listed in Table A.5.

Appendix B. Modeling of multiple romosozumab injections

In order to calculate the amount of romosozumab in the depot (i.e. subcutaneous tissue) and the serum at any given time t, we use the algorithm schematically described in Figure B.11. Before the first injection we set $C^{\mathsf{D}}_{\mathsf{SclAb}}$ to zero. At the time of the first injection, the concentration of drug in the depot is $C^{\mathsf{D}}_{\mathsf{SclAb}} = C^{\mathsf{D,res}}_{\mathsf{SclAb}}$, as defined in Eq. (4). This value is $C^{\mathsf{D,res}}_{\mathsf{SclAb}} = 0$ at the start of the simulation. For each subsequent injection, that value is updated taking into account the remaining amount of drug from the previous injections after its absorption into the central compartment (coefficient k_a). After the last injection, the concentration of drug is calculated accounting for the absorption of the amount of drug present at the time of the last injection.

Hence, at each time point, we are able calculate the time derivative of $C^{\mathsf{C}}_{\mathsf{SclAb}}$ using Equation (2), where we insert the calculated value of $C^{\mathsf{D}}_{\mathsf{SclAb}}$.

Appendix C. Properties of matrix and fluid in the micro-mechanical model

The stiffness tensor of the extravascular bone matrix reads as follows (Kelvin notation):

$$\mathbb{c}_{\mathsf{bm}} = \begin{pmatrix} 18.5 & 10.3 & 10.4 & 0 & 0 & 0 \\ 10.3 & 20.8 & 11.0 & 0 & 0 & 0 \\ 10.4 & 11.0 & 28.4 & 0 & 0 & 0 \\ 0 & 0 & 0 & 12.9 & 0 & 0 \\ 0 & 0 & 0 & 0 & 11.5 & 0 \\ 0 & 0 & 0 & 0 & 0 & 9.3 \end{pmatrix} \text{GPa} \tag{C.1}$$

The stiffness tensor of the saturating fluid is:

$$\mathbb{c}_{\mathsf{vas}} = k_{\mathsf{H_2O}}\mathbb{J} + \mu_{\mathsf{H_2O}}\mathbb{K}, \tag{C.2}$$

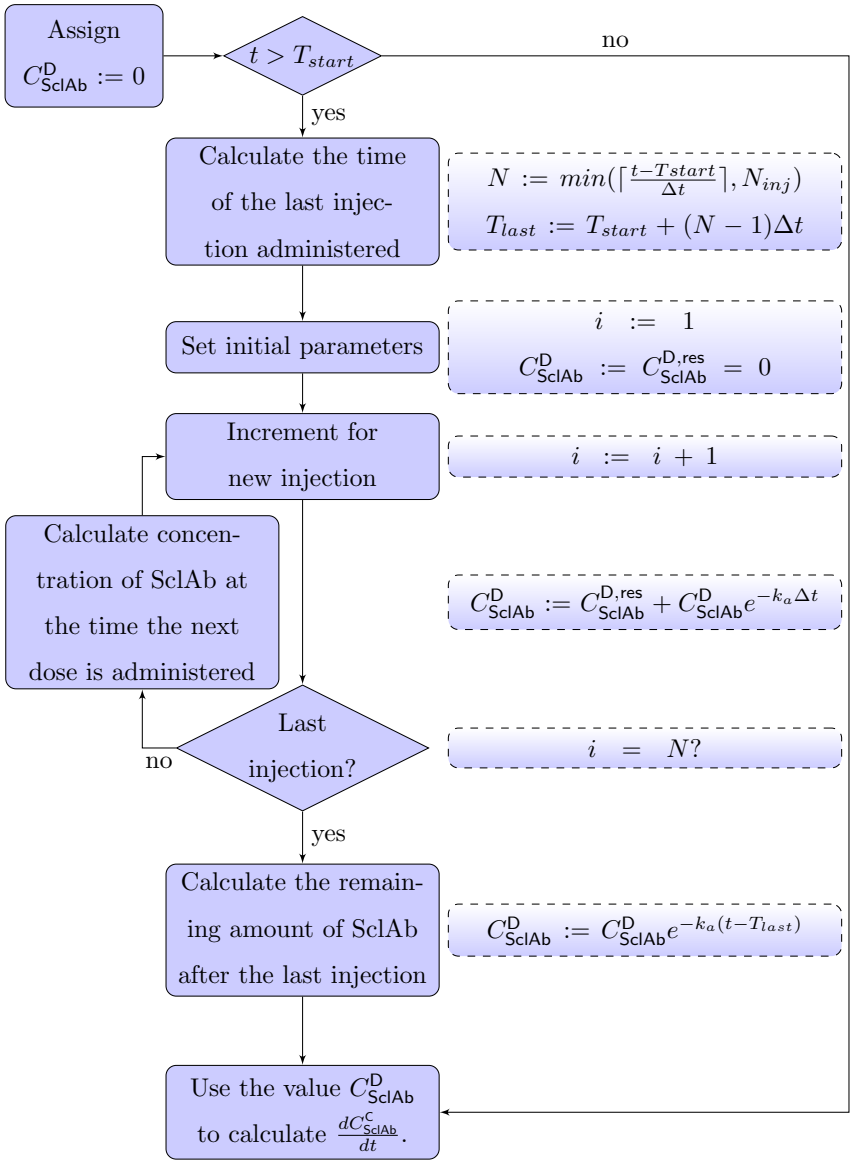

Figure B.11: Flow chart of the calculation of the amount of monoclonal antibody in the depot at the current time t. In the diagram, N is the number of the last injection that has been administered (as opposed to N_{inj}, the total number of injections of the simulated treatment), occurring at T_last, $C^{\mathsf{D}}_{\mathsf{SclAb}}$ is the concentration of antibody in the depot, i is the injection number, k_a is the absorption coefficient of the drug, and Δt is the time between two injections.

where the bulk modulus and the shear modulus are respectively $k_{\mathsf{H_2O}} = 2.3$ GPa and $\mu_{\mathsf{H_2O}} = 0$ GPa, and $\mathbb{J}$ is the volumetric part of the fourth-order unit tensor $\mathbb{I}$, and $\mathbb{K}$ is its deviatoric part, $\mathbb{K} = \mathbb{I} - \mathbb{J}$.

Appendix D. Modelling the degradation rate of sclerostin in PMO

Following a previous work, we assumed an exponential decay of the degradation rate of sclerostin: $\tilde{D}_{\mathsf{Scl}}(t = t_{menop} + \tau) = \tilde{D}_{\mathsf{Scl,PMO}}(\tau)$, where $\tilde{D}_{\mathsf{Scl,PMO}}$ is the function defined in Equation (D.1):

$$\tilde{D}_{\mathsf{Scl,PMO}}(\tau) = \tilde{D}^0_{\mathsf{Scl}}\, \mathsf{exp}(-\frac{\tau}{\tau_{PMO}}), \tag{D.1}$$

where $\tau_{PMO} = 20\mathsf{yr}$.

With this model of PMO, Martin et al. [21] showed that one can retrieve the increase of serum sclerostin reported in post-menopausal subjects [42, 43] and the decrease in sclerostin expression (local mRNA levels) found in animal models of menopause [43].

Appendix E. Nomenclature

The abbreviations used in the present paper are summarized in Table E.6.

References

[1] M. R. McClung, J. P. Brown, A. Diez-Perez, H. Resch, J. Caminis, P. Meisner, M. A. Bolognese, S. Goemaere, H. G. Bone, J. R. Zanchetta, J. Maddox, S. Bray, A. Grauer, Effects of 24 Months of Treatment With Romosozumab Followed by 12 Months of Denosumab or Placebo in Postmenopausal Women With Low Bone Mineral Density: A Randomized, Double-Blind, Phase 2, Parallel Group Study, Journal of Bone and Mineral Research 33 (8) (2018) 1397–1406. doi:10.1002/jbmr.3452.

[2] B. L. Langdahl, C. Libanati, D. B. Crittenden, M. A. Bolognese, J. P. Brown, N. S. Daizadeh, E. Dokoupilova, K. Engelke, J. S. Finkelstein,

H. K. Genant, S. Goemaere, L. Hyldstrup, E. Jodar-Gimeno, T. M. Keaveny, D. Kendler, P. Lakatos, J. Maddox, J. Malouf, F. E. Massari, J. F. Molina, M. R. Ulla, A. Grauer, Romosozumab (sclerostin monoclonal antibody) versus teriparatide in postmenopausal women with osteoporosis transitioning from oral bisphosphonate therapy: a randomised, open-label, phase 3 trial, The Lancet 390 (10102) (2017) 1585–1594. doi:10.1016/S0140-6736(17)31613-6.

[3] H. Ishibashi, D. B. Crittenden, A. Miyauchi, C. Libanati, J. Maddox, M. Fan, L. Chen, A. Grauer, Romosozumab increases bone mineral density in postmenopausal Japanese women with osteoporosis: A phase 2 study, Bone 103 (2017) 209–215. doi:10.1016/j.bone.2017.07.005.

[4] H. M. Frost, Bone "mass" and the "mechanostat": A proposal, The Anatomical Record 219 (1) (1987) 1–9. doi:10.1002/ar.1092190104. URL http://onlinelibrary.wiley.com.ezproxy.u-pec.fr/doi/10.1002/ar.1092190104/abstracthttp://doi.wiley.com/10.1002/ar.1092190104

[5] R. L. van Bezooijen, B. A. Roelen, A. Visser, L. van der Wee-Pals, E. de Wilt, M. Karperien, H. Hamersma, S. E. Papapoulos, P. ten Dijke, C. W. Löwik, Sclerostin Is an Osteocyte-expressed Negative Regulator of Bone Formation, But Not a Classical BMP Antagonist, The Journal of Experimental Medicine 199 (6) (2004) 805–814. doi:10.1084/jem.20031454. URL http://www.jem.org/lookup/doi/10.1084/jem.20031454

[6] D. G. Winkler, M. K. Sutherland, J. C. Geoghegan, C. Yu, T. Hayes, J. E. Skonier, D. Shpektor, M. Jonas, B. R. Kovacevich, K. Staehling-Hampton, M. Appleby, M. E. Brunkow, J. A. Latham, Osteocyte control of bone formation via sclerostin, a novel BMP antagonist., The EMBO journal 22 (23) (2003) 6267–76. doi:10.1093/emboj/cdg599. URL http://emboj.embopress.org/cgi/doi/10.1093/emboj/

cdg599http://www.ncbi.nlm.nih.gov/pubmed/14633986http://www.pubmedcentral.nih.gov/articlerender.fcgi?artid=PMC291840

[7] B. Langdahl, S. Ferrari, D. W. Dempster, Bone modeling and remodeling: potential as therapeutic targets for the treatment of osteoporosis, Therapeutic Advances in Musculoskeletal Disease 8 (6) (2016) 225–235. doi:10.1177/1759720X16670154.

[8] L. F. Bonewald, M. L. Johnson, Osteocytes, mechanosensing and Wnt signaling, Bone 42 (4) (2008) 606–615. doi:10.1016/j.bone.2007.12.224.

[9] D. Ke, D. Padhi, C. Paszty, Sclerostin is an Important Target for Stimulating Bone Formation, Restoring Bone Mass and Enhancing Fracture Healing, Bonedoi:10.1016/j.bone.2010.01.022.

[10] K. Warmington, S. Morony, I. Sarosi, J. Gong, P. Stephens, D. G. Winkler, M. K. Sutherland, J. A. Latham, H. Kirby, A. Moore, M. Robinson, P. J. Kostenuik, W. S. Simonet, D. L. Lacey, C. Paszty, Sclerostin Antagonism in Adult Rodents, via Monoclonal Antibody Mediated Blockade, Increases Bone Mineral Density and Implicates Sclerostin as a Key Regulator of Bone Mass During Adulthood, Journal of Bone and Mineral Research 19 (2004) S56–57.

[11] D. Padhi, B. Stouch, G. Jang, L. Fang, M. Darling, H. Glise, M. K. Robinson, S. S. Harris, E. Posvar, AntiSclerostin Antibody Increases Markers of Bone Formation in Healthy Postmenopausal Women, Journal of Bone and Mineral Research 22 (1) (2007) S37–S37.

[12] B. Kruck, E. A. Zimmermann, S. Damerow, C. Figge, C. Julien, D. Wulstein, T. Thiele, M. Martin, R. Hamdy, M. K. Reumann, Others, Sclerostin-neutralizing antibody treatment enhances bone formation but does not rescue mechanically-induced delayed healing, Journal of Bone and Mineral Research.

[13] A. Markham, Romosozumab: First Global Approval, Drugs 79 (4) (2019) 471–476. doi:10.1007/s40265-019-01072-6.
URL https://doi.org/10.1007/s40265-019-01072-6http://link.springer.com/10.1007/s40265-019-01072-6

[14] Y. Cao, W. J. Jusko, Incorporating target-mediated drug disposition in a minimal physiologically-based pharmacokinetic model for monoclonal antibodies, Journal of pharmacokinetics and pharmacodynamics 41 (4) (2014) 375–387. doi:10.1007/s10928-014-9372-2.

[15] P. Dua, E. Hawkins, P. H. van der Graaf, A {Tutorial} on {Target}-{Mediated} {Drug} {Disposition} ({TMDD}) {Models}, CPT: Pharmacometrics & Systems Pharmacology 4 (6) (2015) 324–337. doi:10.1002/psp4.41.

[16] R. J. Eudy, M. R. Gastonguay, K. T. Baron, M. M. Riggs, Connecting the dots: Linking osteocyte activity and therapeutic modulation of sclerostin by extending a multiscale systems model, CPT: Pharmacometrics and Systems Pharmacologydoi:10.1002/psp4.12013.

[17] C. C. Tang, C. Benson, J. McColm, A. Sipos, B. Mitlak, L. J. Hu, Population Pharmacokinetics and Pharmacodynamics of Blosozumab, in: American Conference on Pharmacokinetics, Arlington, Virginia, USA, 2015, pp. W–15.

[18] P. Pivonka, J. Zimak, D. W. Smith, B. S. Gardiner, C. R. Dunstan, N. A. Sims, T. John Martin, G. R. Mundy, Model structure and control of bone remodeling: A theoretical study, Bone 43 (2) (2008) 249–263. doi:10.1016/j.bone.2008.03.025.

[19] P. Pivonka, J. Zimak, D. W. Smith, B. S. Gardiner, C. R. Dunstan, N. A. Sims, T. John Martin, G. R. Mundy, Theoretical investigation of the role of the RANKRANKLOPG system in bone remodeling, Journal of Theoretical Biology 262 (2) (2010) 306–316. doi:10.1016/j.jtbi.2009.09.021.

URL https://linkinghub.elsevier.com/retrieve/pii/S002251930900441X

[20] S. Scheiner, P. Pivonka, C. Hellmich, Coupling systems biology with multiscale mechanics, for computer simulations of bone remodeling, Computer Methods in Applied Mechanics and Engineering 254 (2013) 181–196. arXiv:NIHMS150003, doi:10.1016/j.cma.2012.10.015.

[21] M. Martin, V. Sansalone, D. M. L. Cooper, F. P. Pivonka, Mechanobiological osteocyte feedback drives mechanostat regulation of bone in a multiscale computational model, Biomechanics and Modeling in Mechanobiologydoi:10.1007/s10237-019-01158-w.

[22] J. Martínez-Reina, P. Pivonka, Effects of long-term treatment of denosumab on bone mineral density: insights from an in-silico model of bone mineralization, Bone 125 (2019) 87–95. doi:10.1016/j.bone.2019.04.022.
URL https://linkinghub.elsevier.com/retrieve/pii/S8756328219301607

[23] D. Padhi, G. Jang, B. Stouch, L. Fang, E. Posvar, Single-dose, placebo-controlled, randomized study of AMG 785, a sclerostin monoclonal antibody, Journal of Bone and Mineral Research 26 (1) (2011) 19–26. doi:10.1002/jbmr.173.

[24] D. M. Paton, MONOGRAPH, Drugs of the Future 39 (8) (2014) 553–556. doi:10.1358/dof.2014.39.8.2164452.

[25] Evenity [Prescribing Information], Tech. rep., Amgen Inc., Thousand Oaks, California (2019).
URL https://www.pi.amgen.com/{~}/media/amgen/repositorysites/pi-amgen-com/evenity/evenity{_}pi{_}hcp{_}english.ashx

[26] V. Klika, F. Marsk, A thermodynamic model of bone remodelling: The

influence of dynamic loading together with biochemical control, Journal of musculoskeletal and neuronal interactions 10 (2010) 220–30.

[27] S. V. Komarova, R. J. Smith, S. J. Dixon, S. M. Sims, L. M. Wahl, Mathematical model predicts a critical role for osteoclast autocrine regulation in the control of bone remodeling, Bone 33 (2) (2003) 206–215. doi:10.1016/S8756-3282(03)00157-1.

[28] S. Maldonado, S. Borchers, R. Findeisen, F. Allgöwer, Mathematical modeling and analysis of force induced bone growth, Conference proceedings: ... Annual International Conference of the IEEE Engineering in Medicine and Biology Society. IEEE Engineering in Medicine and Biology Society. Annual Conference 1 (2006) 3154–3157. doi:10.1109/IEMBS.2006.260532.

[29] M.-I. Pastrama, S. Scheiner, P. Pivonka, C. Hellmich, A mathematical multiscale model of bone remodeling, accounting for pore space-specific mechanosensation, Bone 107 (2018) 208–221. doi:10.1016/j.bone.2017.11.009.

[30] V. Lemaire, F. L. Tobin, L. D. Greller, C. R. Cho, L. J. Suva, Modeling the interactions between osteoblast and osteoclast activities in bone remodeling, Journal of Theoretical Biology 229 (3) (2004) 293–309. doi:10.1016/j.jtbi.2004.03.023.
URL http://www.sciencedirect.com/science/article/pii/S0022519304001407

[31] X. Fan, E. Roy, L. Zhu, T. C. Murphy, C. Ackert-Bicknell, C. M. Hart, C. Rosen, M. S. Nanes, J. Rubin, Nitric Oxide Regulates Receptor Activator of Nuclear Factor-κB Ligand and Osteoprotegerin Expression in Bone Marrow Stromal Cells, Endocrinology 145 (2) (2004) 751–759. doi:10.1210/en.2003-0726.

[32] J. W. M. Chow, S. W. Fox, J. M. Lean, T. J. Chambers, Role of Nitric Oxide and Prostaglandins in Mechanically Induced Bone Formation, J Bone Miner Res 13 (6) (1998) 1039–1044. doi:10.1359/jbmr.1998.13.6.1039.

[33] G. Zaman, a. a. Pitsillides, S. C. F. Rawlinson, R. F. L. Suswillo, J. R. Mosley, M. Z. Cheng, L. a. M. Platts, M. Hukkanen, J. M. Polak, L. E. Lanyon, Mechanical Strain Stimulates Nitric Oxide Production by Rapid Activation of Endothelial Nitric Oxide Synthase in Osteocytes, J Bone Miner Res 14 (7) (1999) 1123–1131. doi:10.1359/jbmr.1999.14.7.1123.

[34] A. Gaudio, P. Pennisi, C. Bratengeier, V. Torrisi, B. Lindner, R. A. Mangiafico, I. Pulvirenti, G. Hawa, G. Tringali, C. E. Fiore, Increased sclerostin serum levels associated with bone formation and resorption markers in patients with immobilization-induced bone loss, J Clin Endocrinol Metab 95 (5) (2010) 2248–2253. doi:10.1210/jc.2010-0067.

[35] J. M. Spatz, M. N. Wein, J. H. Gooi, Y. Qu, J. L. Garr, S. Liu, K. J. Barry, Y. Uda, F. Lai, C. Dedic, M. Balcells-Camps, H. M. Kronenberg, P. Babij, P. D. Pajevic, The Wnt inhibitor sclerostin is up-regulated by mechanical unloading in osteocytes in vitro, J Biol Chem 290 (27) (2015) 16744–16758. doi:10.1074/jbc.M114.628313.

[36] X. Li, Y. Zhang, H. Kang, W. Liu, P. Liu, J. Zhang, S. E. Harris, D. Wu, Sclerostin binds to LRP5/6 and antagonizes canonical Wnt signaling, J Biol Chem 280 (20) (2005) 19883–19887. doi:10.1074/jbc.M413274200.

[37] E. Bourhis, C. Tam, Y. Franke, J. F. Bazan, J. Ernst, J. Hwang, M. Costa, A. G. Cochran, R. N. Hannoush, Reconstitution of a Frizzled8-Wnt3a-LRP6 signaling complex reveals multiple Wnt and Dkk1 binding sites on LRP6, J Biol Chem 285 (12) (2010) 9172–9179. doi:10.1074/jbc.M109.092130.

[38] IUPHAR BPS Guide to Pharmacology, Romosozumab.
URL http://www.guidetopharmacology.org/GRAC/LigandDisplayForward?tab=biology{&}ligandId=8092

[39] S. Jabbar, J. Drury, J. N. Fordham, H. K. Datta, R. M. Francis, S. P. Tuck, Osteoprotegerin, RANKL and bone turnover in postmenopausal osteoporosis, J Clin Pathol 64 (4) (2011) 354–357. doi:10.1136/jcp.2010.086595.

[40] U. Lerner, Bone Remodeling in Post-menopausal Osteoporosis, J Dent Res 85 (7) (2006) 584–595. doi:10.1177/154405910608500703.

[41] M. McClung, Role of RANKL inhibition in osteoporosis, Arthritis Res Ther 9 (SUPPL.1) (2007) 1–6. doi:10.1186/ar2167.

[42] M. S. M. Ardawi, H. A. Al-Kadi, A. A. Rouzi, M. H. Qari, Determinants of serum sclerostin in healthy pre- and postmenopausal women, Journal of Bone and Mineral Research 26 (12) (2011) 2812–2822. doi:10.1002/jbmr.479.

[43] S. Jastrzebski, J. Kalinowski, M. Stolina, F. Mirza, E. Torreggiani, I. Kalajzic, H. Y. Won, S.-K. Lee, J. Lorenzo, Changes in bone sclerostin levels in mice after ovariectomy vary independently of changes in serum sclerostin levels, Journal of Bone and Mineral Research 28 (3) (2013) 618–626. doi:10.1002/jbmr.1773.
URL http://doi.wiley.com/10.1002/jbmr.1773

[44] E. Legrand, D. Chappard, C. Pascaretti, M. Duquenne, P. Krebs, V. Rohmer, Trabecular Bone Microarchitecture , Bone Mineral Density ,, Journal of Bone and Mineral Research 15 (1) (2000) 13–19.

[45] A. Nazarian, J. Muller, D. Zurakowski, R. Müller, B. D. Snyder, Densitometric, morphometric and mechanical distributions in the human proximal femur, Journal of Biomechanics 40 (11) (2007) 2573–2579. doi:10.1016/j.jbiomech.2006.11.022.

[46] B. E. C. Nordin, A. G. Need, B. E. Chatterton, M. Horowitz, H. A. Morris, The Relative Contributions of Age and Years since Menopause to Postmenopausal Bone Loss, J Clin Endocrinol Metab 70 (1) (1990) 83–88. doi:10.1210/jcem-70-1-83.

[47] J. S. Finkelstein, M.-L. T. Lee, M. Sowers, B. Ettinger, R. M. Neer, J. L. Kelsey, J. A. Cauley, M.-H. Huang, G. A. Greendale, Ethnic Variation in

Bone Density in Premenopausal and Early Perimenopausal Women: Effects of Anthropometric and Lifestyle Factors, The Journal of Clinical Endocrinology & Metabolism 87 (7) (2002) 3057–3067. doi:10.1210/jcem.87.7.8654.
URL https://academic.oup.com/jcem/article/87/7/3057/2846531

[48] M. Stolina, D. Dwyer, Q. T. Niu, K. S. Villasenor, P. Kurimoto, M. Grisanti, C. Y. Han, M. Liu, X. Li, M. S. Ominsky, H. Z. Ke, P. J. Kostenuik, Temporal changes in systemic and local expression of bone turnover markers during six months of sclerostin antibody administration to ovariectomized rats, Bone 67 (2014) 305–313. doi:10.1016/j.bone.2014.07.031.

[49] P. Pivonka, P. Buenzli, C. Dunstan, A systems approach to understanding bone cell interactions in health and disease, in: S. Gowder (Ed.), Cell Interaction, IntechOpen, Rijeka, 2012, Ch. 7. doi:10.5772/51149.
URL https://doi.org/10.5772/51149

[50] M. C. Peterson, M. M. Riggs, A physiologically based mathematical model of integrated calcium homeostasis and bone remodeling, Bone 46 (1) (2010) 49–63. doi:10.1016/j.bone.2009.08.053.
URL http://www.sciencedirect.com/science/article/pii/S8756328209018821

Table A.4: Values of the cell population model parameters

Symbol	Value	Unit
$N_{\mathsf{Ob}_p}^{\mathsf{LRP5/6}}$	50.00	-
$K_D^{\mathsf{Wnt-LRP5/6}}$	1.000	nM
$K_D^{\mathsf{Scl-LRP5/6}}$	10.00	pM
$\tilde{D}_{\mathsf{Scl-LRP5/6}}$	50.00	pM Scl-LRP5/6 / day
$\tilde{D}_{\mathsf{Scl}}$	1.000	pM Scl / day
$\mathsf{Scl}_{\mathsf{max}}$	70.00	pM Scl
$\beta_{\mathsf{Scl,Ot}}$	$3.000\,10^{8}$	pM Scl / pmol cell
$[Wnt]$	170	pM
$k_{D,\mathsf{act}}^{\mathsf{PTH}}$	0.6500	pM
$k_{D,\mathsf{rep}}^{\mathsf{NO}}$	0.2226	pM
$\tilde{D}_{\mathsf{PTH}}$	86.00	pM PTH / day
$\tilde{D}_{\mathsf{NO}}$	$2.100\,10^{-3}$	pM NO / day
$\mathsf{NO}_{\mathsf{max}}$	$2.000\,10^{8}$	pM NO
β_{PTH}	$2.500\,10^{2}$	pM PTH
$\beta_{\mathsf{NO,Ot}}$	$2.852\,10^{7}$	pM NO / pmol cell
λ_s	0.4505	-
λ_c	0.9009	-
$N_{\mathsf{Oc}_p}^{\mathsf{RANK}}$	$1.000\,10^{3}$	-
$K_D^{\mathsf{OPG-RANKL}}$	$1.511\,10^{-2}$	pM
$K_D^{\mathsf{RANK-RANKL}}$	10.00	pM
$\tilde{D}_{\mathsf{OPG}}$	$5.326\,10^{5}$	pM OPG / day
$\tilde{D}_{\mathsf{RANKL}}$	10.13	pM RANKL / day
$\tilde{D}_{\mathsf{OPG-RANKL}}$	10.13	pM OPG-RANKL / day
$\tilde{D}_{\mathsf{RANK-RANKL}}$	10.13	pM RANK-RANKL / day
$\mathsf{RANKL}_{\mathsf{max}}$	$3.051\,10^{3}$	pM RANKL
$\beta_{\mathsf{RANKL},\mathsf{Ob}_p}$	$2.360\,10^{4}$	pM RANKL / pM cell
$\beta_{\mathsf{RANKL,Ot}}$	$5.660\,10^{6}$	pM RANKL / pM cell
$\beta_{\mathsf{OPG},\mathsf{Ob}_a}$	$1.625\,10^{8}$	pM OPG / pM cell

Table A.5: Values of the osteocyte mechanical feedback parameters

Symbol	Value	Unit
γ_{act}	7	-
γ_{rep}	9	-
δ_{act}	$4.368\,10^{-6}$	-
δ_{rep}	$9.226\,10^{-6}$	-
σ_{ss}	-3.35	MPa
$\breve{\Psi}_{\mathsf{bm}}$	$6.652\,10^{-6}$	MPa

Table E.6: Nomenclature

Symbol	Description
	Cells
Ob_u, Ob_p, Ob_a	Osteoblast uncommited precursor cells, precursor cells, active osteoblasts
Oc_p, Oc_a	Osteoclast precursor cells, active osteoclasts
Ot	Osteocytes
η	Concentration of osteocytes in the bone matrix
	Ligands, hormones
LRP5/6	Lipoprotein receptor-related proteins 5/6
NO	Nitric oxide
OPG	Osteoprotegerin
PTH	Parathyroid hormone
RANK	Receptor activator of nuclear factor kappa-B
RANKL	Receptor activator of nuclear factor kappa-B ligand
Scl	Sclerostin
SclAb	Sclerostin monoclonal antibody
TGF-β	Transforming growth factor beta
	Mechanics
Ψ_{bm}	Strain energy density
f_{bm}	Volume fraction of bone matrix
BMD	Bone mineral density
	Pharmocokinetics
MM	Michaelis-Menten
PMO	Postmenopausal osteoporosis
PK	Pharmacokinetic
PD	Pharmacodynamic

Chapter 5

Bone orthotropic remodeling as a thermodynamically-driven evolution

This chapter presents an article accepted in the Journal of Mechanics in Medicine and Biology [121].

Among phenomenological models – which give a quantitative description of biological tissue properties via remodeling laws (see Chapter 2, Section 2.3), most propose *ad hoc* laws to capture the tissue evolution. Since the end of the 19th century, efforts have been made to derive these evolution laws from general theoretical frameworks. In this context, several theories based on extensions of classical continuum mechanics were developed.

In particular, the evolution of living tissues density has been widely studied, being in the context of growth or remodeling. On the one hand, soft tissues typically undergo volumetric growth, which involves an evolution of mass that can lead to an incompatibility of growth strains and the generation of residual stresses. Following the early works of Skalak [178], theories of soft tissue growth typically quantify mass increase in soft tissue by expressing the mass source $\mathcal{R}_0$ as a function of the growth velocity gradient $\mathbf{L}_g$ [131, 165, 182]:

$$\mathcal{R}_0 = \rho_0 \operatorname{tr} \mathbf{L}_g, \tag{5.1}$$

where tr refers to the trace operator and ρ_0 is the referential mass density.

This dissertation focuses on bone, which undergoes a change in properties (remodeling) and growth through surface apposition. As underlined in Section 2.3, most phenomenological models are based on *ad hoc* laws stemming from Wolff's functional adaptation principle. Hence, instead of a linear relation to growth (Equation (5.1)), the mass source is defined as a function depending on a target state and a mechanical stimulus.

Several works investigated the thermodynamics of the evolution of living tissue, and, in particular, the energetic dissipation. The link between dissipation and free energy evolution is obtained via the definition of a constitutive framework and the first and second principles of thermodynamics [43, 131]. This expression of the dissipation allows the quantification of free energy variations that uncover the dynamics of underlying biochemical mechanisms, as highlighted by Narayanan et al. [139]. While most of energetic approaches were applied to soft tissue growth [130, 44, 139], several theories were developed for bone remodeling in the same vein.

Many of the bone remodeling theories based on energetic principles involve the quantification of bone damage. It is well accepted that osteocytes modulate bone remodeling, regulating the action of bone multicellular units that remove micro-damage accumulated in the bone matrix during repeated mechanical loading: osteoclasts first remove damaged bone and osteoblasts deposit new bone to replace it [94] (see Figure 2.6 for an illustration of the action of a BMU in cortical bone). In the late 20th century, Levenston and Carter proposed a stimulus for bone adaptive response based on two components [111]. One component was not related to damage, as per the contemporary peer work [12, 84], and expressed as a polynomial function of an effective strain summed over daily loading cycles. Conversely, the damage-related second component of the stimulus was the dissipated energy over the loading cycles, which they calculated by substracting the viscous dissipation from the total energy dissipation. Finally, Levenston and Carter found that *in vivo* literature measurements of bone surface strains were consistent with their dissipation-driven adaptation theory [111]. Since this seminal work, several studies investigated thermodynamics of bone remodeling through the representation of bone damage. Damage-repair theories are

based on the introduction of a damage variable d that affects the material properties [124, 160]. In particular, in their thermodynamically-consistent theory, Ramtani and Zidi proposed the introduction of two state variables in their generalized continuum mechanics framework, additionally to the macroscopic deformation [160]. They define a remodeling state variable – the volume fraction of the undamaged matrix in the unstrained reference state – and an internal state variable – the damage, whose evolutions are coupled via the mass balance. After a statement of constitutive equations, Ramtani and Zidi write the Clausius-Duhem inequality based on the second principle of thermodynamics. Several years later, a similar approach was proposed to investigate bone rotary remodeling [42], based on DiCarlo et al.'s original work, which is the base for the study presented hereafter.

As presented earlier (Subsection 2.2.1), bone functional adaptation was first observed while looking at femoral trabecular patterns [206] that coincided with principal stress directions. Several macroscopic theories were introduced over the past decades to model how bone may adapt its microstructural orientation to mechanical loads [35, 39, 46, 135, 152, 199]. One may stress the particularly important work of Cowin on that matter, who introduced the *fabric tensor* (a measure of tissue anisotropy [35]) and largely investigated the optimal micro-orientations of bone under varying loading configurations [35, 37]. In his 1986 work, Cowin finds that, at remodeling equilibrium, the eigenspaces of the stress and strain tensors are aligned. This sound observation is also derived mathematically later on by Sansalone et al. as a result of the dissipation principle [171].

In the article presented in this chapter, bone rotary equilibrium is investigated using energetic considerations based on DiCarlo et al.'s original theory [42]. In this formulation, the continuum mechanics framework is enriched with the introduction of a state variable R that accounts for the micro-rotation of bone tissue microstructure. Hence, DiCarlo et al. proposed a constitutive equation defining the free energy as a function of the visible (macroscopic) deformation E and the micro-rotation R as follows:

$$\psi = \frac{1}{2}\ (\mathbb{C} : \mathsf{E}) : \mathsf{E}\,, \tag{5.2}$$

where $\mathbb{C}$ is the time-dependent 4th-order elastic tensor. The elastic stiffness $\mathbb{C}$ represents the prototype elastic tensor $\mathbb{C}_0$ (which itself is time-independent) rotated by the action of a rotation tensor R, namely:

$$\forall\, \mathsf{E},\ \mathbb{C}(\mathsf{E}) = \mathsf{R}\,\mathbb{C}_0(\mathsf{R}^{\mathsf{T}}\mathsf{E}\,\mathsf{R})\,\mathsf{R}^{\mathsf{T}}\,. \tag{5.3}$$

Additionally, DiCarlo et al. postulated a passive remodeling: the outer remodeling couple (a skew-symmetric couple) is assumed to be null, meaning that no external action targeted at bone rotary remodeling is accounted for. In this scope, bone remodeling is driven by the mechanical forces. Moreover, they assumed classically that the deformation E does not induce dissipation, which means that the dissipation would only come from the remodeling process.

Hence, one can propose an expression of the dissipation due to the remodeling process based on common considerations in finite strain plasticity (Equation (5.4)). Moreover, Clausius-Duhem inequality leads to an expression of the dissipation couple $\overset{+}{\mathsf{T}}$ (assumed to be linearly related to the remodeling rate $\dot{\mathsf{R}}\,\mathsf{R}^{\mathsf{T}}$) as a function of macroscopic strain E and stress S:

$$\mathcal{D}_{int} = \overset{+}{\mathsf{T}}(\dot{\mathsf{R}}\,\mathsf{R}^{\mathsf{T}})\,, \tag{5.4}$$

$$\overset{+}{\mathsf{T}} = \mathbb{D}\,(\dot{\mathsf{R}}\,\mathsf{R}^{\mathsf{T}}) = [\mathsf{S},\mathsf{E}]\,, \tag{5.5}$$

where $\mathbb{D}$ represents the 4th-order dissipation tensor which can be interpreted as a resistance to remodeling, and the brackets denote the commutator operator:
$\forall\ (\mathsf{A},\,\mathsf{B}) \in\ \mathsf{Lin},\ [\mathsf{A},\mathsf{B}] = \mathsf{A}\,\mathsf{B} - \mathsf{B}\,\mathsf{A} = 2\,\mathsf{skw}(\mathsf{A}\,\mathsf{B})$.

As observed by Cowin [35], an alignment of stresses and strains implies a remodeling equilibrium. However, in their 2006 work on 2D micro-rotation, DiCarlo et al. show that the alignment of the microstructure orientation with that of strains and stresses does not lead to a stable equilibrium configuration. A few years later, Sansalone et al. found that rotary equilibrium stability was dependent on material properties, and, more specifically, was highly dependent on the value of the tissue shear modulus [171].

The following article presents the energetic conditions for the existence and stability of rotary remodeling equilibrium states. This analysis focuses on the variations of the tfree energy with respect to the micro-rotation state. As expected, the free energy variations and equilibrium stability are linked. For instance, for a given strain E, the derivative of the potential energy density ψ^{E} is proportional to the rotation rate $\dot{\alpha}$ and the dissipation coefficient d_0:

$$\frac{\partial \psi^{\mathsf{E}}}{\partial \alpha} = -2\, d_0\, \dot{\alpha} \tag{5.6}$$

Hence, a free energy stationary point is a remodeling equilibrium state, and vice versa. Derivating Equation (5.6) gives the relationship between free energy concavity and equilibrium stability, leading to the following energetic characterization of stable rotary remodeling states:

$$\alpha^{\mathsf{SE}} \text{ stable equilibrium} \Leftrightarrow \text{local minimum of } \alpha \mapsto \psi^{\mathsf{E}} \Leftrightarrow \text{local maximum of } \alpha \mapsto \psi^{\mathsf{S}},$$

where ψ^{S} is the bulk density of the complementary energy.

As a result, one retrieves a classical result from mechanics: stable equilibrium states correspond to minima of the potential energy and to maxima of the complementary energy. This result was confirmed by numerical simulations that, in line with Sansalone et al. [171], highlighted that alignment of principal stress, principal strain and material directions is only achieved for sufficiently high values of the shear modulus.

The sound results provided by numerical simulations and theoretical developments highlighted the role of material properties in remodeling equilibrium. These results obtained for homogeneous strains and stresses are encouraging and are the first step towards the application to more complex boundary conditions and the integration of the role of biochemistry. The former application will be introduced in Chapter 6, proposing a benchmark study of bone orthotropic remodeling in the human femur. The latter is introduced as a novel formulation coupling the action of cells, mineralization, micro-rotation and evolution of density in Chapter 7.

Journal of Mechanics in Medicine and Biology

Bone orthotropic remodeling as a thermodynamically-driven evolution

M. MARTIN

Laboratoire Modélisation et Simulation Multi Echelle, Université Paris-Est Créteil, 61 avenue du Général de Gaulle, 94010 Créteil Cedex, France
Biomechanics and Spine Research Group, School of Chemistry, Physics and Mechanical Engineering, Queensland University of Technology, 2 George St, Brisbane City QLD 4000, Australia
madge.martin@u-pec.fr

T. LEMAIRE

Laboratoire Modélisation et Simulation Multi Echelle, Université Paris-Est Créteil, 61 avenue du Général de Gaulle, 94010 Créteil Cedex, France
lemaire@u-pec.fr

G. HAIAT

Laboratoire Modélisation et Simulation Multi Echelle, Université Paris-Est Créteil, 61 avenue du Général de Gaulle, 94010 Créteil Cedex, France
haiat@u-pec.fr

P. PIVONKA

Biomechanics and Spine Research Group, School of Chemistry, Physics and Mechanical Engineering, Queensland University of Technology, 2 George St, Brisbane City QLD 4000, Australia
peter.pivonka@qut.edu.au

V. SANSALONE

Laboratoire Modélisation et Simulation Multi Echelle, Université Paris-Est Créteil, 61 avenue du Général de Gaulle, 94010 Créteil Cedex, France
vittorio.sansalone@u-pec.fr

Received (Day Month Year)
Accepted (Day Month Year)

In this contribution we present and discuss a model of bone remodeling set up in the framework of the theory of generalized continuum mechanics and first introduced by DiCarlo *et al.*[1]. Bone is described as an orthotropic body experiencing remodeling as a rotation of its microstructure. Thus, the complete kinematic description of a material point is provided by its position in space and a rotation tensor describing the orientation of its microstructure. Material motion is driven by energetic considerations, namely by the application of the Clausius-Duhem inequality to the microstructured material. Within this framework of orthotropic remodeling, some key features of the remodeling equilibrium configurations are deduced in the case of homogeneous strain or stress loading conditions. First, it is shown that remodeling equilibrium configurations correspond to energy extrema. Second, stability of the remodeling equilibrium configurations is as-

sessed in terms of the local convexity of the strain and complementary energy functionals hence recovering some classical energy theorems. Eventually, it is shown that the remodeling equilibrium configurations are not only highly dependent on the loading conditions, but also on the material properties.

Keywords: bone; remodeling; rotation; thermodynamics

1991 Mathematics Subject Classification: 22E46, 53C35, 57S20

1. Introduction

The present work focuses on the representation of bone adaptation as an evolution of the material principal directions. Bone is a living material constantly undergoing microstructural changes. Since the theory of the *mechanostat* by Frost[2], it has been widely accepted that the evolution of bone mass and structure can be seen as a feedback from the mechanical environment. In particular, the early work of von Meyer[3] and Wolff[4] on the one hand and of Roux[5] on the other hand underline the anisotropic pattern of bone architecture.

In 1867, benefiting from his collaboration with the German civil engineer Culmann, Von Meyer notes a striking connection between the stress lines in a crane and the trabecular architecture in a femur[3,6]. A few years later, Wolff introduces a new idea about bone remodeling, known as Wolff's law, stating that the mechanical function of bone drives the evolution of its architecture[4]. The work of Wolff[7,8] inspired a wealth of experimental studies investigating the heterogeneous distribution of mass in bone and the pattern of bone architecture[9,10,11,12,13].

Towards the end of the 20th century, the pioneering work of Carter and Cowin opens the way to two modeling approaches to bone remodeling aiming at explaining the trabecular pattern of bone–considered as evidence of Wolff's law–in terms of mechanical stimuli. On the one hand, Carter and coworkers[14] interpret the trabecular pattern in terms of the heterogeneous distribution of bone mass density. Initially proposed for an isotropic material, this approach is later extended to account for anisotropic remodeling[15]. On the other hand, Cowin introduces the *fabric tensor* to translate the orthotropic arrangement of the microstructure of a porous material to the continuum level[16,17]. Since the first works of Carter and Cowin, several studies have been aiming to address how the connection between mechanical loading and bone remodeling can explain bone anisotropy. Some of them investigate the change in trabecular anisotropic architecture using Finite Element simulations at the microstructural scale (μFE) to assess bone apposition and resorption. The majority of these micro-scale models rely on the well-documented experimental evidence of a connection between bone remodeling and mechanical loading[18,19,20] and introduce remodeling laws driven by either the strain energy[18,21,22,23,24,25,26,27], the strain[19] or the stress[28]. Other voxel-based models include uncertainty in the remodeling process, with[21,22] or without mechanical feedback[29,30].

Besides these micro-scale models, other works attempt to describe bone orthotropic remodeling at a higher scale. Among the studies dealing with anisotropy

at the tissue scale, the majority of works are concerned with characterizing the final stage of bone adaptation which is intended as an optimal state of the trabecular architecture. In 1986, Cowin[17] introduces a mathematical condition for the remodeling equilibrium of bone trabecular architecture. He argues that, according to Wolff's law, the principal axes of the bone fabric tensor–encoding the orientation of bone microstructure–and of the stress tensor must coincide at the remodeling equilibrium. Moreover, he demonstrates that these directions also correspond to the principal axes of the strain tensor. A few years later, several studies focused on material orthotropic optimization. In all generality with respect to an orthotropic material, Rovati et Taliercio[31] and, later on, Banichuk[32], study material orthotropic optimization in relation with the variations of the strain energy, showing that energy extrema always correspond to the alignment of the material axes with principal strains. In 1989, Pedersen performs a 2D study showing that the strain energy density is always stationary for a configuration where material axes and strain principal axes are aligned[33]. Pedersen, joined by Cowin[34,35], underlines that the nature of the optimum depends on the elastic moduli and in particular on the shear stiffness[33]. Additionally, Cowin demonstrates that, unlike for cubic symmetries, the optimization of strain energy not only depends on orientation but also on the loading configuration. Several authors also apply the concept of bone structural optimization to compare it with known trabecular patterns[36,37]: the optimization relies on the minimization of an energy-related cost function, while guaranteeing balance equations.

Other studies address bone anisotropic remodeling as a continuous evolution of the tissue-scale material properties. Several of them find the anisotropic pattern as a consequence of the inhomogeneity of the mass density gradient[14,15,38,39]. Others use a multi-linear law–in line with the ideas of Huiskes[40]–to quantify the rotation of the material axes[41] or the evolution of both elastic moduli (possibly derived from the bone density) and material axes[42,43], or design a polynomial law for the time rates of the density and fabric tensor[44]. To the authors' knowledge, Jacobs *et al*are the pioneers in the development of a remodeling law for an anisotropic material[15]. They use the instantaneous dissipation rate, *i.e.* the difference between the power associated with the external loads and the rate-of-change of the internal energy, as a measure of the effectiveness of the adaptive response and eventually derive the expression of the rate-of-change of the elastic tensor by solving a constrained optimization problem. The notion of dissipation plays also a central role–yet different than in Jacobs' work–in other modeling approaches drawing on the theory of continuum thermodynamics[45,46,47,48,49,50]. In particular, DiCarlo and coworkers[1] developed a novel, thermodynamically-consistent theory to describe bone orthotropic remodeling. Instead of devising a remodeling criterion, they derived the evolution law of the material axes from the dissipation principle through a generalized continuum formulation without any *ad hoc* assumption.

All the above models provide a phenomenological description of bone remodeling

since they connect mechanical stimuli and bone response disregarding the underlying biological phenomena. In the last decades, stepping from the pioneering work of Roux[5], a wealth of work at the interface of engineering and biology paved the way to a new class of mechanobiological models of bone. These approaches, bridging a mathematical modeling of cell dynamics with a continuum description of bone, have the potential to provide a much deeper insight on the complex interactions between mechanics and biochemistry that trigger bone cell activity and, in turn, bone remodeling[51,52,53,54,55,56]. Mechanobiological models can effectively contribute to understand the biological basis of bone remodeling and have progressively displaced the focus of the bone community from the structure to the process–that is from Wolff's to Roux' point of view. Nevertheless, phenomenological models are still useful, especially in those situations where the focus is set on the mechanical stimuli (*e.g.* for a better design of prostheses[40]) since they allow a straightforward view of the long term macroscopic influence of changes in the external stress field on the overall trend of bone material properties.

In the present paper, we use the theoretical framework proposed by DiCarlo and coworkers[1] and describe bone remodeling as a stress-driven process set up in the framework of generalized continuum mechanics and thermodynamics. As described in the early works of Germain[57], generalized continuum mechanics allows the description of the complex behavior of materials with microstructure. In this framework, the classical Cauchy continuum model is enriched with additional parameters which are meant to provide an average description of the state of the underlying microstructure at the continuum scale. In the case of bone remodeling, these additional parameters may be related to bone micro-architecture as well as its biological and chemical composition. While the work of DiCarlo[1] focuses on the evolution of the material axes, the framework that they developed lies within the general concept of material evolution stemming from the generalized continuum mechanics. In the present work, we keep that framework and evaluate the consistency of our formulation through several theoretical and numerical considerations. Hence, we study here the relationship between the variations of the strain energy through remodeling and the stress and strain state, as well as the material properties. Our main results concern some sound energetic conditions characterizing the remodeling equilibrium. Moreover, we perform a numerical study showing in which cases the alignment of the fabric- with principal stress- and strain directions inferred by Cowin[17] is verified and in which cases it is *not*.

2. Modeling bone as a continuum with rotating microstructure

The theory of material remodeling proposed by DiCarlo and co-workers in the early 2000s[47] paved the way for the general idea to describe the adaptive behavior of living materials in a thermodynamically consistent framework. Functional adaptation of living materials – emerging as the appearance of residual stress or changes in material properties–is described in this theory as the time-evolution of suitable

kinematic parameters describing the material state at the continuum level. Evolution laws of these parameters are obtained through a generalized statement of the virtual power principle and thermodynamically consistent constitutive assumptions.

This general theory was used by DiCarlo *et al*[1] to describe bone remodeling as a rotation of bone material principle directions. In general, bone remodeling results from the change of both density and microarchitecture of the bone material triggered by mechanical and biochemical stimuli. In terms of elasticity, this phenomenon emerges as an evolution of the elastic moduli and principle directions. Following DiCarlo *et al*[1], in this paper we are only concerned with this latter feature and leave the development of the general model to future work. As long as the elastic moduli do not change, bone remodeling solely emerges from the rotation of the elasticity axes and will be called *rotary* remodeling. Assuming bone to be an orthotropic material, remodeling will thus depict the rotation of the orthotropy material axes. In the following subsection we will outline the kinematics, balance and constitutive theory introduced by DiCarlo *et al*[1].

2.1. *Kinematics*

We model a piece of bone as a body $\mathcal{B}$–a continuum collection of material points b–occupying at each time t of the time-line $\mathcal{T}$ a closed region of the 3-dimensional (3D) Euclidean manifold $\mathcal{E}$. Thereafter, the dependency of the different fields on space and time is left understood where unnecessary.

In our framework, the evolution of $\mathcal{B}$ from a reference shape $\mathcal{S}_0 \in \mathcal{E}$ is thoroughly described by two kinematic fields related to its shape and texture. On the one hand, its visible shape $\mathcal{S} \in \mathcal{E}$ is described by the gross (i.e. coarse grain) displacement field $\mathbf{u}$. On the other hand, the textural change is depicted by a rotation tensor field R describing the orientation of the microstructure–to be called micro-orientation for short–with respect to a fixed frame. Thus, the tensor R bears quite the same meaning as the fabric tensor introduced by Cowin[17]. Note that, since the strain experienced by bone tissue is small (it does not exceed 1% *in vivo* [58]), the small strain tensor E (*i.e.*, the symmetric part of the displacement gradient) can be used to describe the gross deformation of the body. However, the rotation tensor R does not need to be small. Fig. 1 depicts the basic kinematic ingredients of our model.

In view of the above assumptions, the complete motion of $\mathcal{B}$ is described through the gross and remodeling velocity fields $\mathbf{v} := \dot{\mathbf{u}}$ and $\mathsf{W} := \dot{\mathsf{R}}\mathsf{R}^{\mathsf{T}}$, respectively, where a superposed dot denotes time differentiation and superscript "T" denotes transposition. Note that $\mathbf{u}$ and $\mathbf{v}$ take values in $\mathbf{V}$ – the vector spaces of the translations of $\mathcal{E}$, R in Orth^+ – the vector space of the 2nd-order rotation tensors, and W in Skw – the vector spaces of the skew-symmetric 2nd-order tensors.

2.2. *Balance*

The balance laws governing the evolution of $\mathcal{B}$ are obtained through a generalized statement of the principle of virtual power. To this aim, test velocities related to

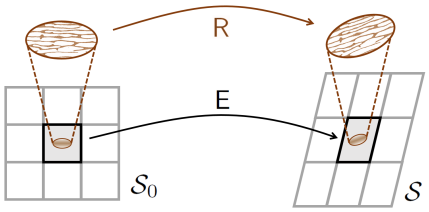

Fig. 1. Kinematic description of a body undergoing deformation and rotary remodeling. The visible deformation from the reference shape $\mathcal{S}_0$ to the actual shape $\mathcal{S}$ is described by the small strain tensor E and the rotation of the microstructure is described by the rotation tensor R.

the gross and remodeling velocities are introduced and the following expressions of the powers of internal and external forces are postulated:

$$\begin{aligned} P_i(\hat{\mathbf{v}},\hat{\mathsf{W}}) &= \int_{\mathcal{B}}(\mathbf{b}_i\cdot\hat{\mathbf{v}} - \mathsf{S}:\nabla\hat{\mathbf{v}} + \overset{\text{i}}{\mathsf{T}}:\hat{\mathsf{W}})\,, \\ P_e(\hat{\mathbf{v}},\hat{\mathsf{W}}) &= \int_{\mathcal{B}}(\mathbf{b}\cdot\hat{\mathbf{v}} + \overset{\circ}{\mathsf{T}}:\hat{\mathsf{W}}) + \int_{\partial\mathcal{B}}\mathbf{t}_\partial\cdot\hat{\mathbf{v}}\,. \end{aligned} \tag{1}$$

In the above expressions, integrals are taken either on the body $\mathcal{B}$ or on its boundary $\partial\mathcal{B}$. Moreover, $\hat{\mathbf{v}}$ stands for the $\mathbf{V}$-valued virtual gross velocity and $\hat{\mathsf{W}}$ for the Skw-valued virtual micro-rotation velocity. Additionally, $\mathbf{b}_i$ and $\mathbf{b}$ are the inner and outer bulk forces, respectively, $\mathbf{t}_\partial$ the boundary traction, S the stress tensor, and $\overset{\text{i}}{\mathsf{T}}$ and $\overset{\circ}{\mathsf{T}}$ the inner and outer skew-symmetric remodeling couples, respectively. Finally, centered dots and double dots denote the inner products in $\mathbf{V}$ and Lin (the space of 2nd order tensors), respectively, and ∇ is the gradient operator. Before going further, a couple of remarks are in order. First, the generalized fores entering Eq. (1) belong to two different classes. On the one hand, $\mathbf{b}_i$, S, and $\overset{\text{i}}{\mathsf{T}}$ are inner actions and shall therefore be related to the kinematic fields through thermodynamically consistent constitutive relations. On the other hand, no thermodynamic restrictions apply on the external actions $\mathbf{b}$, $\mathbf{t}_\partial$, and $\overset{\circ}{\mathsf{T}}$. In particular, $\overset{\circ}{\mathsf{T}}$ encodes the biochemical stimuli *directly* triggering remodeling[a]. Second, it can be noticed that this theory is of order 1 in $\mathbf{u}$ and of order 0 in R. Therefore, since no power is expended on the rotation gradients, the rotation of the material axes at one point is insensitive to the rotation at the neighboring points.

The principle of material frame-indifference leads to $\mathbf{b}_i = 0$ and to the symmetry of the stress tensor S. Hence, the balance laws governing material motion derive from a generalized statement of the principle of virtual power, *i.e.* from the requirement that the total virtual power–the sum of the powers of internal and external forces–shall be null for any admissible virtual velocity:

$$\forall\,(\hat{\mathbf{v}},\hat{\mathsf{W}}),\ P_i(\hat{\mathbf{v}},\hat{\mathsf{W}}) + P_e(\hat{\mathbf{v}},\hat{\mathsf{W}}) = 0\,. \tag{2}$$

[a]As it will be shown later, mechanical forces also do trigger remodeling.

Replacing the expressions of P_i and P_e given in Eq. (1) and using the divergence theorem, this reads:

$$\int_{\mathcal{B}} \left((\mathsf{div}\,\mathsf{S} + \mathbf{b}) \cdot \hat{\mathbf{v}} + (\overset{\mathsf{i}}{\mathsf{T}} + \overset{\circ}{\mathsf{T}}) : \hat{\mathsf{W}} \right) + \int_{\partial\mathcal{B}} (\mathbf{t}_\partial - \mathsf{S}\,\mathbf{n}_\partial) \cdot \hat{\mathbf{v}} = 0 \quad \forall\, (\hat{\mathbf{v}}, \hat{\mathsf{W}})\,, \tag{3}$$

where div is the divergence operator and $\mathbf{n}_\partial$ is the outer unit normal to $\partial\mathcal{B}$.

By standard localization arguments, the integral expression of the principle of virtual power in Eq. (3) leads to the local balance equations:

$$\begin{aligned} \mathsf{div}\,\mathsf{S} + \mathbf{b} = 0 \quad &\text{in } \mathcal{B}\,, \quad \mathsf{S}\,\mathbf{n}_\partial = \mathbf{t}_\partial \quad \text{on } \partial\mathcal{B}\,, \\ \overset{\mathsf{i}}{\mathsf{T}} + \overset{\circ}{\mathsf{T}} = 0 \quad &\text{in } \mathcal{B}\,. \end{aligned} \tag{4}$$

2.3. *Constitutive theory*

Our constitutive theory rests on the specification of the strain energy of the material and on the enforcement of a generalized dissipation principle.

The strain energy Ψ^{E} is assumed to admit a bulk density ψ^{E} such that $\Psi^{\mathsf{E}} = \int_{\mathcal{B}} \psi^{\mathsf{E}}$. In turn, the strain energy density ψ^{E} is postulated as a quadratic form of the small strain tensor E:

$$\psi^{\mathsf{E}} = \frac{1}{2}\, \mathbb{C}(\mathsf{E}) : \mathsf{E}\,, \tag{5}$$

where $\mathbb{C}$ is the 4th-order elastic tensor. The latter is assumed to be able to evolve in time, which corresponds to material remodeling. Since we focus on rotary remodeling, the actual elastic tensor $\mathbb{C}$ can be obtained through the action of a rotation tensor R (the kinematic variable describing material remodeling) on a prototype elastic tensor $\mathbb{C}_0$, namely:

$$\forall\, \mathsf{E},\ \mathbb{C}(\mathsf{E}) = \mathsf{R}\,\mathbb{C}_0(\mathsf{R}^{\mathsf{T}}\mathsf{E}\,\mathsf{R})\,\mathsf{R}^{\mathsf{T}}\,. \tag{6}$$

Therefore, the strain energy density ψ^{E} depends on both the strain E–explicitly–and on the micro-orientation R–implicitly, via $\mathbb{C}$.

In order to simplify the notation, one may use the conjugation product, defined as[59]:

$$\forall\, \{\mathsf{A}, \mathsf{B}, \mathsf{M}\} \in \mathsf{Lin}\,, (\mathsf{A} \boxtimes \mathsf{B})\,\mathsf{M} = \ \mathsf{A}\,\mathsf{M}\,\mathsf{B}^{\mathsf{T}}\,. \tag{7}$$

Hence, noting that $(\mathsf{A} \boxtimes \mathsf{B})^{\mathsf{T}} = \mathsf{A}^{\mathsf{T}} \boxtimes \mathsf{B}^{\mathsf{T}}$ and letting $\mathbb{R} := \mathsf{R} \boxtimes \mathsf{R}$, one can easily recover the following results:

Lemma 2.1.

$$\mathsf{R}^{\mathsf{T}}\mathsf{E}\mathsf{R} = \mathbb{R}^{\mathsf{T}}(\mathsf{E})\,, \tag{8}$$

$$\mathbb{C} = \mathbb{R}\,\mathbb{C}_0\,\mathbb{R}^{\mathsf{T}}\,. \tag{9}$$

Proof. The proof is straightforward. □

2.4. *Deriving the local remodeling law from thermodynamics*

Thermodynamic restrictions on the constitutive mappings of the inner actions S and $\overset{\mathsf{i}}{\mathsf{T}}$ are obtained by enforcing a generalized statement of the dissipation principle. The latter is a direct consequence of the first and second principles of thermodynamics and binds the power of internal forces P_i to the strain energy rate by requiring the intrinsic dissipation D_{int} to be non-negative along any realized velocity $(\mathbf{v}, \mathsf{W})$:

$$D_{int} := -P_i(\mathbf{v}, \mathsf{W}) - \dot{\Psi}^{\mathsf{E}} \geq 0\,. \tag{10}$$

It can be shown that the rate of strain energy density change can be written as:

$$\dot{\psi}^{\mathsf{E}} = \frac{1}{2}(\mathbb{C}(\mathsf{E}) : \mathsf{E}) = \mathbb{C}(\mathsf{E}) : \Big(\dot{\mathsf{E}} - [\dot{\mathsf{R}}\,\mathsf{R}^{\mathsf{T}}, \mathsf{E}]\Big) = \mathbb{C}(\mathsf{E}) : \dot{\mathsf{E}} - [\mathbb{C}(\mathsf{E}), \mathsf{E}] : \dot{\mathsf{R}}\,\mathsf{R}^{\mathsf{T}}\,, \tag{11}$$

where the brackets denote the commutator operator: $\forall\,(\mathsf{A}\,\mathsf{B}) \in \mathsf{Lin}$, $[\mathsf{A}, \mathsf{B}] = \mathsf{A}\,\mathsf{B} - \mathsf{B}\,\mathsf{A} = 2\,\mathsf{skw}(\mathsf{A}\,\mathsf{B})$. Thus, in view of the definition of the inner power in Eq. (1), the local form of Eq. (10) expands to:

$$(\mathsf{S} - \mathbb{C}(\mathsf{E})) : \dot{\mathsf{E}} + \left(-\overset{\mathsf{i}}{\mathsf{T}} + [\mathbb{C}(\mathsf{E}), \mathsf{E}]\right) : (\dot{\mathsf{R}}\,\mathsf{R}^{\mathsf{T}}) \geq 0\,. \tag{12}$$

No dissipation is assumed to be related to the gross (elastic) deformation, leading to $\mathsf{S} = \partial\psi^{\mathsf{E}}/\partial\mathsf{E} = \mathbb{C}(\mathsf{E})$. Note that S depends on both E–explicitly–and R–implicitly, via $\mathbb{C}$, see Eq. (9). Therefore, the local form of the reduced dissipation inequality reads:

$$\left([\mathsf{S}, \mathsf{E}] - \overset{\mathsf{i}}{\mathsf{T}}\right) : (\dot{\mathsf{R}}\,\mathsf{R}^{\mathsf{T}}) = \overset{\mathsf{+}}{\mathsf{T}} : (\dot{\mathsf{R}}\,\mathsf{R}^{\mathsf{T}}) \geq 0\,, \tag{13}$$

where $\overset{\mathsf{+}}{\mathsf{T}} := [\mathsf{S}, \mathsf{E}] - \overset{\mathsf{i}}{\mathsf{T}}$ denotes the dissipation couple related to remodeling. For the sake of simplicity, let us assume $\overset{\mathsf{+}}{\mathsf{T}}$ to be proportional to the remodeling velocity:

$$\overset{\mathsf{+}}{\mathsf{T}} = \mathbb{D}\,(\dot{\mathsf{R}}\,\mathsf{R}^{\mathsf{T}})\,, \tag{14}$$

where $\mathbb{D}$ represents the 4th-order dissipation tensor which can be interpreted as a resistance to remodeling. Note that $\mathbb{D}$ belongs to $\mathsf{Skw} \otimes \mathsf{Skw}$–the vector space of endomorphisms of Skw–and therefore admits the following representation:

$$\mathbb{D} = \sum_{ij} d_{ij}\,\mathsf{W}_i \otimes \mathsf{W}_j\,, \tag{15}$$

where $\{i, j\} \in \{\mathsf{x}, \mathsf{y}, \mathsf{z}\}$, d_{ij} are scalar coefficients and the tensors W_i constitute a basis of Skw, namely: $\mathsf{W}_\mathsf{x} := \mathbf{e}_3 \otimes \mathbf{e}_2 - \mathbf{e}_2 \otimes \mathbf{e}_3$, $\mathsf{W}_\mathsf{y} := \mathbf{e}_1 \otimes \mathbf{e}_3 - \mathbf{e}_3 \otimes \mathbf{e}_1$, and $\mathsf{W}_\mathsf{z} := \mathbf{e}_2 \otimes \mathbf{e}_1 - \mathbf{e}_1 \otimes \mathbf{e}_2$. Moreover, in order for the reduced dissipation inequality in Eq. (13) to be satisfied, $\mathbb{D}$ must be non-negative on any skew-symmetric tensor: $\mathbb{D}(\mathsf{W}) : \mathsf{W} \geq 0\ \forall\,\mathsf{W} \in \mathsf{Skw}$, which implies the coefficients d_{ii} to be non-negative and the other coefficients to be null. Thus, the reduced form of $\mathbb{D}$ reads:

$$\mathbb{D} = \sum_{i} d_{ii}\,\mathsf{W}_i \otimes \mathsf{W}_i\,. \tag{16}$$

Thus, a thermodynamically-consistent remodeling evolution law is readily obtained, reading:

$$\mathbb{D}\left(\dot{\mathsf{R}}\,\mathsf{R}^{\mathsf{T}}\right) = [\mathsf{S},\mathsf{E}] - \mathring{\mathsf{T}}\,. \tag{17}$$

2.5. *Passive remodeling and remodeling equilibrium*

A simple but significant case is obtained by considering the outer remodeling couple $\mathring{\mathsf{T}}$ to be null. In this situation, remodeling is only driven by the stress and strain and is therefore called *passive* remodeling. For the sake of simplicity, we further assume that the dissipation tensor is constant: $\mathbb{D} = \mathbb{D}_0$. Hence, at each material point, the rotation of the material axes is coupled to the stress and strain by the following equation:

$$\mathbb{D}_0\left(\dot{\mathsf{R}}\,\mathsf{R}^{\mathsf{T}}\right) = [\mathsf{S},\mathsf{E}]\,. \tag{18}$$

It follows that, provided the material properties $\mathbb{C}_0$ and $\mathbb{D}_0$, the rotation rate $\dot{\mathsf{R}}$ only depends on the strain E and the micro-orientation R.

Remodeling equilibrium is achieved when material properties no longer evolve, corresponding to a stationary state of the rotation, *i.e.* $\dot{\mathsf{R}} = 0$. In the case of passive remodeling, it is worth noting that this model predicts the principal axes of the strain and stress tensors to be locally collinear at the remodeling equilibrium[60]. This condition is similar to that inferred by Cowin for trabecular bone[17]. In line with the rationale of the Wolff's law[8], Cowin assumed that trabecular bone remodels itself by stiffening in load bearing directions and concluded that this assumption implies that the principal axes of the stress, strain and fabric tensors all coincide at remodeling equilibrium. Here, we recover the alignment of the principal directions of stress and strain without any *ad-hoc* assumption. However, our model does not necessarily require the material principal axes to align.

2.6. *Comparison with other modeling approaches*

As previously mentioned, a couple of studies aim at describing bone rotary remodeling while acknowledging the role of dissipation in this process[15,45]. These approaches describe the evolution of the fabric tensor orientation and bone density under certain criteria defining the dead zone, where by definition there is no (or little) remodeling. Jacobs and collaborators[15] use an efficiency measure defined as the difference between the power induced by external actions and the change in total internal energy. In other words, their remodeling law relies on Kuhn-Tucker conditions deriving from the minimization of the dissipation. This global optimization leads to an evolution law for the elastic moduli and bone density. While Jacobs and coworkers use the fourth-order stiffness tensor $\mathbb{C}$ and the density ρ as the variables describing bone remodeling, Doblaré and García[45] account instead for the fabric tensor $\widehat{\mathsf{H}}$ (and therefore, tissue orientation) and the density ρ, arguing that the

evolutions of $\mathbb{C}$ and ρ are directly coupled in Jacobs *et al*'s model. By describing remodeling through damage theory, they introduce a remodeling tensor H entering the definition of the remodeling stimulus. Hence, the remodeling law is derived from multi-surface plasticity theory, using criteria on the stimulus for resorption and formation as the boundaries of the dead zone.

The model originally developed by Di Carlo and collaborators[1] that we investigate here lies within the framework of generalized continuum mechanics. This approach relies on balance laws (Eq. (4)) obtained for all the variables through a generalized statement of the virtual power principle (Eq. (3)). A generalized dissipation principle is enforced (Eq. (10)) to obtain strict conditions on the admissible constitutive laws. This approach is essentially different from that of Doblaré and García, as they consider the remodeling tensor as an internal variable, whose evolution is represented by the damage tensor. The latter is associated to bone resorption and apposition, leading to the possibility of both increase and decrease of the damage. This feature, which is not considered in classical damage mechanics, opens the possibility for the mechanical dissipation to take negative values. Meanwhile, generalized continuum mechanics ensures the positivity of the dissipation as an intrinsic feature. In other words, in the present work, since our model derives from energetic considerations, the evolution of the fabric abides the laws of thermodynamics.

Moreover, differently from Jacobs *et al*' approach, we do not require the dissipation to be minimized but simply relate it to remodeling (by assuming a linear relationship with the remodeling rate, see Eq. (14)). Hence, no optimization is enforced: the minimization is here merely a result of the remodeling process since the dissipation–which takes positive values during the remodeling process–decreases to zero as the material remodels towards equilibrium.

Eventually, unlike the aforementioned models, we recall that our model does not require the microstructure to be aligned with the principal stress an strain directions at the remodeling equilibrium. This feature will be illustrated by means of numerical simulations in the Sec. 4.

3. Energetic characterization of the rotary remodeling equilibrium

3.1. *Extremal properties of the rotary remodeling equilibrium*

In the present section, we show that, when considering a rotation of the material axes around a fixed axis, equilibrium states are closely bound to the variations of the strain and complementary energy with respect to the rotation angle.

Let us consider a fixed orthonormal frame $\mathbf{e}_i$, with $i = 1 \dots 3$. We assume – for the sake of simplicity and without loss of generality – that the fixed rotation axis is $\mathbf{e}_3$ (see Appendix A in Sec. 6 for the general case of any fixed axis of the 3D space). In this situation, the rotation tensor R is parametrised by one scalar–the angle α describing the orientation of the material axes in the plane $(\mathbf{e}_1, \mathbf{e}_2)$. Thus, the strain energy density is a function of two variables: the small strain tensor E and the angle

α, reading: $\psi^{\mathsf{E}} : (\mathsf{E}, \alpha) \mapsto \psi^{\mathsf{E}}(\mathsf{E}, \alpha)$. Similarly, the complementary energy density is a function of the stress tensor S and of the angle α, reading: $\psi^{\mathsf{S}} : (\mathsf{S}, \alpha) \mapsto \psi^{\mathsf{S}}(\mathsf{S}, \alpha)$.

A sound criterion to detect the remodeling equilibrium can be expressed in terms of the partial derivative of the strain and complementary energy densities with respect to α. To this aim, let us first establish the following result which provides an explicit expression of the above derivatives:

Proposition 3.1. *The derivatives of the potential and complementary energy densities with respect to the rotation angle read:*

$$-\frac{\partial \psi^{\mathsf{E}}}{\partial \alpha} = \frac{\partial \psi^{\mathsf{S}}}{\partial \alpha} = 2\,(\mathsf{S}\,\mathsf{E}) : \mathsf{W}_{\mathsf{z}}\,. \tag{19}$$

Proof. Let R be a rotation around the axis $\mathbf{e}_3$ and $\mathbb{R} = \mathsf{R} \boxtimes \mathsf{R}$. We refer the reader to lemmas 7.1, 7.2 and 7.3 in Appendix B (Section 7) for keys to the demonstration.

In view of Eq. (5), the partial derivative of the strain energy density with respect to the rotation angle α reads:

$$\frac{\partial \psi^{\mathsf{E}}}{\partial \alpha} = \frac{1}{2}\frac{\partial \mathbb{C}}{\partial \alpha}(\mathsf{E}) : \mathsf{E} = \frac{1}{2}\frac{\partial}{\partial \alpha}\left(\mathbb{R}\mathbb{C}_0\mathbb{R}^{\mathsf{T}}\right)(\mathsf{E}) : \mathsf{E} \tag{20}$$

$$= \frac{1}{2}\left(\frac{\partial \mathbb{R}}{\partial \alpha}\mathbb{C}_0\mathbb{R}^{\mathsf{T}} + \mathbb{R}\mathbb{C}_0\frac{\partial \mathbb{R}^{\mathsf{T}}}{\partial \alpha}\right)(\mathsf{E}) : \mathsf{E}\,. \tag{21}$$

We can now calculate separately the two terms of the sum appearing in this expression. The first term can be expressed as follows:

$$\begin{aligned}\frac{1}{2}\left(\frac{\partial \mathbb{R}}{\partial \alpha}\mathbb{C}_0\mathbb{R}^{\mathsf{T}}\right)(\mathsf{E}) : \mathsf{E} &= \frac{1}{2}\frac{\partial \mathbb{R}}{\partial \alpha}\left(\mathbb{C}_0\mathbb{R}^{\mathsf{T}}(\mathsf{E})\right) : \mathsf{E} \\ &= \mathsf{sym}\left(\mathsf{W}_{\mathsf{z}}\,\mathbb{R}\mathbb{C}_0\mathbb{R}^{\mathsf{T}}(\mathsf{E})\right) : \mathsf{E} \\ &= \mathsf{W}_{\mathsf{z}}\,\mathsf{S} : \mathsf{E} \\ &= \mathsf{S}\,\mathsf{E} : \mathsf{W}_{\mathsf{z}}^{\mathsf{T}} \\ &= -\mathsf{S}\,\mathsf{E} : \mathsf{W}_{\mathsf{z}}\,,\end{aligned} \tag{22}$$

where, in the second equality, we made use of Lemma 7.2. The second term of the sum in Eq. (21) can be expressed as follows:

$$\begin{aligned}\frac{1}{2}\left(\mathbb{R}\mathbb{C}_0\frac{\partial \mathbb{R}}{\partial \alpha}\right)(\mathsf{E}) : \mathsf{E} &= \frac{1}{2}\mathbb{R}\mathbb{C}_0\left(\frac{\partial \mathbb{R}}{\partial \alpha}(\mathsf{E})\right) : \mathsf{E} \\ &= \mathbb{R}\mathbb{C}_0\left(\mathsf{W}_{\mathsf{z}}^{\mathsf{T}}\,\mathbb{R}^{\mathsf{T}}(\mathsf{E})\right) : \mathsf{E} \\ &= \mathbb{R}\mathbb{C}_0\mathbb{R}^{\mathsf{T}}\left(\mathsf{W}_{\mathsf{z}}^{\mathsf{T}}\,\mathsf{E}\right) : \mathsf{E} \\ &= \mathsf{W}_{\mathsf{z}}^{\mathsf{T}}\,\mathsf{E} : \mathsf{S} \\ &= \mathsf{E}\,\mathsf{S} : \mathsf{W}_{\mathsf{z}}\end{aligned} \tag{23}$$

where, in the second and third equality, we made use of Lemmas 7.3 and 7.1, respectively.

Finally, combining the results of Eqs. (22-23) and recalling that $\mathsf{W_z}$ is skew-symmetric, we obtain:

$$\frac{\partial \psi^{\mathsf{E}}}{\partial \alpha} = -(\mathsf{S\,E} - \mathsf{E\,S}) : \mathsf{W_z} = -2\,\mathsf{skw}(\mathsf{S\,E}) : \mathsf{W_z} = -2\,(\mathsf{S\,E}) : \mathsf{W_z}\,. \tag{24}$$

Note that, in this expression, the stress S is meant to be calculated from the strain E as $\mathsf{S} = \mathbb{C}(\mathsf{E}) = \mathbb{R}\mathbb{C}_0\mathbb{R}^{\mathsf{T}}(\mathsf{E})$.

An equivalent result can be obtained in terms of the complementary energy Ψ^{S}. Let us assume $\Psi^{\mathsf{S}} = \int_{\mathcal{B}} \psi^{\mathsf{S}}$ and postulate the bulk density ψ^{S} as a quadratic form of the stress tensor S:

$$\psi^{\mathsf{S}} = \frac{1}{2}\,\mathbb{C}^{-1}(\mathsf{S}) : \mathsf{S}\,, \tag{25}$$

where $\mathbb{C}^{-1}$ is the 4th-order compliance tensor. Hence, using a similar rationale to the one leading to Eq. (24), we eventually obtain:

$$\frac{\partial \psi^{\mathsf{S}}}{\partial \alpha} = 2\,(\mathsf{S\,E}) : \mathsf{W_z}\,, \tag{26}$$

where the strain E is meant to be calculated from the stress S as $\mathsf{E} = \mathbb{C}^{-1}(\mathsf{S}) = \mathbb{R}\mathbb{C}_0^{-1}\mathbb{R}^{\mathsf{T}}(\mathsf{S})$.

Finally, Eq. (19) readily follows from Eq. (24) and Eq. (26). □

Corollary 3.1. ***Characterization of the rotary remodeling equilibrium***

The rotary remodeling equilibrium is characterized by the following extremal conditions:

$$\frac{\partial \psi^{\mathsf{E}}}{\partial \alpha} = 0 \quad \Leftrightarrow \quad \frac{\partial \psi^{\mathsf{S}}}{\partial \alpha} = 0 \quad \Leftrightarrow \quad [\mathsf{S},\mathsf{E}]|_{\mathcal{P}_{\mathbf{e}_3^\perp}} = 0\,, \tag{27}$$

where, in the last equality, the commutator $[\mathsf{S},\mathsf{E}]$ *is restricted to* $\mathcal{P}_{\mathbf{e}_3^\perp}$ *– the plane orthogonal to the rotation axis* $\mathbf{e}_3$*.*

Proof. The criterion for remodeling equilibrium given in Eq. (27) readily follows from Eq. (19) by noting that $2\,(\mathsf{S\,E}) : \mathsf{W_z} = 2\,\mathsf{skw}(\mathsf{S\,E}) : \mathsf{W_z} = [\mathsf{S},\mathsf{E}] : \mathsf{W_z}$ and that, in this inner product, only the restriction of $[\mathsf{S},\mathsf{E}]$ to the plane $\mathcal{P}_{\mathbf{e}_3^\perp}$ matters. □

It is worth noting that a classical mechanical result is recovered in the above characterization, namely that (remodeling) equilibrium states correspond to (partial) extrema of the strain and complementary energy.

3.2. *Stability of equilibrium states*

The stability of the equilibrium states identified in Sec. 3.1 can be assessed by observing the evolution of the material axes close to these states. As in Sec. 3.1, let us assume that the material axes can rotate around the direction $\mathbf{e}_3$ and call α their current orientation. An orientation α^{SE} will be said to correspond to a stable

equilibrium (SE) configuration if it is a local attractor–*i.e.*, if the material axes will tend to align as per α^{SE} when they are oriented as per α close to α^{SE}.

The goal of this section is to characterize these stable equilibrium states using an energetic argument. Let us first consider the following proposition:

Lemma 3.1. *For a given strain* E*, the derivative of the potential energy is proportional to the rotation rate:*

$$\frac{\partial \psi^{\mathsf{E}}}{\partial \alpha} = -2\, d_0\, \dot{\alpha} \tag{28}$$

Proof. Recall from Proposition 3.1 that:

$$\frac{\partial \psi^{\mathsf{E}}}{\partial \alpha} = -2(\mathsf{S}\,\mathsf{E}) : \mathsf{W}_{\mathsf{z}} = -[\mathsf{S}, \mathsf{E}] : \mathsf{W}_{\mathsf{z}}\,, \tag{29}$$

The remodeling law given in Eq. (18) provides:

$$\frac{\partial \psi^{\mathsf{E}}}{\partial \alpha} = -\mathbb{D}_0\,(\dot{\mathsf{R}}\,\mathsf{R}^{\mathsf{T}}) : \mathsf{W}_{\mathsf{z}}\,.$$

Noting that $\dot{\mathsf{R}}\,\mathsf{R}^{\mathsf{T}} = \dot{\alpha}\,\mathsf{W}_{\mathsf{z}}$, only one coefficient of $\mathbb{D}_0$ matters in the above scalar product, namely d_{zz}. Renaming this coefficient d_0, Eq. (28) is readily obtained. □

For a given strain E, the values taken by the strain energy and its derivatives depend on the orientation of the microstructure, *i.e.* the angle α. This allows us to express the stability of an equilibrium state in terms of convexity of the strain energy with respect to α. Let us first introduce the following proposition:

Proposition 3.2. *An orientation* α^{SE} *corresponds to a stable equilibrium configuration if and only if*

$$\frac{\partial^2 \psi^{\mathsf{E}}}{\partial \alpha^2}(\alpha^{\mathrm{SE}}) > 0\,. \tag{31}$$

Proof. For a given strain E, let us introduce the function $\rho = \alpha \mapsto \rho(\alpha) = -[\mathsf{S}(\mathsf{E}, \alpha), \mathsf{E}] : \mathsf{W}_{\mathsf{z}}$. Thus, Eq. (19) can be rewritten as:

$$\frac{\partial \psi^{\mathsf{E}}}{\partial \alpha} = \rho\,. \tag{32}$$

It is worth noting that the rotary equilibrium configurations correspond to the roots of ρ since this latter is noting but the rotation rate, but a negative coefficient–see Eq. (28). In view of Lemma 3.1, the following identity holds at any time t:

$$\rho(\alpha(t)) = -2\, d_0\, \dot{\alpha}(t)\,. \tag{33}$$

Let us assume that α^{SE} corresponds to a stable equilibrium configuration for the material. Thus, if the orientation α of the material axes is slightly shifted from α^{SE}, the material axes will rotate towards α^{SE}. In particular, if $\alpha < \alpha^{\mathrm{SE}}$, α will

increase toward α^{SE} and then $\dot{\alpha} > 0 \equiv \rho(\alpha) < 0$. Conversely, if $\alpha > \alpha^{\mathrm{SE}}$, α will decrease toward α^{SE} and then $\dot{\alpha} < 0 \equiv \rho(\alpha) > 0$. Provided that the function ρ is regular enough, this implies that:

$$\frac{\partial \rho}{\partial \alpha}(\alpha^{\mathrm{SE}}) > 0 \tag{34}$$

and therefore Eq. (31) holds true.

On the other way around, Eq. (31) implies, on the one hand, that $\rho(\alpha) < 0$ and thus $\dot{\alpha} > 0$ if $\alpha < \alpha^{\mathrm{SE}}$; and, on the other hand, that $\rho(\alpha) > 0$ and thus $\dot{\alpha} < 0$ if $\alpha > \alpha^{\mathrm{SE}}$. (In both cases, α is assumed to lie in a neighborhood of α^{SE}.) In turn, this implies the stability of α^{SE}. □

Proposition 3.2 and Eq. (19) allow us to deduce the following result:

Proposition 3.3. *An orientation α corresponds to a stable equilibrium configuration if and only if*

$$\frac{\partial^2 \psi^{\mathsf{S}}}{\partial \alpha^2}(\alpha) < 0\,. \tag{35}$$

Thus, in view of Propositions 3.2 and 3.3, it is possible to state the following key characterization:

Corollary 3.2. ***Characterization of stable rotary remodeling states***

α^{SE} stable equilibrium $\Leftrightarrow$ local minimum of $\alpha \mapsto \psi^{\mathsf{E}}$ $\Leftrightarrow$ local maximum of $\alpha \mapsto \psi^{\mathsf{S}}$

As a conclusion, we retrieve another classical result from mechanics, which is that stable equilibrium states correspond to minima of the potential energy and to maxima of the complementary energy.

4. Numerical assessment of the influence of loading conditions and material properties on the remodeling

Numerical simulations were performed to study the response of the model and the remodeling equilibrium states with respect to different loading conditions and for different elastic moduli. Without lack of generality, we assume hereinafter that the material axes rotate around the axis $\mathbf{e}_3$. Therefore, the problem will be studied in the 2D plane $(\mathbf{e}_1, \mathbf{e}_2)$.

As in DiCarlo *et al*[1], the material is assumed to be transversely isotropic, the axis $\mathbf{e}_1$ being orthogonal to the isotropy plane. The relevant elastic moduli, adapted from [61], are summarized in Table 1 with the Kelvin notation. Three types of materials are considered in this study, characterized by high (A), mild (B), and low (C) values of the shear modulus C_{66}.

In the following sections, we first analyze the application of a uniaxial stress in the $\mathbf{e}_1$ direction: we depict the variations of the strain energy with respect to the

Table 1. Two-dimensional material elastic properties (compressed Kelvin notation).

Material type	C_{11}	C_{22}	C_{12}	C_{16}	C_{26}	C_{66}	d_0
A						20 GPa	
B	30 GPa	20.85 GPa	11.49 GPa	0 GPa	0 GPa	13.2 GPa	555 kPa.day
C						2 GPa	

material orientation and show how its evolution can lead to different equilibrium states when changing the initial orientation or material properties. Furthermore, we discuss the dependency on material properties and loading conditions thanks to analytical and numerical considerations.

4.1. *Equilibrium states and energy*

Numerical simulations were performed to investigate the rotary remodeling of the material in uniaxial, i.e. stress/strain conditions. Fig. 2 shows the results obtained by applying either a uniaxial strain (subplots (a,b,c)) $\mathsf{E} = E_{11}\mathsf{e}_1 \otimes \mathsf{e}_1$ or stress (subplots (d,e,f)) $\mathsf{S} = S_{11}\mathsf{e}_1 \otimes \mathsf{e}_1$ and for material types A (high shear modulus, subplots (a,d)), B (mild shear modulus, subplots (b,e)) and C (low shear modulus, subplots (c,f)), see Table 1. The function ρ (solid blue lines), the strain energy (brown dotted lines) and the complementary energy (dark green dotted lines) are plotted versus the angle α describing the orientation of the material axes in the plane $(\mathbf{e}_1, \mathbf{e}_2)$. As expected, the roots of the function ρ –*i.e.*, the remodeling equilibrium states of the material– correspond to extrema of the potential (a,b,c) and complementary (d,e,f) energy. Stable roots (green knots) are attained where the potential energy reaches a local minimum (a,b,c) and the complementary energy reaches a local maximum (d,e,f). Conversely, unstable roots (red knots) correspond to local maxima of the potential energy (a,b,c) and local minima of the complementary energy (d,e,f).

Numerical simulations were also performed to investigate the evolution of the strain and complementary energy during remodeling. The effects of the initial orientation (α_0) of the material axes were investigated in uniaxial strain conditions. Whatever the initial orientation of the material axes, the system underwent rotary remodeling until achieving a stable equilibrium configuration. In agreement with the theoretical results, these stable remodeling equilibrium states were found to correspond to minima of the strain energy. Results of these simulations are shown in Fig. 3 where are plotted the time courses of the strain energy for material types A (subplot (a)) and C (subplot (b)) and for different initial orientations of the material axes (uniaxial strain).

For the material type A, characterized by a high shear modulus, two stable equilibrium states are observed: one corresponds to an alignment of the material axes with the loading direction ($\alpha^{\mathrm{SE}} = 0$), and the other corresponds to a rotation towards the normal to that direction ($\alpha^{\mathrm{SE}} = \frac{\pi}{2}$). The unstable equilibrium states observed in Fig. 2(a) do not appear in this plot. For the material type C,

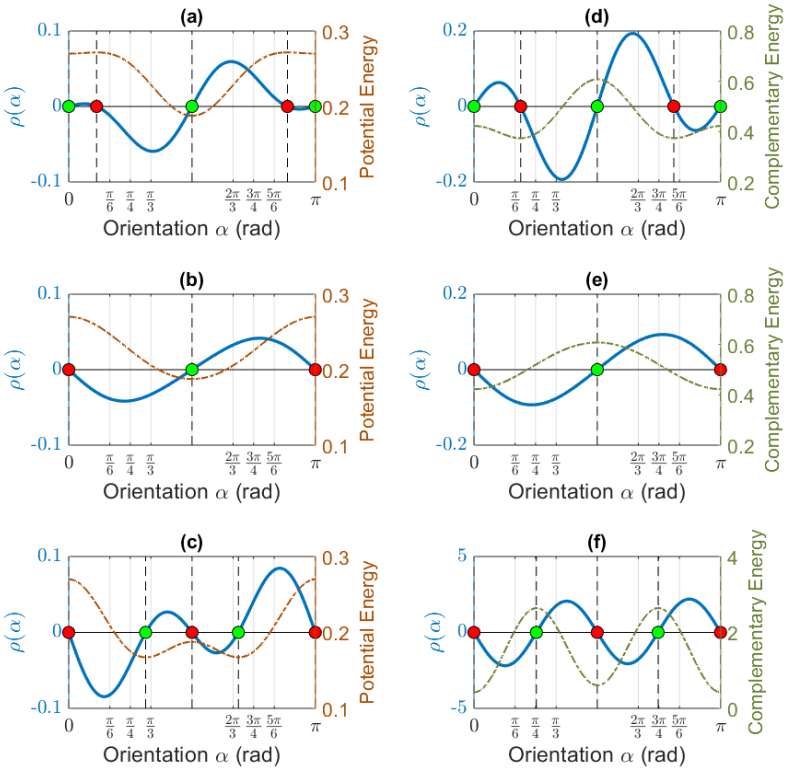

Fig. 2. Rotary remodeling in uniaxial strain/stress conditions: functions ρ (solid blue lines), strain energy ψ^{E}(brown dotted lines) and complementary energy ψ^{S} (dark green dotted lines) versus the angle α describing the orientation of material axes in the plane $(\mathbf{e}_1, \mathbf{e}_2)$. Subplots (a,b,c) refer to uniaxial strain in the $\mathbf{e}_1$ direction ($E_{11} = 3000\mu\epsilon$) and material types A (a), B (b) and C (c). Subplots (d,e,f) refer to uniaxial stress in the $\mathbf{e}_1$ direction ($S_{11} = 100$MPa) and material types A (d), B (e) and C (f). Stable and unstable equilibrium points are depicted by green and red knots, respectively.

characterized by a low shear modulus, three equilibrium states are found in Fig. 3, corresponding to stable and unstable states observed in Fig. 2(c). One can note that $\alpha = 0$ and $\alpha = \frac{\pi}{2}$ are not stable and are attained only by assigning either of these values as initial condition for α_0. For any other initial orientation of the material axes, the strain energy would tend to another–stable–equilibrium state.

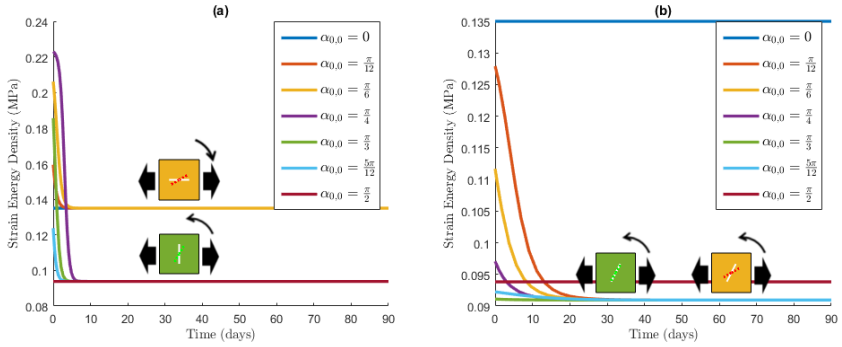

Fig. 3. Evolution of the strain energy of a 2D body under uniform uniaxial strain, with varying initial states $\{\alpha_0 = k\frac{\pi}{12}, k \in \{0,1,2,3,4,5,6\}\}$. (a) Material A (high shear modulus); (b) Material C (low shear modulus)

4.2. *Influence of material properties and loading conditions*

This section is devoted to present and discuss the effects of the material properties and of different loading conditions on the remodeling equilibrium states. As a direct application of Corollaries 3.1 and 3.2, the existence and the stability of equilibrium configurations is assessed searching for the roots of the function ρ (Eq. (32)) and studying the sign of its derivative around the roots.

4.2.1. *On the alignment of the microstructure with principal stresses*

Let us assume our medium to subjected to a uniaxial stress $\mathsf{S} = S_{11}\mathsf{e}_1 \otimes \mathsf{e}_1$ and the stiffest direction to be initially oriented along the stress axis $\mathbf{e}_1$ ($\alpha_0 = 0$). Hence, we investigated the relationships between the elastic coefficients of the material and the stability of this configuration.

In this context, the function ρ reads:

$$\rho(\alpha) = -\frac{\partial \psi^{\mathsf{S}}}{\partial \alpha}(\alpha) = \frac{S_{11}^2}{\mathsf{det}\mathbb{C}_0}\left(f_1(\mathbb{C}_0)\,\sin 2\alpha + \frac{f_2(\mathbb{C}_0)}{2}\,\sin 4\alpha\right), \tag{36}$$

where f_1 and f_2 are functions of $\mathbb{C}_0$ and $\mathsf{det}\mathbb{C}_0$ is the determinant of the stiffness tensor (explicit expressions are provided in the Appendix C in Sec. 8). Hence, since $\rho(0) = 0$, we find–in line with Cowin[17]–that the alignment of the material axes with the stress principal direction correspond to a remodeling equilibrium state. However, this configuration is not necessarily stable and the material does not necessarily tend to realign with the stress direction after a perturbation. In order for $\alpha = 0$ to be a stable equilibrium state, the derivative of ρ has to be positive. In the present scope,

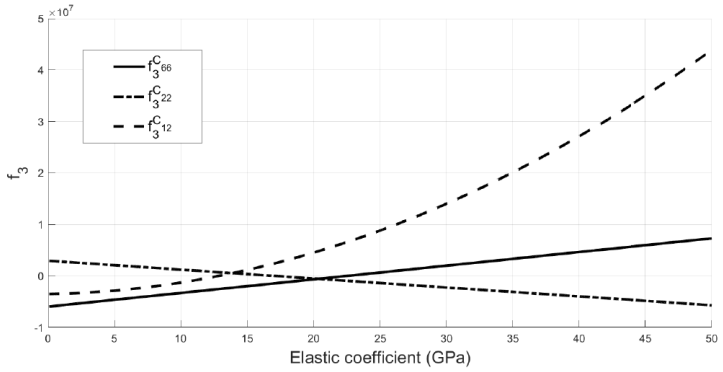

Fig. 4. Variations of the function f_3 as a function of C_{66}, C_{22} and C_{12}, where the reference material properties are type A (Table 1, high shear modulus).

this condition reads:

$$\frac{\partial \rho}{\partial \alpha}(0) = \frac{S_{11}^2}{\det \mathbb{C}_0} f_3(\mathbb{C}_0) > 0\,, \tag{37}$$

where f_3 is a function of $\mathbb{C}_0$ (its explicit expression is provided in the Appendix C in Sec. 8).

Fig. 4 shows the evolution of the function f_3 by varying one elastic coefficient at once and fixing the other elastic moduli to the values of material A in Table 1. The orientation $\alpha = 0$, aligned with principle stresses, is a stable equilibrium only if the function f_3 stays positive. This is not the case if the transverse modulus C_{22} is too high (transverse direction takes over; dash-dotted line in Fig. 4), or either of moduli C_{66} (shear; solid line) or C_{12} (axial coupling; dashed line) is too low. Hence, we find here a strong dependency of the stability of the configuration $\alpha = 0$ on the material properties.

4.2.2. *Numerical identification of equilibrium states*

Expanding the analysis of the previous section, we investigated the effects of the loading conditions and of the shear modulus on the remodeling equilibrium states. Let us assume the material axes to be initially oriented along the axis $\mathbf{e}_1$, *i.e.* $\alpha_0 = 0$. It was shown in the previous section that this is either a stable or an unstable remodeling equilibrium configuration in uniaxial loading conditions. It is interesting to study the response of the material and the new remodeling equilibrium configuration–*i.e.* the closest stable equilibrium state to 0–that it would reach due to a change of the loading conditions. For the sake of simplicity, only two types of loading conditions, namely biaxial plane stress and combined axial/shear plane

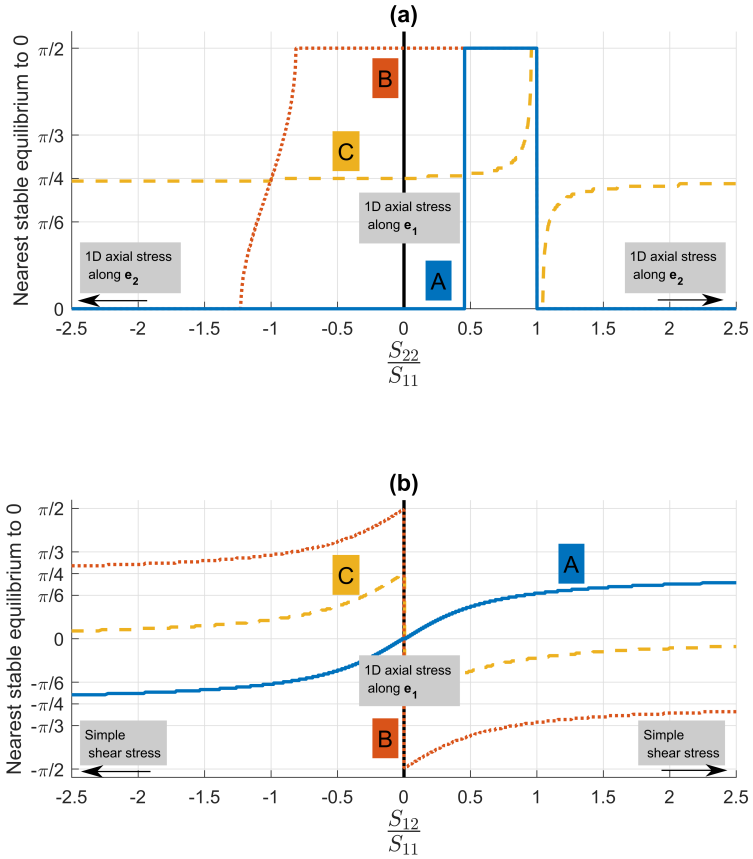

Fig. 5. Closest stable equilibrium states to initial configuration $\alpha_0 = 0$, for varying (a) transverse/longitudinal stress ratio $\frac{S_{22}}{S_{11}}$ ($S_{12} = 0$) and (b) shear/longitudinal stress ratio $\frac{S_{12}}{S_{11}}$ ($S_{22} = 0$). The three curves account for the 3 material types in Table 1characterized by high (A, solid blue lines), mild (B, dotted dark-red lines), and low (C, dashed orange lines) shear moduli.

stress in the plane $(\mathbf{e}_1, \mathbf{e}_2)$, and the three material types in Table 1 are considered here. Results of this study are shown in Fig. 5, where the effects of the two loading conditions are investigated independently, and in Fig. 6, which refers to a general 2D stress state.

In the case of longitudinal axial loading ($S_{11} = 1$ MPa, $S_{12} = 0, S_{22} = 0$), both

Fig. 5.a and 5.b indicate that $\alpha = 0$ is a stable state only for high shear moduli (material type A). For lower shear moduli (material properties B,C), the material remodels by rotating its axes toward an orientation $\alpha^{\mathrm{SE}} \in [\frac{\pi}{4}, \frac{\pi}{2}]$. These results confirm what has been observed in Fig. 2.

On the one hand, when only shear and longitudinal stress are to account for ($S_{22} = 0$, Fig. 5 (b)), the function ρ reads:

$$\rho(\alpha) = (S_{11}\sin 2\alpha - S_{12}\cos 2\alpha)\,(f_1(\mathbb{C}_0)S_{11} + f_2(\mathbb{C}_0)(S_{11}\cos 2\alpha + S_{12}\sin 2\alpha)) \quad (38)$$

Hence, the addition of shear necessarily leads to a change in the principal stress directions and therefore shifts the equilibrium state ($\rho(\alpha) = 0$), as suggested by Pedersen[33]. This result can be visualized in Fig. 5 (b): the closest stable equilibrium to $\alpha = 0$ is never 0, except if, as shown in Fig. 6, the addition of a transverse axial stress compensates this effect. Moreover, as one could predict, there is a central symmetry around $\{S_{12} = 0, \alpha = 0\}$ as the equilibrium state is symmetrical with respect to $S_{12} = 0$: $\alpha^{\mathrm{SE}}_{right} = -\alpha^{\mathrm{SE}}_{left}$.

On the other hand, for a configuration involving both longitudinal and transverse axial stress but no shear stress ($S_{12} = 0$, Fig. 5 (a)), the dependency of ρ on the material properties is more complex. In this case, very high values of the ratio $\frac{S_{22}}{S_{11}}$ depict a loading configuration similar to a simple traction or compression along the transverse axis (negligible longitudinal loading and no shear loading). In that configuration, $\alpha = 0$ is a stable equilibrium for high and mild shear moduli (material types A and B), and $\alpha^{\mathrm{SE}} \in [0, \frac{\pi}{4}[$ for low shear moduli (material type C).

Fig. 6 displays three 3D plots giving the closest stable equilibrium states to 0 as a function of both S_{12} and S_{22} for the 3 material types (A, B, C) in Table 1. The lines depicted in Fig. 5 are superimposed on the surfaces using the same line colors and styles. These results underline the complexity of the coupling between the loading components in how they affect remodeling. Moreover, it is apparent that the material response strongly depends on the value of the shear modulus (subplot (a): material A, high shear modulus; (b): material B, mild shear modulus; (c): material C, low shear modulus). Recalling that $\alpha = 0$ corresponds to a configuration where the material axes are aligned with the longitudinal stress, it can be noticed that the latter (described by the white areas of the surfaces) is a stable remodeling equilibrium state only in very special conditions depending on both the loading conditions and the material properties.

4.3. *Mixed boundary conditions*

Because *in vivo* loading conditions are complex, living tissue is subjected to mixed boundary conditions and an inhomogeneous stress/strain state. Hence, the evolution of the system is more complex and the local minimization and maximization principles derived in Section 3 do not apply any more.

In order to describe the adaptation of bone in a complex loading configuration, we coupled the remodeling law (Eq. (17)) to a finite element analysis, using Com-

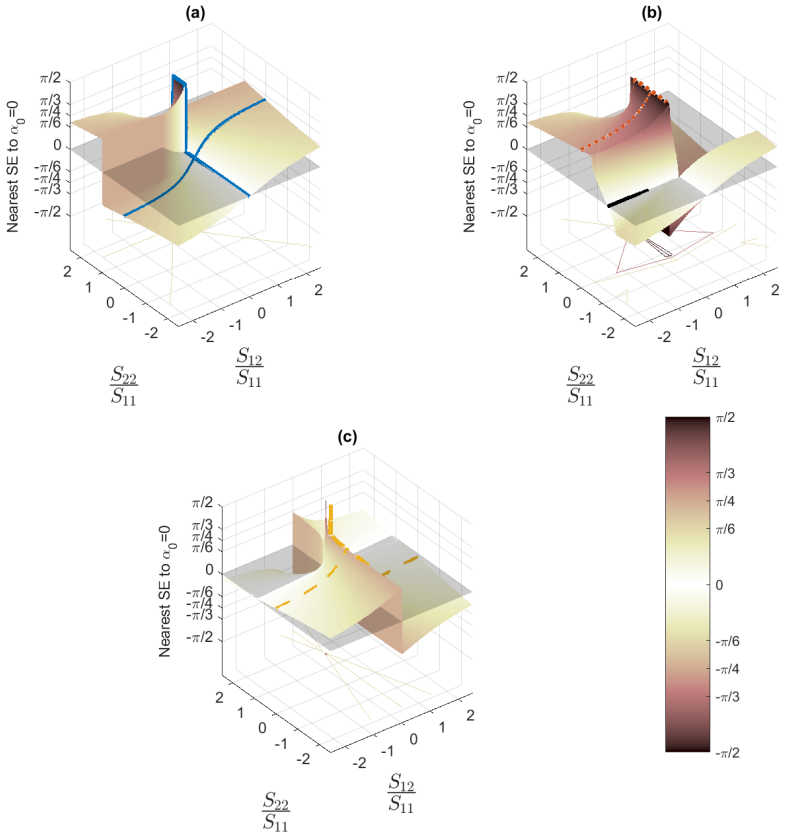

Fig. 6. Closest stable equilibrium states to the initial configuration $\alpha_0 = 0$ as a function of transverse/longitudinal stress ratio $\frac{S_{22}}{S_{11}}$ and shear/longitudinal stress ratio $\frac{S_{12}}{S_{11}}$. The three plots (a,b,c) account for the 3 material types (A, B, C) in Table 1, respectively. Bold lines superimposed to the surfaces represent the lines in Fig. 5.

sol with Matlab v5.3a. We subjected the 2D structure displayed in Fig. 7, a toy model of a human proximal femur, to loading and boundary conditions approximating *in vivo* conditions, as per Beaupré *et al*[62]. The cortical tissue (plain black) was assumed isotropic with a Young's modulus $E_c = 14$ GPa and a Poisson's ratio $\nu_c = 0.3$. Trabecular bone was assumed to be transversely isotropic and undergoing rotary remodeling, with $C_{11} = 2.50$ GPa, $C_{22} = 1.42$ GPa, $C_{12} = 636$ MPa and $C_{66} = 1.20$ GPa. Figure 7 describes the evolution of the micro-orientation in the

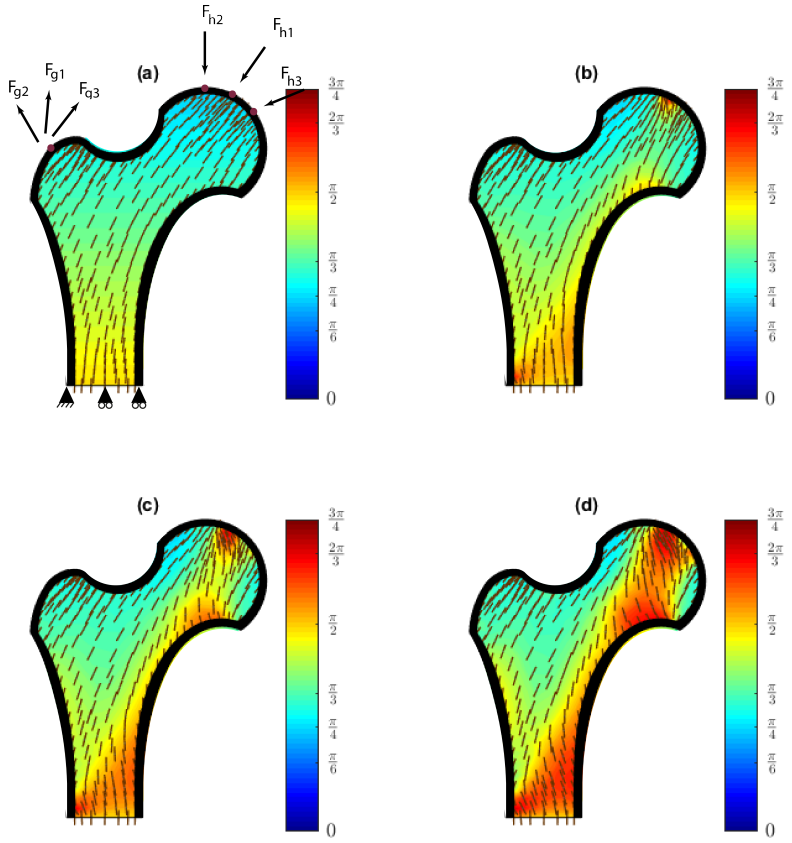

Fig. 7. Evolution of the strain energy and micro-orientation during remodeling in a 2D toy model of the proximal femur: micro-orientation (brown sticks, and color map (rad)) at the start of the simulation, with loading and boundary conditions (a), after 500 (b), 1000 (c) and 2000 (d) time increments (arbitrary time scale).

proximal femur. An arbitrary, yet reasonable initial micro-orientation field was assigned (see Fig. 7(a)). Starting from this configuration, material remodeling changes the microstructural alignment in response to the loading conditions. Despite its simplicity, the model provides a reasonable distribution of the micro-orientation after remodeling.

5. Conclusions

In this paper, we described a thermodynamically consistent model for orthotropic bone remodeling and showed its ability to describe the evolution of material axes in 2D. In particular, we demonstrated that the remodeling response of the material is highly dependent on its material properties and on the loading conditions.

In the present study, we demonstrated that the model retrieves classical energy theorems. In particular, stable remodeling equilibrium states have been shown to correspond to local minima of the strain energy (in strain-controlled loading conditions) and maxima of the complementary energy (in stress-controlled boundary conditions). The authors stress the importance of the local aspect of the energy theorems demonstrated in Section 3: the energetic theorems demonstrated previously are valid *solely* in the case of homogeneous and stationary stresses or strains. Indeed, in uniform strain conditions, the stress experienced by the material evolves in time with the reorientation of the material axes but the strain stays stationary. Conversely, in uniform stress conditions, the strain evolves in time but the stress stays stationary. If mixed boundary conditions are applied (as, for example, in boundary value problems where both displacements and stress may be applied on the boundary of the system), the evolution of the system is more complex as the environment surrounding a point is constantly evolving. Furthermore, typically, neither the strain nor the stress are stationary: the evolution of the strain energy is therefore more complex and no energetic theorems have been obtained so far for general boundary conditions.

The model delivered sound results on the influence of material properties and boundary conditions.

First, we have shown that the mathematical condition for remodeling equilibrium described by Cowin[17] – *i.e.* the alignment of principal stress, principal strain and material directions – is attained only in special cases, namely for sufficiently high values of the shear modulus. Otherwise, only the first part of this statement holds true but the material axes do not necessarily align with the principal stress and strain directions at the remodeling equilibrium. Second, we have highlighted the strong effects of the mechanical environment and of the material properties on remodeling equilibrium. On the one hand, the addition of shear or transverse stress strongly modifies the remodeling equilibrium configuration. On the other hand, the material properties themselves play a role in the achievement of the equilibrium as the alignment of stresses and strains merely ensure to have reached an equilibrium but not whether it is stable or not.

The formulation of a thermodynamically-driven process has the potential to model complex processes, like bone remodeling, which involve mechanical as well as biochemical regulations. Furthermore, the constant evolution of living tissue implies that remodeling equilibrium is a global point of view as homeostasis remains a dynamic state.

Acknowledgments

This project has received funding from the European Research Council (ERC) under the European Union's Horizon 2020 research and innovation program (grant agreement No 682001, project ERC Consolidator Grant 2015 BoneImplant).

6. Appendix A: From a rotation around the Z-axis to a rotation around any fixed axis in the 3D space

Corollary 6.1. Generalization of Proposition 19 to any fixed axis of the 3D space.

Proposition 19 can be extended to the case of any fixed axis $\mathbf{u}$ *in the 3D space as follows:*

$$\frac{\partial \psi^{\mathsf{E}}}{\partial \alpha} = 2(\mathsf{E_P}.\mathsf{S_P}) : (\mathsf{W_z}), \tag{39}$$

where P *is the (unique) rotation that transforms* $\mathbf{u}$ *into* $\mathbf{e}_3$ *and* $\mathsf{E_P} = \mathsf{PEP}^{\mathsf{T}}$, $\mathsf{S_P} = \mathsf{PSP}^{\mathsf{T}}$ *and* $\mathcal{P}_{\mathbf{u}} = Vect(\mathbf{u} \otimes \mathbf{u})^{\perp}$, *leading to the criterion for equilibrium:*

$$\frac{\partial \psi^{\mathsf{E}}}{\partial \alpha} = 0 \Leftrightarrow [\mathsf{S_P}, \mathsf{E_P}]|_{\mathcal{P}_{\mathbf{u}}} = 0. \tag{40}$$

Proof. We define here the (unique) rotation P that transforms $\mathbf{u}$ into $\mathbf{e}_3$.
This rotation defines a new frame $\mathcal{R}_{X'Y'Z'}$. Subsequently, we can determine the rotation R_0 around $\mathbf{e}_3$ such that $\mathsf{R}_0 = \mathsf{P}.\mathsf{R}.\mathsf{P}^{\mathsf{T}} = \mathbb{P}[\mathsf{R}]$ where $\mathbb{P} = \mathsf{P} \boxtimes \mathsf{P}$. Hence, we also have $\mathsf{R} = \mathbb{P}^{\mathsf{T}}\mathsf{R}_0$. The strain energy density reads:

$$\psi = \frac{1}{2}(\mathsf{S} : \mathsf{E}) = \frac{1}{2}\left(\mathbb{R}\mathbb{C}_0\mathbb{R}^{\mathsf{T}}\right)(\mathsf{E}) : \mathsf{E} \tag{41}$$

$$= \frac{1}{2}\left((\mathsf{P}^{\mathsf{T}}.\mathsf{R}_0.\mathsf{P}).(\mathbb{C}_0[(\mathsf{P}^{\mathsf{T}}.\mathsf{R}_0.\mathsf{P})^T.\mathsf{E}.(\mathsf{P}^{\mathsf{T}}.\mathsf{R}_0.\mathsf{P})].(\mathsf{P}^{\mathsf{T}}.\mathsf{R}_0.\mathsf{P})^T\right) : \mathsf{E} \tag{42}$$

$$= \frac{1}{2}\left(\mathbb{P}\mathbb{C}_0(\mathbb{P}^{\mathsf{T}}.(\mathsf{R}_0^{\mathsf{T}}.\mathbb{P}^{\mathsf{T}}(\mathsf{E}).\mathsf{R}_0))\right) : \left(\mathsf{R}_0^{\mathsf{T}}.\mathbb{P}(\mathsf{E}).\mathsf{R}_0\right) \tag{43}$$

We now define the fourth-order tensor $\mathbb{C}_{\mathsf{P}}$ accounting for the endomorphism $\widetilde{\mathbb{C}_{\mathsf{P}}}$ acting in the space of second-order tensors in the following manner: $\widetilde{\mathbb{C}_{\mathsf{P}}} = \mathsf{A} \mapsto \mathbb{P}\mathbb{C}_0(\mathbb{P}^{\mathsf{T}}\mathsf{A}) = \mathbb{P}\mathbb{C}_0\mathbb{P}^{\mathsf{T}}(A)$. The tensor $\mathbb{C}_{\mathsf{P}}$ naturally inherits from the symmetries of $\mathbb{C}_0$, and represents the stiffness matrix in the new frame $\mathcal{R}_{X'Y'Z'}$. In addition, we define the strain tensor in the rotated frame $\mathsf{E_P} = \mathbb{P}^{\mathsf{T}}\mathsf{E}$.

Consequently, we can write the strain energy density as follows:

$$\psi = \tfrac{1}{2}\mathbb{C}_{\mathsf{P}}(\mathbb{R}_0^{\mathsf{T}}\mathsf{E_P}) : (\mathbb{R}_0^{\mathsf{T}}\mathsf{E_P}) \tag{44}$$

As a result, finding the extrema of the strain energy is strictly equivalent to finding them for a material with elastic properties $\mathbb{C}_{\mathsf{P}}$ submitted to a strain $\mathsf{E_P}$.

Finally, for any fixed axis, the energy reaches an extremum (minimum or maximum) *if and only if* the restriction of product of the newly-defined rotated stress $\mathsf{S_P} = \mathbb{R}_0^{\mathsf{T}}\mathbb{C}_{\mathsf{P}}\mathbb{R}_0^{\mathsf{T}}\mathsf{E_P}$ and strain $\mathsf{E_P}$ principal axes to the plane $\mathcal{P}_{\mathbf{u}}$ is symmetric. □

7. Appendix B: Key properties of the rotation and elasticity tensors

We give here several key properties to ease the reading of the demonstrations in Section 3. Each of the following lemmas can be easily proven by simple algebraic calculations.

Lemma 7.1. Properties of the rotations.

$$\begin{aligned}
\mathsf{R}\,\mathsf{W}_\mathsf{z} &= \mathsf{W}_\mathsf{z}\,\mathsf{R}\,,\\
\mathbb{R}\,\mathsf{W}_\mathsf{z} &= \mathsf{W}_\mathsf{z}\,,\\
\mathbb{R}\,(\mathsf{W}_\mathsf{z}\,\mathsf{A}) &= \mathsf{W}_\mathsf{z}\,\mathbb{R}(\mathsf{A}) \quad \forall \mathsf{A}\in\mathsf{Lin}\,,\\
\mathbb{R}\,(\mathsf{A}\,\mathsf{W}_\mathsf{z}) &= \mathbb{R}(\mathsf{A})\,\mathsf{W}_\mathsf{z} \quad \forall \mathsf{A}\in\mathsf{Lin}\,.
\end{aligned}$$

Lemma 7.2. Properties of the derivatives of the rotation tensors.

$$\begin{aligned}
\tfrac{\partial \mathsf{R}}{\partial\alpha} &= \mathsf{R}\,\mathsf{W}_\mathsf{z} \;=\; \mathsf{W}_\mathsf{z}\,\mathsf{R}\,,\\
\tfrac{\partial \mathsf{R}^\mathsf{T}}{\partial\alpha} &= \mathsf{R}^\mathsf{T}\,\mathsf{W}_\mathsf{z}^\mathsf{T} \;=\; \mathsf{W}_\mathsf{z}^\mathsf{T}\,\mathsf{R}^\mathsf{T}\,,\\
\tfrac{\partial \mathbb{R}}{\partial\alpha} &= \tfrac{\partial}{\partial\alpha}(\mathsf{R}\boxtimes\mathsf{R}) \;=\; (\mathsf{W}_\mathsf{z}\,\mathsf{R})\boxtimes\mathsf{R} + \mathsf{R}\boxtimes(\mathsf{W}_\mathsf{z}\,\mathsf{R})\,,\\
\tfrac{\partial \mathbb{R}^\mathsf{T}}{\partial\alpha} &= \tfrac{\partial}{\partial\alpha}(\mathsf{R}^\mathsf{T}\boxtimes\mathsf{R}^\mathsf{T}) \;=\; \left(\mathsf{W}_\mathsf{z}^\mathsf{T}\,\mathsf{R}^\mathsf{T}\right)\boxtimes\mathsf{R}^\mathsf{T} + \mathsf{R}^\mathsf{T}\boxtimes\left(\mathsf{W}_\mathsf{z}^\mathsf{T}\,\mathsf{R}^\mathsf{T}\right)\,,\\
\tfrac{\partial \mathbb{R}}{\partial\alpha}(\mathsf{A}) &= 2\,\mathsf{sym}\,(\mathsf{W}_\mathsf{z}\,\mathbb{R}(\mathsf{A})) \quad \forall \mathsf{A}\in\mathsf{Sym}\,,\\
\tfrac{\partial \mathbb{R}^\mathsf{T}}{\partial\alpha}(\mathsf{A}) &= 2\,\mathsf{sym}\left(\mathsf{W}_\mathsf{z}^\mathsf{T}\,\mathbb{R}^\mathsf{T}(\mathsf{A})\right) \quad \forall \mathsf{A}\in\mathsf{Sym}\,.
\end{aligned}$$

Lemma 7.3. Properties of the elasticity tensor.

$$\begin{aligned}
\mathbb{C}\left(\tfrac{\partial \mathbb{R}}{\partial\alpha}(\mathsf{A})\right) &= 2\,\mathbb{C}\,(\mathsf{W}_\mathsf{z}\,\mathbb{R}(\mathsf{A})) \quad \forall \mathsf{A}\in\mathsf{Lin}\,,\\
\mathbb{C}\left(\tfrac{\partial \mathbb{R}^\mathsf{T}}{\partial\alpha}(\mathsf{A})\right) &= 2\,\mathbb{C}\left(\mathsf{W}_\mathsf{z}^\mathsf{T}\,\mathbb{R}^\mathsf{T}(\mathsf{A})\right) \quad \forall \mathsf{A}\in\mathsf{Lin}\,.
\end{aligned}$$

8. Appendix C: Explicit expressions of the function ρ and of its derivative

Assuming to apply a uniaxial tensile stress $\mathsf{S} = S_{11}\mathsf{e}_1\otimes\mathsf{e}_1$, the expression of ρ reads (Eq. (36)):

$$\rho(\alpha) = \frac{S_{11}^2}{\mathsf{det}\mathbb{C}_0}\left(f_1(\mathbb{C}_0)\,\sin 2\alpha + \frac{f_2(\mathbb{C}_0)}{2}\,\sin 4\alpha\right)\,,$$

where

$$\begin{aligned}
f_1(\mathbb{C}_0) &= C_{44}C_{55}C_{66}\left(C_{13}^2 - C_{23}^2 - C_{11}C_{33} + C_{22}C_{33}\right)\,,\\
f_2(\mathbb{C}_0) &= C_{44}C_{55}(2\sqrt{2}C_{11}C_{23}^2 + 2\sqrt{2}C_{12}^2C_{33} - 2\sqrt{2}C_{11}C_{22}C_{33} + C_{13}^2(2\sqrt{2}C_{22} - C_{66})\\
&\quad - C_{23}^2C_{66} + C_{11}C_{33}C_{66} + 2C_{12}C_{33}C_{66} + C_{22}C_{33}C_{66}\\
&\quad - C_{13}C_{23}(2\sqrt{2}C_{12} + C_{66}))\,,\\
\mathsf{det}\mathbb{C}_0 &= C_{44}C_{55}C_{66}\left(C_{13}^2C_{22} - 2C_{12}C_{13}C_{23} + C_{12}^2C_{33} + C_{11}(C_{23}^2 - C_{22}C_{33})\right)\,.
\end{aligned}$$

In the above expression, C_{ij} represent the coefficients of $\mathbb{C}_0$ in the Kelvin notation.

The derivative of ρ reads:

$$\frac{\partial \rho}{\partial \alpha} = \frac{2\, S_{11}^2}{\mathsf{det}\mathbb{C}_0}\ (f_1(\mathbb{C}_0)\ \cos 2\alpha + f_2(\mathbb{C}_0)\ \cos 4\alpha)\ .$$

In particular:

$$\frac{\partial \rho}{\partial \alpha}(0) = \frac{2\, S_{11}^2}{\mathsf{det}\mathbb{C}_0}\ (f_1(\mathbb{C}_0) + f_2(\mathbb{C}_0)) = \frac{2\, S_{11}^2}{\mathsf{det}\mathbb{C}_0}\, f_3(\mathbb{C}_0)$$

where

$$\begin{aligned} f_3(\mathbb{C}_0) &= 2\,(f_1(\mathbb{C}_0) + f_2(\mathbb{C}_0)) \\ &= 2\ C_{44}C_{55}(\sqrt{2}C_{13}^2C_{22} + \sqrt{2}C_{12}^2C_{33} + \sqrt{2}C_{11}(C_{23}^2 - C_{22}C_{33}) \\ &\quad -C_{23}^2C_{66} + C_{12}C_{33}C_{66} + C_{22}C_{33}C_{66} - C_{13}C_{23}(2\sqrt{2}C_{12} + C_{66})) \end{aligned}$$

References

1. DiCarlo A, Naili S, Quiligotti S, Sur le remodelage des tissus osseux anisotropes, *Comptes Rendus Mécanique* **334(11)**:651–661, 2006.
2. Frost HM, Bone "mass" and the "mechanostat": A proposal, *The Anatomical Record* **219(1)**:1–9, 1987.
3. Von Meyer GH, Die Architektur der Spongiosa. (Zehnter Beitrag zur Mechanik des menschlichen Knochgerüstes), *Archiv fur Anatomie, Physiologie, und wissenschaftliche Medizin* **6**:615–628, 1867.
4. Wolff J, Ueber die innere Architectur der Knochen und ihre Bedeutung fr die Frage vom Knochenwachsthum, *Virchows Archiv Pathol Anat Physio* **50**:389–450, 1870.
5. Roux W, *Der Kampf der Teile des Organismus*, Engelmann, Leipzig, 1881.
6. Culmann K, *Die graphische Statik*, Meyer & Zeller (A . Reimann), Zürich, 1866.
7. Wolff J, Das Gesetz der Transformation der Knochen, Hirschwald, Berlin, Germany, 1892.
8. Wolff J, The classic: on the inner architecture of bones and its importance for bone growth. 1870, *Clinical orthopaedics and related research* **468(4)**:1056–1065, 2010.
9. Garden, RS, The Structure and Function of the Proximal End of the Femur, *Journal of Bone and Joint Surgery* **43-B(3)**: 576–589, 1961.
10. Singh M, Nagrath AR, Maini PS, Changes in trabecular pattern of the upper end of the femur as an index of osteoporosis, *Journal of Bone and Joint Surgery* , **52(3)**: 457-67, 1970.
11. Whitehouse WJ, The quantitative morphology of anisotropic trabecular bone, *Journal of microscopy* **101(Pt 2)**:153–68, 1974.
12. Takechi H, Trabecular Architecture of the Knee Joint, *Acta Orthopaedica*, **48(6)**: 673–681, 1977.
13. Tobin WJ, The Internal Architecture of the Femur and Its Clinical Significance: The Upper End, *Journal of Bone and Joint Surgery*, **37(1)**: 57–88, 1955
14. Carter DR, Orr TE, Fyhrie D P, Relationships between loading history and femoral cancellous bone architecture, *Journal of Biomechanics* **22(3)**:231–244,1989.
15. Jacobs CR, Simo JC, Beaupré GS, Carter DR, Adaptive bone remodeling incorporating simultaneous density and anisotropy considerations, *Journal of Biomechanics* **30(6)**:603–613, 1997.
16. Cowin SC, The relationship between the elasticity tensor and the fabric tensor, *Mechanics of Materials* **4(2)**:137–147, 1985.

17. Cowin SC, Wolff's Law of Trabecular Architecture at Remodeling Equilibrium, *Journal of Biomechanical Engineering* **108(1)**:83, 1986.
18. Christen P, Ito K, Ellouz R, Boutroy S, Sornay-Rendu E, Chapurlat RD, Van Rietbergen B, Bone remodelling in humans is load-driven but not lazy, *Nature Communications* **5**:1–5, 2014.
19. Schulte FA, Ruffoni D, Lambers FM, Christen D, Webster DJ, Kuhn G, Müller R, Local Mechanical Stimuli Regulate Bone Formation and Resorption in Mice at the Tissue Level, *PLoS ONE* **8(4)**:e62172, 2013.
20. Sugiyama T, Price JS, Lanyon LE, Functional adaptation to mechanical loading in both cortical and cancellous bone is controlled locally and is confined to the loaded bones, *Bone* **46(2)**:314–321, 2010.
21. Huiskes R and Ruimerman R, van Lenthe GH, Janssen JD, Effects of mechanical forces on maintenance and adaptation of form in trabecular bone, *Nature* **405(6787)**:704–706, 2000.
22. Ruimerman R, Van Rietbergen B, Hilbers P, Huiskes R, A 3-dimensional computer model to simulate trabecular bone metabolism, *Biorheology* **40**(1-3):315–20, 2003.
23. Van Der Linden JC, Verhaar JAN, Weinans H, A Three-Dimensional Simulation of Age-Related Remodeling in Trabecular Bone, *Journal of Bone and Mineral Research* **16(4)**: doi = 10.1359/jbmr.2001.16.4.688, 688–696, 2001.
24. Badilatti SD, Christen P, Levchuk A, Marangalou JH, van Rietbergen B, Parkinson I, Müller R, Large-scale microstructural simulation of load-adaptive bone remodeling in whole human vertebrae, *Biomechanics and Modeling in Mechanobiology* **15(1)**:83–95, 2016.
25. Mullender MG, Huiskes R, Proposal for the Regulatory Mechanism of Wolff's Law, *Journal of Orthopaedic Research* **13(4)**:503–12, 1995.
26. Van Oers RFM, Ruimerman R, Tanck E, Hilbers PAJ, Huiskes R, A unified theory for osteonal and hemi-osteonal remodeling, *Bone* **42(2)**:250–259, 2008.
27. Van Oers RFM, Van Rietbergen B, Ito K, Hilbers PAJ, Huiskes R, A sclerostin-based theory for strain-induced bone formation, *Biomechanics and Modeling in Mechanobiology* **10(5)**:663–670, 2011.
28. Tsubota KI, Adachi T, Tomita Y, Functional adaptation of cancellous bone in human proximal femur predicted by trabecular surface remodeling simulation toward uniform stress state, *Journal of Biomechanics* **35(12)**:1541–1551, 2002.
29. Langton CM, Haire TJ, Ganney PS, Dobson CA, Fagan MJ, Dynamic Stochastic Simulation of Cancellous Bone Resorption, *Bone* **22(4)**:375–380, 1998.
30. Thomsen JS, Mosekilde L, Boyce RW, Mosekilde E, Stochastic simulation of vertebral trabecular bone remodeling, *Bone* **15(6)**:655–666, 1994.
31. Rovati M, Taliercio A, Optimal Orientation of the Symmetry Axes of Orthotropic 3-D Materials, in Eschenauer, HA, Mattheck C, Olhoff N (eds.), *Engineering Optimization in Design Processes*, pp. 127–134, 1991.
32. Banichuk NV, Optimization of Anisotropic Properties for Continuum Bodies and Structural Elements Using Spectral Methods of Tensor Analysis, *Mechanics of Structures and Machines* **24(1)**:71–87, 1996.
33. Pedersen P, On optimal orientation of orthotropic materials, *Structural Optimization* **1(2)**:101–106, 1989.
34. Cowin SC, Optimization of the strain energy density in linear anisotropic elasticity, *Journal of Elasticity* **34(1)**:45–68, 1994.
35. Cowin SC, On the minimization and maximization of the strain energy density in cortical bone tissue, *Journal of Biomechanics* **28(4)**:445–447, 1995.
36. Fernandes P, Rodrigues H, Jacobs CR, A Model of Bone Adaptation Using a Global

Optimisation Criterion Based on the Trajectorial Theory of Wolff, *Computer Methods in Biomechanics and Biomedical Engineering* **2(2)**:125–138, 1999.
37. Fyhrie DP, Carter DR, A unifying principle relating stress to trabecular bone morphology, *Journal of Orthopaedic Research* **4(3)**:304:317, 1986.
38. Fyhrie DP, Schaffler MB, The adaptation of bone apparent density to applied load, *Journal of Biomechanics* **28(2)**:135–146, 1995.
39. Waffenschmidt T, Menzel A, Kuhl E, Anisotropic density growth of bone–A computational micro-sphere approach, *International Journal of Solids and Structures*, **49**:1928–1946, 2012.
40. Huiskes R, Weinans H, Grootenboer HJ, Dalstra M, Fudala B, Slooff TJ, Adaptive bone-remodeling theory applied to prosthetic-design analysis, *Journal of Biomechanics* **20(11-12)**:1135–1150, 1987.
41. Miller Z, Fuchs MB, Arcan M, Trabecular bone adaptation with an orthotropic material model, *Journal of Biomechanics* **35(2)**:247–256, 2002.
42. Pettermann HE, Reiter TJ, Rammerstorfer FG, Computational simulation of internal bone remodeling, *Archives of Computational Methods in Engineering* **4(4)**:295–323, 1997.
43. Geraldes DM, Modenese L, Phillips ATM, Consideration of multiple load cases is critical in modelling orthotropic bone adaptation in the femur, *Biomechanics and Modeling in Mechanobiology* **15(5)**:1029–1042, 2016.
44. Cowin SC, Sadegh AM, Luo GM, An Evolutionary Wolff's Law for Trabecular Architecture, *Journal of Biomechanical Engineering* **114(1)**:129, 1992.
45. Doblaré M, García JM, Anisotropic bone remodelling model based on a continuum damage-repair theory, *Journal of Biomechanics* **35(1)**:1–17, 2002.
46. Ramtani S, Zidi M, Damaged-bone remodeling theory: Thermodynamical approach, *Mechanics Research Communications* **26(6)**:701–708, 1999.
47. DiCarlo A, Quiligotti S, Growth and balance, *Mechanics Research Communications* **29(6)**:449–456, 2002.
48. Menzel A, Modelling of anisotropic growth in biological tissues, *Biomechanics and Modeling in Mechanobiology* **3(3)**:147–171, 2005.
49. Reina JM, García-Aznar JM, Domínguez J, Doblaré M, Numerical estimation of bone density and elastic constants distribution in a human mandible, *Journal of Biomechanics* **40(4)**:828–836, 2007.
50. Goda I, Ganghoffer JF, Maurice G, Combined bone internal and external remodeling based on Eshelby stress, *International Journal of Solids and Structures* **94–95**:138–157, 2016.
51. Klika V, Pérez MA; García-Aznar JM; Maršík F; Doblaré M, A coupled mechano-biochemical model for bone adaptation, *Journal of Mathematical Biology* **69(6–7)**:1383–1429, 2014.
52. Komarova SV, Mathematical model of paracrine interactions between osteoclasts and osteoblasts predicts anabolic action of parathyroid hormone on bone, *Endocrinology* **146(8)**:3589–3595, 2005.
53. Lemaire V, Tobin FL, Greller LD, Cho CR, Suva LJ, Modeling the interactions between osteoblast and osteoclast activities in bone remodeling, *Journal of Theoretical Biology* **229(3)**:293–309, 2004.
54. Maldonado S, Borchers S, Findeisen R, Allgöwer F, Mathematical modeling and analysis of force induced bone growth,*Conference proceedings: ... Annual International Conference of the IEEE Engineering in Medicine and Biology Society. IEEE Engineering in Medicine and Biology Society. Annual Conference* **1**:3154–3157, 2006.
55. Martínez-Reina J, García-Aznar JM, Domínguez J, Doblaré M, A bone remodelling

model including the directional activity of BMUs, *Biomechanics and Modeling in Mechanobiology* **8(2)**:111–127, 2009.

56. Pivonka P, Zimak J, Smith DW, Gardiner BS, Dunstan CR, Sims NA, Martin TJ, Mundy GR, Model structure and control of bone remodeling: A theoretical study, *Bone* **43(2)**:249–263, 2008.
57. Germain P, The Method of Virtual Power in Continuum Mechanics. Part 2: Microstructure, *SIAM Journal on Applied Mathematics* **25(3)**:556–575, 1973.
58. Al Nazer R, Lanovaz J, Kawalilak C, Johnston JD, Kontulainen S, Direct in vivo strain measurements in human bone-A systematic literature review, *Journal of Biomechanics* **45(1)**:27–40, 2012.
59. Podio-Guidugli P, *A Primer in Elasticity*, Springer Netherlands, Dordrecht, 2000.
60. Sansalone V, Naili S, Di Carlo A, On the rotary remodelling equilibrium of bone,*Computer Methods in Biomechanics and Biomedical Engineering* **14(sup1)**:203–204, 2011.
61. Van Buskirk WC, Ashman R, The elastic moduli of bone, in Cowin SC (ed.), *Mechanical Properties of Bone*, American Society of Mechanical Engineers, Colorado, pp. 131–143, 1981.
62. Beaupré GS, Orr TE, Carter DR, An approach for time-dependent bone modeling and remodeling-theoretical development,*Journal of Orthopaedic Research* **5(8)**:651–661, 1990.

Chapter 6

Evolution of bone fabric governed by the dissipation principle: a preliminary finite-element study

This chapter introduces a 2D finite-element study of bone rotary remodeling based on the previously-introduced framework [42, 121] (Chapter 5). This work focuses on two benchmark problems. The first benchmark is a square with cortical bone properties on which a tensile load is applied (Figure 6.1). This example aims to investigate algorithmic convergence and dependency on some solver parameters (iteration method, meshing method and time step). The second example illustrates the proposed algorithm using a simplified 2D femur geometry and boundary conditions as per Beaupré et al. [12], see Figure 6.2.

As Skedros et al. note in their study of trabecular 'trajectories', a popular example for cancellous bone functional adaptation is the human femur, even though the first experiment showing the close correspondence between arched trabecular patterns and orientations of principal strain was performed on sheep calcanei [108] which undergo simpler loading conditions [179]. Hence, several numerical studies attempted to recover the identified femoral neck patterns (see the illustration of the variety in the representation of trabecular and stress patterns in Figure 6.3). These works rely on optimization theories [55, 86, 114] or on bone remodeling algorithms based on an *ad*

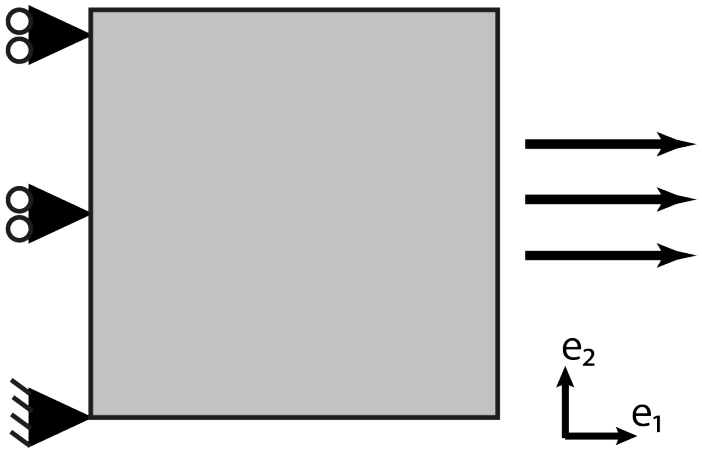

Figure 6.1: Benchmark 1. Model of a 10 mm x 10 mm square under boundary traction: the load is distributed over a 2 mm region at the center of the right side of the square. Plane stress conditions are assumed.

hoc expression of directional elastic moduli evolution laws [69, 135, 176] or continuum damage mechanics [45].

On the one hand, optimization theories rely on the definition and minimization of an objective function $\mathcal{Q}$ of the microstructural orientation (θ) under a certain load σ, that can also depend on other variables such as density (ρ):

$$\mathcal{Q}(\rho, \hat{\theta}, \sigma) = \min \mathcal{Q}(\rho, \theta, \sigma), \tag{6.1}$$

where $\hat{\theta}$ is the optimal orientation. Optimization theories usually also include constraints, generally on mass. For instance, Fyrhie and Carter developed an optimization theory using a cost function based on the strain energy, which is interpreted as a measure of bone's structural integrity depending both on density and orientation [63]. This concept was used later on by Luo and An who also formulated two constraints, being the stationarity of the total mass and an upper-limit value to density (saturated cancellous bone density) [115]. In the same vein, Jacobs et al. built a model minimizing the dissipation, therefore measuring the efficiency of the translation of external loads into a variation of the internal energy [86]. In their model based on Lagrangian optimization, the imposed constraint is a criterion to remodeling, ensuring that net bone remodeling only takes place when the criterion is violated. Building from this work, Fernandes et al. proposed an approach accounting for the metabolism needed

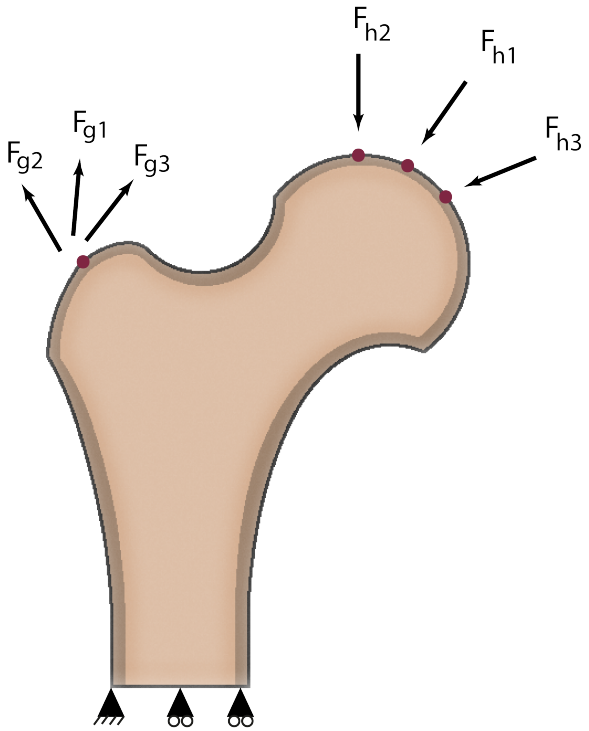

Figure 6.2: Benchmark 2. Simplified femur model: geometry and boundary conditions. (See text for more details.)

to maintain tissue: their model relies on a minimization of the sum of the compliance and the metabolic cost (assumed to be proportional to tissue mass), while respecting the principle of virtual power [55]. On the other hand, several models rely on the mathematical expression of the evolution of directional elastic moduli $\{\mathsf{E}_i\}_{i\in\{1,2,3\}}$ [69, 70, 135, 176]. In these approaches, the evolution of the elastic moduli are dependent on directional measures of strain [69, 70] or stress [135, 176]. In 2001, Doblaré and García proposed a continuum damage mechanics framework for bone remodeling, including the stimultaneous evolution of the density and the directions of the material axes. In their theory, the remodeling tensor is considered as an internal variable and its evolution follows from the definition of suitable damage criteria which depend on the local principal directions of anisotropy and the principal directions of equivalent strains.

In this chapter, a bone remodeling algorithm is developed and tested for two benchmark problems, stemming from the theory presented earlier (Chapter 5). In this scope, several computational issues, such as the influences of mesh, time step,

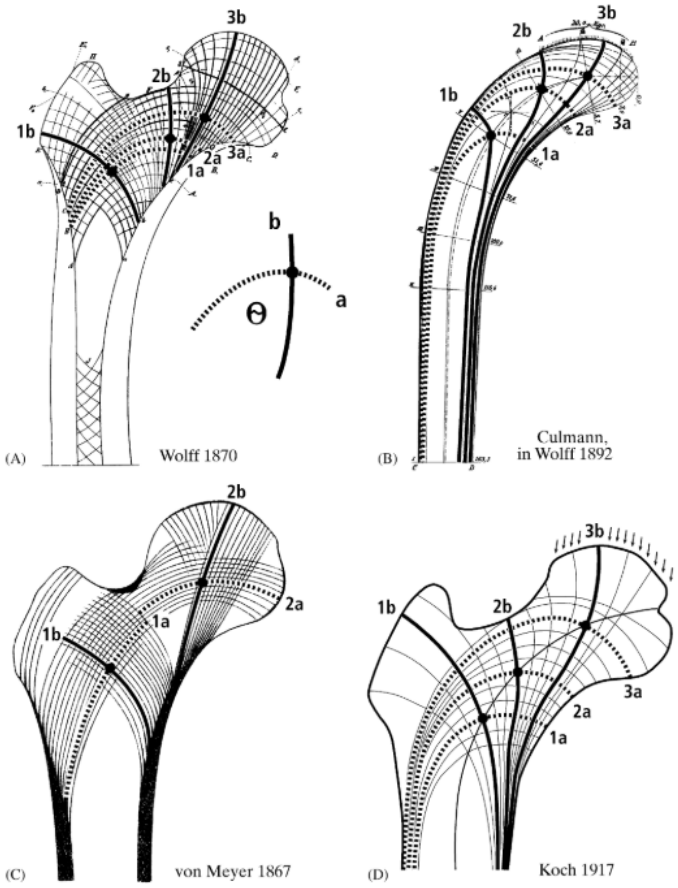

Figure 6.3: Examples of the diversity in femoral trabecular trajectories representations: (A) Wolff's femur [206]; Culmann's crane [207]; (C) von Meyer's femur [195]; (D) Koch's drawing [99]. Labeled trabecular tracts mark main trajectories. From Skedros et al. [179], with permission.

approximation method, geometry and material properties, are investigated.

6.1 Materials and Methods

6.1.1 Kinematics and remodeling law

As noted earlier, a 2D rotary remodeling law based on the energetic considerations developed by DiCarlo et al. [42] is used, as introduced previously (Chapter 5). Hence, in this framework of generalized continuum mechanics, the state of each material point $\mathbf{X}$ in the space Ω is described by:

(i) the position $\mathbf{x} = \xi(\mathbf{X}, t)$,

(ii) the local orientation of the microstructure $\mathsf{R} = \widehat{\mathsf{R}}(\mathbf{X}, t)$.

Additionally, the material behavior is assumed to be linearly elastic. The elastic tensor $\mathbb{C}$ can evolve with time, as it is dependent on the tissue orientation R (see Equation (5.3)). Thus, the stress-strain relationship reads:

$$\mathsf{S} = \mathbb{C} : \mathsf{E}\,, \tag{6.2}$$

where S is the stress tensor, E is the small strain tensor and the double-dot operator denotes the tensor inner product.

In 2D, one can simplify the expression of the dissipation derived in the previous chapter (Equation (5.4)) and obtain the rotation rate as a function of the stress/strain state of a material point:

$$2\, d_0\, \dot{\alpha} = (\mathsf{S}\,\mathsf{E} - \mathsf{E}\,\mathsf{S}) : \mathsf{W}_\mathsf{z}, \tag{6.3}$$

where d_0 is a dissipation coefficient representing the resistance to remodeling, $\mathsf{W}_\mathsf{z} := \mathbf{e}_2 \otimes \mathbf{e}_1 - \mathbf{e}_1 \otimes \mathbf{e}_2$, and $\mathbf{e}_1$ and $\mathbf{e}_2$ are the basis vectors of the 2D Euclidean space.

6.1.2 Numerical solution

The algorithm developed to study bone remodeling implements an iterative method depicted in Figure 6.4. At each iteration, two main steps are carried out: first, solving a boundary value problem (by means of Finite Element Analysis, FEA) while keeping fixed the material properties; then, updating the orientation of the material microstructure – to be called micro-orientation for short–and therefore the material properties.

The algorithm is initialized by defining the geometry, the boundary conditions and the initial value of the micro-orientation field. Moreover, the FE mesh and the remodeling grid are constructed. After assigning the initial orientation on the nodes of the remodeling grid, the iterative loop starts. At each step n, current material properties are calculated based on the values of the micro-orientation on the remodeling grid points $(\alpha_i^n)_{i\in\mathbb{I}}$, the index $i \in \mathbb{I}$ corresponding to a remodeling

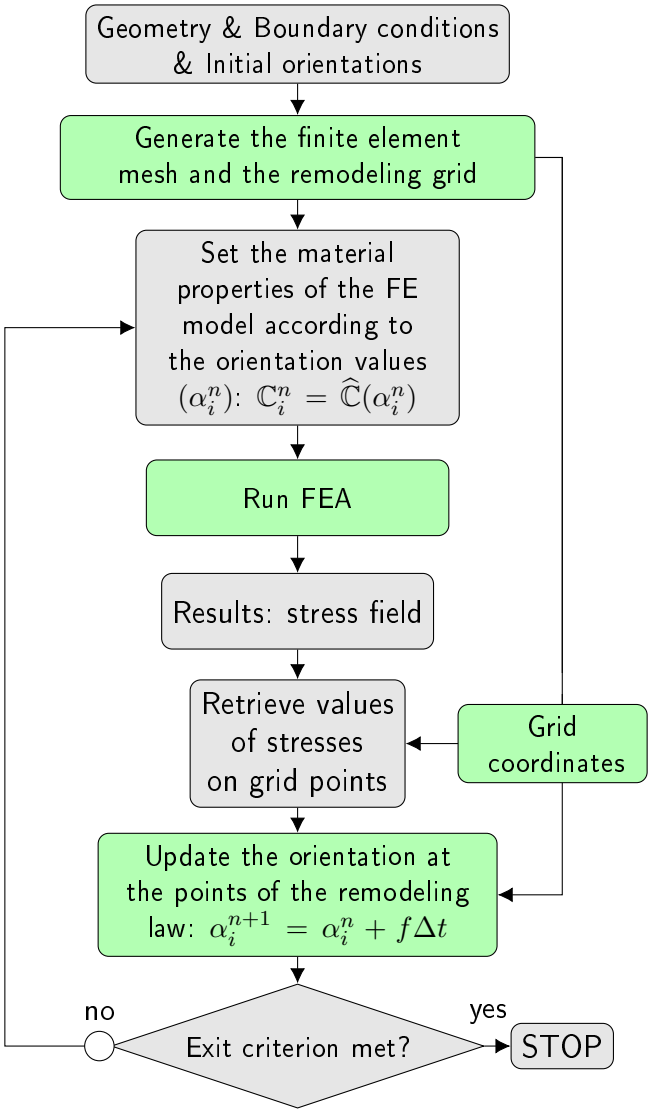

Figure 6.4: Algorithm structure. Block colors identify computational calculation (green) or data processing (gray). 'FEA' refers to finite-element analysis.

grid point and $\mathbb{I}$ being the set of points of the remodeling grid. FEA is performed to compute the distribution of stress and strain fields. Stress and strain fields are then projected onto the nodes of the remodeling grid to update the micro-orientation therein using the remodeling law (Equation (6.3)). Eventually, if the exit criterion is not met, the new values of micro-orientation are eventually made available to the FE model to restart the loop.

FE mesh and remodeling grid As depicted in Figure 6.5, the nodes of the FE mesh (black lines) may be different from those of the remodeling grid (red

dots). If the nodes of the remodeling grid coincide with the FE mesh (case (a) in Figure 6.5), there is a one-to-one correspondence between the node-wise results of the FEA and the nodes where the micro-orientation is computed. Hence, the remodeling law is directly computed at the mesh nodes as a result of the FEA. Otherwise, the FE mesh can be finer than the remodeling grid (case (b) in Figure 6.5). In the latter case, the results of the FEA will be interpolated to evaluate the rotation rate at the remodeling grid points.

Boundary value problem. This step is carried out using a commercial FE software (Comsol Multiphysics® 5.3a) [1]. Explicit formulas giving the relationship between each elastic modulus and micro-orientation are implemented in the finite-element model: $\mathbb{C}(x,y) = \widehat{\mathbb{C}}(\alpha(x,y))$, where x and y denote the 2D spatial coordinates. Micro-orientations $\alpha(x,y)$ are interpolated from the values at remodeling grid points $(\alpha_i^n)_{i\in\mathbb{I}}$, which are updated at each step in an external file from the remodeling law calculation. Thus, the material properties at Gauss points $\mathbb{C}(x_{\mathsf{G}}, y_{\mathsf{G}})$ are defined. FEA is performed using the plane stress approximation and quadratic elements.

Updating micro-orientation. This step is carried out using the Livelink™ for MATLAB® module by COMSOL AB [2, 3]. More precisely, at the n-th iteration ($n \in \mathbb{N}$), the discrete version of the remodeling law Equation (6.3) in a remodeling grid point $i \in \mathbb{I}$ reads:

$$\alpha_i^{n+1} = \alpha_i^n + f\Delta t \qquad \forall n \in \mathbb{N},\, \forall i \in \mathbb{I}\,. \tag{6.4}$$

The accuracy of the above formula depends on the choice of the time step Δt and of the function f. This latter represents a discrete approximation of $\dot{\alpha}$. Two approximation methods are considered here: Euler-Cauchy (EC) and fourth-order Runge-Kutta (RK). Both of them are one-step explicit methods. Therefore, the function f depends only on the current values of the micro-

orientation and strain (or, equivalently, stress), reading:

$$f = f(\alpha_i^n, \mathsf{E}_i^n)\,, \tag{6.5}$$

where E_i^n is interpolated from the FEA strain field. In the case of Euler-Cauchy approximation, the function f is the current value of $\dot{\alpha}$, reading:

$$f_{EC}(\alpha_i^n, \mathsf{E}_i^n) = \dot{\alpha}_i^n = \frac{1}{2\,d_0}\,(\mathsf{S}_i^n\,\mathsf{E}_i^n - \mathsf{E}_i^n\,\mathsf{S}_i^n) : \mathsf{W}_\mathsf{z}\,, \tag{6.6}$$

where S_i^n is computed using Equation (6.2): $\mathsf{S}_i^n = \mathbb{C}(\alpha_i^n) : \mathsf{E}_i^n$.

The 4th-order Runge-Kutta approximation incorporates the approximation of the micro-orientation at intermediate time steps:

$$f_{RK}(\alpha_i^n, \mathsf{E}_i^n) = \frac{1}{6}\,(k_1 + 2\,k_2 + 2\,k_3 + k_4)\,, \tag{6.7}$$

where

$$k_1 = f_{EC}(\alpha_i^n, \mathsf{E}_i^n)\,, \tag{6.8}$$

$$k_2 = f_{EC}(\alpha_i^n + \frac{k_1}{2}\Delta t, \mathsf{E}_i^n)\,, \tag{6.9}$$

$$k_3 = f_{EC}(\alpha_i^n + \frac{k_2}{2}\Delta t, \mathsf{E}_i^n)\,, \tag{6.10}$$

$$k_4 = f_{EC}(\alpha_i^n + k_3\Delta t, \mathsf{E}_i^n)\,. \tag{6.11}$$

Exit criterion. Several exit criteria have been considered based on local or global convergence of mechanical quantities such as the strain energy of the system or the micro-orientation. All these criteria require to define a threshold which can be hardly identified based on biological arguments. Therefore, a simpler criterion was set, by fixing a threshold on the duration (physical time) of the remodeling process.

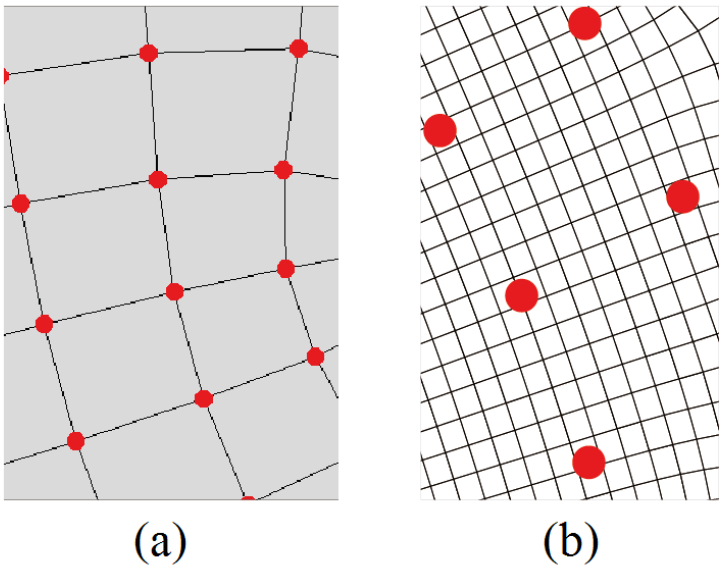

Figure 6.5: Meshing options: (a) One grid strategy; (b) Two-grid strategy.

6.2 Results

In this section, the influence of several solver and modeling parameters is investigated using the two benchmarks in Figures 6.1 and 6.2. Concerning the solver parameters, the focus is set on the meshing methods and on the two key parameters used to update the micro-orientation (Equation (6.4)), namely the time step Δt and the approximation function f. If not stated differently, the FE mesh coincides with the remodeling grid (case (a) in Figure 6.5) and a $\Delta t = 1$ day time step and the Runge-Kutta approximation (Equation (6.7)) are used to update the micro-orientation. The femur model is also used to investigate the effects of the material parameters and of the geometry.

The first benchmark is the toy example illustrated in Figure 6.1, a square piece of cortical bone (1 cm $\times$ 1 cm). A surface tensile load $\Sigma_{app} = 100\,\text{MPa}$ is applied on the central part of the edge of the square, leading to strains $\epsilon_{\max} = \max(|\epsilon_i|) < 4000\ \mu\epsilon, \bar{\epsilon} = \text{mean}(|\epsilon_i|) \simeq 10^3\ \mu\epsilon$. The material is assumed to be orthotropic and the relevant material properties are listed in Table 6.1. The dependency of the evolution of the system with respect to different meshing and iteration methods is analyzed globally via the total strain energy and locally via the micro-orientation at selected

Table 6.1: Benchmark 1. Material properties for the toy problem in Figure 6.1. (Kelvin notation is used for the elastic coefficients.)

Elastic coefficients	GPa
C_{11}	30
C_{22}	20.85
C_{12}	11.49
C_{66}	13.2
Dissipation coefficient	kPa.day
d_0	555

points of interest (A, B, C). The location of the latter can be visualized in Figure 6.6.

The second benchmark represents a simplified model of the human proximal femur. Geometry and boundary conditions are depicted in Figure 6.2. Arrows represent point loads resulting from joint reaction forces (F_{hi}) and hip abductor forces (F_{gi}) (see [12]). The values of the forces are listed in Table 6.3. The material properties and forces magnitudes are respectively listed in Table 6.2 and Table 6.3. The properties of the shell (brown, in Figure 6.2) were interpolated linearly between its values at the external boundary (constant cortical properties as per Table 6.2) and the properties at the inner boundary (evolving elastic properties of the trabecular bone as per Table 6.2), unless otherwise specified.

Table 6.2: Benchmark 2. Material properties of cortical and trabecular bone (plane stress). (Kelvin notation is used for the elastic coefficients.)

Material property	**Symbol**	**Value**
Cortical bone		
Young modulus	E_c	14 GPa
Poisson's ratio	ν_c	0.3
Trabecular bone		
Elastic modulus	C_{11}	2.50 GPa
Elastic modulus	C_{22}	1.42 GPa
Elastic modulus	C_{12}	636 MPa
Elastic modulus	C_{66}	1.20 GPa
Dissipation coefficient	$\tilde{d}_0$	555 kPa.τ

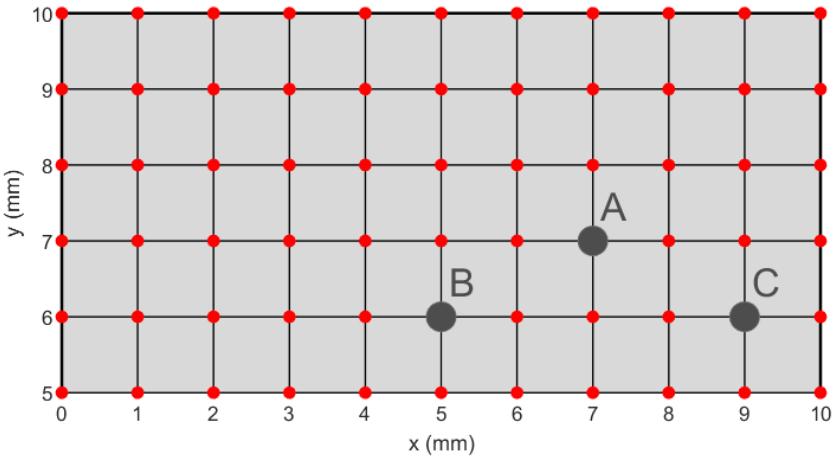

Figure 6.6: 10x10 remodeling grid of the square under boundary traction (see Figure 6.1, only the upper half is represented here) and location of points of interest (A, B, C).

6.2.1 Meshing strategy

In this subsection, different approaches are investigated for the evaluation of the strain/stress at the remodeling grid points. In the first case (named 1M in the figures), the remodeling grid coincides with the FE nodes (Figure 6.5(a)). Thus, stress/strain are directly transferred from the FE model to the remodeling grid. In a second strategy (named 2M in the figures), stress/strain in the nodes of the remodeling grid points (the coarse grid, corresponding to the red dots in Figure 6.5(b)) are obtained by interpolating the stress/strain fields obtained from the FEA. (Runge-Kutta method

Table 6.3: Benchmark 2. Loading conditions: Orientation and magnitude of the point forces applied on the femur (see Figure 6.2).

Force	Angle	Value
$\mathbf{F_{g1}}$	28°	421.2 N
$\mathbf{F_{g2}}$	-8°	70.20 N
$\mathbf{F_{g3}}$	35°	93.60 N
$\mathbf{F_{h1}}$	24°	-1390 N
$\mathbf{F_{h2}}$	-15°	-213.6 N
$\mathbf{F_{h3}}$	56°	-309.6 N

and a time step $\Delta t = 1$ day are used to update the micro-orientation.)

In Figure 6.7, the effect of the above meshing strategies are evaluated with respect to Benchmark 1. The 1M and 2M meshing strategies are compared, including several 2M FE mesh options of increasing densities, from a mesh 2.5 times finer than the remodeling grid to 10 times finer. Results obtained with the 1M strategy are represented with solid lines in Figure 6.7 whereas the results of the 2M strategy are represented with dotted (2.5 x), dash-dotted (5 x), and dashed (10 x) lines.

The meshing strategy affects the evolution of the system to different extents. The effect is clearly small with respect to the local micro-orientation in points A, B, and C (Figure 6.7(a)). However, larger differences exist when looking at the total strain energy (Figure 6.7(b)). These differences are mainly due to the mesh dependency of the FE solution in the singular points of the system (data not shown).

6.2.2 Quadrature of micro-rotation rate

This section assesses the role of the approximation scheme (function f) and time discretization (time step Δt) in the quadrature of the micro-rotation rate, Equation (6.4). (The 1M meshing strategy is used throughout this subsection.)

Figure 6.8 shows the results of a sensitivity analysis with respect to Benchmark 1. Simulations were undertaken with time steps Δt ranging from 0.5 day to 2 days. In parallel, two different approximation schemes were used, namely fourth-order Runge-Kutta (RK) and Euler-Cauchy (EC). The evolution of the micro-orientation at the points of interest A, B and C (blue, green, and red lines, respectively) is shown for

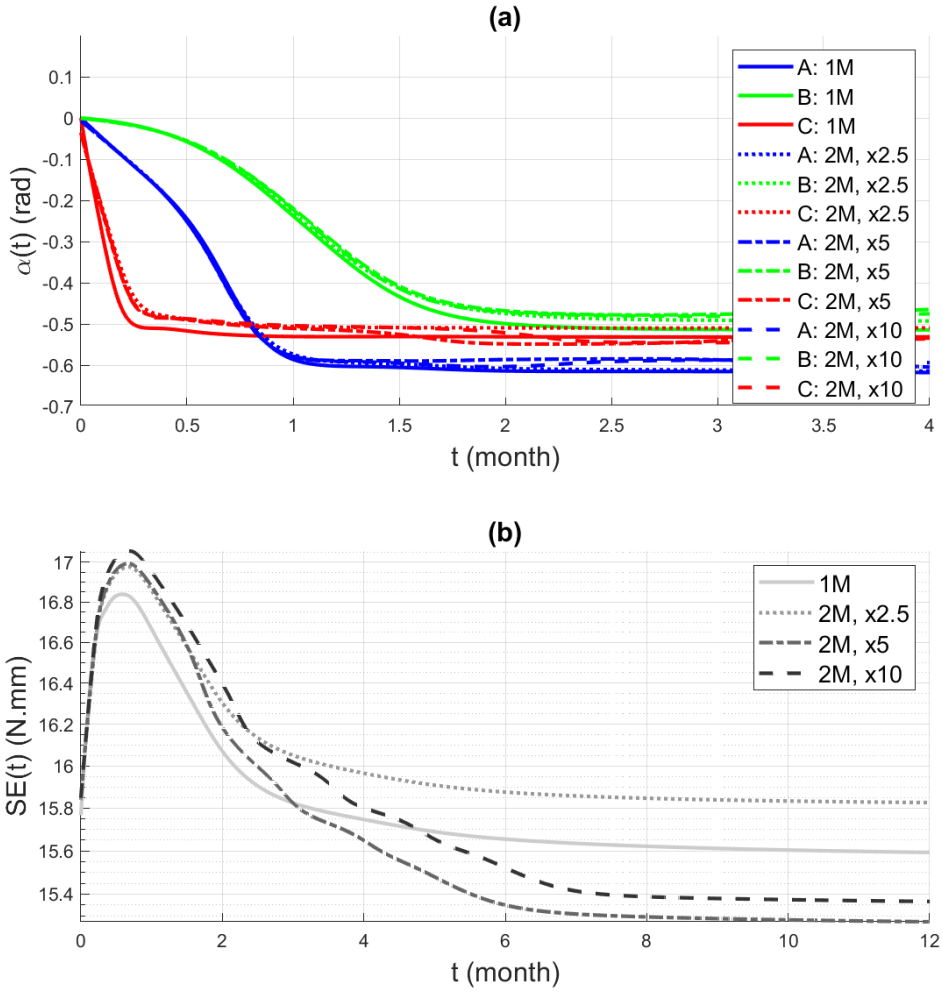

Figure 6.7: Evolutions of (a) micro-orientations in points A, B and C and (b) total strain energy (SE) with respect to time, for varying mesh strategies (one mesh (1M) and two meshes (2M)).

three different time steps $\Delta t \in \{0.5, 1, 2\}$ day (bright, dark, and very dark colors, respectively) and the RK and EC quadrature schemes (dashed and solid lines, respectively). As expected, the RK scheme performs better than the EC scheme. The former renders a stable evolution of the micro-orientation even for large time steps and the behavior of the system is approximately the same, irrespective of the time step (see the dashed lines in any of the points of interest). By contrast, the EC scheme leads to numerical instabilities for large time steps (see the very dark red solid line in Figure 6.8 corresponding to point C and a time step $\Delta t = 2$ day).

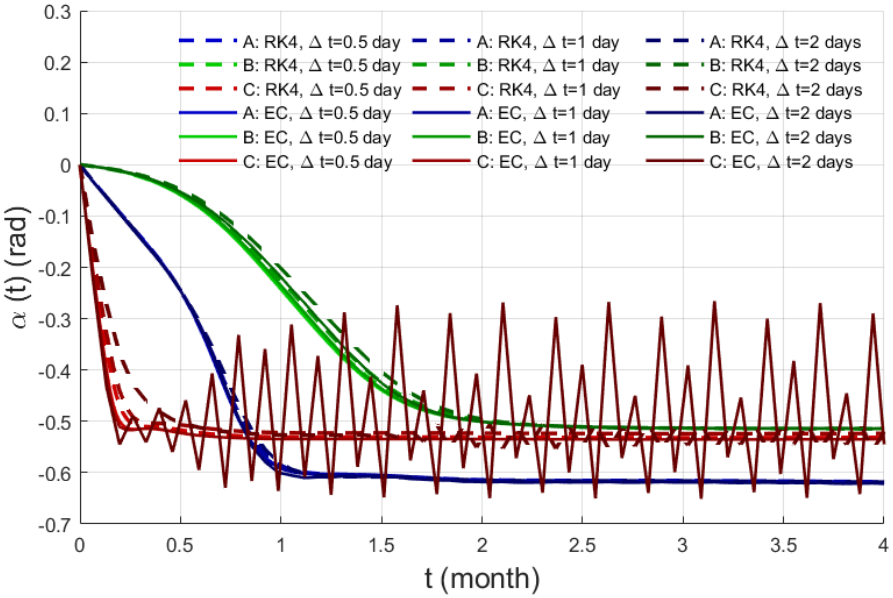

Figure 6.8: Square plate benchmark problem: evolutions of the micro-orientation in points A, B and C for varying time steps (0.5, 1 and 2 days) and approximation methods (EC and RK).

A similar analysis was performed on the femur model of Benchmark 2. The time steps was varied between from 0.5 to 20 units time (τ) and both EC and RK quadrature schemes were used.

The evolution of the system did not vary when imposing different approximation and time discretization methods from 0.5 to 20 time units. The results of the remodeling simulations are displayed in Figure 6.9, which illustrates the finite-element mesh (a), initial micro-orientation field (b), and micro-orientation fields after 5000 (c) and 10000 (d) time units. Note that, as expected, the strain energy map changes with time (Figure 6.9(b-d)).

6.2.3 Geometry

In this subsection the effect of the presence of the marrow cavity on the remodeling process in the proximal femur is investigated. Therefore, an ellipsoidal cavity was added in the diaphysis of the original femur model to account for the marrow cavity. In one case (Figure 6.10(b)), the cavity was assumed empty. In the other case (Figure 6.10(c)), the marrow cavity was filled with a linearly elastic, almost incompressible

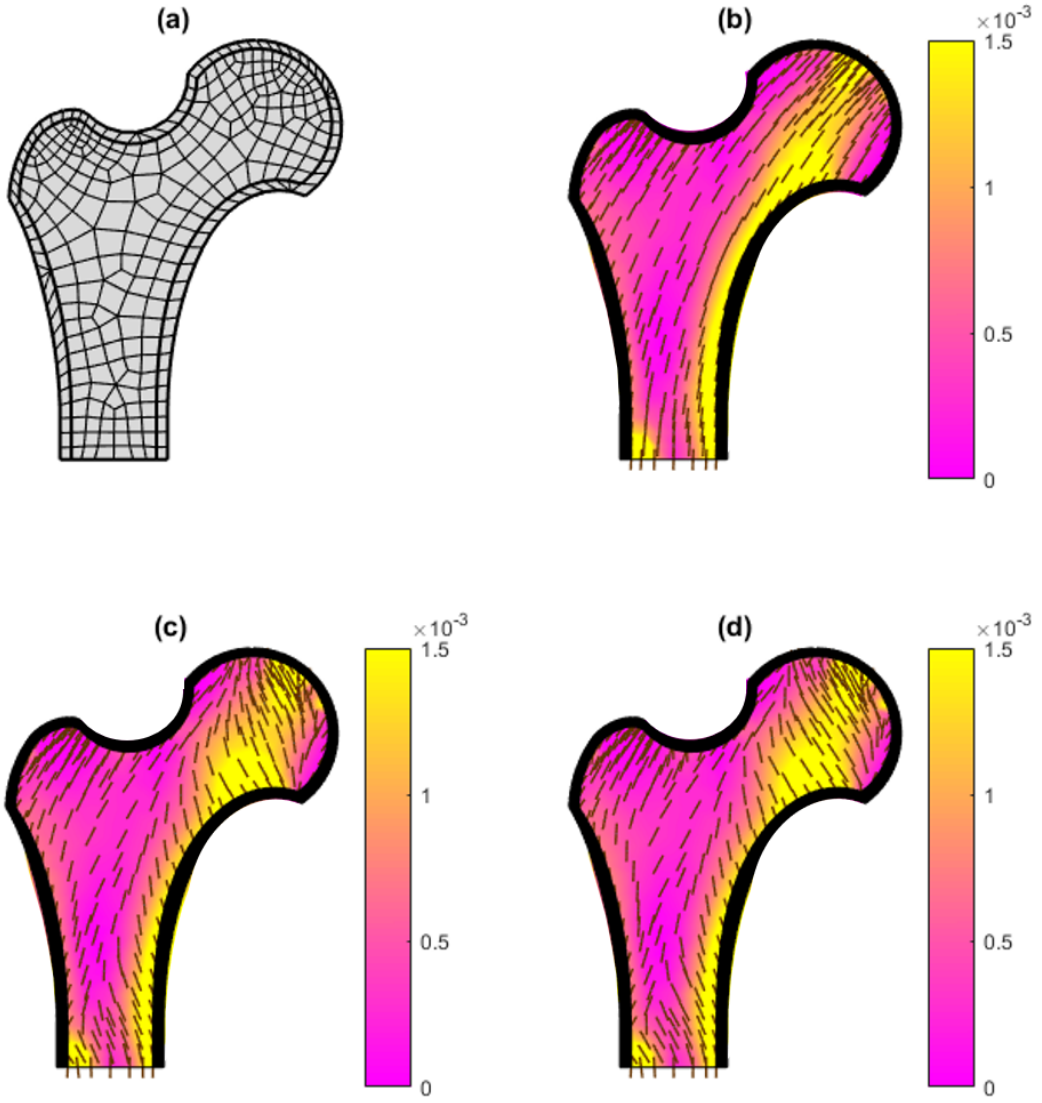

Figure 6.9: Evolution of the micro-orientation (brown sticks) in the femur model: (a) finite-element mesh; (b) initial micro-orientation field; (c) micro-orientation field after 5000 time units; (d) micro-orientation field after 10000 time units. Color map: strain energy density (MPa).

isotropic material ($E_m = 10$ kPa, $\nu_m = 0.499$) mimicking the presence of the marrow.

Figure 6.10 displays the results of the previously-mentioned simulations as well as the original femur model (Figure 6.10(a)). These simulations were performed with a time step of 1 time unit and with the 1M method. In all cases, the initial micro-orientation fields was assumed as in Figure 6.9(b). While there is a significant discrepancy in the results when introducing the marrow cavity in the geometry, the

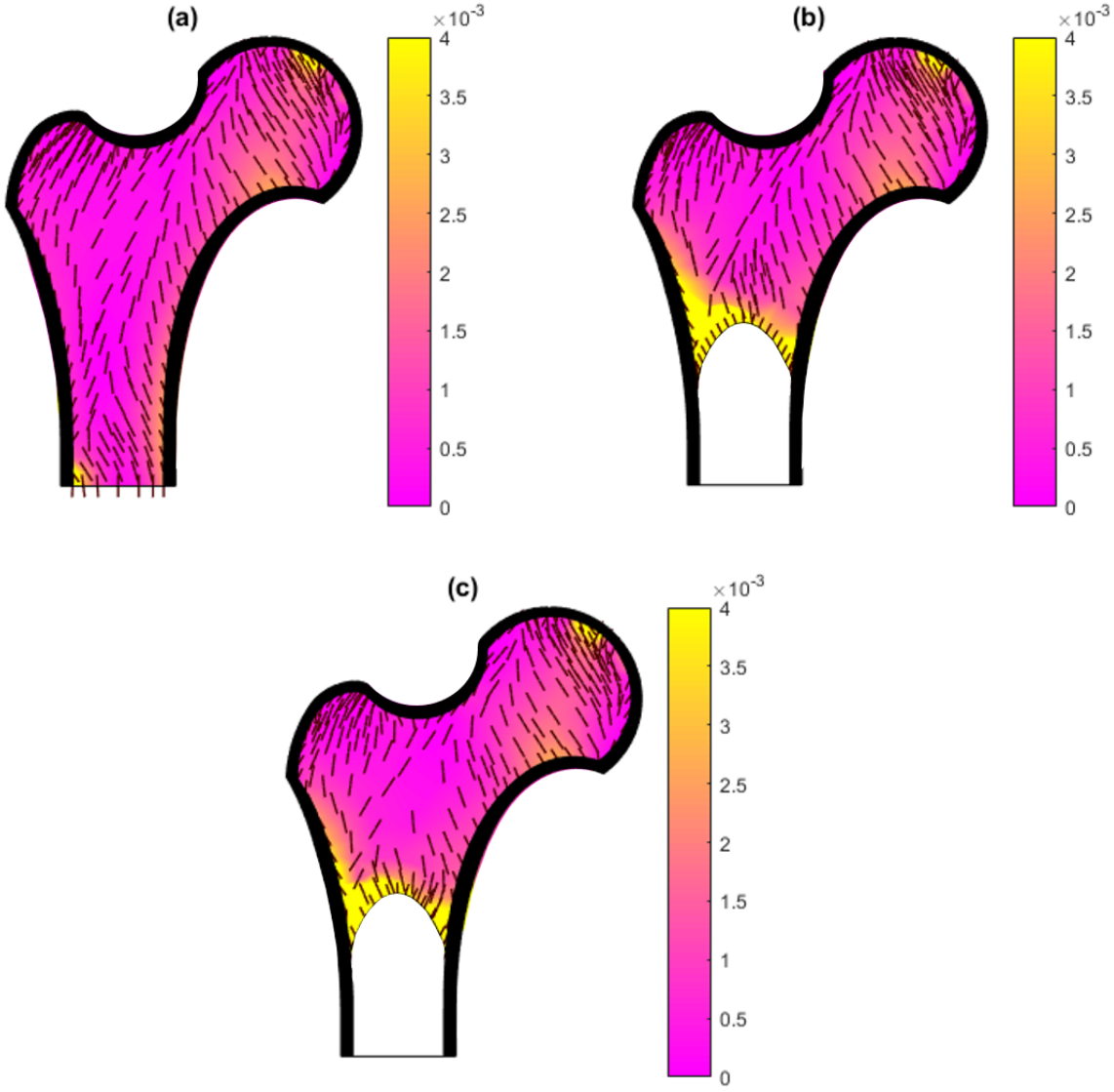

Figure 6.10: Micro-orientations (brown sticks) in the femur model after 10000 units time for varying geometries: (a) original model; (b) empty marrow cavity; (c) filled marrow cavity. Color map: strain energy density (MPa).

specific values of the material properties of the marrow space (Figure 6.10(c)) do not seem to notably impact the micro-orientation field in the femur.

6.2.4 Material properties

Material properties of bone tissue play a substantial role in remodeling. In particular, the modification of the shear modulus of trabecular bone may change the remodeling response dramatically. Hence, one can also infer that a change in mechanical loading

is not the only trigger to a change in bone remodeling activity: changes in bone structure and composition also prompt a different bone cell activity, as the mechanical environment changes. Here, this issue is addressed by considering a modification of the shear modulus C_{66} which is set to twice its original value: $C_{66} = 2.4\,\text{GPa}$.

Analytically, a different shear modulus can modify the material response to loading in terms of micro-rotation. The influence of material properties on rotary remodeling has been investigated in Chapter 5 considering a uniaxial, stationary load. In that scope, the remodeling response has been shown to strongly depend on the sign of the function f_3 defined hereafter:

$$\begin{aligned} f_3(\{C_{ij}\}) = 2\ C_{44}C_{55}(\sqrt{2}C_{13}^2C_{22} + \sqrt{2}C_{12}^2C_{33} + \sqrt{2}C_{11}(C_{23}^2 - C_{22}C_{33}) \\ -C_{23}^2C_{66} + C_{12}C_{33}C_{66} + C_{22}C_{33}C_{66} - C_{13}C_{23}(2\sqrt{2}C_{12} + C_{66})). \end{aligned} \tag{6.12}$$

The function f_3 governs the tendency of the microstructure to align with the principal stress directions. In particular, it has been shown in Chapter 5 that a necessary condition for the micro-orientation to align with the 1D stress direction is the function f_3 to take positive value.

The analytical results of Chapter 5 cannot be applied straightforwardly to the femur model since the stress state is more complex and evolves in time. However, it is reasonable to expect the shear modulus to affect the remodeling process by favoring the alignment of the material axes with the principal stress directions when f_3 is positive. Actually, the function f_3 takes negative value when using the elastic coefficients in Table 6.2. However, f_3 takes positive value assuming $C_{66} = 2.4\,\text{GPa}$. One may also note that, as previously mentioned by Cowin [37] about cortical tissue, experimental values of bone tissue material properties suggest that the material microstructure does not always tend to align with strains and stresses (from energetic considerations).

Remodeling of the trabecular tissue can be also affected by the elasticity of the surrounding cortical shell. A linear transition of material properties was postulated through the cortical shell (with $C_{66} = 1.2$ GPa). This research hypothesis was investigated by smoothing the trabecular-to-cortical transition. To this end, a parabolic

variation of the elastic moduli through the cortical shell was also considered. The elastic moduli variations are displayed in Figure 6.11.

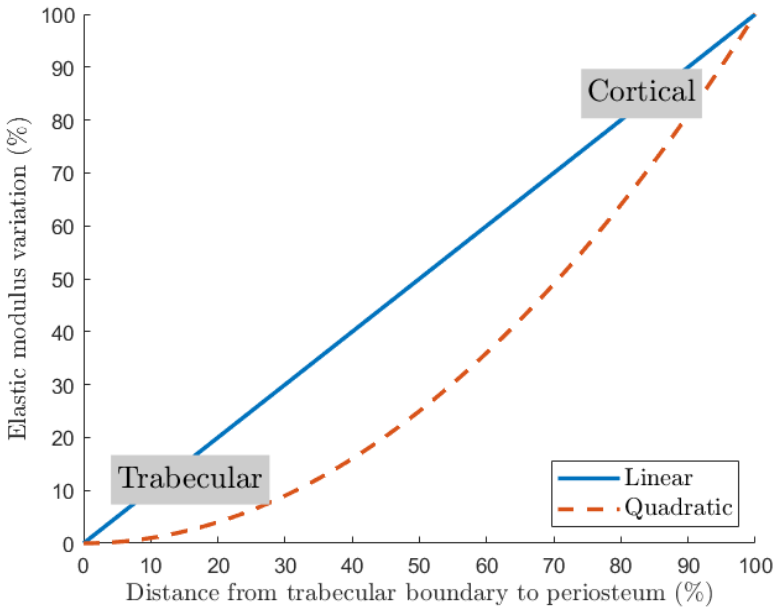

Figure 6.11: Evolution of the elastic moduli: trabecular-to-cortical transition in the linear and quadratic interpolation cases.

Figure 6.12 depicts the material orientations after 10000 units time, using a time step of 1 time unit, a 1M meshing method and varying material properties. The material properties of the original model are shown in the subplot (a). Subplot (b) shows the results obtained when the shear modulus of the trabecular is increased ($C_{66} = 2.4\,\mathrm{GPa}$). One can note the significant changes in the micro-orientation field, in particular at the femoral head. Subplot (c) shows the results obtained by considering a quadratic variation of the elastic moduli through the cortical shell. It is apparent that there are no major changes to the orientations associated with this choice.

6.3 Conclusions

This chapter on numerical solutions of benchmark problems shows the potential of the proposed algorithm and the relevance of the questions of mesh, time discretization, geometry and material properties. These questions are closely related to the problem

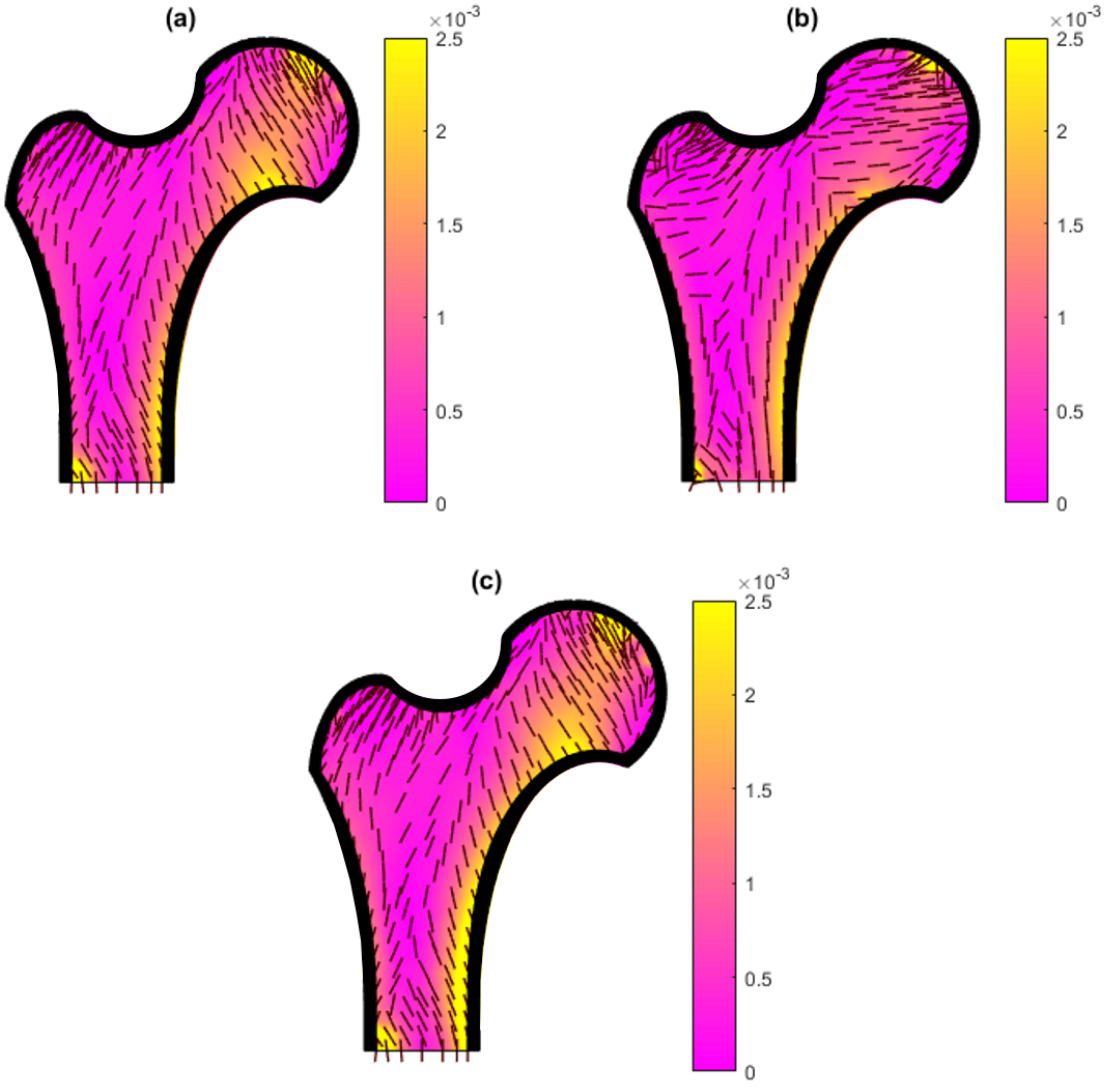

Figure 6.12: Micro-orientations (brown sticks) in the femur model after 10000 units time for varying material properties: (a) original model; (b) modified trabecular elastic modulus ($C_{66} = 2.4\,\mathrm{GPa}$); (c) quadratic interpolation between the boundaries of the cortical shell. Color map: strain energy density (MPa).

studied, in particular when dealing with complex *in vivo* geometries, where one must find a balance between model convergence and physical meaning. One of the findings of this study is the importance of the definition of material properties, in accordance with earlier theoretical developments (Chapter 5). Noting that the remodeling algorithm proposed in this Chapter could be adapted to another remodeling law, a further development of this work would be the coupling of the effect of mechanobiology on material properties and the evolution of micro-orientation. This will be addressed

with a unifying theory of bone remodeling presented in the next chapter (Chapter 7).

The results of this study are encouraging for future applications to clinical questions such as bone remodeling around implants or the underlying mechanisms of bone pathologies such as adolescent idiopathic scoliosis (AIS). The advantage of the presented algorithm is that it provides a framework for the analysis of bone remodeling for realistic geometries. Although the data is not shown here, the model was already adapted and tested in 3D. Chapter 8 provides the perspective of a commencing clinical study of bone remodeling on AIS. While the model developed in this chapter and the previous one (Chapter 5) is dedicated to passive (*i.e.* mechanically driven) bone remodeling, an extension of this theory is proposed in the next chapter (Chapter 7) in order to integrate the roles of chemistry and biology and their interactions with mechanics.

Chapter 7

Development of a thermodynamic framework coupling cellular activities, bone remodeling and mineralization

Since Herissant's first experiments in 1758 [80], it is well accepted that bone tissue is a composite material made of organic and mineral components. Hence, additionally to the mechanobiological feedback, bone remodeling also involves mineralization kinetics.

Several theories investigated phase transformation kinetics using thermodynamics, in particular in the context of civil engineering. One may highlight the contributions of Ulm et al. [190] and Bary [11] who investigated the leaching of cement-based materials within the framework of poroelasticity. On the other hand, in the context of bone remodeling, Ganghoffer and coworkers developed a phase field approach based on thermodynamics: the definition of dissipation contributions associated with phase field, mechanical, chemical, and thermal phenomena leads to the equations of evolution of bone tissue [64, 65]. In particular, they introduced a diffuse interface behavior between marrow and new bone, and described mineral content with a phase field. In their 2019 model, they added the description of growth in a second-gradient approach to account for bone mass production and internal microstructure evolution. Another significant contribution to bone remodeling and mineralisation was made by

Klika and coworkers who represented cells behavior by a series of reaction schemes, from osteoblasts precursors to new (non-mineralized) bone, and from pre-osteoclasts to the degradation of old (mineralized) bone by active osteoclasts [97]. Hence, they introduced in their original model 16 main substances N_i which were products or reactives of given reactions and proposed relationships between the concentrations $[N_i]$ of these substances. With chosen stoechiometric coefficients ($\nu_{\alpha,i}$ and $\nu'_{\alpha,i}$ correspond respectively to the substances N_i entering and leaving the α-th reaction), the evolution of the concentration of the substances is driven by a system of ODEs based on the reaction rates r_α and the addition of inflow and outflow fluxes J_i (Equation (7.1)), and regulated by mechanics via the strain rate tensor first invariant $d_{(1)}$, representing volume change (Equation (7.2)):

$$[\dot{N}_i] = \sum_{\alpha=1}^{5}(\nu'_{\alpha,i} - \nu_{\alpha,i})r_\alpha + J_i\,, \tag{7.1}$$

$$r_\alpha = k_\alpha^+ \prod_{\alpha=1}^{n_\alpha^+}[N_i]^{\nu_{\alpha,i}} - k_\alpha^- \prod_{\alpha=1}^{n_\alpha^-}[N_i]^{\nu_{\alpha,i}} - l_{\alpha v} d_{(1)}\,, \tag{7.2}$$

where k_α^+ and k_α^- are the forward and backward reaction rate constants, $l_{\alpha v}$ a phenomenological constant and n_α^+ and n_α^- are respectively the number of reactives and products for reaction α.

Over the past decades, several other bone remodeling frameworks accounted for mineralization. In 2000, Hernandez and coworkers developed a feedback model for bone structure and bone mineral content relying on two feedback loops controlled by daily stimuli, where the regulating inputs were not only the mechanics but also the bone cells activity. The daily metabolic and stress stimuli respectively regulated the mineralization and bone structure, via a test against a certain setpoint. This model, directly in line with Frost's 'mechanostat' framework, delivers a local evolution law for the bone 'porous volume', 'mineralized volume', and 'osteoid volume' depending on BMU activity (*sic*, terminology from the text). This formulation was used later on by Hambli [75] who combined the Hernandez et al.'s mineralization law with the biological evolution in the tissue, accounting for cells and porosity evolution using Komarova et al.'s [101] and Bonfoh et al.'s [20] works. Note that Ganghoffer et al. also described bone cells activity using Komarova's model [64].

In 2005, García-Aznar et al. introduced a novel model of mineralization [66]. Bone was described as a three-phase material constituted of an inorganic phase (mineral), an organic phase (mostly collagen), and water. In that study, a law for the evolution of ash fraction (a measure of the degree of mineralization) was defined: the primary phase of mineralization, known to happen very quickly, was implemented as instantaneous and the secondary phase followed an exponential law to reach the maximum mineral content. In later works [14, 124], this model was modified and the primary mineralization was modelled as a linear evolution. In the aforementioned models, the ash fraction evolution law was integrated in a damage mechanics framework where the crack density and the BMU activity enters the bone density balance. Eventually, an average ash fraction was defined integrating different mineralization stages over the volume element.

The present work describes a framework that uses the coarse representation inherent to phenomenological models while embedding textural information in the continuum that renders the biological and chemical activity taking place at the microscale. Biochemical events inherent to bone remodeling are accounted for via their energetic contribution, as one can assume that they respond to the laws of thermodynamics. Hence, the evolution of the tissue is described through its macroscopic deformation, as well as its micro-architecture, macroscopic porosity, mineral volume fraction, osteoblasts and osteoclasts concentrations. After defining the kinematic framework and representative volume, the generalized principle of virtual power is stated. Then, a free energy is defined, which bears a mechanical component (dependent on the porosity, mineral content and orientation of the microstructure), a chemical component (dependent on the macro-porosity and mineral volume fraction, which define the chemical composition of the bone volume), and a biological component (dependent on cell concentrations). From constitutive equations (expression (7.5) of the strain energy density) and the definition of actions on bone remodeling, one can derive an expression for the second principle of thermodynamics. Finally, the actions acting on the rate of changes of the kinematic descriptors are defined, which leads to the expression of the power of internal and external actions.

The model was tested by simulating two cases: variation of calcium concentra-

tion, which directly impacts mineralization, and reduced loading, modulating the mechanobiological feedback. The results obtained with numerical simulations are promising and could be applied to real geometries thanks to a similar algorithm as proposed earlier (Chapter 6).

7.1 Materials and Methods

7.1.1 Description of bone tissue

The present framework aims at describing the evolution of bone material in terms of micro-architecture and mineral content in function of its biological, physical and chemical environment. Hence, a microscopic volume of bone is represented here as a biological tissue with evolving biological (cells), chemical (mineral content) and structural (macro-porosity, micro-orientation) compositions. Figure 7.1 illustrates the representative volume elements of cancellous and cortical bone tissue (respectively top-left and bottom-left) and their composition (right).

Remodeling cells (osteoblasts, osteoclasts) evolve in the fluid space, filling the macroscopic pores of bone tissue (see Figure 7.1). This space is assumed to be a chemical pool providing necessary nutrients and raw materials, that relies on a continuous supply from the marrow and vasculature, although this chemical pool can be perturbed by a diseased state or drug treatment. The macro-pores volume fraction in a representative volume element is represented by the porosity ϕ *i.e.* the ratio between the volume of the macro-pores (V_ϕ) and the volume of the RVE (V_{RVE}). Apposition and resorption of bone happen on bone surfaces, which implies that osteoblasts and osteoclasts activities are dependent on the surface availability, which is accounted for via the specific surface $s_V = \widehat{s_V}(\phi)$. Note that bone with a very high or very low porosity ϕ is also characterized by a low surface availability (see Appendix 7.D for mathematical details).

Bone is a highly organized living material. Its micro-architecture has preferred orientations, depending on the micro-environment, and in particular the mechanical environment [208]. To address the complexity of the organization of bone matrix

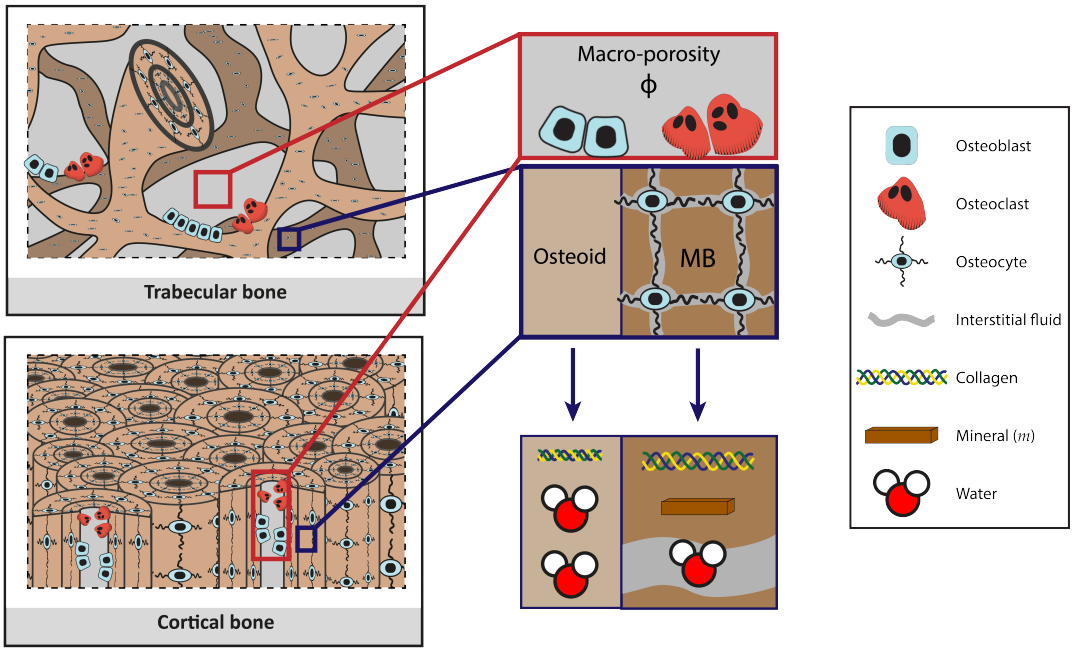

Figure 7.1: Representation of the material. Left: illustration of the representative volume element (RVE) for cortical (bottom) and cancellous/trabecular (top) bone. Top-right: decomposition into macro-pores (where osteoblasts and osteoclasts live), osteoid (newly-formed bone matrix) and mineralized bone matrix (MB). Bottom-right: composition of osteoid and mineralized bone matrix.

in the tissue, a tensor R representing the local microstructural orientation in a representative volume element is introduced as introduced in earlier theories [42, 121]. Additionally, in order to represent the varying degree of mineralization in the bone matrix, a variable m is introduced, denoting the mineral volume fraction in the bone matrix, which is defined as the ratio between the volume of mineral V_m and the volume of bone matrix V_{bm}.

Bone-forming cells – osteoblasts (Ob) – and bone-resorbing cells – osteoclasts (Oc) – respond to a continuous regulation by soluble biochemical factors. Osteoblast and osteoclast numbers can increase via cell proliferation or via differentiation of their precursors into active remodeling cells (Ob, Oc). Remodeling cells also undergo apoptosis (cell death). Signalling pathways regulating cells fate are not only governed by the chemical environment and cellular interactions, but also by mechanics [16, 19,

50]. In fact, cells embedded in the bone matrix (osteocytes) have the capacity to sense mechanical stimuli and modify the chemical environment [19]. In the present theory, osteocytes mechanosensation are not directly accounted for but rather for the result of their actions on cells dynamics and ligand concentrations. Here, osteoblasts and osteoclasts respective volume concentrations (expressed as cell number per unit RVE volume: $C_X = \frac{N_X}{V_{RVE}}$) are referred to as C_{Ob} and C_{Oc}. Note that the actual volume occupied by cells is not accounted for in the calculation of the macroscopic porosity (hosting osteoblasts and osteoclasts) and the microscopic porosity (lacuno-canalicular network, hosting osteocytes).

7.1.2 Generalized kinematics

The present model is set in the framework of generalized continuum mechanics [71, 72]. Thus, bone tissue is modeled as a continuum medium $\mathcal{B}$ occupying a closed region $\mathcal{S} \in \mathcal{E}$ of the 3-dimensional (3D) Euclidean manifold $\mathcal{E}$ at each instant t of the time-line $\mathcal{T}$. Each material point $b \in \mathcal{B}$ carries information about its position in space and the local microstructure.

In light of the previous considerations (Subsection 7.1.1), the state of bone (living) material is described with six kinematic fields, related to its constitution, structure and shape:

- the displacement vector ξ, describing the visible shape;
- the fabric tensor R, characterizing the local orientation of the microstructure;
- the volume fraction of mineral in the bone matrix $m = \frac{V_m}{V_{bm}}$;
- the volume fraction of macro-pores $\phi = \frac{V_\phi}{V_{RVE}} = 1 - \frac{V_{bm}}{V_{RVE}}$;
- the volume concentration of osteoblasts $C_{\mathsf{Ob}} = \frac{N_{\mathsf{Ob}}}{V_{RVE}}$;
- the volume concentration of osteoclasts $C_{\mathsf{Oc}} = \frac{N_{\mathsf{Oc}}}{V_{RVE}}$.

Note that all the above definitions are meant in a Lagrangian sense, *i.e.* as the ratio between the actual value of a variable and a reference ($t = 0$) volume.

Therefore, the complete motion of the body of $\mathcal{B}$ is described by the velocity fields $(\mathbf{v},\mathsf{W},v_\phi,v_m,v_{C_{\mathsf{Ob}}},v_{C_{\mathsf{Oc}}})$, where $\mathbf{v} := \dot{\xi}$ is associated with the displacement ξ, $\mathsf{W} := \dot{\mathsf{R}}\mathsf{R}^{\mathsf{T}}$ with the rotation of the microstructure R, $v_\phi := \dot{\phi}$ with the porosity, $v_m := \dot{m}$ with the mineral volume fraction, $v_{C_{\mathsf{Ob}}} := \dot{C}_{\mathsf{Ob}}$ and $v_{C_{\mathsf{Oc}}} := \dot{C}_{\mathsf{Oc}}$ with the concentrations of osteoblasts and osteoclasts, respectively. Note that the *dot* operator denotes time derivative.

Additionally, the macroscopic displacement ξ and velocity $\mathbf{v}$ take values in $\mathbf{V}$ – the vector spaces of the translations of $\mathcal{E}$; R in Orth^+ – the vector space of the 2nd-order rotation tensors; W in Skw – the vector spaces of the skew-symmetric 2nd-order tensors; v_ϕ, v_m, $v_{C_{\mathsf{Ob}}}$ and $v_{C_{\mathsf{Oc}}}$ in $\mathbb{R}$.

7.1.3 Balance equations

Definition of the forces This paragraph defines the forces representing the actions on the remodeling variables R, ϕ, m, C_{Ob} and C_{Oc}. Hence, the associated inner (i) and outer (o) actions are introduced as follows:

- on the orientation of the microstructure: Λ^i_{R}, Λ^o_{R};
- on the macro-pores: λ^i_ϕ, λ^o_ϕ;
- on the mineral volume fraction: λ^i_m, λ^o_m;
- on osteoblasts concentration: λ^i_{Ob}, λ^o_{Ob};
- on osteoclasts concentration: λ^i_{Oc}, λ^o_{Oc}.

Additionally, as previously introduced [42], one can define $\mathbf{b}^i$ and $\mathbf{b}$ respectively as the inner and outer bulk forces, $\mathbf{t}_\partial$ as the boundary traction and S as the stress tensor.

Generalized principle of virtual power In order to derive the principle of virtual power, test velocity fields are introduced $(\tilde{\mathbf{v}},\tilde{\mathsf{W}},\tilde{\mathsf{v}}_\phi,\tilde{\mathsf{v}}_m,\tilde{\mathsf{v}}_{C_{\mathsf{Ob}}},\tilde{\mathsf{v}}_{C_{\mathsf{Oc}}})$, associated with $(\mathbf{v},\mathsf{W},v_\phi,v_m,v_{C_{\mathsf{Ob}}},v_{C_{\mathsf{Oc}}})$. One can now write the virtual powers of internal and external

forces:

$$
\begin{aligned}
P_i(\tilde{\mathbf{v}}, \tilde{\mathsf{W}}, \tilde{\mathsf{v}}_\phi, \tilde{\mathsf{v}}_m, \tilde{\mathsf{v}}_{C_{\mathsf{Ob}}}, \tilde{\mathsf{v}}_{C_{\mathsf{Oc}}}) &= \int_{\mathcal{B}} (\mathbf{b}^i \cdot \tilde{\mathbf{v}} - \mathsf{S} : \nabla \tilde{\mathbf{v}} + \Lambda^i_{\mathsf{R}} : \tilde{\mathsf{W}} \\
&\quad + \lambda^i_\phi \, \tilde{\mathsf{v}}_\phi + \lambda^i_m \, \tilde{\mathsf{v}}_m + \lambda^i_{\mathsf{Ob}} \, \tilde{\mathsf{v}}_{C_{\mathsf{Ob}}} + \lambda^i_{\mathsf{Oc}} \, \tilde{\mathsf{v}}_{C_{\mathsf{Oc}}}) \, , \\
P_e(\tilde{\mathbf{v}}, \tilde{\mathsf{W}}, \tilde{\mathsf{v}}_\phi, \tilde{\mathsf{v}}_m, \tilde{\mathsf{v}}_{C_{\mathsf{Ob}}}, \tilde{\mathsf{v}}_{C_{\mathsf{Oc}}}) &= \int_{\mathcal{B}} (\mathbf{b} \cdot \tilde{\mathbf{v}} + \Lambda^o_{\mathsf{R}} : \tilde{\mathsf{W}} \\
&\quad + \lambda^o_\phi \, \tilde{\mathsf{v}}_\phi + \lambda^o_m \, \tilde{\mathsf{v}}_m + \lambda^o_{\mathsf{Ob}} \, \tilde{\mathsf{v}}_{C_{\mathsf{Ob}}} + \lambda^o_{\mathsf{Oc}} \, \tilde{\mathsf{v}}_{C_{\mathsf{Oc}}}) \\
&\quad + \int_{\partial \mathcal{B}} \mathbf{t}_\partial \cdot \tilde{\mathbf{v}} \, .
\end{aligned}
\tag{7.3}
$$

In Eq. (7.3), centered dots and double dots denote the inner products in $\mathbf{V}$ and Lin (the space of 2nd order tensors), respectively, and ∇ is the gradient operator.

The following balance laws directly derive from the principle of virtual power:

$$
\begin{aligned}
\mathsf{div}\, \mathsf{S} + \mathbf{b} = 0 \quad &\text{on } \mathcal{B} \, , \qquad \mathsf{S}\, \mathbf{n}_\partial = \mathbf{t}_\partial \quad \text{on } \partial\mathcal{B} \, , \\
\Lambda^i_{\mathsf{R}} + \Lambda^o_{\mathsf{R}} = 0 \quad &\text{on } \mathcal{B} \, , \\
\lambda^i_\phi + \lambda^o_\phi = 0 \quad &\text{on } \mathcal{B} \, , \\
\lambda^i_m + \lambda^o_m = 0 \quad &\text{on } \mathcal{B} \, , \\
\lambda^i_{\mathsf{Ob}} + \lambda^o_{\mathsf{Ob}} = 0 \quad &\text{on } \mathcal{B} \, , \\
\lambda^i_{\mathsf{Oc}} + \lambda^o_{\mathsf{Oc}} = 0 \quad &\text{on } \mathcal{B} \, .
\end{aligned}
\tag{7.4}
$$

Additionally, the principle of material frame-indifference leads classically to $\mathbf{b}^i = 0$ and to the symmetry of the stress tensor S.

7.1.4 Constitutive relations: definition of a free energy

This subsection define a free energy density (with respect to the reference volume) composed of three components:

$$
\psi \left(\mathsf{E}, \mathsf{R}, \phi, m, C_{\mathsf{Ob}}, C_{\mathsf{Oc}} \right) \overset{\text{hyp}}{=} \psi_{mech} \left(\mathsf{R}, \mathsf{E}, \phi, m \right) + \psi_\chi \left(\phi, m \right) + \psi_\beta \left(C_{\mathsf{Ob}}, C_{\mathsf{Oc}} \right) . \tag{7.5}
$$

The first part ψ_{mech} is mechanical and depends on material properties. The term ψ_χ accounts for the purely chemical contribution of the free energy, relying on the chemical potential of the phases (pores, bone matrix of varying degree of mineral-

ization). Finally, the biological term ψ_β describes the energy available from cellular activity and biochemical interactions.

Mechanical contribution The mechanical term ψ_{mech} of the free energy is the classical (macroscopic) strain energy density, depending here on material microstructural properties: orientation of the principal axes of the material R, porosity (ϕ) and mineral volume fraction (m).

$$\psi_{mech}\left(\mathsf{E},\mathsf{R},\phi,m\right) \;\; = \tfrac{1}{2}\mathbb{C}\,\mathsf{E} \;:\mathsf{E} \tag{7.6}$$

where E is the infinitesimal strain tensor, and $\mathbb{C} = \widehat{\mathbb{C}}\left(\mathsf{R},\phi,m\right)$ is the symmetric orientation-, porosity- and mineralization-dependent elasticity tensor. Note that the fourth-order elastic tensor $\mathbb{C}$ can be written as follows:

$$\mathbb{C} = \widehat{\mathbb{C}}(\mathbb{C}_0,\mathsf{R}) = \mathbb{R}\mathbb{C}_0\mathbb{R}^{\mathsf{T}}, \tag{7.7}$$

where $\mathbb{R}$ is the fourth-order rotation tensor associated to R and $\mathbb{C}_0 = \widehat{\mathbb{C}}_0(\phi,m)$ is a prototype elastic tensor.

Assuming ψ_{mech} to be totally differentiable, the time derivative of the mechanical free energy can be derived mathematically and reads as follows:

$$\frac{\mathsf{d}\psi_{mech}}{\mathsf{d}t} = \frac{\partial\psi_{mech}}{\partial\mathsf{E}} : \dot{\mathsf{E}} + \frac{\partial\psi_{mech}}{\partial\mathsf{R}} : \dot{\mathsf{R}} + \frac{\partial\psi_{mech}}{\partial\phi}\dot{\phi} + \frac{\partial\psi_{mech}}{\partial m}\dot{m}, \tag{7.8}$$

where (see Appendix 7.A):

$$\frac{\partial\psi_{mech}}{\partial\mathsf{E}} \;\; = \;\; \mathsf{R}\left(\mathbb{C}_0 : \mathsf{E}^{\triangleleft}\right)\mathsf{R}^{\mathsf{T}}, \tag{7.9}$$

$$\frac{\partial\psi_{mech}}{\partial\mathsf{R}} \;\; = \;\; \left[\mathsf{E},\left(\mathsf{R}\left(\mathbb{C}_0 : \mathsf{E}^{\triangleleft}\right)\mathsf{R}^{\mathsf{T}}\right)\right]\mathsf{R}, \tag{7.10}$$

$$\frac{\partial\psi_{mech}}{\partial\phi} \;\; = \;\; \frac{1}{2}\left(\mathbb{C}_{0,\phi} : \mathsf{E}^{\triangleleft}\right) : \mathsf{E}^{\triangleleft}, \tag{7.11}$$

$$\frac{\partial\psi_{mech}}{\partial m} \;\; = \;\; \frac{1}{2}\left(\mathbb{C}_{0,m} : \mathsf{E}^{\triangleleft}\right) : \mathsf{E}^{\triangleleft}. \tag{7.12}$$

$\mathbb{C}_{0,\phi}$ and $\mathbb{C}_{0,m}$ are the partial derivatives of the elastic tensor function $\widehat{\mathbb{C}}_0$ with respect to porosity ϕ and mineral volume fraction m, $\mathsf{E}^{\triangleleft} = \mathsf{R}^{\mathsf{T}}\mathsf{E}\mathsf{R}$ is the pullback

of the infinitesimal strain tensor, and $[\,,\,] = (\mathsf{A},\mathsf{B}) \mapsto [\mathsf{A},\mathsf{B}] = \mathsf{AB} - \mathsf{BA}$ is the commutation operator.

If I is the identity tensor, note that the function $\widehat{\mathbb{C}}_0 = (\phi, m) \mapsto \widehat{\mathbb{C}}\,(\mathsf{I}, \phi, m) = \mathbb{C}_0$ maps the values of the un-rotated homogenized fourth-order elastic tensor. The function $\widehat{\mathbb{C}}_0$ is defined in Appendix 7.B.

Chemical contribution The chemical energy in the RVE is represented by the Gibbs free energy of a system of three components:

- the pore space whose volume fraction is ϕ, that is assumed to be a pool of species in the aqueous solution allowing the evolution of the mineral and matrix fractions, with electrolytes (el) in solution;
- osteoid (SO), whose volume fraction is ϕ_{SO}, composed of a water-based collageneous gel that is deposited by osteoblasts during the bone formation process;
- mineralized bone (MB), whose volume fraction is ϕ_{MB}, with a solid fraction (SMB) composed of mineralized collagen and a fluid fraction (FMB) composed of water with electrolytes (el) in solution (lacuno-canalicular network).

Note that, as illustrated in Figure 7.1, the volume of fluid in the mineralized matrix is defined as the volume occupied by the lacuno-canalicular spaces. Conversely, the volume fraction of fluid in the osteoid is trapped in the collageneous unmineralized matrix. Hence, in this model, only ions exchanges between the pore spaces situated in the marrow, vascular and lacuno-canalicular spaces are accounted for.

In this framework, the osteoid (SO) is not mineralized, while the mineralized matric (MB) is fully mineralized. Then, the intrinsic composition of SO and MB does not change in time (*i.e.* the proportions of collagen, water, and mineral in SO and MB do not change). The osteoid has a collageneous phase (volume fraction f_{Col}) and a fluid phase (volume fraction f_w^{SO}), whose proportions are linked by the relation: $f_{Col} = 1 - f_w^{\mathsf{SO}}$. The volume fraction of collagen in the matrix is assumed to be constant during mineralization (thus, the same between SO and MB). The mineral volume fraction in the mineralized matrix is defined mathematically as f_m^{MB}, therefore verifying the

following relationship with the remodeling variable m: $f_m^{\mathsf{MB}}\phi_{\mathsf{MB}} = m(1-\phi)$. Thus, the volume fraction of interstitial fluid (FMB fraction of the MB phase) in the mineralized matrix is $f_w^{\mathsf{MB}} = 1 - (f_{Col} + f_m^{\mathsf{MB}})$.

In order to evaluate the local evolution of the chemical energy density in a material point (ψ_χ), one can first calculate the evolution of the total chemical energy Ψ_χ of an RVE of the system:

$$\begin{aligned} \mathsf{d}\Psi_\chi &\overset{\text{hyp}}{=} \sum_i \mu_i \, \mathsf{d}n_i \\ &= \mu^*_{\mathsf{SMB}} \, \mathsf{d}n_{SMB} + \mu^*_{\mathsf{SO}} \, \mathsf{d}n_{SO} + \sum_{el} \mu_{el} \, \mathsf{d}n_{el}, \end{aligned} \quad , \tag{7.13}$$

where μ_i is the chemical potential of the substance i (in $J.mol^{-1}$) and $\mathsf{d}n_i$ is the infinitesimal change in number of moles of species i. The chemical potential μ_i^* stands for the standard potential, as the chemical potential is constant in the solid phases.

Additionally, using Equations (7.75)-(7.77) in Appendix 7.C, the infinitesimal change $\mathsf{d}n_{el}$ in number of moles of species (el) can be expressed in function of the concentration c_{el} of the electrolyte (el) in the macro- (volume V_ϕ) and micro-pores (volume V_{FMB}):

$$\begin{aligned} \mathsf{d}n_{el} &= c_{el}(\mathsf{d}V_{\mathsf{FMB}} + \mathsf{d}V_\phi) \\ &= c_{el}\left(\mathsf{d}\left(f_w^{\mathsf{MB}}\phi_{\mathsf{MB}}V_{RVE}\right) + \mathsf{d}V_\phi\right) \\ &= c_{el}\left(\mathsf{d}\left(\frac{f_w^{\mathsf{MB}}m(1-\phi)}{f_m^{\mathsf{MB}}}V_{RVE}\right) + \mathsf{d}V_\phi\right) \\ &= c_{el}\left[(1 - m\,\frac{f_w^{\mathsf{MB}}}{f_m^{\mathsf{MB}}})\mathsf{d}V_\phi + \frac{f_w^{\mathsf{MB}}}{f_m^{\mathsf{MB}}}(V_{RVE} - V_\phi)\mathsf{d}m\right]. \end{aligned} \tag{7.14}$$

Note that it is assumed here that electrolytes transport occurs sufficiently fast compared to the remodeling and mineralization process. Hence, in the following developments, diffusion of electrolytes is neglected. Therefore, the concentration c_{el} of each electrolyte el is assumed to be uniform in the pores. Additionally, it is postulated that these concentrations are not time-independent, aside from perturbations (*e.g.* modification of the hormonal state).

After mathematical calculations given in Appendix 7.C, the expression of the evolution of the chemical energy is obtained as follows:

$$\dot{\psi_\chi} = \mu_\phi \dot{\phi} + \mu_m \dot{m}, \tag{7.15}$$

with the contributions μ_ϕ and μ_m defined as:

$$\mu_\phi = \widehat{\mu}_\phi(m) = \frac{f_w^{\mathsf{MB}} - 1}{f_m^{\mathsf{MB}}} \widehat{\mu}^*_{\mathsf{SMB}} m + (\frac{m}{f_m^{\mathsf{MB}}} - 1)\widehat{\mu}^*_{\mathsf{SO}} - \left(1 - \frac{f_w^{\mathsf{MB}}}{f_m^{\mathsf{MB}}} m\right) \sum_{el} \mu_{el} c_{el}, \tag{7.16}$$

$$\mu_m = \widehat{\mu}_m(\phi) = \frac{1-\phi}{f_m^{\mathsf{MB}}} \left(1 - f_w^{\mathsf{MB}} \widehat{\mu}^*_{\mathsf{SMB}} - f_{Col} \widehat{\mu}^*_{\mathsf{SO}} + f_w^{\mathsf{MB}} \sum_{el} \mu_{el} c_{el}\right), \tag{7.17}$$

where the chemical potential $\hat{\mu}_i^* = \frac{\mu_i^*}{V_{m,i}}$ stands for the standard potential of the solid phase i per unit volume, and $V_{m,i}$ is its molar volume. The chemical contributions μ_ϕ and μ_m can be interpreted as *effective* chemical potentials of the porosity and mineral volume fractions. Note that μ_ϕ and μ_m are partial derivatives of the chemical energy with respect to ϕ and m, respectively. Therefore, the fact that μ_ϕ and μ_m respectively do not depend on ϕ and m actually stems from the linear definition of the free chemical energy (Eq. (7.13)). Qualitatively, one may interpret these quantities as chemical potentials, which are intrinsic properties of the corresponding substance (here, ϕ or m) and independent of the volume of that substance. However, chemical potentials do depend on the state of the substance, namely the presence of chemical bonds, and therefore the surrounding bone composition.

Biological contribution For the sake of simplicity, the free energy density of bone tissue that arises from cellular activity is defined as a quadratic function of cell concentrations:

$$\psi_\beta(C_{\mathsf{Ob}}, C_{\mathsf{Oc}}) = \frac{1}{2}\beta_{\mathsf{Ob}} C_{\mathsf{Ob}}^2 + \beta_{\mathsf{Oc}} C_{\mathsf{Oc}}^2, \tag{7.18}$$

where β_{Ob} and β_{Oc} are positive real numbers.

The biological energy is assumed to be totally differentiable. This leads to an

expression of the time-derivative of ψ_β:

$$\dot{\psi_\beta}(C_{\mathsf{Ob}}, C_{\mathsf{Oc}}) = \beta_{\mathsf{Ob}} C_{\mathsf{Ob}} \dot{C}_{\mathsf{Ob}} + \beta_{\mathsf{Oc}} C_{\mathsf{Oc}} \dot{C}_{\mathsf{Oc}}, \tag{7.19}$$

Thus, this biological energy ψ_β accounts for the energy available from cells and their activity through metabolism.

7.1.5 Dissipation principle

An isotherm evolution is postulated, which is consistent with the study of bone tissue as a biological system. In the defined framework of generalized continuum mechanics, the Clausius-Duhem equation reads as follows:

$$D_{int} = -\mathsf{p}_i(\mathbf{v}, \mathsf{W}, \dot{\phi}, \dot{m}, \dot{C}_{\mathsf{Ob}}, \dot{C}_{\mathsf{Oc}}) - \dot{\psi}\left(\mathsf{E}, \mathsf{R}, \phi, m, C_{\mathsf{Ob}}, C_{\mathsf{Oc}}\right) \geq 0, \tag{7.20}$$

where D_{int} is the total intrinsic dissipation of the system and p_i is the inner power bulk density.

From the definition of the free energy Eq. (7.5), one can write the evolution of the free energy ψ as the sum of a mechanical (ψ_{mech}, see Eq. (7.8)), a chemical (ψ_χ, see Eq. (7.15)) and a biological (ψ_β, see Eq. (7.19)) component:

$$\dot{\psi} = \dot{\psi}_{mech} + \dot{\psi_\chi} + \dot{\psi_\beta}. \tag{7.21}$$

Given the expression of the power of external actions and the derivative of the free energy Eq. (7.21), the Clausius-Duhem inequality Eq. (7.20) can be now developed as:

$$D_{int} = \boldsymbol{\mathcal{D}}_{\mathsf{E}} : \dot{\mathsf{E}} + \boldsymbol{\mathcal{D}}_{\mathsf{R}} : (\dot{\mathsf{R}}\mathsf{R}^{\mathsf{T}}) + \mathcal{D}_\phi \dot{\phi} + \mathcal{D}_m \dot{m} + \mathcal{D}_{\mathsf{Ob}} \dot{C}_{\mathsf{Ob}} + \mathcal{D}_{\mathsf{Oc}} \dot{C}_{\mathsf{Oc}} \geq 0, \tag{7.22}$$

where $\boldsymbol{\mathcal{D}}_{\mathsf{E}}$, $\boldsymbol{\mathcal{D}}_{\mathsf{R}}$, $\mathcal{D}_\phi$, $\mathcal{D}_m$, $\mathcal{D}_{\mathsf{Ob}}$ and $\mathcal{D}_{\mathsf{Oc}}$ are generalized dissipative forces related to the differences between the energy conveyed to the system by the external actions and the evolution of the free energy with respect to the visible deformation E, the tissue orientation R, the fraction of macro-pores ϕ, the mineral volume fraction m, the con-

centration of osteoblasts C_{Ob} and the concentration of osteoclasts C_{Oc}, respectively. They are functions of the state variables that can be developed as follows:

$$\boldsymbol{\mathcal{D}}_{\mathsf{E}} \overset{\text{def}}{=} \mathsf{S} - \frac{\partial \psi}{\partial \mathsf{E}} \in \mathsf{Sym}, \tag{7.23}$$

$$\boldsymbol{\mathcal{D}}_{\mathsf{R}} \overset{\text{def}}{=} -\Lambda^i_{\mathsf{R}} - \frac{\partial \psi}{\partial \mathsf{R}} \mathsf{R}^{\mathsf{T}} \in \mathsf{Skw}, \tag{7.24}$$

$$\mathcal{D}_{\phi} \overset{\text{def}}{=} -\lambda^i_{\phi} - \frac{\partial \psi}{\partial \phi} \in \mathbb{R}, \tag{7.25}$$

$$\mathcal{D}_{m} \overset{\text{def}}{=} -\lambda^i_{m} - \frac{\partial \psi}{\partial m} \in \mathbb{R}, \tag{7.26}$$

$$\mathcal{D}_{\mathsf{Ob}} \overset{\text{def}}{=} -\lambda^i_{\mathsf{Ob}} - \frac{\partial \psi}{\partial C_{\mathsf{Ob}}} \in \mathbb{R}, \tag{7.27}$$

$$\mathcal{D}_{\mathsf{Oc}} \overset{\text{def}}{=} -\lambda^i_{\mathsf{Oc}} - \frac{\partial \psi}{\partial C_{\mathsf{Oc}}} \in \mathbb{R}. \tag{7.28}$$

Note that, while not written explicitly, external actions can depend on all state variables E, R, ϕ, m, C_{Ob} and C_{Oc}.

The following mathematical assumptions are made, that will establish the evolution laws of the kinematic variables:

$$\boldsymbol{\mathcal{D}}_{\mathsf{E}} \overset{\text{hyp}}{=} 0, \tag{7.29}$$

$$\boldsymbol{\mathcal{D}}_{\mathsf{R}} \overset{\text{hyp}}{=} \mathbb{D}_0 : (\dot{\mathsf{R}}\mathsf{R}^{\mathsf{T}}), \tag{7.30}$$

$$\mathcal{D}_{\phi} \overset{\text{hyp}}{=} d_{\phi}\dot{\phi}, \tag{7.31}$$

$$\mathcal{D}_{m} \overset{\text{hyp}}{=} d_{m}\dot{m}, \tag{7.32}$$

$$\mathcal{D}_{\mathsf{Ob}} \overset{\text{hyp}}{=} d_{\mathsf{Ob}}\dot{C}_{\mathsf{Ob}}, \tag{7.33}$$

$$\mathcal{D}_{\mathsf{Oc}} \overset{\text{hyp}}{=} d_{\mathsf{Oc}}\dot{C}_{\mathsf{Oc}}, \tag{7.34}$$

where $\mathbb{D}_0$ is a fourth-order dissipation tensor ($\forall \mathsf{W} \in \mathsf{Skw}, (\mathbb{D}_0 : \mathsf{W}) : \mathsf{W} \geq 0$; $\mathbb{D}_0 : \mathsf{Skw} \to \mathsf{Skw}$) and d_{ϕ}, d_m, d_{Ob} and d_{Oc} are positive scalar dissipation coefficients respectively associated with the evolution of porosity, mineralization, osteoblasts and osteoclasts concentrations. Equations (7.29)-(7.34) ensure the positivity of the dissipation. Eq. (7.29) states that the dissipation due to the evolution of the visible deformation is neglected. This classical assumption leads to the expression of the

second-order symmetric stress tensor: $\mathsf{S} = \mathsf{R}(\mathbb{C}_0 : \mathsf{E}^{\triangleleft})\mathsf{R}^{\mathsf{T}}$.

Equations (7.30)-(7.34) represent the dissipative processes originating from microstructural changes. With these equations, it is assumed that bone remodeling is a linearly dissipative process that can be quantified with a quadratic function of the rates of the remodeling variables R, ϕ, m, C_{Ob} and C_{Oc}.

7.1.6 Evolution law of bone remodeling

The present section outlines the consequences of Equations (7.30)-(7.34) on bone remodeling dynamics. Definitions of external actions are proposed, leading to an evolution law for bone remodeling. Material properties and activity coefficients defined and used in the following paragraphs are outlined in Table 7.3.

Evolution of the local orientation Using Equations (7.24) and (7.30), one can derive the following expression:

$$\mathbb{D}_0 : (\dot{\mathsf{R}}\mathsf{R}^{\mathsf{T}}) = \Lambda^o_{\mathsf{R}} - [\mathsf{R}(\mathbb{C}_0 : \mathsf{E}^{\triangleleft})\mathsf{R}^{\mathsf{T}}, \mathsf{E}]. \tag{7.35}$$

This equation has been extensively studied in the case of an isotropic dissipation ($\mathbb{D}_0 = d_0\ \mathbb{I}$) with no biochemical stimulation ($\Lambda^o_{\mathsf{R}} = 0$) [42, 121]. The case of bone orthotropic rotary remodeling is not investigated, assuming an alignment of the orientation of the microstructure with the applied stress, resulting in a null rotation velocity $\dot{\mathsf{R}}\mathsf{R}^{\mathsf{T}}$.

Evolution of the porosity and balance of collagen in the RVE Equations (7.31) (remodeling law) and (7.25) (definition) describe the evolution of bone porosity as a function of the state variables as follows:

$$\dot{\phi} = \frac{1}{d_\phi}\left(\lambda^o_\phi - \frac{\partial \psi_{mech}}{\partial \phi} - \mu_\phi\right). \tag{7.36}$$

The external action on porosity is assumed to rely entirely on the remodeling activity of bone cells. Hence, the function λ^o_ϕ is dependent on the actual concentrations of osteoblasts C_{Ob} and osteoclasts C_{Oc} which regulate bone turnover. In order

to investigate the biological action on bone porosity, one can first analyze collagen balance.

Collagen can be laid down by osteoblasts, forming the early bony tissue, the osteoid. It can also be broken down through the acidic action of osteoclasts on the bone matrix. These two actions can be depicted by two reactions: the formation of collagen by osteoblasts, and its resorption by osteoclasts.

Michaelis-Menten kinetics gives a framework to quantify kinetic rate enhancement of a reaction due to the presence of an enzyme. Here, the formation and resorption of collagen are assumed to be mediated by bone cells in a process similar to reaction catalysis. In this scope, the concentration of catalysts (Ob and Oc, around 10^{-4} pM) is much smaller than that of collagen (a few 10^{-3} M). Hence, the cell-mediated collagen production rate (p^{β}_{Col}) is proportional to the concentration of osteoblasts and its degradation rate (δ^{β}_{Col}) is proportional to the concentration of osteoclasts. Thus one can obtain the following expression of rate of collagen quantity evolution in the RVE (v^{β}_{Col}) attributed to biological processes:

$$v^{\beta}_{Col} = p^{\beta}_{Col} - \delta^{\beta}_{Col}, \qquad \begin{aligned} p^{\beta}_{Col} &= k_p C_{\mathsf{Ob}} s_V, \\ \delta^{\beta}_{Col} &= k_d C_{\mathsf{Oc}}\, s_V. \end{aligned} \tag{7.37}$$

where k_p and k_d are defined as positive coefficients accounting for the actions of osteoblasts and osteoclasts, respectively and $s_V = \widehat{s_V}(\phi)$ represents the specific surface, as surface availability is necessary for bone cells to resorb or deposit matrix. The mathematical expression of $\hat{s_V}$ is given in Appendix 7.D.

The number of moles of collagen in bone matrix is assumed not to depend on mineralization (mineral cristallizes and replaces water in unmineralized bone). Therefore, one can write the evolution of porosity due to the presence of bone cells $\dot{\phi}^{\beta}$ as follows:

$$\dot{\phi}^{\beta} = -\kappa\, v^{\beta}_{Col}, \tag{7.38}$$

where κ is a proportionality constant.

In Eq. (7.36), the biological component driving the evolution of porosity resides in

the external actions. Hence, the external action on porosity λ_ϕ^o is defined as follows:

$$\lambda_\phi^o = s_V(k_{\mathsf{res}} C_{\mathsf{Oc}} - k_{\mathsf{form}} C_{\mathsf{Ob}}), \tag{7.39}$$

where $k_{\mathsf{form}} = \kappa k_p$ and $k_{\mathsf{res}} = \kappa k_d$ reflect the actions of remodeling cells on the porosity and the factor s_V the dependency of external actions on surface availability.

Evolution of the mineral content Using Equations (7.26) – definition – and (7.32) – remodeling law, one can infer the evolution of bone mineral volume fraction $\dot{m}$ as a function of the state variables as follows:

$$\dot{m} = \frac{1}{d_m}\left(\lambda_m^o - \frac{\partial \psi_{mech}}{\partial m} - \mu_m\right). \tag{7.40}$$

It is assumed that the external action on mineral content λ_m^o depends on osteoclasts action λ_{Oc}^m (osteoclasts resorb mineralized bone by locally acidifying the medium) and on the chemical environment through λ_χ:

$$\lambda_m^o = \lambda_{\mathsf{Oc}}^m(\phi, m, C_{\mathsf{Oc}}) + \lambda_\chi, \tag{7.41}$$

Here, λ_χ depends on the concentration of electrolytes in solution via their chemical potentials μ_{el} and λ_{Oc}^m is proportional to osteoclasts concentration C_{Oc}:

$$\lambda_{\mathsf{Oc}}^m(\phi, m, C_{\mathsf{Oc}}) = -\alpha_{\mathsf{Oc}}^m C_{\mathsf{Oc}}(1-\phi) m s_V, \tag{7.42}$$

$$\lambda_\chi = \alpha_\chi^m \sum_{el} \nu_{el}\mu_{el}, \tag{7.43}$$

where α_{Oc}^m and α_χ^m are activity coefficients (positive real numbers), respectively in $\mathsf{mm.mol.m}^{-3}$ and Pa.

The action of osteoclasts is assumed proportional to $(1-\phi)m$, which is proportional to the fraction of mineralized matrix. This assumption is supported by the fact that osteoclasts preferentially resorb mineralized bone. The action of osteoclasts λ_{Oc}^m in Eq. (7.43) is proportional to s_V, the specific surface. This translates the fact that a

small specific surface – which can be due to low or high porosity levels – results into a lesser access of resorbing cells to bone surface. Moreover, the chemical action λ_χ described in Eq. (7.43) is proportional to the weighted sum of the chemical potentials of the reactives of the reaction of mineralization into hydroxyapatite crystals.

Evolution of cells concentration Equations (7.27), (7.28), (7.33) and (7.34) lead to the formulation of the evolution laws of osteoblasts and osteoclasts populations:

$$\dot{C}_{\mathsf{Ob}} = \frac{1}{d_{\mathsf{Ob}}}\left(\lambda^o_{\mathsf{Ob}} - \frac{\partial \psi_\beta}{\partial C_{\mathsf{Ob}}}\right), \tag{7.44}$$

$$\dot{C}_{\mathsf{Oc}} = \frac{1}{d_{\mathsf{Oc}}}\left(\lambda^o_{\mathsf{Oc}} - \frac{\partial \psi_\beta}{\partial C_{\mathsf{Oc}}}\right). \tag{7.45}$$

The external actions on osteoblasts and osteoclasts concentrations are assumed to originate from effects of soluble factors produced by bone cells. Hence, one can separate autocrine regulation (biochemical processes affecting the cell type which also regulates or produces them) and paracrine actions (processes affecting another cell type). Note that only two cell types are considered, namely Ob and Oc, since osteocytes are not explicitly described in the model. Based on previous works [101], power laws are proposed to describe these regulations. Hence, exponents g_{xy} are defined to represent the processes affecting or regulated by osteoblasts ($x, y = b$) and osteoclasts ($x, y = c$). Thus, the external actions related to osteoblasts (λ^o_{Ob}) and osteoclasts (λ^o_{Oc}) are assumed to depend on osteoblasts ($N_{\mathsf{Ob}} = C_{\mathsf{Ob}} V_{RVE}$) and osteoclasts ($N_{\mathsf{Oc}} = C_{\mathsf{Oc}} V_{RVE}$) numbers in the RVE, as follows:

$$\lambda^o_{\mathsf{Ob}} = p_{\mathsf{Ob}} N_{\mathsf{Oc}}^{g_{cb}} N_{\mathsf{Ob}}^{g_{bb}}\,, \tag{7.46}$$

$$\lambda^o_{\mathsf{Oc}} = p_{\mathsf{Oc}} N_{\mathsf{Oc}}^{g_{cc}} N_{\mathsf{Ob}}^{g_{bc}}, \tag{7.47}$$

where p_{Ob} and p_{Oc} are regulation coefficients of osteoblasts and osteoclasts, respectively. Note that the exponents g_{xy} can designate either autocrine (g_{xx}) or paracrine (g_{xy}, $x \neq y$) processes.

Using the derivative of the biological component of the free energy Eq. (7.19), Equations (7.44-7.45) become:

$$\dot{C}_{\mathsf{Ob}} = \frac{1}{d_{\mathsf{Ob}}} \left(p_{\mathsf{Ob}} N_{\mathsf{Oc}}^{g_{cb}} N_{\mathsf{Ob}}^{g_{bb}} - \beta_{\mathsf{Ob}} C_{\mathsf{Ob}} \right), \tag{7.48}$$

$$\dot{C}_{\mathsf{Oc}} = \frac{1}{d_{\mathsf{Oc}}} \left(p_{\mathsf{Oc}} N_{\mathsf{Oc}}^{g_{cc}} N_{\mathsf{Ob}}^{g_{bc}} - \beta_{\mathsf{Oc}} C_{\mathsf{Oc}} \right). \tag{7.49}$$

Here, one finds the same system of equations as one of the classical mechanobiology works on bone remodeling, by Komarova et al. [101]. The parameters β_{Ob} and β_{Oc} that stand for cells removal rates in the original work [101] are recovered as the result of the variation of free energy. Note that the same structure of bone remodeling evolution laws was used in similar mechanobiological approaches [110, 154, 172]. Hence, cells turnover is regulated by the external work, here in the form of the action of bone multicellular units, which competes with the variation of energy of the system, that occurs through regulation of cell numbers. Note that, in order to implement more complex quantitative mechanological approaches such as the work of Pivonka and colleagues [122, 156], one could postulate a different expression for external actions related to osteoblasts and osteoclasts concentrations, therefore leading to new evolution laws.

Osteocytes are differentiated bone cells embedded in the matrix that have the ability to sense mechanical stimuli and modulate their signals to remodeling cells. Mathematically, osteocytes mechanosensation is integrated into Equations (7.48-7.49) via the parameters of the external actions λ^o_{Ob} and λ^o_{Oc}. In particular, in line with previous work [122], two mechanically sensitive signalling pathways are accounted for, relying on the production of two molecules by osteocytes:

- The production of sclerostin, inhibited by an increase in mechanical stimulus, down-regulates osteoblasts proliferation through a competitive binding to osteoblast Wnt receptors.

- The production of nitric oxide, inhibited by a decrease in mechanical stimulus, inhibits osteoclasts proliferation by inhibiting RANKL production by osteoblastic (precursor) cells.

From these considerations, autocrine ($\widehat{g}_{bb}(\varsigma)$) and paracrine ($\widehat{g}_{bc}(\varsigma)$) functions are defined, which modulate the influence of osteoblastic cells on remodeling via the mechanical stimulus assumed to be the strain energy density which, in turn, depends on the remodeling state of the material $\varsigma = \widehat{\psi}_{mech}(\mathsf{R}, \mathsf{E}, \phi, m)$. The autocrine and paracrine functions read as follows:

$$\widehat{g}_{bb}(\varsigma) = \begin{cases} g^0_{bb} + 0.2\, f_{\mathsf{Hill}}(\varsigma - \varsigma_0) & \text{if } \varsigma > \varsigma_0, \\ g^0_{bb} & \text{otherwise}, \end{cases} \tag{7.50}$$

$$\widehat{g}_{bc}(\varsigma) = \begin{cases} g^0_{bc} + 0.2\, f_{\mathsf{Hill}}(\varsigma - \varsigma_0) & \text{if } \varsigma < \varsigma_0, \\ g^0_{bc} & \text{otherwise}, \end{cases} \tag{7.51}$$

where $f_{\mathsf{Hill}}(\Delta) = \dfrac{\Delta^2}{K^2_{\mathsf{Hill}} + \Delta^2}$ is a second-order Hill function, classically used to model the action or behavior of a ligand [151], and here to model the role of mechanics in cells dynamics. The steady-state value of the mechanical stimulus is given by ς_0. The values of the mechanobiological parameters are given in Table 7.1. Autocrine (g_{bb}, blue) and paracrine (g_{bc}, red) mechanobiological functions are illustrated in Figure 7.2.

Table 7.1: Mechanobiological and biochemical regulation parameters .

Symbol	Value	Unit
p_{Ob}	4	day^{-1}
p_{Oc}	3	day^{-1}
g^0_{bb}	0	-
g^0_{bc}	-0.5	-
g_{cb}	1	-
g_{cc}	0.5	-
k_{res}	$4.1 \cdot 10^6$	N.
k_{form}	$2.0 \cdot 10^3$	N
K_{Hill}	50	Pa

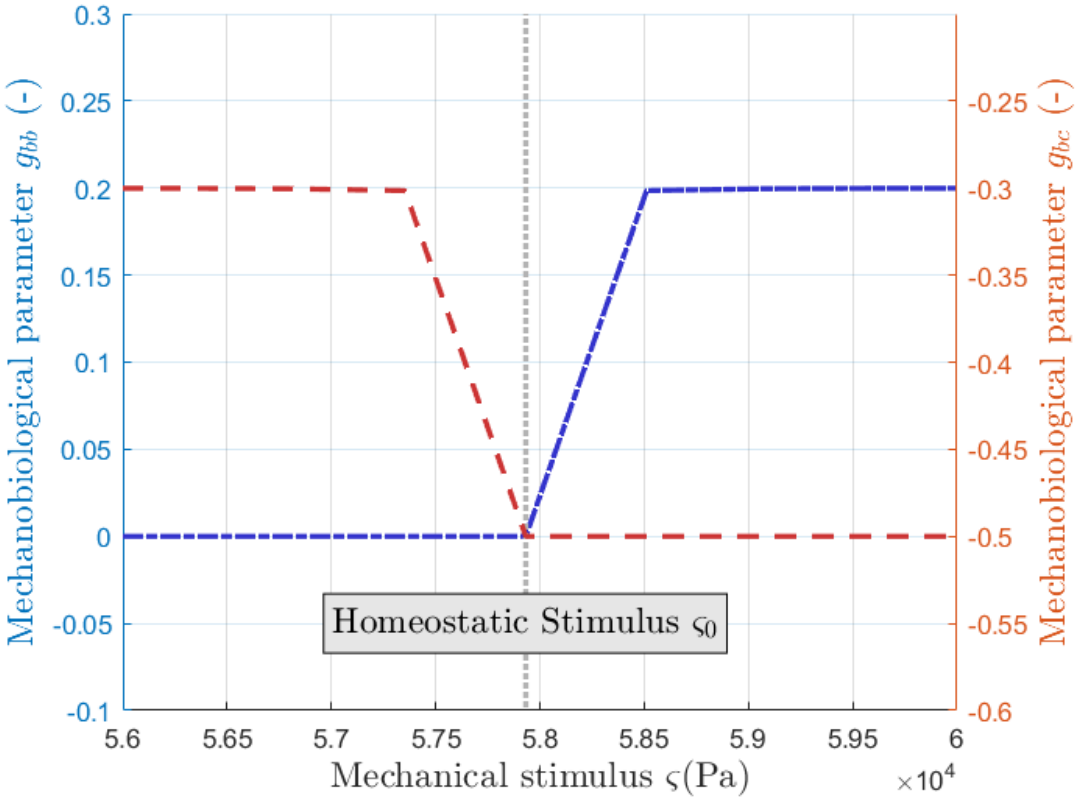

Figure 7.2: Evolution of biological mechano-sensitive parameters g_{bb} (blue) and g_{bc} (red) with respect to mechanical stimulus $\widehat{\Psi}$.

7.2 Results and Discussion

This section presents simulations illustrating the dynamics of bone remodeling in terms of mineralization, porosity and cells turnover. For all simulations, a uniaxial macroscopic compressive stress $\mathsf{S} = \sigma(t)\mathbf{e} \otimes \mathbf{e}$ ($\sigma(t) < 0$) is applied to the RVE along the material axis (see Appendix 7.B for the homogenization of material properties). Unless otherwise specified, the stress magnitude is constant and equal to its initial value $\sigma(t) = \sigma_0$ (see Table 7.2).

The presented results are obtained from computational simulations using Matlab® R2017b ODE solver [3]. Unless otherwise stated, the initial values displayed in Table 7.2 were used for the system state variables, and Table 7.3 for material properties. Note that the values of initial remodeling variables were obtained with a simulation, by finding a steady-state corresponding to the imposed stress σ_0. Moreover, the

homeostatic stimulus ς_0 was calculated arbitrarily as the strain energy of trabecular bone with a macroscopic porosity $\phi = 0.8$ and mineral fraction in bone matrix $m = 0.3$ under the imposed stress σ_0.

Additionally, one may recall here that microstructure rotation is not accounted for in the simulations of this study to focus on the novel elements of the present theory.

Table 7.2: Initial values of remodeling variables and parameters.

Symbol	Value	Unit
ϕ	0.823	-
m	0.390	-
C_{Ob}	247	mm^{-3}
C_{Oc}	0.955	mm^{-3}
σ^0	-10	MPa
ς_0	$57.9 \cdot 10^3$	Pa

7.2.1 Separate influences of chemistry, mechanics and biology

First, chemo-mechanics and mechanobiology are analyzed separately, respectively in Figures 7.3 and 7.4. First, in Figure 7.3, the biological contribution is set to zero with the condition: $\forall t \geq 0$, $C_{\mathsf{Ob}}(t) = 0$, $C_{\mathsf{Oc}}(t) = 0$. Therefore, the external actions on porosity λ^o_ϕ and mineral content $\lambda^o_m = \lambda_\chi$ are only chemical and the variations of free energy with respect to porosity $\frac{\partial \psi}{\partial \phi}$ and mineral content $\frac{\partial \psi}{\partial m}$ depend on chemistry and mechanics:

$$\lambda^o_\phi = 0, \tag{7.52}$$

$$\lambda^o_m = \lambda_\chi, \tag{7.53}$$

$$\frac{\partial \psi}{\partial \phi} = \mu_\phi + \frac{\partial \psi_{mech}}{\partial \phi}, \tag{7.54}$$

$$\frac{\partial \psi}{\partial m} = \mu_m + \frac{\partial \psi_{mech}}{\partial m}. \tag{7.55}$$

Without any cells, the material naturally tends to mineralize, proportionally to the difference between external actions λ_χ (via the chemical potential of the reactive species in solution for precipitation) and the variation of free energy with respect

Table 7.3: Material properties of bone tissue and external actions parameters: dissipation coefficients (Diss. coeff.) relative to specific turnovers (turn.), chemical concentrations (conc.) and potentials, activity coefficients, composition volume fractions. Values were either set by calibration (C) or recovered from literature (L).

Symbol	Value	Unit	Definition	Source
f_{Col}	0.30	-	Collagen vol. frac. in matrix	L [79]
f_m^{MB}	0.45	-	Mineral vol. frac. in MB	L [79]
d_ϕ	$1.0 \cdot 10^5$	$\mathsf{MPa.day}^{-1}$	Diss. coeff. (matrix turn.)	C
d_m	$1.6 \cdot 10^3$	$\mathsf{MPa.day}^{-1}$	Diss. coeff. (mineral turn.)	C
$[\mathsf{Ca}^{2+}]$	$2.5 \cdot 10^{-3}$	$\mathsf{mol.L}^{-1}$	Calcium conc.	L [73]
$[\mathsf{PO}_4^{3-}]$	$1.3 \cdot 10^{-3}$	$\mathsf{mol.L}^{-1}$	Phosphate conc.	L [8]
$[\mathsf{OH}^-]$	$2.5 \cdot 10^{-7}$	$\mathsf{mol.L}^{-1}$	Hydroxyde conc.	L [8]
$\nu_{\mathsf{Ca}^{2+}}$	5	-	Stoechiometric coeff.	L [58]
$\nu_{\mathsf{PO}_4^{3-}}$	3	-	Stoechiometric coeff.	L [58]
ν_{OH^-}	1	-	Stoechiometric coeff.	L [58]
$\mu_{\mathsf{Ca}^{2+}}$	$-5.5 \cdot 10^2$	$\mathsf{kJ.mol}^{-1}$	Chemical potential	L [89]
$\mu_{\mathsf{PO}_4^{3-}}$	$-1.0 \cdot 10^3$	$\mathsf{kJ.mol}^{-1}$	Chemical potential	L [89]
μ_{OH^-}	$-1.6 \cdot 10^2$	$\mathsf{kJ.mol}^{-1}$	Chemical potential	L [89]
$\widehat{\mu}^*_{\mathsf{SMB}}$	$-1.0 \cdot 10^3$	$\mathsf{J.m}^{-3}$	Chemical potential	C
$\widehat{\mu}^*_{\mathsf{SO}}$	$-1.0 \cdot 10^3$	$\mathsf{J.m}^{-3}$	Chemical potential	C
β_{Ob}	0.020	N	Osteoblastic force	L [101]
β_{Oc}	0.20	N	Osteoblastic force	L [101]
d_{Ob}	1.0	$\mathsf{MPa.day}^{-1}$	Diss. coeff. (Ob turn.)	L [101]
d_{Oc}	1.0	$\mathsf{MPa.day}^{-1}$	Diss. coeff. (Oc turn.)	L [101]
α^m_{Oc}	$-1.8 \cdot 10^6$	$\mathsf{mm.mol.m}^{-3}$	Activity coefficient	C
α^m_χ	$2.0 \cdot 10^{-3}$	Pa	Activity coefficient	C

to mineral content m (Eq. (7.40)). Moreover, one can note that the variation of free energy with respect to porosity is strictly negative (Figure 7.3(b)), leading to an increase in macroscopic porosity with time. This remark matches the observation of Sansalone and coworkers, who noticed a decay in biological tissue properties in the absence of an "external stimulus" (attributed to biochemistry) [98]. Note that, for high porosities, the present model may reach the limits of its application as the mixture theory for the material properties homogenization (see Appendix 7.B) would be inadequate.

In Figure 7.4, the focus is set on mechanobiology. Cell dynamics are analyzed by

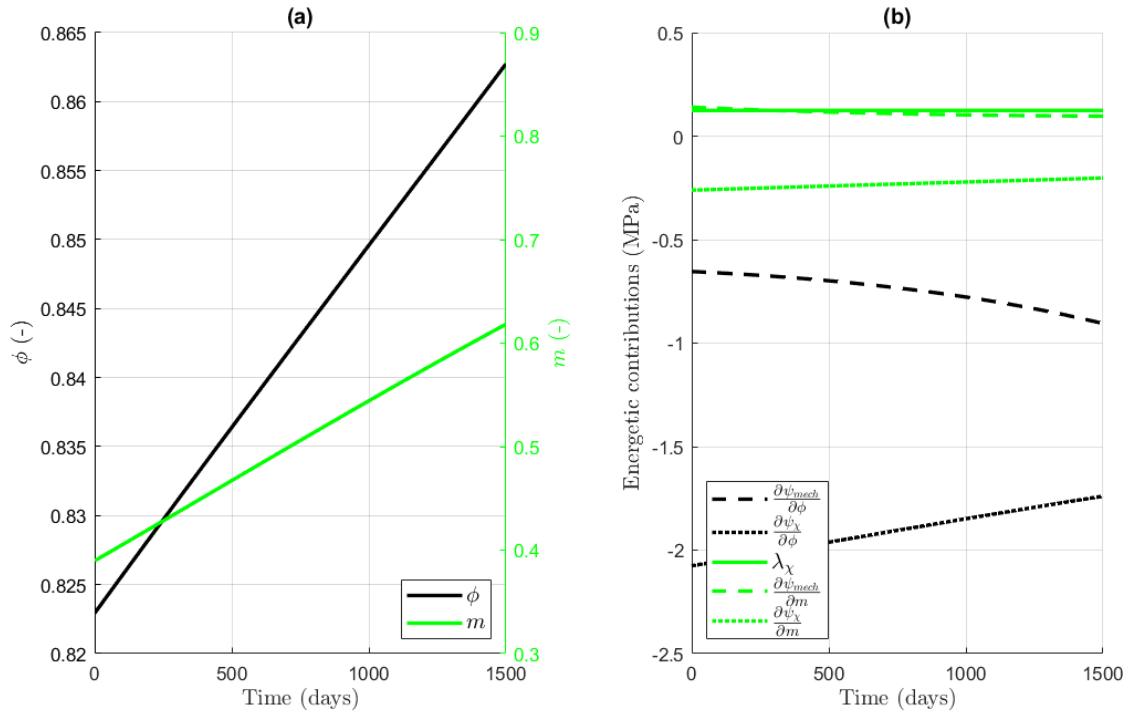

Figure 7.3: Evolution of the system without the influence of cells ($C_{\mathsf{Ob}} = 0$, $C_{\mathsf{Oc}} = 0$): variation of porosity ϕ and mineral content m (a) and contributions of mechanical and chemical energy (b).

prescribing the mechanical stimulus $\varsigma(t)$:

$$\varsigma(t) = \begin{cases} 1.05\,\varsigma_0, & \text{if } 50\,\text{day} \leq t \leq 100\,\text{day}, \\ 0.95\,\varsigma_0, & \text{if } 150\,\text{day} \leq t \leq 200\,\text{day}, \\ \varsigma_0, & \text{otherwise.} \end{cases} \tag{7.56}$$

Here, the influence of different values of the Hill coefficient K_{Hill} on the evolution of osteoblasts and osteoclasts numbers is evaluated in parallel with the mechanical stimulus ς (a) and the autocrine and paracrine mechano-sensitive parameters g_{bb} and g_{bc} (b). In line with early theories on bone remodeling [26, 27, 62] and later numerical works [83, 172], the catabolic response (towards bone resorption) to a decrease in mechanical loading is much stronger than the anabolic response (towards bone formation) in case of overload. Mathematically, this phenomenon is represented by the choice of the mechanobiological parameters β_{Ob} and β_{Oc} driving the cell popula-

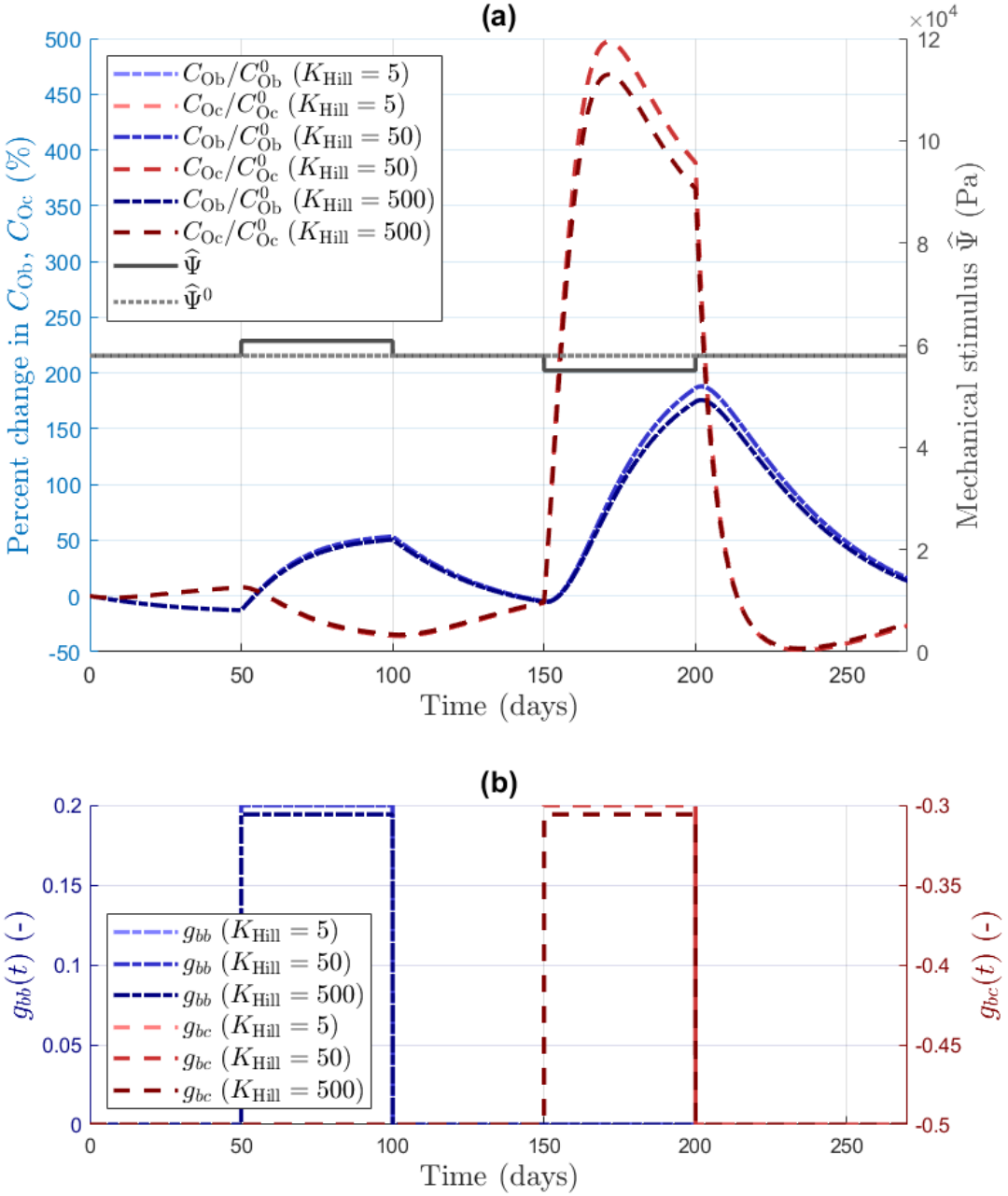

Figure 7.4: Evolution of osteoblasts and osteoclasts numbers driven by the mechanical stimulus ς with respect to time (a) and biological mechano-sensitive parameters g_{bb} and g_{bc} with respect to time (b).

tions evolutions. As there is a slower response by osteoblasts than by osteoclasts, the coefficient β_{Oc} is set much larger than β_{Ob} ($\beta_{\mathsf{Oc}} = 10\,\beta_{\mathsf{Ob}}$) (Figure 7.4(a)). Finally, one can also note that the Hill parameter K_{Hill} regulating the cellular response has

a small effect on both the evolution of cell populations and the mechano-sensitive parameters g_{xy} (the curves corresponding to $K_{\mathsf{Hill}} = 5\,\mathsf{MPa}$ and $K_{\mathsf{Hill}} = 50\,\mathsf{MPa}$ are superimposed in Figure 7.4).

7.2.2 Combined influences of mechanics, chemistry and biology

This subsection presents results of the full model (still without microstructure rotation) and analyze the effects of a modification of the environment, in terms of chemical concentrations, mechanical loading and biological turnover.

Modification of the chemical environment Here, a decrease in calcium serum concentration is simulated over a given period of time $[T_{\mathsf{start}}, T_{\mathsf{end}}]$ ($T_{\mathsf{start}} = 100\,\mathsf{day}$, $T_{\mathsf{end}} = 500\,\mathsf{day}$). In this context, one can observe the biological (a) and microstructural (b) responses, as presented in Figure 7.5. During the period highlighted in gray $[T_{\mathsf{start}}, T_{\mathsf{end}}]$, the concentration of calcium is reduced by 20%.

One can see that during the low calcium period, the mineral fraction m decreases, and then slowly recovers after reinstatement of the homeostatic calcium ions concentration. Hence, as expected, a decreased amount of serum calcium shifts the equilibrium of the mineral precipitation reaction, leading to a decrease of the mineral content.

Cells concentrations are also slightly modified with a small decrease in osteoclast numbers and increase in osteoblast numbers, most likely as a response to the loss of bone stiffness with mineral dissolution (Figure 7.5(a)). One can also note the decrease in porosity, to a lesser extent. This decay is a consequence of the change in osteoclasts and osteoblasts concentrations, triggering an augmentation of bone matrix volume fraction.

Modification of the mechanical environment and impact on mechanobiology The bone tissue is now submitted to a decrease in the mechanical stress S during a defined period of time $[T_{\mathsf{start}}, T_{\mathsf{end}}]$, where $T_{\mathsf{start}} = 100\,\mathsf{day}$ and $T_{\mathsf{end}} = 500\,\mathsf{day}$.

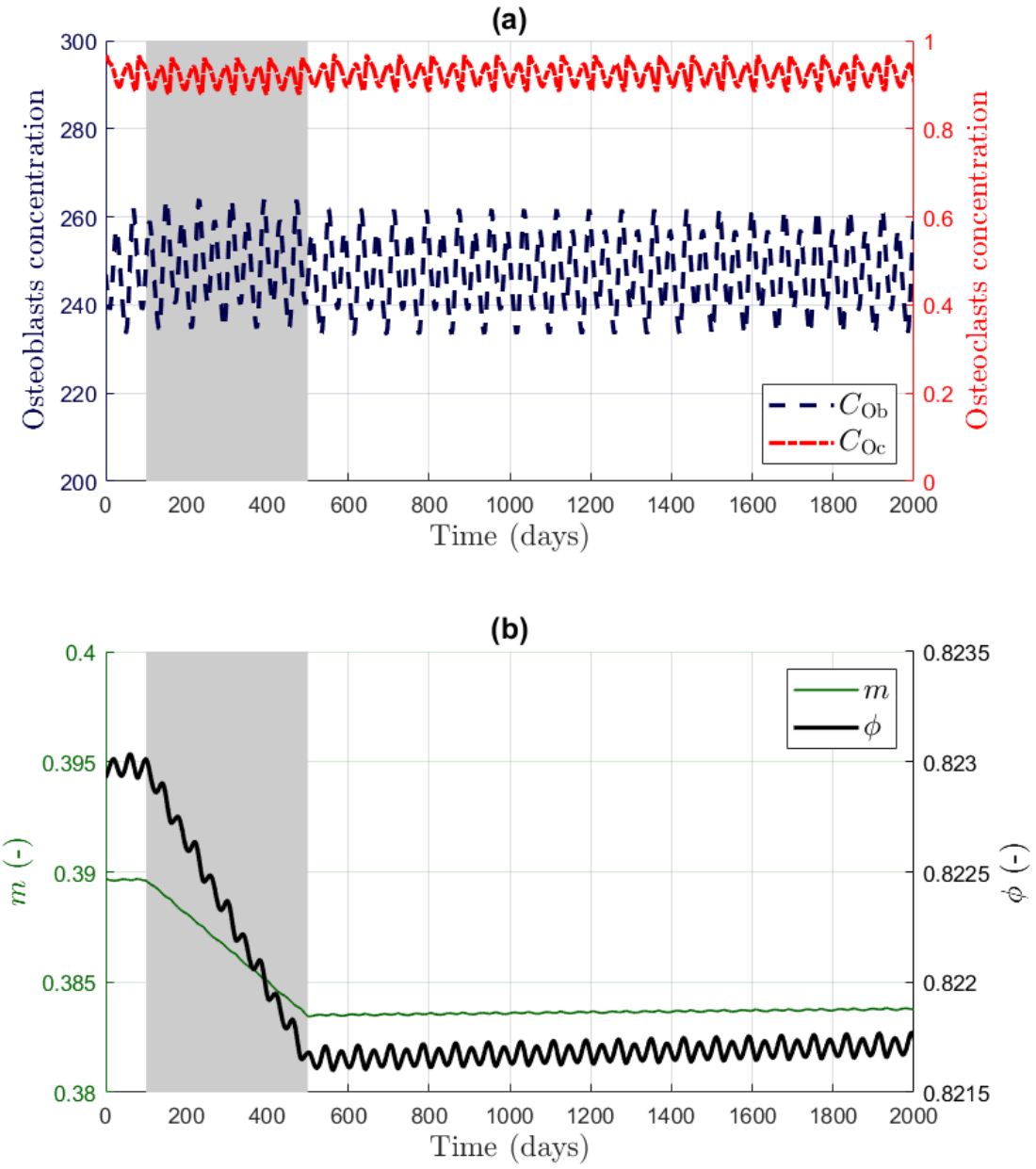

Figure 7.5: Evolution of osteoblasts (dashed, blue) and osteoclasts (dash-dotted, red) concentrations (a) and bone mineral fraction m (thin, green) and porosity (thick, black) (b). Calcium concentration is reduced by 20% between $T_{\mathsf{start}} = 100\,\mathsf{day}$ and $T_{\mathsf{end}} = 500\,\mathsf{day}$ (gray-shaded areas).

To perform this numerical simulation, the following law for the macroscopic stress is implemented:

$$\sigma(t) = \begin{cases} 0.9\,\sigma^0 & \text{if } T_{\text{start}} \leq t \leq T_{\text{end}}, \\ \sigma^0 & \text{otherwise.} \end{cases} \tag{7.57}$$

Figure 7.6 depicts the evolution of cell concentrations (a) and microstructural properties (b) during the simulation.

Results show that, following the decrease in mechanical stress, there is a peak in osteoblasts and osteoclasts numbers (Figure 7.6(a)). This peak is observed also when changing the function describing the variations of the stress $\sigma(t)$ by smoothing the step at T_{start} via the implementation of a ramp over one or a few days to get to the lower value $\sigma(t) = 0.9\,\sigma^0$ (data not shown). In fact, the sudden increase in bone turnover may be due to the decrease of mechanical loading that promotes osteoblastic and osteoclastic activity, as stated in earlier theories [60, 62]. Here, disuse leads to an increase in bone turnover via the osteoblasts-mediated Wnt and RANKL pathways [122].

The increase in osteoblasts and osteoclasts numbers results in a rapid increase in porosity and decrease in mineral content (Figure 7.6(b)). If the homeostatic load is not reinstated, the porosity and mineral fraction stabilize at different values than the initial ones. As expected, in line with Wolff's law [208] and later similar theories [27, 60], the model retrieves that mechanical properties of the tissue eventually decrease as a result of a reduced mechanical demand. Here, the mechanobiological model structure (power law in Equations (7.46)-(7.47)) drives cell numbers back to their initial values, therefore preventing the long-term positive mechanical feedback. The use of another mechanobiological model could account for long-term cells turnover changes (see for example [156]), unlike Komarova et al.'s model which represented single remodeling events [101].

Reuse, simulated by reinstating the initial stress σ^0, leads to an increase in mineral fraction and decrease in porosity. Note that cell numbers and microstructural properties evolve towards their initial values during reuse.

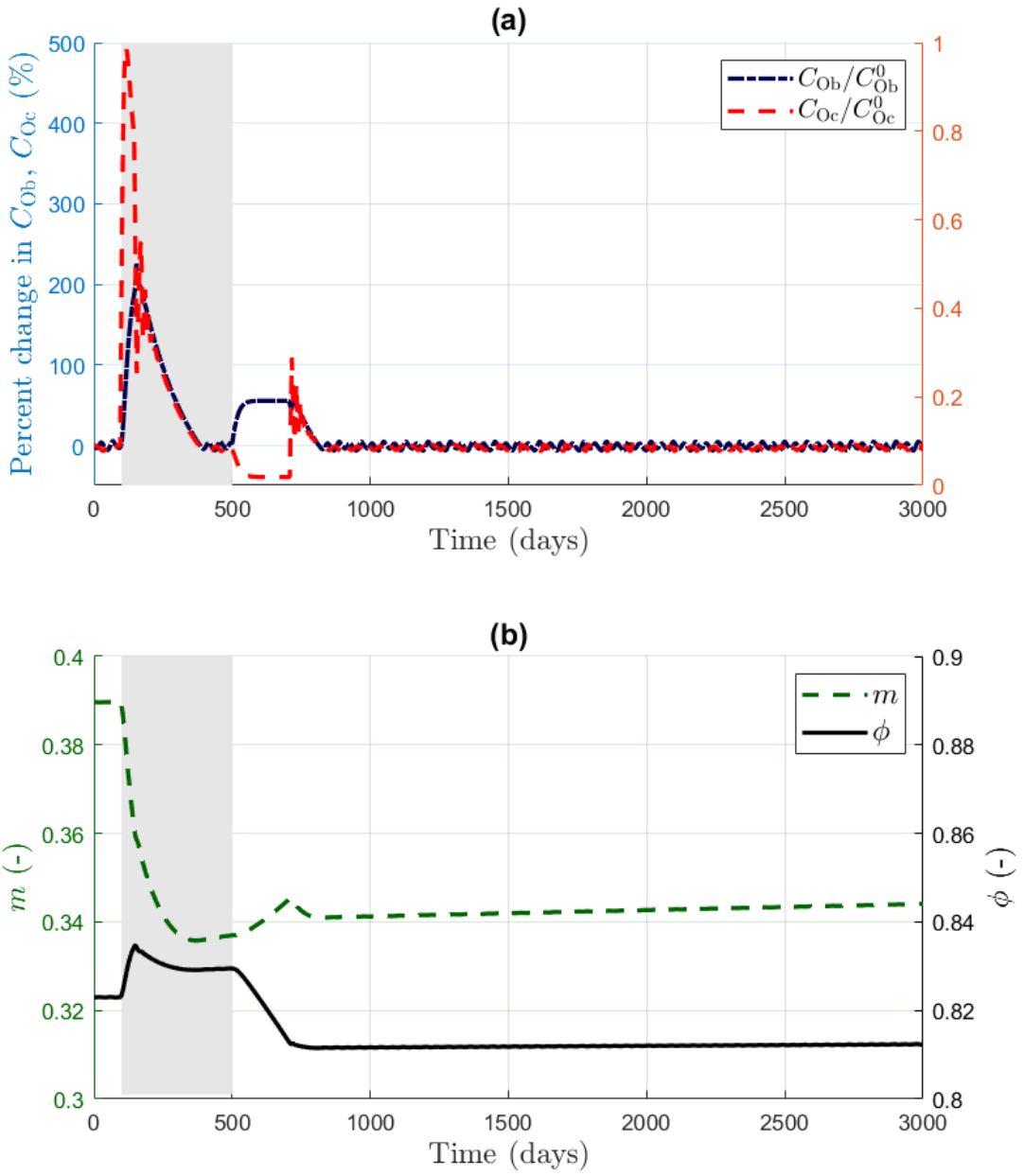

Figure 7.6: Percent changes in osteoblasts (dashed, blue) and osteoclasts (dash-dotted, red) concentrations (a) and bone mineral fraction m (thin, green) and porosity (thick, black) (b).Mechanical loading is reduced by 10% between $T_{\mathsf{start}} = 100\,\mathsf{day}$ and $T_{\mathsf{end}} = 500\,\mathsf{day}$ (gray-shaded areas).

7.3 Conclusions

This section presented a novel multiscale approach of bone remodeling bridging mechanobiology, chemistry and macro-scale mechanics.

By introducing a free-energy depending on these three above-mentioned phenomena and developing consistent formulations for external actions, the model was able to catch the interactions between the different physics. In particular, a lack of calcium modified mineralization reaction kinetics, triggering mineral dissolution.

Additionnally, the decrease of mechanical loading leads to an increase in bone cells turnover and an increase in bone macro-pores fraction (ϕ). These preliminary results are encouraging and could be associated in the future with a more comprehensive framework of mechanobiological dynamics as presented by Martin and coworkers [122].

Ultimately, the joint study of mechanobiology and chemistry aims at capturing complex metabolic dynamics, as the role of mineralization can be essential to the understanding of bone turnover in the context of pathologies and their treatments (see the recent work of Martinez-Reina and Pivonka on a model of bone mineralization and remodeling in the context of an anti-catabolic treatment of osteoporosis [125]).

Appendices

7.A Deriving the evolution of the free energy

As defined in Eq. (7.6), the mechanical term ψ_{mech} of the free energy is the classical (macroscopic) strain energy density that depends on four variables: E, R, ϕ and m. Classically, one can assume that the mechanical free energy ψ_{mech} has a total derivative, leading to:

$$\dot{\psi}_{mech} = \frac{\partial \psi_{mech}}{\partial \mathsf{E}} : \dot{\mathsf{E}} + \frac{\partial \psi_{mech}}{\partial \mathsf{R}} : \dot{\mathsf{R}} + \frac{\partial \psi_{mech}}{\partial \phi}\dot{\phi} + \frac{\partial \psi_{mech}}{\partial m}\dot{m} \tag{7.58}$$

If one isolates the terms relative to the evolution of displacement and orientation,

the derivative becomes now:

$$\frac{\mathsf{d}\psi_{mech}}{\mathsf{d}t}|_{\phi,m} = \frac{\partial\psi_{mech}}{\partial\mathsf{E}} : \dot{\mathsf{E}} + \frac{\partial\psi_{mech}}{\partial\mathsf{R}} : \dot{\mathsf{R}}. \tag{7.59}$$

From the definition of the rotated small strain tensor $\mathsf{E}^{\triangleleft} = \mathsf{R}^{\mathsf{T}}\mathsf{E}\mathsf{R}$, Eq. (7.6) becomes:

$$\psi_{mech} = \frac{1}{2}\left(\mathsf{R}(\mathbb{C}_0 : \mathsf{E}^{\triangleleft})\mathsf{R}^{\mathsf{T}}\right) : \mathsf{E} = \frac{1}{2}(\mathbb{C}_0 : \mathsf{E}^{\triangleleft}) : \mathsf{E}^{\triangleleft}. \tag{7.60}$$

Therefore, one can derive the following developments for the time derivative:

$$\begin{aligned}
\frac{\mathsf{d}\psi_{mech}}{\mathsf{d}t}|_{\phi,m} &= \frac{1}{2}\frac{(\mathbb{C}_0 : \mathsf{E}^{\triangleleft}) : \mathsf{E}^{\triangleleft})}{\mathsf{d}t}|_{\phi,m} \\
&= \frac{1}{2}\frac{\partial((\mathbb{C}_0 : \mathsf{E}^{\triangleleft}) : \mathsf{E}^{\triangleleft})}{\partial\mathsf{E}^{\triangleleft}} : \frac{\mathsf{d}(\mathsf{R}^{\mathsf{T}}\mathsf{E}\mathsf{R})}{\mathsf{d}t} \\
&= (\mathbb{C}_0 : \mathsf{E}^{\triangleleft}) : \left((\dot{\mathsf{E}})^{\triangleleft} + \dot{\mathsf{R}^{\mathsf{T}}}\mathsf{E}\mathsf{R} + \mathsf{R}^{\mathsf{T}}\mathsf{E}\dot{\mathsf{R}}\right) \\
&= (\mathbb{C}_0 : \mathsf{E}^{\triangleleft}) : \left((\dot{\mathsf{E}})^{\triangleleft} + (-\mathsf{R}^{\mathsf{T}}\dot{\mathsf{R}}\mathsf{R}^{\mathsf{T}})\mathsf{E}\mathsf{R} + \mathsf{R}^{\mathsf{T}}\mathsf{E}\dot{\mathsf{R}}\right) \\
&= \left(\mathsf{R}(\mathbb{C}_0 : \mathsf{E}^{\triangleleft})\mathsf{R}^{\mathsf{T}}\right) : \left(\dot{\mathsf{E}} - (\dot{\mathsf{R}}\mathsf{R}^{\mathsf{T}})\mathsf{E} + \mathsf{E}(\dot{\mathsf{R}}\mathsf{R}^{\mathsf{T}})\right) \\
&= \left(\mathsf{R}\left(\mathbb{C}_0 : \mathsf{E}^{\triangleleft}\right)\mathsf{R}^{\mathsf{T}}\right) : \dot{\mathsf{E}} \\
&\qquad - \left(\left(\mathsf{R}(\mathbb{C}_0 : \mathsf{E}^{\triangleleft})\mathsf{R}^{\mathsf{T}}\right)\mathsf{E} + \mathsf{E}\left(\mathsf{R}(\mathbb{C}_0 : \mathsf{E}^{\triangleleft})\mathsf{R}^{\mathsf{T}}\right)\right) : \left(\dot{\mathsf{R}}\mathsf{R}^{\mathsf{T}}\right) \\
&= \left(\mathsf{R}(\mathbb{C}_0 : \mathsf{E}^{\triangleleft})\mathsf{R}^{\mathsf{T}}\right) : \dot{\mathsf{E}} - [\mathsf{E}, \mathsf{R}(\mathbb{C}_0 : \mathsf{E}^{\triangleleft})\mathsf{R}^{\mathsf{T}}] : \left(\dot{\mathsf{R}}\mathsf{R}^{\mathsf{T}}\right),
\end{aligned} \tag{7.61}$$

where the brackets denote the commutator operator: $\forall\,(\mathsf{A}\,\mathsf{B}) \in \mathsf{Lin},\ [\mathsf{A},\mathsf{B}] = \mathsf{A}\,\mathsf{B} - \mathsf{B}\,\mathsf{A}$.

Then, one can derive the second part of the mechanical free energy. To this end, one can isolate the terms relative to the evolution of chemical composition (via ϕ and m) in Eq. (7.58):

$$\frac{\mathsf{d}\psi_{mech}}{\mathsf{d}t}|_{\mathsf{E},\mathsf{R}} = \tfrac{1}{2}\dot{\phi}\,(\mathbb{C}_{0,\phi} : \mathsf{E}^{\triangleleft}) : \mathsf{E}^{\triangleleft} + \tfrac{1}{2}\dot{m}\,(\mathbb{C}_{0,m} : \mathsf{E}^{\triangleleft}) : \mathsf{E}^{\triangleleft}. \tag{7.62}$$

$\mathbb{C}_{0,\phi}$ and $\mathbb{C}_{0,m}$ are the derivatives of the elastic tensor $\mathbb{C}_0$ with respect to porosity ϕ and mineral volume fraction m, respectively.

Finally, the partial derivatives of the mechanical component of the free energy ψ_{mech} from Equations (7.61) and (7.62) read:

$$\frac{\partial \psi_{mech}}{\partial \mathsf{E}} = \mathsf{R}\left(\mathbb{C}_0 : \mathsf{E}^{\triangleleft}\right)\mathsf{R}^{\mathsf{T}}, \tag{7.63}$$

$$\frac{\partial \psi_{mech}}{\partial \mathsf{R}} = \left[\mathsf{E}, \mathsf{R}\left(\mathbb{C}_0 : \mathsf{E}^{\triangleleft}\right)\mathsf{R}^{\mathsf{T}}\right].\mathsf{R}, \tag{7.64}$$

$$\frac{\partial \psi_{mech}}{\partial \phi} = \frac{1}{2}\left(\mathbb{C}_{0,\phi} : \mathsf{E}^{\triangleleft}\right) : \mathsf{E}^{\triangleleft}, \tag{7.65}$$

$$\frac{\partial \psi_{mech}}{\partial m} = \frac{1}{2}\left(\mathbb{C}_{0,m} : \mathsf{E}^{\triangleleft}\right) : \mathsf{E}^{\triangleleft}. \tag{7.66}$$

7.B Homogenized material properties

In the present study, in order to account for the variations of bone elastic properties with respect to porosity and mineralization, a law of mixture is proposed as follows:

$$\widehat{\mathbb{C}}_0(\phi, m) = \phi\,\mathbb{C}_{\mathsf{w}} + (1-\phi)\left(m\,\mathbb{C}_{\mathsf{HA}} + (1-m)\mathbb{C}_{\mathsf{SO}}\right), \tag{7.67}$$

where $\mathbb{C}_{\mathsf{w}}$, $\mathbb{C}_{\mathsf{SO}}$ and $\mathbb{C}_{\mathsf{HA}}$ are respectively the fourth-order stiffness tensors of water (pores), osteoid (collageneous unmineralized matrix) and hydroxyapatite (mineral). The individual tensors read as follows:

$$\mathbb{C}_{\mathsf{w}} = 3\,k_{\mathsf{w}}\mathbb{J} + \mu_{\mathsf{w}}\mathbb{K}, \tag{7.68}$$

$$\mathbb{C}_{\mathsf{SO}} = \frac{1}{3}\mathbb{C}_{\mathsf{w}} + \frac{2}{3}\mathbb{C}_{\mathsf{Col}}, \tag{7.69}$$

$$\mathbb{C}_{\mathsf{HA}} = 3\,k_{\mathsf{HA}}\mathbb{J} + \mu_{\mathsf{HA}}\mathbb{K}, \tag{7.70}$$

$$\mathbb{C}_{\mathsf{Col}} = 3\,k_{\mathsf{Col}}\mathbb{J} + \mu_{\mathsf{Col}}\mathbb{K}, . \tag{7.71}$$

where the parameters k_{X} and μ_{X} are respectively the bulk modulus and the shear modulus of the phase X, $\mathbb{J}$ is the volumetric part of the fourth-order unit tensor $\mathbb{I}$, and $\mathbb{K}$ is its deviatoric part: $\mathbb{K} = \mathbb{I} - \mathbb{J}$. Water, mineral and collagen are assumed to be isotropic materials.

The parameters used in the previous Equations (7.68)-(7.70) are listed in Table 7.4.

Table 7.4: Initial values of remodeling variables and parameters.

Symbol	Value	Unit
k_{w}	2.3	kPa
μ_{w}	0	kPa
k_{Col}	5.8	kPa
μ_{Col}	3.8	kPa
k_{HA}	82.6	GPa
μ_{HA}	44.9	GPa

7.C Deriving the evolution of the chemical free energy

The fractions of osteoid (SO) and solid fraction of mineralized bone (SMB) in the RVE verify:

$$m(1-\phi) = f_m^{\mathsf{MB}}\phi_{\mathsf{MB}}, \tag{7.72}$$

$$\phi_{\mathsf{SO}} + \phi_{\mathsf{MB}} + \phi = 1, \tag{7.73}$$

$$\phi_{\mathsf{SMB}} = (1 - f_w^{\mathsf{MB}})\phi_{\mathsf{MB}}, \tag{7.74}$$

where f_m^{MB} and f_w^{MB} are the volume fractions of mineral and interstitial fluid in mineralized bone ϕ_{MB}, respectively.

This leads to:

$$\phi_{\mathsf{MB}} = \frac{m(1-\phi)}{f_m^{\mathsf{MB}}}, \tag{7.75}$$

$$\phi_{\mathsf{SMB}} = \frac{1 - f_w^{\mathsf{MB}}}{f_m^{\mathsf{MB}}} m(1-\phi), \tag{7.76}$$

$$\phi_{\mathsf{SO}} = 1 - \phi - \frac{m(1-\phi)}{f_m^{\mathsf{MB}}}. \tag{7.77}$$

Stemming from Equations (7.13) and (7.14), one can write the fluid component

of the change in chemical energy as follows:

$$\sum_{el} \mu_{el}\, \mathsf{d}n_{el} = V_{RVE} \sum_{el} \mu_{el} c_{el} \left[(1 - \frac{f_w^{\mathsf{MB}}}{f_m^{\mathsf{MB}}} m)\mathsf{d}\phi + \frac{f_w^{\mathsf{MB}}}{f_m^{\mathsf{MB}}}(1-\phi)\mathsf{d}m \right]. \tag{7.78}$$

Note that the change in chemical free energy in the representative volume of tissue Ψ_χ is linked to the chemical energy density ψ_χ in a material point, which can be interpreted as an average quantity over the representative element: $\Psi_\chi = \psi_\chi V_{RVE}$.

Hence, the density ψ_χ of chemical free energy verifies:

$$\begin{aligned} \mathsf{d}\psi_\chi = \frac{1 - f_w^{\mathsf{MB}}}{f_{min}^m} \frac{\mu^*_{\mathsf{SMB}}}{V_{m,SMB}} \mathsf{d}\left(m\,(1-\phi)\right) \\ + \frac{\mu^*_{\mathsf{SO}}}{V_{m,SO}} \mathsf{d}\left(1 - \phi - \frac{m(1-\phi)}{f_{min}^m}\right) \\ - \sum_{el} \mu_{el} c_{el} \left[\left(1 - \frac{f_w^{\mathsf{MB}}}{f_m^{\mathsf{MB}}} m\right) \mathsf{d}\phi + \frac{f_w^{\mathsf{MB}}}{f_m^{\mathsf{MB}}}(1-\phi)\mathsf{d}m \right], \end{aligned} \tag{7.79}$$

where $V_{m,SMB}$ and $V_{m,SO}$ are respectively the molar volume of the solid fraction of mineralized matrix and osteoid.

This leads to the time-derivative of the density of the chemical free energy:

$$\dot{\psi_\chi} = \mu_\phi \dot{\phi} + \mu_m \dot{m}, \tag{7.80}$$

where

$$\begin{aligned} \mu_\phi = &- \frac{1 - f_w^{\mathsf{MB}}}{f_{min}^m} \frac{\mu^*_{\mathsf{SMB}}}{V_{m,SMB}} m + \frac{\mu^*_{\mathsf{SO}}}{V_{m,SO}} f_{Col}(\frac{m}{f_{min}^m} - 1) \\ &- \sum_{el} \mu_{el} c_{el} \left(1 - \frac{f_w^{\mathsf{MB}}}{f_m^{\mathsf{MB}}} m\right) \end{aligned} \tag{7.81}$$

$$\mu_m = (1-\phi) \left(\frac{1 - f_w^{\mathsf{MB}}}{f_{min}^m} \frac{\mu^*_{\mathsf{SMB}}}{V_{m,SMB}} - \frac{f_{Col}}{f_{min}^m} \frac{\mu^*_{\mathsf{SO}}}{V_{m,SO}} - \frac{f_w^{\mathsf{MB}}}{f_m^{\mathsf{MB}}} \sum_{el} \mu_{el} c_{el} \right). \tag{7.82}$$

7.D Specific surface

In his original 1984 work, Martin performed measurements of specific surface in function of porosity [123]. From these experimental results, a fifth order polynomial fit was proposed (see Eq. (7.83)). Therefore, following earlier works [155], the following approximation is used, to account for the dependency of specific surface on porosity:

$$s_V(\phi) = a\,\phi + b\,\phi^2 + c\,\phi^3 + d\,\phi^4 + e\,\phi^5, \tag{7.83}$$

where $a = 32.3\,\mathsf{mm}^{-1}$, $b = 93.9\,\mathsf{mm}^{-1}$, $c = 134\,\mathsf{mm}^{-1}$, $d = 101\,\mathsf{mm}^{-1}$, and $e = 28.8\,\mathsf{mm}^{-1}$.

Chapter 8

Future perspectives: bone remodeling in adolescent idiopathic scoliosis

A clinical preliminary study

Bone turnover is key to several skeletal diseases. In line with previous works [129, 180], one may postulate that its interactions with mechanics may lead to scoliotic deformity progression. In particular, given the close connection between bone biology and mechanics highlighted earlier in this thesis (Chapter 2), there is a motivation to investigate the interplay between the scoliotic abnormal loading and bone microstructure. The present chapter describes the objectives and protocol of a clinical application developed to assert whether there is a correlation between *in vivo* loading conditions in Adolescent Idiopathic Scoliosis (AIS) patients and their bone composition and microarchitecture, and quantify that link. This study received approval from Children's Health Queensland (number HREC/2018/QCHQ/45601) and Queensland University of Technology's Office of Research Ethics and Integrity (number 1800001128).

Aetiology and prevalence of AIS Scoliosis is the most common spinal deformity affecting children and adolescents. Scoliosis is a three-dimensional deviation of the spine, characterized by lateral curvature exceeding 10°, rotation of spinal column and loss of the normal sagittal spine profile. In many cases, this condition is a progressive deformity that cannot be explained by one of the known potential scoliosis

causes (congenital, neuromuscular or mesenchymal). If known causes are excluded, the scoliosis is classified as idiopathic. Most of idiopathic scoliosis cases in children fall within the subgroup of AIS, developing at the age of 11-18 years [102]. Konieczny et al. identified an overall prevalence of 0.47-5.2% in children from various studies from four different continents [102].

Progressive and severe curves in the growing adolescent, if left untreated, typically lead to an increased mortality rate (about twice that of the general population), as reported in Wong and Tan's 2010 review [209]. The latter also reveals that this higher mortality is most likely due to disabling diseases resulting from the scoliosis (backache, cardiopulmonary diseases, mental health deterioration). For the more severe and progressive cases, the only effective treatment option is surgical correction and fusion of the affected region of the spine, with the use of structural metal implants.

Bone histomorphometry in AIS Over the past decades, several studies have assessed the trabecular bone micro-architecture and mineral content in adolescent idiopathic scoliosis using iliac crest biopsies [30, 197, 214]. In 2008, Li et al. undertook a comprehensive literature review of such studies, revealing that there is a consensus on the correlation of low bone mineral density (BMD) with AIS [113], although Cheng et al. found that the presence of a lower BMD was not correlated to the severity of the scoliosis [30]. There are only a couple of studies analyzing the role of micro-architectural properties in such pathologies [30, 183, 197]. Wang et al. [197] used HR-pQCT (high-resolution peripheral quantitative computed tomography, for 3D imaging) to investigate trabecular structure and quality in iliac crest bone biopsies, showing a structural and mineralization abnormality in AIS patients' bone tissue [197]. They reported a reduced bone volume fraction (-5%), trabecular thickness (-0.7%) and trabecular number (-4%).

Among the research reporting bone histomorphometry in AIS, there is little data on the properties of vertebral bone [30, 183]. In those studies, the biopsies were obtained from the spinous processes of AIS patients scheduled for posterior corrective spinal surgery. Cheng et al. reported reduced bone resorption and apposition rates in AIS patients, both in iliac crest and spinous processes biopsies [30]. They inferred

that the difference in bone turnover might be at the origin of the deformity, and not a result of the deformity. In the same vein, Hung et al. demonstrated that low bone mass in hip and spine was one of the key factors in the risk of curve progression [85].

Objectives of the study and protocol The aim of this study is to assess the links between AIS, bone remodeling and mechanics. In particular, vertebral bodies are subjected to a significant load and the asymmetrical mechanical loading environment in the AIS spine directly affects these tissues and their remodelling. With posterior approaches to correction surgery, former studies were not able to access vertebral bodies, and only retrieved tissues where the impact of the atypical curvature on the mechanical environment was not as significant (spinous process, iliac crest). The surgeons of the Biomechanics and Spine Research Group (BSRG) are highly experienced in performing anterior approaches to scoliosis correction surgery, providing a unique opportunity to collect biopsies from vertebral body bone. This study enables the investigation of the links between the spinal deformity and bone adaptation in AIS: the goal is to discover bone architectural and content parameters for AIS vertebral bone and how they correlate with mechanical loading. To this end, a surgical protocol was designed, enabling the acquisition of the vertebral bone samples. This study also includes samples analysis and the comparison of experimental results with patient-specific simulation results of bone remodeling. Figure 8.1 depicts the clinical and experimental steps of the workflow.

Surgical procedure In order to address the research question, bone biopsies are retrieved from the vertebral bodies of AIS patients during their planned scoliosis correction surgery, provided they gave their informed consent. Unlike existing studies [30, 197], surgeons do not excise spinous processes or use iliac crest samples, but instead retrieve vertebral bone cylindrical cores.

Bone samples are acquired from AIS patients treated surgically at the Queensland Children's Hospital. Samples are taken intra-operatively from 3-4 vertebral bodies (thoracic or lumbar) using a bone biopsy tool during the spinal instrumentation surgery. Anterior spinal fusion surgery for scoliosis correction requires that

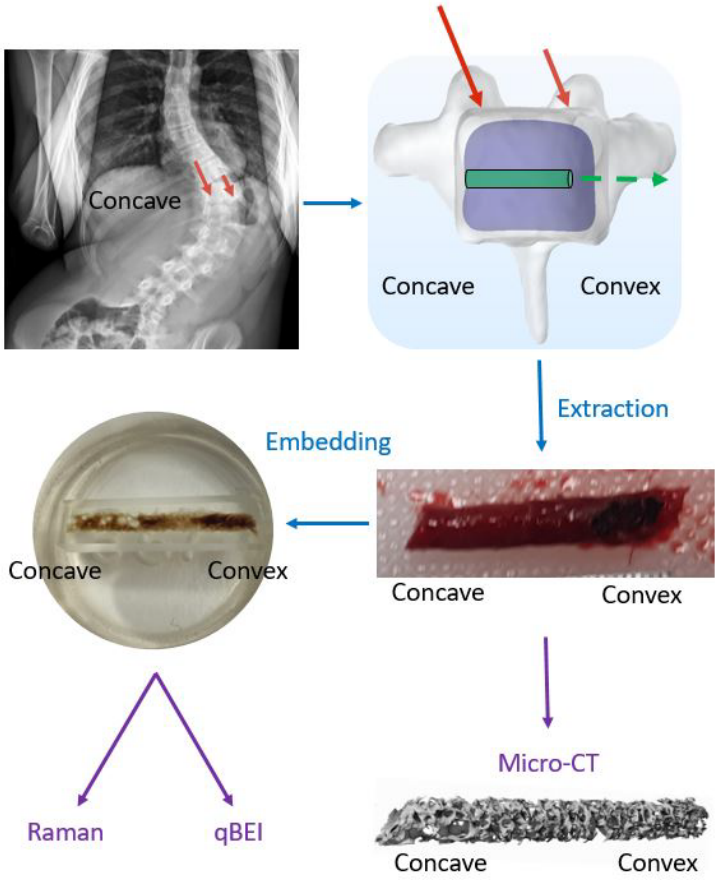

Figure 8.1: Workflow overview for vertebral bone characterization in AIS. Credits: Laure Stickel (QUT & BSRG intern).

screws are inserted into the vertebral bodies. Standard surgical practice for inserting vertebral screws during anterior fusion surgery requires a 'starter' or pilot hole to be created through the vertebra laterally, creating a path through which the vertebral screw will be inserted. The pilot hole is typically produced by a bone awl and the bony material discarded.

In this study, the pilot hole for 3-4 screws at the apex (vertebra with the farthest deviation from the midline of the body) of the spinal deformity is created using a commercial bone biopsy tool in place of the bone awl. The outer diameter of the pilot hole created with the biopsy tool is comparable to that created using the bone awl. Figure 8.2 depicts the collection of the bone core from the biopsy tool.

A preliminary study investigated the pull-out force of vertebral screws to compare the standard and new surgery protocols in fresh sheep bones. To this end, vertebral

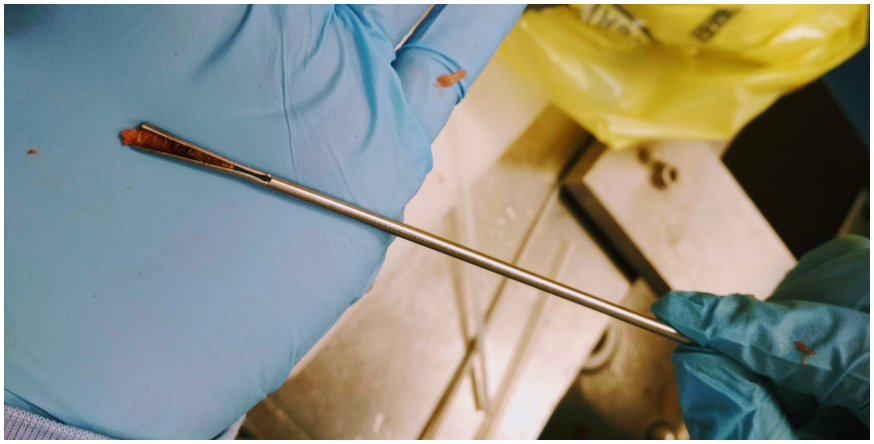

Figure 8.2: Samples collection: a bone core is taken out of the biopsy tool. The sample will be notched at the end (see micro-CT reconstruction in Figure 8.1) to mark the orientation.

screws were inserted in vertebrae with pilot holes (standard procedure) or where a core was taken out prior to insertion (new procedure). This study is illustrated in Figure 8.3. The results – not shown in the present thesis – did not depict a modification of the structural stability of the bone-implant system, therefore confirming the feasibility of the study in human.

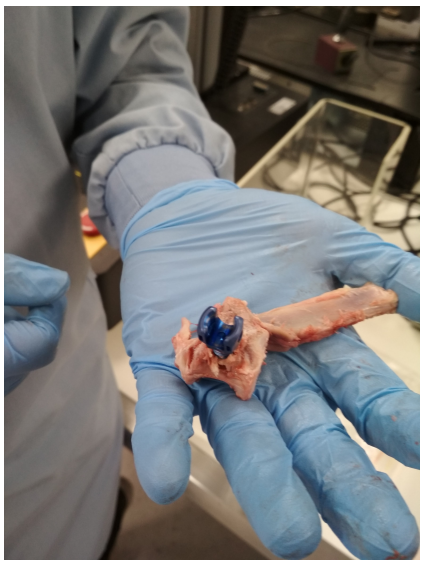

(a) Sheep thoracic vertebra, where a vertebral screw was inserted.

(b) Pull-out test of a vertebral screw in a T8 thoracic sheep vertebra.

Figure 8.3: Pilot study: pull-out force in implanted sheep vertebrae.

Samples analysis Following surgeries, the biopsies are fixated and analyzed using several techniques. The properties of the AIS bone are quantified using micro-computed tomography (micro-CT), Raman spectroscopy, quantitative back-scattering imaging (qBEI) and histology. Histomorphometric data, as well as bone anisotropy and mineral content is retrieved using these techniques and the correlation with the severity of the scoliotic curve is calculated.

Patient-specificity and 3D mechanical modeling The present study implies the conception of a model that can be adapted in function of patient data. In particular, here, thoracic and lumbar vertebral bone reconstructions is developed from the MRI of an adolescent healthy subject. In function of the scans obtained from patient data, patient-specific boundary conditions are determined and implemented in a finite-element model based on the 3D reconstructions of healthy vertebral bones. Figure 8.4 presents the 3D reconstruction of a human healthy thoracic vertebra.

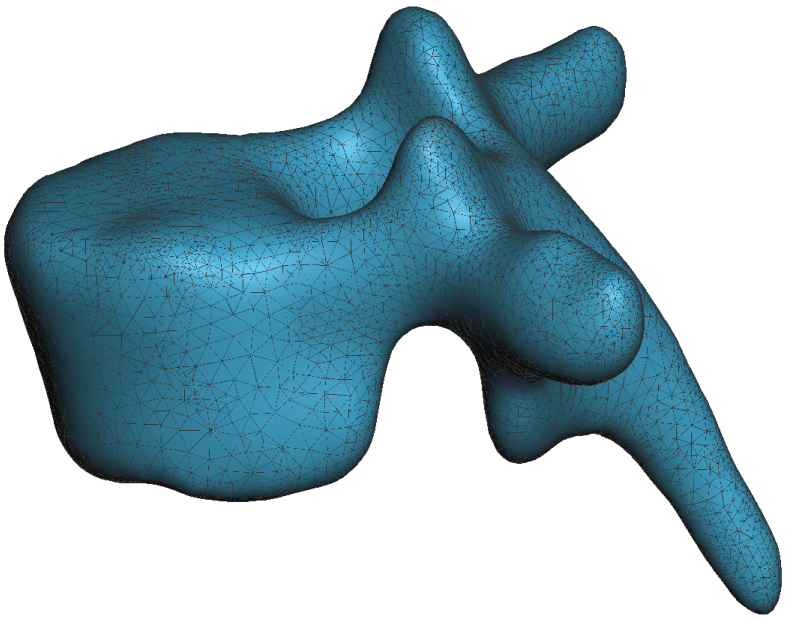

Figure 8.4: 3D reconstruction of a human healthy thoracic vertebra (female, 18 years old).

Conclusions The collaboration with highly skilled orthopaedic surgeons, in particular with respect to anterior approaches to scoliosis correction surgery, gives us

a unique opportunity to access vertebral body bone. As a result, this world first study will provide a better understanding of AIS by characterizing vertebral bone tissue properties in these patients. Additionally, with this study, biopsies of bones that experience a pathological mechanical environment that is directly linked to the deformity will be retrieved: the influence of the curvature on the stresses in vertebral bodies is substantial, especially when compared to the spinal process and iliac crest tissues. Therefore, the results of this study will give insights as to the connection between the mechanical environment (impacted by the curvature phenotype) and its link to mineral content, bone density and anisotropy. Hence, this will provide an application for an existing computation model of bone remodeling (Chapter 7). Finally, this study will not only be useful in the understanding of AIS, but also has the potential to shed light on other bone-related diseases and conditions, enabling the use of the previously-developed model for the development of better treatment options.

To summarize, the study presented in this chapter provides a unique perspective to the work outlined in this thesis and a first step towards more applications.

Acknowledgements On top of general acknowledgements in the dedicated section of this thesis, I would like to have a special word for colleagues whose expertise or work made this study possible. I thank Dr Labrom and Dr Askin for their collaboration, which allowed the design and start of a unique project. Finally, I want to acknowledge the outstanding work of Laure Stickel and Jurgis Ruza during their respective internships.

Chapter 9

Conclusions and perspectives

The study of bone, in particular as a living tissue, dates back to the 19th century when bone cells lineages were identified. Bone complex architecture, as well as its ability to modify its structure and composition through *bone remodeling* has been studied widely since then. In the present work, different concepts were studied, aiming at representing the role of mechanics in this process or, in other words, *mechanomics* of bone remodeling.

In this dissertation, several approaches were presented for the modeling of bone continuous microstructural evolution, bone remodeling. First, a mathematical framework based on mechanobiology was proposed, and in particular integrating osteocytes mechanosensivity. In this context, bone cells turnover was regulated by osteocytes biochemical signalling and, in turn, modified tissue porosity and, consequently, the cells mechanical environment. Because this fine description catches underlying signalling mechanisms of bone remodeling, the model was able to integrate the effects of the administration of a post-menopausal osteoporosis drug based on an anti-sclerostin antibody, romosozumab. This mathematical formulation, validated for various dosages and bone sites, provides quantitative insights as to the effects of a certain dosage on bone gain, which could therefore enable the specific adaptation of treatments to patients.

Then, a macroscopic framework of bone remodeling was introduced, which is based on generalized continuum thermodynamics. In this theory, bone tissue was repre-

sented by a collection of material points whose kinematics was not only described by their displacement, but also microstructural properties. First, using the original formulation of DiCarlo et al. [42], rotary remodeling was investigated by enriching the continuum description with a remodeling variable accounting for microstructure rotation. In this framework, a relationship between strain energy variations and remodeling equilibrium states was found. In particular, analytical developments demonstrated that stable rotary remodeling equilibrium states correspond to local minima of the strain energy (in strain-controlled loading conditions). Additionally, in line with Cowin's observations [35], the alignment of principal stress and strain was shown to be a necessary condition for equilibrium. However, in contrast to Cowin's original findings, theoretical developments demonstrated that material axes are indeed collinear to strains and stresses in remodeling equilibrium states only under specific conditions on material properties. This framework was then used to study 2D benchmark models using an algorithm based on an iterative finite-element analysis. This model was applied to the classic example of the proximal human femur.

Furthermore, stemming from both microscopic and macroscopic points of view developed earlier, a bridging framework was proposed, enabling the description of bone remodeling encompassing biology, chemistry and mechanics. Hence, DiCarlo et al.'s original formulation was enriched with new microstructural information. Therefore, additionally to the original rotary remodeling variable, several remodeling variables were introduced, giving indications on cellular activity and bone tissue composition. This novel formulation uses cellular dynamics equations proposed by Komarova et al. [101] who simplified autocrine and paracrine cellular regulations using a small number of parameters to describe globally the effects of signalling pathways. While sound results are obtained with this novel formulation, a more comprehensive and stable framework could be obtained by integrating cellular population dynamics as per the mechanobiological concepts presented earlier.

The main interest of this thesis is to provide insights to better understand bone remodeling and quantify the effects of mechanics, especially in the context of pathologies or peri-implant remodeling. These questions are particularly critical in adolescent idiopathic scoliosis, where patients vertebral bodies undergo abnormal loading condi-

tions. In this thesis, the first steps of a clinical study were outlined, coupling surgery, material analysis and 3D finite-element simulations. The multiphysical model developed in this thesis, which integrates bone mechanobiology, may help targeting signalling pathways and designing less invasive treatments. For this purpose, future work will involve the clinical application of this work to bone remodeling in AIS and the extension of the developed unifying model to capture the dynamics of drug treatment options in osteoporosis.

Bibliography

[1] Comsol Multiphysics® (5.3a). COMSOL AB, Stockholm, Sweden. www.comsol.com. 3, 143

[2] Livelink™ for Matlab® (5.3a). COMSOL AB, Stockholm, Sweden. www.comsol.com. 143

[3] MATLAB® (R2017b). Matlab Inc., Natwick, Massachusetts. www.mathworks.com. 3, 143, 177

[4] Académie des Sciences. *Gazette médicale de Paris*. Paris, Jules Guérin edition, Jan. 1847. 18

[5] Amgen Inc. Evenity [Prescribing Information]. Technical report, Amgen Inc., Thousand Oaks, California, 2019. 56

[6] S. D. Badilatti, P. Christen, A. Levchuk, J. H. Marangalou, B. van Rietbergen, I. Parkinson, and R. Müller. Large-scale microstructural simulation of load-adaptive bone remodeling in whole human vertebrae. *Biomechanics and Modeling in Mechanobiology*, 15(1):83–95, 2016. 23

[7] W. Balemans, M. Ebeling, N. Patel, E. Van Hul, P. Olson, M. Dioszegi, C. Lacza, W. Wuyts, J. Van Den Ende, P. Willems, a. F. Paes-Alves, S. Hill, M. Bueno, F. J. Ramos, P. Tacconi, F. G. Dikkers, C. Stratakis, K. Lindpaintner, B. Vickery, D. Foernzler, and W. Van Hul. Increased bone density in sclerosteosis is due to the deficiency of a novel secreted protein (SOST). *Human Molecular Genetics*, 10(5):537–543, 2001. 54

[8] V. K. Bansal. *Serum Inorganic Phosphorus*. Butterworth, Boston, 1990. 179

[9] Z. Bar-Shavit. The osteoclast: A multinucleated, hematopoietic-origin, bone-resorbing osteoimmune cell. *Journal of Cellular Biochemistry*, 102(5):1130–1139, 2007. 17

[10] C. Barragan-Adjemian, D. Nicolella, V. Dusevich, M. R. Dallas, J. D. Eick, and L. F. Bonewald. Mechanism by which MLO-A5 late osteoblasts/early osteocytes mineralize in culture: Similarities with mineralization of lamellar bone. *Calcified Tissue International*, 79(5):340–353, 2006. 16, 17

[11] B. Bary. Simplified coupled chemo-mechanical modeling of cement pastes behavior subjected to combined leaching and external sulfate attack. *International Journal for Numerical and Analytical Methods in Geomechanics*, 32(14):1791–1816, Oct. 2008. 157

[12] G. S. Beaupré, T. E. Orr, and D. R. Carter. An approach for time-dependent bone modeling and remodeling-application: A preliminary remodeling simulation. *Journal of Orthopaedic Research*, 8(5):662–670, Sept. 1990. 1, 23, 24, 104, 137, 146

[13] G. H. Bell, D. P. Cuthbertson, and J. Orr. Strength and size of bone in relation to calcium intake. *The Journal of Physiology*, 100(3):299–317, Nov. 1941. 19

[14] M. Berli, C. Borau, O. Decco, G. Adams, R. B. Cook, J. M. García Aznar, and P. Zioupos. Localized tissue mineralization regulated by bone remodelling: A computational approach. *PLOS ONE*, 12(3):e0173228, 2017. 159

[15] M. J. Berridge, M. D. Bootman, and P. Lipp. Calcium–a life and death signal. *Nature*, 395(6703):645–648, 1998. 8

[16] P. V. N. Bodine and B. S. Komm. Wnt signaling and osteoblastogenesis. *Reviews in Endocrine and Metabolic Disorders*, 7(1-2):33–39, 2006. 162

[17] L. F. Bonewald. Osteocytes as dynamic multifunctional cells. *Annals of the New York Academy of Sciences*, 1116:281–290, 2007. 21, 22

[18] L. F. Bonewald. The amazing osteocyte. *Journal of Bone and Mineral Research*, 26(2):229–238, 2011. 16, 17

[19] L. F. Bonewald and M. L. Johnson. Osteocytes, mechanosensing and Wnt signaling. *Bone*, 42(4):606–615, 2008. 21, 25, 27, 55, 162

[20] N. Bonfoh, E. Novinyo, and P. Lipinski. Modeling of bone adaptative behavior based on cells activities. *Biomechanics and Modeling in Mechanobiology*, 10(5):789–798, 2011. 158

[21] A. Broca, R. Proust, and E. Feindel. *Bulletins de la Société Anatomique de Paris*. Paris, 1870. 10, 11, 12

[22] T. G. Bromage, H. M. Goldman, S. C. McFarlin, J. Warshaw, A. Boyde, and C. M. Riggs. Circularly polarized light standards for investigations of collagen fiber orientation in bone. *Anatomical Record - Part B New Anatomist*, 274(1):157–168, 2003. 9, 10

[23] M. E. Brunkow, J. C. Gardner, J. Van Ness, B. W. Paeper, B. R. Kovacevich, S. Proll, J. E. Skonier, L. Zhao, P. J. Sabo, Y. Fu, R. S. Alisch, L. Gillett, T. Colbert, P. Tacconi, D. Galas, H. Hamersma, P. Beighton, and J. Mulligan. Bone dysplasia sclerosteosis results from loss of the SOST gene product, a novel cystine knot-containing protein. *American Journal of Human Genetics*, 68(3):577–89, 2001. 54

[24] Y. Cao and W. J. Jusko. Incorporating target-mediated drug disposition in a minimal physiologically-based pharmacokinetic model for monoclonal antibodies. *Journal of Pharmacokinetics and Pharmacodynamics*, 41(4):375–387, 2014. 56

[25] D. Carter, T. Orr, and D. Fyhrie. Relationships between loading history and femoral cancellous bone architecture. *Journal of Biomechanics*, 22(3):231–244, Jan. 1989. 24, 25

[26] D. R. Carter. The relationship between in vivo strains and cortical bone remodeling. *Critical Reviews in Biomedical Engineering*, 8(1):1–28, 1982. 180

[27] D. R. Carter. Mechanical Loading Histories and Cortical Bone Remodeling. *Calcified Tissue International*, 36:S19–S24, Mar. 1984. 180, 184

[28] D. R. Carter, D. Fyhrie, and R. Whalen. Trabecular bone density and loading history: Regulation of connective tissue biology by mechanical energy. *Journal of Biomechanics*, 20(8):785–794, Jan. 1987. 24

[29] S. Checa and P. J. Prendergast. Effect of cell seeding and mechanical loading on vascularization and tissue formation inside a scaffold: A mechano-biological model using a lattice approach to simulate cell activity. *Journal of Biomechanics*, 43(5):961–968, Mar. 2010. 25

[30] J. C. Cheng, S. P. Tang, X. Guo, C. W. Chan, and L. Qin. Osteopenia in adolescent idiopathic scoliosis: a histomorphometric study. *Spine*, 26(3):E19–23, Feb. 2001. 194, 195

[31] J. W. M. Chow, S. W. Fox, J. M. Lean, and T. J. Chambers. Role of Nitric Oxide and Prostaglandins in Mechanically Induced Bone Formation. *Journal of Bone and Mineral Research*, 13(6):1039–1044, June 1998. 30

[32] C. B. Confavreux. Bone: From a reservoir of minerals to a regulator of energy metabolism. *Kidney International*, 79(Suppl 121):S14–S19, 2011. 8

[33] Consensus Development Conference. Diagnosis, prophylaxis, and treatment of osteoporosis. *The American Journal of Medicine*, 94(6):646–50, June 1993. 55

[34] S. C. Cowin. Mechanical modeling of the stress adaptation process in bone. *Calcified Tissue International*, 36 Suppl 1:S98–S103, 1984. 20

[35] S. C. Cowin. Wolff's Law of Trabecular Architecture at Remodeling Equilibrium. *Journal of Biomechanical Engineering*, 108(1):83, 1986. 105, 106, 202

[36] S. C. Cowin. Optimization of the strain energy in linear anisotropic elasticity. *Journal of Elasticity*, 34:45–68, 1994. 25

[37] S. C. Cowin. On the minimization and maximization of the strain energy density in cortical bone tissue. *Journal of Biomechanics*, 28(4):445–447, 1995. 105, 153

[38] S. C. Cowin and D. H. Hegedus. Bone remodeling I: theory of adaptive elasticity. *Journal of Elasticity*, 6(3), 1976. 20

[39] S. C. Cowin, A. M. Sadegh, and G. M. Luo. An Evolutionary Wolff's Law for Trabecular Architecture. *Journal of Biomechanical Engineering*, 114(1):129, 1992. 105

[40] K. Culmann. *Die graphische Statik*. Meyer & Zeller (A. Reimann), Zurich, 1866. 18

[41] W. T. Dempster and R. T. Liddicoat. Compact bone as a non-isotropic material. *American Journal of Anatomy*, 91(3):331–362, Nov. 1952. 19

[42] A. DiCarlo, S. Naili, and S. Quiligotti. Sur le remodelage des tissus osseux anisotropes. *Comptes Rendus Mécanique*, 334(11):651–661, Nov. 2006. 3, 6, 26, 105, 137, 140, 161, 163, 171, 202

[43] A. DiCarlo and S. Quiligotti. Growth and balance. *Mechanics Research Communications*, 29(6):449–456, Nov. 2002. 3, 104

[44] A. DiCarlo, V. Sansalone, A. Tatone, and V. Varano. Growth and Remodelling of Intracranial Saccular Aneurysms. *COMSOL Conference in Milan*, (1):1–7, 2009. 104

[45] M. Doblaré and J. M. García. Application of an anisotropic bone-remodelling model based on a damage-repair theory to the analysis of the proximal femur before and after total hip replacement. *Journal of Biomechanics*, 34(9):1157–1170, 2001. 138

[46] M. Doblaré and J. M. García. Anisotropic bone remodelling model based on a continuum damage-repair theory. *Journal of Biomechanics*, 35(1):1–17, 2002. 23, 105

[47] C. L. Donaldson, S. B. Hulley, J. M. Vogel, R. S. Hattner, J. H. Bayers, and D. E. McMillan. Effect of prolonged bed rest on bone mineral. *Metabolism*, 19(12):1071–1084, Dec. 1970. 20

[48] P. Dua, E. Hawkins, and P. van der Graaf. A Tutorial on Target-Mediated Drug Disposition (TMDD) Models. *CPT: Pharmacometrics & Systems Pharmacology*, 4(6):324–337, June 2015. 56

[49] R. L. Duncan and C. H. Turner. Mechanotransduction and the functional response of bone to mechanical strain. *Calcified Tissue International*, 57:344–358, 1995. 25

[50] E. F. Eriksen. Cellular mechanisms of bone remodeling. *Reviews in Endocrine and Metabolic Disorders*, 11(4):219–227, 2010. 22, 162

[51] R. Eudy, M. Gastonguay, K. Baron, and M. Riggs. Connecting the Dots: Linking Osteocyte Activity and Therapeutic Modulation of Sclerostin by Extending a Multiscale Systems Model. *CPT: Pharmacometrics & Systems Pharmacology*, 4(9):527–536, Sept. 2015. 57

[52] F. G. Evans. The Mechanical Properties of Bone. *Artificial Limbs: A Review of Current Developments*, 13(1):37–48, 1969. 19

[53] F. G. Evans. *Mechanical properties of bone*. Thomas, Springfield, Illinois, 1973. 19

[54] X. Fan, E. Roy, L. Zhu, T. C. Murphy, C. Ackert-Bicknell, C. M. Hart, C. Rosen, M. S. Nanes, and J. Rubin. Nitric Oxide Regulates Receptor Activator of Nuclear Factor-κB Ligand and Osteoprotegerin Expression in Bone Marrow Stromal Cells. *Endocrinology*, 145(2):751–759, 2004. 30

[55] P. Fernandes, H. Rodrigues, and C. R. Jacobs. A Model of Bone Adaptation Using a Global Optimisation Criterion Based on the Trajectorial Theory of Wolff. *Computer Methods in Biomechanics and Biomedical Engineering*, 2(2):125–138, Jan. 1999. 25, 137, 139

[56] J. Frame, P.-Y. Rohan, L. Corté, and R. Allena. A mechano-biological model of multi-tissue evolution in bone. *Continuum Mechanics and Thermodynamics*, 31(1):1–31, Jan. 2019. 25

[57] T. A. Franz-Odendaal, B. K. Hall, and P. E. Witten. Buried alive: How osteoblasts become osteocytes. *Developmental Dynamics*, 235(1):176–190, 2006. 16

[58] P. Fratzl, H. S. Gupta, E. P. Paschalis, and P. Roschger. Structure and mechanical quality of the collagen-mineral nano-composite in bone. *Journal of Materials Chemistry*, 14(14):2115–2123, 2004. 179

[59] H. M. Frost. Tetracycline-based histological analysis of bone remodeling. *Calcified Tissue Research*, 3(1):211–237, 1969. 15

[60] H. M. Frost. Bone "mass" and the "mechanostat": A proposal. *The Anatomical Record*, 219(1):1–9, 1987. 18, 20, 23, 28, 184

[61] H. M. Frost. Perspectives: a proposed general model of the "mechanostat" (suggestions from a new skeletal-biologic paradigm). *The Anatomical record*, 244(2):139–147, 1996. 20

[62] H. M. Frost and W. S. S. Jee. Perspectives: A vital biomechanical model of the endochondral ossification mechanism. *The Anatomical Record*, 240(4):435–446, Dec. 1994. 180, 184

[63] D. P. Fyhrie and D. R. Carter. A unifying principle relating stress to trabecular bone morphology. *Journal of Orthopaedic Research*, 4(3):304–317, 1986. 25, 138

[64] J.-F. Ganghoffer, R. Rahouadj, J. Boisse, and S. Forest. Phase field approaches of bone remodeling based on TIP. *Journal of Non-Equilibrium Thermodynamics*, 41(1):49–75, Jan. 2016. 157, 158

[65] J.-F. Ganghoffer, R. Rahouadj, J. Boisse, and J. Schiavi. A phase field approach for bone remodeling based on a second-gradient model. *Mechanics Research Communications*, 96:37–44, 2019. 157

[66] J. M. García-Aznar, T. Rueberg, and M. Doblare. A bone remodelling model coupling microdamage growth and repair by 3D BMU-activity. *Biomechanics and Modeling in Mechanobiology*, 4(2-3):147–167, 2005. 159

[67] C. Gegenbauer. *Untersuchungen zur vergleichenden Anatomie der Wirbeltiere*. Leipzig, schultergt edition, 1864. 11

[68] D. George, R. Allena, and Y. Rémond. A multiphysics stimulus for continuum mechanics bone remodeling. *Mathematics and Mechanics of Complex Systems*, 6(4):307–319, 2018. 25

[69] D. M. Geraldes, L. Modenese, and A. T. Phillips. Consideration of multiple load cases is critical in modelling orthotropic bone adaptation in the femur. *Biomechanics and Modeling in Mechanobiology*, 15(5):1029–1042, 2016. 138, 139

[70] D. M. Geraldes and A. T. M. Phillips. A comparative study of orthotropic and isotropic bone adaptation in the femur. *International Journal for Numerical Methods in Biomedical Engineering*, 30(9):873–889, Sept. 2014. 139

[71] P. Germain. La méthode des puissances virtuelles en mécanique des milieux continus. *Journal de Mécanique*, 12(2):235–274, 1973. 3, 162

[72] P. Germain. The Method of Virtual Power in Continuum Mechanics. Part 2: Microstructure. *SIAM Journal on Applied Mathematics*, 25(3):556–575, Nov. 1973. 3, 162

[73] D. A. Goldstein. *Serum Calcium*. Butterworths, Boston, 1990. 179

[74] A. E. Goodship, L. E. Lanyon, and H. McFie. Functional adaptation of bone to increased stress. An experimental study. *The Journal of Bone and Joint Surgery. American Volume*, 61(4):539–46, June 1979. 20

[75] R. Hambli. Connecting Mechanics and Bone Cell Activities in the Bone Remodeling Process: An Integrated Finite Element Modeling. *Frontiers in Bioengineering and Biotechnology*, 2:1–12, Apr. 2014. 158

[76] R. Hambli, M. H. Boughattas, J. L. Daniel, and A. Kourta. Prediction of denosumab effects on bone remodeling: A combined pharmacokinetics and finite element modeling. *Journal of the Mechanical Behavior of Biomedical Materials*, 60:492–504, 2016. 25

[77] S. Harris and B. Dawson-Hughes. Rates of change in bone mineral density of the spine, heel, femoral neck and radius in healthy postmenopausal women. *Bone and Mineral*, 17(1):87–95, Apr. 1992. 55

[78] R. Hart. Bone modeling and remodeling: theories and computation. In S. C. Cowin, editor, *Bone Mechanics Handbook, Second Edition*, chapter 31, pages 31–1–31–42. CRC Press, Boca Raton, 2003. 24

[79] C. Hellmich, J. F. Barthélémy, and L. Dormieux. Mineral-collagen interactions in elasticity of bone ultrastructure - A continuum micromechanics approach. *European Journal of Mechanics, A/Solids*, 23(5):783–810, 2004. 179

[80] M. Herissant. Eclaircissemens sur les maladies des os. In B. De Fontenelle, J.-J. Dortous Mairan, J. P. Grandjean de Fouchy, and J.-A.-N. d. C. De Condorcet, editors, *Histoire de l'Académie royale des sciences ... avec les mémoires de mathématique & de physique*, pages 419–438. Imprimerie du Pont, Paris, 1758. 157

[81] E. Hernlund, A. Svedbom, M. Ivergård, J. Compston, C. Cooper, J. Stenmark, E. V. McCloskey, B. Jönsson, and J. A. Kanis. Osteoporosis in the European Union: Medical management, epidemiology and economic burden: A report prepared in collaboration with the International Osteoporosis Foundation (IOF) and the European Federation of Pharmaceutical Industry Associations (EFPIA). *Archives of Osteoporosis*, 8(1-2), 2013. 56

[82] K. Holmbeck, P. Bianco, I. Pidoux, S. Inoue, R. C. Billinghurst, W. Wu, K. Chrysovergis, S. Yamada, H. Birkedal-Hansen, and A. R. Poole. The metalloproteinase MT1-MMP is required for normal development and maintenance of

osteocyte processes in bone. *Journal of Cell Science*, 118(Pt 1):147–156, 2005. 17

[83] R. Huiskes, R. Ruimerman, G. H. van Lenthe, and J. D. Janssen. Effects of mechanical forces on maintenance and adaptation of form in trabecular bone. *Nature*, 405(6787):704–706, 2000. 1, 23, 24, 180

[84] R. Huiskes, H. Weinans, H. J. Grootenboer, M. Dalstra, B. Fudala, and T. J. Slooff. Adaptive bone-remodeling theory applied to prosthetic-design analysis. *Journal of Biomechanics*, 20(11-12):1135–1150, 1987. 23, 104

[85] V. W. Hung, L. Qin, C. S. Cheung, T. P. Lam, B. K. Ng, Y. K. Tse, X. Guo, K. M. Lee, and J. C. Cheng. Osteopenia: A new prognostic factor of curve progression in adolescent idiopathic scoliosis. *Journal of Bone and Joint Surgery - Series A*, 87(12 I):2709–2716, 2005. 195

[86] C. R. Jacobs, J. C. Simo, G. S. Beaupré, and D. R. Carter. Adaptive bone remodeling incorporating simultaneous density and anisotropy considerations. *Journal of Biomechanics*, 30(6):603–613, June 1997. 137, 138

[87] W. S. S. Jee. *Integrated Bone Tissue Physiology: Anatomy and Physiology*, pages 1.1–1.68. 2001. 8

[88] W. S. S. Jee and X. Y. Tian. The benefit of combining non-mechanical agents with mechanical loading: A perspective based on the Utah paradigm of skeletal physiology. *Journal of Musculoskeletal Neuronal Interactions*, 5(2):110–118, 2005. 20

[89] Table of chemical potentials. 179

[90] R. D. Kamm. The role of molecular mechanics in intracellular signaling: Mechanisms and models. *Journal of Biomechanics*, 39:S4, Jan. 2006. 21

[91] J. A. Kanis. Assessment of osteoporosis at the primary health care level. Technical report, World Health Organization Collaborating Centre for Metabolic Bone Diseases, University of Sheffield, UK, Sheffield, UK, 2007. 55, 56

[92] J. A. Kanis, O. Johnell, A. Oden, B. Jonsson, C. De Laet, and A. Dawson. Risk of hip fracture according to the World Health Organization criteria for osteopenia and osteoporosis. *Bone*, 27(5):585–90, 2000. 56

[93] D. Ke, D. Padhi, and C. Paszty. Sclerostin is an Important Target for Stimulating Bone Formation, Restoring Bone Mass and Enhancing Fracture Healing. *Bone*, 46:S15, Mar. 2010. 30, 55

[94] L. Kidd, A. Stephens, J. Kuliwaba, N. Fazzalari, A. Wu, and M. Forwood. Temporal pattern of gene expression and histology of stress fracture healing. *Bone*, 46(2):369–378, Feb. 2010. 104

[95] E. Klein. *Elements of Histology*. Lea Brothers and Co, Philadelphia, 1889. 13, 14

[96] J. Klein-Nulend, A. D. Bakker, R. G. Bacabac, A. Vatsa, and S. Weinbaum. Mechanosensation and transduction in osteocytes. *Bone*, 54(2):182–190, 2013. 17, 21, 22

[97] V. Klika and F. Marsik. A thermodynamic model of bone remodelling: the influence of dynamic loading together with biochemical control. *Journal of musculoskeletal & neuronal interactions*, 10(3):220–30, 2010. 158

[98] M. L. Knothe Tate, P. W. Gunning, and V. Sansalone. Emergence of form from functionâĂŤMechanical engineering approaches to probe the role of stem cell mechanoadaptation in sealing cell fate. *BioArchitecture*, 6(5):85–103, 2016. 179

[99] J. C. Koch. The laws of bone architecture. *American Journal of Anatomy*, 21(2):177–298, 1917. 19, 140

[100] S. V. Komarova. Mathematical model of paracrine interactions between osteoclasts and osteoblasts predicts anabolic action of parathyroid hormone on bone. *Endocrinology*, 2005. 25

[101] S. V. Komarova, R. J. Smith, S. J. Dixon, S. M. Sims, and L. M. Wahl. Mathematical model predicts a critical role for osteoclast autocrine regulation in the control of bone remodeling. *Bone*, 2003. 1, 158, 174, 175, 179, 184, 202

[102] M. R. Konieczny, H. Senyurt, and R. Krauspe. Epidemiology of adolescent idiopathic scoliosis. *Journal of Children's Orthopaedics*, 7(1):3–9, 2013. 194

[103] B. Krølner and B. Toft. Vertebral Bone Loss: An Unheeded Side Effect of Therapeutic Bed Rest. *Clinical Science*, 64(5):537–540, may 1983. 20

[104] B. Krølner, B. Toft, S. P. Nielsen, and E. Tøndevold. Physical Exercise as Prophylaxis against Involutional Vertebral Bone Loss: A Controlled Trial. *Clinical Science*, 64(5):541–546, 1983. 20

[105] B. Kruck, E. A. Zimmermann, S. Damerow, C. Figge, C. Julien, D. Wulsten, T. Thiele, M. Martin, R. Hamdy, M. K. Reumann, G. N. Duda, S. Checa, and B. M. Willie. Sclerostin Neutralizing Antibody Treatment Enhances Bone Formation but Does Not Rescue Mechanically Induced Delayed Healing. *Journal of Bone and Mineral Research*, 33(9):1686–1697, Sept. 2018. 55

[106] M. Lang. Lighting Up the Mechanome Matthew. In *Frontiers of Engineering: Reports on Leading-Edge Engineering from the 2007 Symposium*. National Academies Press, Washington, D.C., national a edition, 2008. 21

[107] B. Langdahl, S. Ferrari, and D. W. Dempster. Bone modeling and remodeling: potential as therapeutic targets for the treatment of osteoporosis. *Therapeutic Advances in Musculoskeletal Disease*, 8(6):225–235, 2016. 55

[108] L. E. Lanyon. Experimental support for the trajectorial theory of bone structure. *Journal of Bone and Joint Surgery - Series B*, 56(1):160–166, 1974. 137

[109] T. Lemaire, J. Kaiser, S. Naili, and V. Sansalone. Parametric study of interstitial fluid flow in the bone lacuno-canalicular network. *Computer Methods in Biomechanics and Biomedical Engineering*, 15(sup1):331–332, Sept. 2012. 21

[110] V. Lemaire, F. L. Tobin, L. D. Greller, C. R. Cho, and L. J. Suva. Modeling the interactions between osteoblast and osteoclast activities in bone remodeling. *Journal of Theoretical Biology*, 229(3):293–309, 2004. 1, 25, 28, 175

[111] M. E. Levenston and D. R. Carter. An energy dissipation-based model for damage stimulated bone adaptation. *Journal of Biomechanics*, 31(7):579–586, July 1998. 104

[112] X. Li, M. S. Ominsky, Q.-T. Niu, N. Sun, B. Daugherty, D. D'Agostin, C. Kurahara, Y. Gao, J. Cao, J. Gong, F. Asuncion, M. Barrero, K. Warmington, D. Dwyer, M. Stolina, S. Morony, I. Sarosi, P. J. Kostenuik, D. L. Lacey, W. S. Simonet, H. Z. Ke, and C. Paszty. Targeted Deletion of the Sclerostin Gene in Mice Results in Increased Bone Formation and Bone Strength. *Journal of Bone and Mineral Research*, 23(6):860–869, 2008. 55

[113] X.-F. Li, H. Li, Z.-D. Liu, and L.-Y. Dai. Low bone mineral status in adolescent idiopathic scoliosis. *European Spine Journal*, 17(11):1431–1440, 2008. 194

[114] J. H. Luo and H. C. Gea. Optimal orientation of orthotropic materials using an energy based method. *Structural Optimization*, 15(3-4):230–236, 1998. 137

[115] Z. P. Luo and K. N. An. A theoretical model to predict distribution of the fabric tensor and apparent density in cancellous bone. *Journal of Mathematical Biology*, 36(6):557–568, 1998. 138

[116] A. Madeo, D. George, T. Lekszycki, M. Nierenberger, and Y. Rémond. A second gradient continuum model accounting for some effects of micro-structure on reconstructed bone remodelling. *Comptes Rendus Mécanique*, 340(8):575–589, 2012. 24

[117] S. Maldonado, S. Borchers, R. Findeisen, and F. Allgower. Mathematical Modeling and Analysis of Force Induced Bone Growth. In *2006 International Conference of the IEEE Engineering in Medicine and Biology Society*, volume 1, pages 3154–3157. IEEE, 2006. 1, 25, 26

[118] S. C. Manolagas. Birth and Death of Bone Cells: Basic Regulatory Mechanisms and Implications for the Pathogenesis and Treatment of Osteoporosis. *Endocrine Reviews*, 21(2):115–137, Apr. 2000. 16, 17

[119] T. Markoe. *A treatise on diseases of the bone*. D. Appleton & Company, New York, 1872. 13

[120] G. Marotti, V. Canè, S. Palazzini, and C. Palumbo. Structure-function relationships in the osteocyte. *Italian Journal of Mineral and Electrolyte Metabolism*, 4(2):93–106, Jan. 1990. 17

[121] M. Martin, P. Pivonka, G. Haiat, T. Lemaire, and V. Sansalone. Bone orthotropic remodeling as a thermodynamically-driven evolution. *Journal of Mechanics in Medicine and Biology*. 103, 137, 161, 171

[122] M. Martin, V. Sansalone, D. M. L. Cooper, M. R. Forwood, and P. Pivonka. Mechanobiological osteocyte feedback drives mechanostat regulation of bone in a multiscale computational model. *Biomechanics and Modeling in Mechanobiology*, 18(5):1475–1496, Oct. 2019. 6, 27, 175, 184, 186

[123] R. B. Martin. Porosity and specific surface of bone. *Critical reviews in biomedical engineering*, 10(3):179–222, 1984. 191

[124] J. Martínez-Reina, J. M. García-Aznar, J. Domínguez, and M. Doblaré. On the role of bone damage in calcium homeostasis. *Journal of Theoretical Biology*, 254(3):704–712, 2008. 26, 105, 159

[125] J. Martínez-Reina and P. Pivonka. Effects of long-term treatment of denosumab on bone mineral density: insights from an in-silico model of bone mineralization. *Bone*, 125:87–95, 2019. 186

[126] B. S. Mather. A method of studying the mechanical properties of long bones. *Journal of Surgical Research*, 7(5):226–230, 1967. 19, 20

[127] V. Mathieu, R. Vayron, G. Richard, G. Lambert, S. Naili, J.-P. Meningaud, and G. Haiat. Biomechanical determinants of the stability of dental implants:

Influence of the bone–implant interface properties. *Journal of Biomechanics*, 47(1):3–13, Jan. 2014. 24

[128] M. R. McClung, J. P. Brown, A. Diez-Perez, H. Resch, J. Caminis, P. Meisner, M. A. Bolognese, S. Goemaere, H. G. Bone, J. R. Zanchetta, J. Maddox, S. Bray, and A. Grauer. Effects of 24 Months of Treatment With Romosozumab Followed by 12 Months of Denosumab or Placebo in Postmenopausal Women With Low Bone Mineral Density: A Randomized, Double-Blind, Phase 2, Parallel Group Study. *Journal of Bone and Mineral Research*, 33(8):1397–1406, 2018. 56

[129] P. L. Mente, l. A. F. Stokes, H. Spence, and D. D. Aronsson. Progression of Vertebral Wedging in an Asymmetrically Loaded Rat Tail Model. *Spine*, 22(12):1292–1296, June 1997. 193

[130] A. Menzel. A fibre reorientation model for orthotropic multiplicative growth : CCConfigurational driving stresses, kinematics-based reorientation, and algorithmic aspects. *Biomechanics and Modeling in Mechanobiology*, 6(5):303–320, 2007. 104

[131] A. Menzel and E. Kuhl. Frontiers in growth and remodeling. *Mechanics Research Communications*, 42:1–14, 2012. 103, 104

[132] O. Messerer. *Über Elasticität und Festigkeit der menschlichen Knochen*. Verlag der J.G. Cotta'schen Buchhandlung, Stuttgart, 1880. 19

[133] R. A. Milch, D. P. Rall, and J. E. Tobie. Bone localization of the tetracyclines. *Journal of the National Cancer Institute*, 19(1):87–93, 1957. 15

[134] S. C. Miller, L. de Saint-Georges, B. M. Bowman, and W. S. Jee. Bone lining cells: structure and function. *Scanning microscopy*, 3(3):953–60; discussion 960–1, Sept. 1989. 16

[135] Z. Miller, M. B. Fuchs, and M. Arcan. Trabecular bone adaptation with an orthotropic material model. *Journal of Biomechanics*, 35(2):247–256, 2002. 105, 138, 139

[136] MM. les secrétaires perpétuels. *Comptes rendus hebdomadaires des séances de l'Académie des sciences*. Paris, Bachelier edition, 1857. 11

[137] M. G. Mullender and R. Huiskes. Proposal for the Regulatory Mechanism of Wolff's Law. *Journal of Orthopaedic Research*, 13:503–512, 1995. 23

[138] G. R. Mundy. The effects of TGF-beta on bone. *Ciba Foundation symposium*, 157:137–43; discussion 143–51, 1991. 8

[139] H. Narayanan, S. N. Verner, K. L. Mills, R. Kemkemer, and K. Garikipati. In silico estimates of the free energy rates in growing tumor spheroids. *Journal of Physics: Condensed Matter*, 22(19):194122, 2010. 104

[140] J. Nefussi, J. Sautier, V. Nicolas, and N. Forest. How osteoblasts become osteocytes: a decreasing matrix forming process. *Journal de Biologie Buccale*, 19(1):75–82, 1991. 16

[141] A. Nélaton. *Clinical lectures on surgery*, volume XXX. J. B. Lippincott & Co., Philadelphia, 1855. 13

[142] J. A. O'Connor, L. E. Lanyon, and H. MacFie. The influence of strain rate on adaptive bone remodelling. *Journal of Biomechanics*, 15(10):767–781, 1982. 20

[143] D. Padhi, M. Allison, A. J. Kivitz, M. J. Gutierrez, B. Stouch, C. Wang, and G. Jang. Multiple doses of sclerostin antibody romosozumab in healthy men and postmenopausal women with low bone mass: A randomized, double-blind, placebo-controlled study. *Journal of Clinical Pharmacology*, 54(2):168–178, 2014. 56

[144] D. Padhi, B. Stouch, G. Jang, L. Fang, M. Darling, H. Glise, M. K. Robinson, S. S. Harris, and E. Posvar. Anti-Sclerostin Antibody Increases Markers of Bone Formation in Healthy Postmenopausal Women. *Journal of Bone and Mineral Research*, 22(1):S37–S37, 2007. 55

[145] N. Paoletti, P. Liò, E. Merelli, and M. Viceconti. Multilevel computational modeling and quantitative analysis of bone remodeling. *IEEE/ACM Transactions on Computational Biology and Bioinformatics*, 9(5):1366–1378, 2012. 25

[146] J. F. Payne, E. R. Lankester, and W. T. Thiselton Dyer. Histology. *Quaterly Journal of Microscopical Science*, 14:403–418, 1874. 13

[147] M. J. Pead, R. Suswillo, T. M. Skerry, S. Vedi, and L. E. Lanyon. Increased 3H-uridine levels in osteocytes following a single short period of dynamic bone loading in vivo. *Calcified Tissue International*, 43(2):92–96, 1988. 17

[148] M. G. M. G. Penido and U. S. Alon. Phosphate homeostasis and its role in bone health. *Pediatric Nephrology*, 27(11):2039–2048, 2012. 8

[149] R. Perrier. *Éléments d'anatomie comparée*. Paris, j.-b. bail edition, 1893. 11, 13

[150] G. Perrusset. *Traitement de l'ankylose angulaire du genou par l'ostéoclasie sus-condylienne*. PhD thesis, Lyon, 1885. 13, 14

[151] M. C. Peterson and M. M. Riggs. Predicting nonlinear changes in bone mineral density over time using a multiscale systems pharmacology model. *CPT: Pharmacometrics & Systems Pharmacology*, 1(11):e14, 2012. 176

[152] H. E. Pettermann, T. J. Reiter, and F. G. Rammerstorfer. Computational simulation of internal bone remodeling. *Archives of Computational Methods in Engineering*, 4(4):295–323, 1997. 105

[153] D. Pflanz, A. I. Birkhold, L. Albiol, T. Thiele, C. Julien, A. Seliger, E. Thomson, I. Kramer, M. Kneissel, G. N. Duda, U. Kornak, S. Checa, and B. M. Willie. Sost deficiency led to a greater cortical bone formation response to mechanical loading and altered gene expression. *Scientific Reports*, 7(1):1–14, 2017. 55

[154] P. Pivonka, P. Buenzli, and C. Dunst. A Systems Approach to Understanding Bone Cell Interactions in Health and Disease. In *Cell Interaction*. InTech, Oct. 2012. 25, 27, 175

[155] P. Pivonka, P. R. Buenzli, S. Scheiner, C. Hellmich, and C. R. Dunstan. The influence of bone surface availability in bone remodelling-A mathematical model including coupled geometrical and biomechanical regulations of bone cells. *Engineering Structures*, 2013. 191

[156] P. Pivonka, J. Zimak, D. W. Smith, B. S. Gardiner, C. R. Dunstan, N. A. Sims, T. John Martin, and G. R. Mundy. Model structure and control of bone remodeling: A theoretical study. *Bone*, 43(2):249–263, 2008. 1, 4, 25, 28, 175, 184

[157] J. Quekett. On the Intimate Structure of Bone, as composing the Skeleton in the four great Classes of Animals, viz., Mammals, Birds, Reptiles, and Fishes, with some Remarks on the great Value of the Knowledge of such Structure in determining the Affinities of Minute. In J. Van Voorst, editor, *Transactions of the Microscopical Society of London*. London, 1844. 14

[158] Raige-Delorme and Bouley. *Nouveau Dictionnaire lexico graphique et descriptif des sciences médicales et vétérinaires*. Paris, 1851. 11, 12

[159] S. Ramtani. Electro-mechanics of bone remodelling. *International Journal of Engineering Science*, 46(11):1173–1182, Nov. 2008. 21

[160] S. Ramtani and M. Zidi. Damaged-bone remodeling theory: Thermodynamical approach. *Mechanics Research Communications*, 26(6):701–708, Nov. 1999. 26, 105

[161] A. A. Rauber. *Elasticität und Festigkeit der Knochen : anatomisch-physiologisch Studie*. Wilhelm Engelmann, Leipzig, 1876. 19

[162] A. Richet. *Traité pratique d'anatomie médico-chirurgicale*. Paris, 1877. 10, 11

[163] E. Rindfleish. *A Text-book of Pathological Histology: An Introduction to the Study of Pathological Anatomy*. Philadelphia, 1872. 14

[164] C. Robin. The marrow of bones, in the healthy and morbid states. *British Medical Journal*, 1:595–597, 1865. 13, 14

[165] E. K. Rodriguez, A. Hoger, and A. D. McCulloch. Stress-dependent finite growth in soft elastic tissues. *Journal of Biomechanics*, 27(4):455–467, Apr. 1994. 103

[166] H. Roesler. The history of some fundamental concepts in bone biomechanics. *Journal of Biomechanics*, 20(11-12):1025–1034, 1987. 18, 19

[167] G. D. Roodman. Advances in Bone Biology: The Osteoclast. *Endocrine Reviews*, 17(4):308–332, Aug. 1996. 17

[168] F. P. Ross. Osteoclasts. *Vitamin D*, pages 335–347, 2011. 17

[169] W. Roux. *Der Kampf der Teile des Organismus*. Engelmann, Leipzig, 1881. 18, 20, 23

[170] V. Sansalone, J. Kaiser, S. Naili, and T. Lemaire. Interstitial fluid flow within bone canaliculi and electro-chemo-mechanical features of the canalicular milieu. *Biomechanics and Modeling in Mechanobiology*, 12(3):533–553, June 2013. 21

[171] V. Sansalone, S. Naili, and A. Di Carlo. On the rotary remodelling equilibrium of bone. *Computer Methods in Biomechanics and Biomedical Engineering*, 14(sup1):203–204, 2011. 105, 106, 107

[172] S. Scheiner, P. Pivonka, and C. Hellmich. Coupling systems biology with multiscale mechanics, for computer simulations of bone remodeling. *Computer Methods in Applied Mechanics and Engineering*, 254:181–196, Feb. 2013. 2, 4, 26, 27, 28, 29, 175, 180

[173] S. Scheiner, P. Pivonka, and C. Hellmich. Poromicromechanics reveals that physiological bone strains induce osteocyte-stimulating lacunar pressure. *Biomechanics and Modeling in Mechanobiology*, 15:9–28, 2016. 21

[174] F. A. Schulte, D. Ruffoni, F. M. Lambers, D. Christen, D. J. Webster, G. Kuhn, and R. Müller. Local Mechanical Stimuli Regulate Bone Formation and Resorption in Mice at the Tissue Level. *PLoS ONE*, 8(4), 2013. 23

[175] L. Schwartz, H. Maitournam, C. Stolz, J. Steayert, M. Ho Ba Tho, and B. Halphen. Growth and cellular differentiation: a physico-biochemical conundrum? The example of the hand. *Medical Hypotheses*, 61(1):45–51, July 2003. 21

[176] Y. Shang, L. Peng, and J. Bai. A Three-dimensional Orthotropic Adaptation Algorithm for Femur Remodeling. In R. Magjarevic and J. H. Nagel, editors, *World Congress on Medical Physics and Biomedical Engineering 2006*, pages 3038–3040, Berlin, Heidelberg, 2007. Springer Berlin Heidelberg. 138, 139

[177] G. F. Shrady. *The Medical Record: A Weekly Journal of Medicine and Surgery*. New York, William Wo edition, 1877. 13

[178] R. Skalak, G. Dasgupta, M. Moss, E. Otten, P. Dullemeijer, and H. Vilmann. Analytical description of growth. *Journal of Theoretical Biology*, 94(3):555–577, Feb. 1982. 103

[179] J. G. Skedros and S. L. Baucom. Mathematical analysis of trabecular 'trajectories' in apparent trajectorial structures: The unfortunate historical emphasis on the human proximal femur. *Journal of Theoretical Biology*, 244(1):15–45, 2007. 137, 140

[180] I. A. F. Stokes, H. Spence, D. D. Aronsson, and N. Kilmer. Mechanical Modulation of Vertebral Body Growth. *Spine*, 21(10):1162–1167, May 1996. 193

[181] M. Stolina, D. Dwyer, Q. T. Niu, K. S. Villasenor, P. Kurimoto, M. Grisanti, C. Y. Han, M. Liu, X. Li, M. S. Ominsky, H. Z. Ke, and P. J. Kostenuik. Temporal changes in systemic and local expression of bone turnover markers during six months of sclerostin antibody administration to ovariectomized rats. *Bone*, 67:305–313, 2014. 56

[182] L. A. Taber. Biomechanics of Growth, Remodeling, and Morphogenesis. *Applied Mechanics Reviews*, 48(8):487–545, Aug. 1995. 103

[183] H. Tanabe, Y. Aota, N. Nakamura, and T. Saito. A histomorphometric study of the cancellous spinal process bone in adolescent idiopathic scoliosis. *European Spine Journal*, 26(6):1600–1609, 2017. 194

[184] C. C. Tang, C. Benson, J. McColm, A. Sipos, B. Mitlak, and L. J. Hu. Population Pharmacokinetics and Pharmacodynamics of Blosozumab. In *American Conference on Pharmacokinetics*, pages W–15, Arlington, Virginia, USA, 2015. 57

[185] A. Tavernier, J.-P. Beaude, E. Beaugrand, P.-L.-B. Caffe, H.-E. Robiquet, L. Gustin, L.-V. Boutereau, and L. Hébert. *Journal des connaissances médicales pratiques en pharmacologie*. Paris, 1857. 13

[186] S. Taylor, M. S. Ominsky, R. Hu, E. Pacheco, Y. D. He, D. L. Brown, J. I. Aguirre, T. J. Wronski, S. Buntich, C. A. Afshari, I. Pyrah, P. Nioi, and R. W. Boyce. Time-dependent cellular and transcriptional changes in the osteoblast lineage associated with sclerostin antibody treatment in ovariectomized rats. *Bone*, 84:148–159, Mar. 2016. 56

[187] F. E. Tilton, J. J. Degioanni, and V. S. Schneider. Long-term follow-up of Skylab bone demineralization. *Aviation, space, and environmental medicine*, 51(11):1209–13, Nov. 1980. 20

[188] J. Tomes and C. S. Tomes. *Traité de chirurgie dentaire, ou Traité complet de l'art du dentiste*. Paris, F Savy edition, 1873. 11

[189] K. N. Tu, J. D. Lie, C. K. V. Wan, M. Cameron, A. G. Austel, J. K. Nguyen, K. Van, and D. Hyun. Osteoporosis: A Review of Treatment Options. *P & T: a peer-reviewed journal for formulary management*, 43(2):92–104, 2018. 56

[190] F.-J. Ulm, E. Lemarchand, and F. H. Heukamp. Elements of chemomechanics of calcium leaching of cement-based materials at different scales. *Engineering Fracture Mechanics*, 70(7-8):871–889, May 2003. 157

[191] M. C. van der Meulen and R. Huiskes. Why mechanobiology? *Journal of Biomechanics*, 35(4):401–414, Apr. 2002. 25

[192] A. H. Van Lierop, N. A. Hamdy, H. Hamersma, R. L. Van Bezooijen, J. Power, N. Loveridge, and S. E. Papapoulos. Patients with sclerosteosis and disease carriers: Human models of the effect of sclerostin on bone turnover. *Journal of Bone and Mineral Research*, 26(12):2804–2811, 2011. 54

[193] R. F. M. van Oers, R. Ruimerman, B. van Rietbergen, P. A. J. Hilbers, and R. Huiskes. Relating osteon diameter to strain. *Bone*, 2008. 24

[194] R. Vayron, M. Matsukawa, R. Tsubota, V. Mathieu, E. Barthel, and G. Haiat. Evolution of bone biomechanical properties at the micrometer scale around titanium implant as a function of healing time. *Physics in Medicine and Biology*, 59(6):1389–1406, Mar. 2014. 24

[195] G. H. von Meyer. Die Architektur der Spongiosa. (Zehnter Beitrag zur Mechanik des menschlichen Knochgerüstes). *Archiv fur Anatomie, Physiologie, und wissenschaftliche Medizin*, 6:615–628, 1867. 18, 140

[196] J. Wang, D. Lü, D. Mao, and M. Long. Mechanomics: an emerging field between biology and biomechanics. *Protein & Cell*, 5(7):518–531, jul 2014. 21

[197] Z. Wang, H. Chen, Y. E. Yu, J. Zhang, K. Y. Cheuk, B. K. Ng, Y. Qiu, X. E. Guo, J. C. Cheng, and W. Y. Lee. Unique local bone tissue characteristics in iliac crest bone biopsy from adolescent idiopathic scoliosis with severe spinal deformity. *Scientific Reports*, 7:1–10, Dec 2017. 194, 195

[198] K. Warmington, S. Morony, I. Sarosi, J. Gong, P. Stephens, D. G. Winkler, M. K. Sutherland, J. A. Latham, H. Kirby, A. Moore, M. Robinson, P. J. Kostenuik, W. S. Simonet, D. L. Lacey, and C. Paszty. Sclerostin Antagonism in Adult Rodents, via Monoclonal Antibody Mediated Blockade, Increases Bone Mineral Density and Implicates Sclerostin as a Key Regulator of Bone Mass During Adulthood. *Journal of Bone and Mineral Research*, 19:S56–57, 2004. 55

[199] A. Watzky and S. Naili. Orthotropic bone remodeling: case of plane stresses. *Mechanics Research Communications*, 31(5):617–625, Sept. 2004. 105

[200] M. N. Wein. Bone Lining Cells: Normal Physiology and Role in Response to Anabolic Osteoporosis Treatments. *Current Molecular Biology Reports*, 3(2):79–84, 2017. 16

[201] H. Weinans, R. Huiskes, and H. J. Grootenboer. The behavior of adaptive bone-remodelling simulation models. *Journal of Biomechanics*, 25(12):1425–1441, 1992. 23

[202] R. Weinkamer, M. A. Hartmann, Y. Brechet, and P. Fratzl. Stochastic lattice model for bone remodeling and aging. *Physical Review Letters*, 93(22):1–4, 2004. 23

[203] G. Wertheim. *Mémoire sur l'élasticité et la cohésion des principaux tissus du corps humain*. 1847. 18

[204] W. J. Whitehouse. The quantitative morphology of anisotropic trabecular bone. *Journal of microscopy*, 101(Pt 2):153–68, July 1974. 20

[205] P. C. Witcher, S. E. Miner, D. J. Horan, W. A. Bullock, K.-E. Lim, K. S. Kang, A. L. Adaniya, R. D. Ross, G. G. Loots, and A. G. Robling. Sclerostin neutralization unleashes the osteoanabolic effects of Dkk1 inhibition. *JCI Insight*, 3(11), June 2018. 56

[206] J. Wolff. Ueber die innere Architectur der Knochen und ihre Bedeutung für die Frage vom Knochenwachsthum. *Archiv für Pathologische Anatomie und Physiologie und für Klinische Medicin*, 50(3):389–450, June 1870. 1, 18, 23, 105, 140

[207] J. Wolff. *Das Gesetz der Transformation der Knochen*. Berlin, Germany, 1892. 140

[208] J. Wolff. The classic: on the inner architecture of bones and its importance for bone growth. 1870. *Clinical orthopaedics and related research*, 468(4):1056–1065, 2010. 18, 160, 184

[209] H.-K. Wong and K.-J. Tan. The natural history of adolescent idiopathic scoliosis. *Indian Journal of Orthopaedics*, 44(1):9, 2010. 194

[210] S. L. Woo, S. C. Kuei, D. Amiel, M. A. Gomez, W. C. Hayes, F. C. White, and W. H. Akeson. The effect of prolonged physical training on the properties of long bone: a study of Wolff's Law. *The Journal of bone and joint surgery. American volume*, 63(5):780–7, June 1981. 20

[211] World Health Organization. Assessment of fracture risk and its application to screening for postmenopausal osteoporosis : report of a WHO study group. Technical report, 1994. 55

[212] J. J. Wysolmerski. Osteocytic osteolysis: time for a second look? *BoneKEy reports*, 1:229, Dec. 2012. 22

[213] G. Zaman, A. A. Pitsillides, S. C. F. Rawlinson, R. F. L. Suswillo, J. R. Mosley, M. Z. Cheng, L. A. M. Platts, M. Hukkanen, J. M. Polak, and L. E. Lanyon. Mechanical Strain Stimulates Nitric Oxide Production by Rapid Activation of Endothelial Nitric Oxide Synthase in Osteocytes. *Journal of Bone and Mineral Research*, 14(7):1123–1131, 1999. 30

[214] F. Zhu, Y. Qiu, H. Y. Yeung, K. M. Lee, and C. Y. J. Cheng. Trabecular bone micro-architecture and bone mineral density in adolescent idiopathic and congenital scoliosis. *Orthopaedic surgery*, 1(1):78–83, 2009. 194

List of publications

Articles in international journals

M. Martin, V. Sansalone, D. M. L. Cooper, M. Forwood, P. Pivonka. Assessment of romosozumab efficacy in the treatment of postmenopausal osteoporosis: results from a mechanistic PK-PD mechanostat model of bone remodeling. *Bone, tentatively accepted*, 2019.

M. Martin, T. Lemaire, G. Haïat, P. Pivonka, V. Sansalone. Material orthotropic remodeling as a thermodynamically-driven evolution. *Journal of Mechanics in Medicine and Biology, accepted*, 2019.

M. Martin, V. Sansalone, D. M. L. Cooper, M. Forwood, P. Pivonka. Mechanobiological osteocyte feedback drives mechanostat regulation of bone in a multiscale computational model. *Biomechanics and Modeling in Mechanobiology*, 18(5):1475-1496, 2019.

M. Martin, T. Lemaire, G. Haïat, P. Pivonka, V. Sansalone. A thermodynamically consistent model of bone rotary remodeling: a 2D study. *Computer Methods in Biomechanics and Biomedical Engineering*, 20(sup1):127-128, 2017.

International conferences

M. Martin, V. Sansalone, D. M. L. Cooper, M. Forwood, P. Pivonka. A multiscale model of remodeling bridging bone mechanics and biochemistry. In *European Society of Biomechanics Conference 2019*, Vienna, Austria, 2019.

M. Martin, P. Pivonka, G. Haïat, T. Lemaire, V. Sansalone. A novel generalized continuum thermodynamics framework to describe bone remodeling and mineralization. In *International Conference on Nonlinear Solid Mechanics*, Roma, Italy, 2019.

M. Martin, V. Sansalone, D. M. L. Cooper, M. Forwood, P. Pivonka. A model of bone mechanostat directed by osteocytes mechanosensation. In *11th Australasian Biomechanics Conference 2018*, Auckland, New Zealand, 2018.

M. Martin, V. Sansalone, D. M. L. Cooper, M. Forwood, L. Bonewald, P. Pivonka. Effect of sclerostin monoclonal antibody therapy on BMD is linked to osteocyte sensitivity – insights from a mechanobiological model of bone remodeling. In *ANZBMS 24th Annual Scientific Meeting*, Queenstown, New Zealand, 2018.

P. Pivonka, M. Martin, S. Scheiner, V. Sansalone, D. M. L. Cooper, M. Forwood, L. Bonewald. A multiscale computational model for mechanostat regulation in bone based on biochemical osteocyte feedback. In *Lacroix, Damien (Ed.) 8th World Congress of Biomechanics*, Dublin, Ireland, 2018.

M. Martin, T. Lemaire, G. Haïat, P. Pivonka, V. Sansalone. Thermodynamics rendering rotary bone remodeling: a 2D model. In *4th ECCOMAS Young Investigators Conference*, Milan, Italy, 2017.

National conferences

M. Martin, P. Pivonka, G. Haïat, V. Sansalone, T. Lemaire. Un modèle multi-échelles de remodelage osseux reliant les influences biochimiques et mécaniques. In *Congrès Français de Mécanique*, Brest, France, 2019.

V. Sansalone, M. Martin, G. Haïat, P. Pivonka, T. Lemaire. Bone remodeling recast in the generalized continuum mechanics. In *Euromech 594 Bone remodeling: multiscale mechanical models and multiphysical aspects*, Nancy, France, 2018.

M. Martin, T. Lemaire, G. Haïat, P. Pivonka, V. Sansalone. A thermodynamically consistent model of bone rotary remodeling: a 2D study. In *42nd Congress of the Société de Biomécanique (SB2017)*, Reims, France, 2017.

Synopsis (Français)

La structure et la composition chimique de nos os changent au cours de la vie : c'est le remodelage osseux. Ces modifications dépendent de multiples facteurs d'origine mécanique ou chimique. En effet, les cellules osseuses vivant dans les pores du tissu osseux sont sensibles aux variations de leur environnement. Dans ce contexte, nous nous intéressons en particulier au mécanome, c'est-à-dire à la description de l'action de la mécanique sur les tissus biologiques.

Pour ce faire, nous approfondissons plusieurs approches de modélisation mécanistique du remodelage osseux : l'une aborde la question à l'échelle cellulaire, l'autre à l'échelle macroscopique de l'organe. Nous proposons finalement une association de ces points de vue dans une théorie unificatrice couplant les stimuli biochimiques et mécaniques du remodelage pour décrire l'évolution du tissu osseux. Enfin, nous présentons les premières étapes d'une application clinique dans le contexte de la scoliose idiopathique de l'adolescent.

Synopsis (English)

The structure and chemical composition of our bones change over the course of life through a process called bone remodeling. These modifications depend on diverse factors of mechanical or chemical origin. Indeed, bone cells living in the pores of bone tissue are sensitive to variations in their environment. In this context, we are particularly interested in the mechanomics, which is the description of the action of mechanics on biological tissues.

Hence, we explore several approaches to mechanistic modeling of bone remodeling: one addresses the question at the cellular level, the other at the macroscopic level of the organ. We finally propose a combination of these points of view in a unifying theory coupling the biochemical and mechanical stimuli of bone remodeling to depict the evolution of the bone tissue. Finally, we present the first steps of a clinical application in the context of adolescent idiopathic scoliosis.